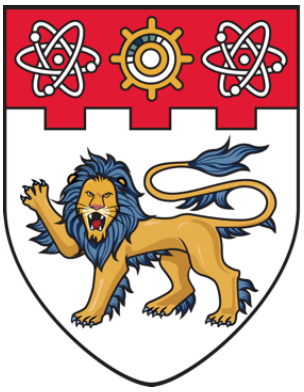

NANYANG TECHNOLOGICAL UNIVERSITY
SINGAPORE

Localised and Bifurcating Structures in Planar Shear Flows

Wang Zhe

Interdisciplinary Graduate School
Energy Research Institute @ NTU

A thesis submitted to the Nanyang Technological University
in partial fulfillment of the requirements for the degree of
Doctor of Philosophy

2019

Statement of Originality

I hereby certify that the work embodied in this thesis is the result of original research, is free of plagiarised materials, and has not been submitted for a higher degree to any other University or Institution.

11 November 2019

Date

Wang Zhe

Supervisor Declaration Statement

I have reviewed the content and presentation style of this thesis and declare it is free of plagiarism and of sufficient grammatical clarity to be examined. To the best of my knowledge, the research and writing are those of the candidate except as acknowledged in the Author Attribution Statement. I confirm that the investigations were conducted in accord with the ethics policies and integrity standards of Nanyang Technological University and that the research data are presented honestly and without prejudice.

11 November 2019

Date

Prof. Claude Guet

Authorship Attribution Statement

This thesis contains material from 1 paper submitted to the Journal of Fluid Mechanics for peer-review, where I was the first and corresponding author.

11 November 2019

Date

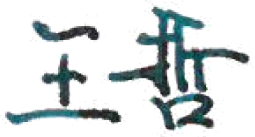

Wang Zhe

Acknowledgements

I wish to express my sincere gratitude to Professor Claude Guet who saved my scientific life by vouching for me and becoming my supervisor at the point when I almost quit my PhD one and half years ago. His deep interest in supporting young physicists in all ways make the present thesis possible. I appreciated very much that, despite how busy he was, Prof Guet was always present to discussing anything on one hand, and gave me almost complete freedom and support on developing my original theory on the transition to turbulence on the other.

I thank Professors Romain Monchuax and Yohann Duguet, who introduced me to the topic of quadrupolar flows and supervised my research during my stay in ENSTA Paris-Tech, Palaiseau, France. Their first-hand knowledge and unpublished data ensured me a quick start in the project and inspired my derivation of the governing equations for the large-scale flows.

I thank Professors Bérengère Dubrulle and Bruno Eckhardt for teaching me mathematics and sharing with me the physical intuitions. Interesting, their ideas always came as "pairs of counter-rotating streamwise vortices"[1], and it was a great experience to discussing physics and deriving equations with them.

I thank Professor Dennis Sullivan who answered from time to time my "cute" questions and led me to theorems which are most relevant to my research. I thank Professor Laurette Tuckerman who pointed me out a mistake before I am going to make it and gave me advises on direct numerical simulations.

[1]Here is an example. While deriving the governing equations for the large-scale flows, I reduced the equation for the wall-normal velocity $\tilde{u}_y$ from a fourth-order differential equation with respect to y to a second-order one. Hence the no-slip boundary conditions $\tilde{u}_y = \partial_y \tilde{u}_y = \tilde{\omega}_y = 0$ at the walls do not apply. As a compromise, the boundary conditions I considered at that time was $\tilde{u}_y = \tilde{\omega}_y = 0$ at the walls. During my discussion with Prof Eckhardt, he suggested to consider the "stress-free" boundary conditions $\tilde{u}_y = \partial_y \tilde{\omega}_y = 0$ at the walls; while when I asked the same question to Prof Dubrulle, she suggested, without a second thought, the following "no-slip" boundary conditions : $\partial_y \tilde{u}_y = \tilde{\omega}_y = 0$ at the walls. It was the investigation of these two "counter-rotating" boundary conditions led me to discover a topological origin of the quadrupolar flows. These two boundary conditions are treated in Chapter 3 and Appendix B, respectively.

Special thank to Professor Paul Manneville, who pointed out the divergence of the asymptotic analysis at $Re > 1$, a method which was originally used in Chapter 3.

I thank Pavan Kashyap for sharing with me his simulation results on turbulent spots in plane Couette flow.

Fruitful discussions with Professors Cyril Touzé, Luc Pastur, Vlad Sergiescu, John Guckenheimer, and Michael Kosterlitz are also gratefully acknowledged.

I thank Professor François Daviaud for initiating the collaboration on the quadrupolar flow project and for his encouragement.

I thank Professor Bo Liedberg who introduced me to Prof Guet and supported my visit to SPEC CEA, Saclay, France.

I thank Professor Subodh Mhaisalkar who hired me as a project officer at Research Energy Institute at Nanyang Technological University (Eri@N) but granted me the freedom to work on my own PhD topic in France.

I would also thank Professor So Ping Lam for enrolling me as a PhD student.

Finally, I would like to thank my mother, Zheng Xiao Ning, who gave me my first course in fluid dynamics when I was a teenager. This thesis would not have been possible without her endless encouragement and understanding.

Wang Zhe
17 June 2019

It is with great sadness that I acknowledge the death of Professor Bruno Eckhardt (1960-2019) on 7 August 2019. Professor Eckhardt was the first one who initiated a theoretical analysis of quadrupolar flows. During the last year of my PhD candidature, Professor Eckhardt helped me with the derivations and proposed the title: "localised and bifurcating structures in planar shear flows", of this thesis. I owe him a debt of gratitude for education, guidance, and leadership.

Wang Zhe
11 November 2019

"The success of attempts to solve problems in turbulence depends strongly on the inspiration involved in making the crucial assumption."

—H. Tennekes and J. L. Lumley

Abstract

Turbulent spots in planar shear flows are always accompanied by the presence of (i) the quadrupolar flows outside the spot; and (ii) the counter-rotating streamwise vortices inside the spot. In the present thesis, those flow structures, i.e. quadrupolar flows and streamwise vortices have been treated analytically :

By exploiting the geometric scale separation inscribed in all planar shear flows, equations governing the large-scale flow surrounding turbulent spots has been derived from the Navier-Stokes equations and solved analytically. Based exclusively on the obtained analytical solutions, the origin of the quadrupolar angular dependence is identified as (i) the presence of the flow shear in the streamwise direction; and (ii) the breaking of the spatial homogeneity in the spanwise direction. The quadrupolar flow decays algebraically with power-law exponent -3 in the far-field and characterised by an exponentially localised reversed flow centred at the turbulent spot. Moreover, the topological origin of the quadrupolar flow is unveiled.

By linearising the Navier-Stokes equations about a pair of counter-rotating rigid vortices and upon a Fourier transform in three spatial directions, a three-dimensional dynamical system is obtained. The proposed model corresponds to the $\mathbb{Z}_2$-symmetric pitchfork/Hopf problem, whose linear instability is the centrifugal instability. As long as the rotational symmetry is preserved, the system can have at most a pair of reflectional symmetric invariant two-tori, signifying the quasiperiodicity. With broken rotational symmetry, periodic orbits can experience a Neimark-Sacker bifurcation leading to a torus, a phase locking, a period doubling cascade, a heteroclinic bifurcation, a coexistence between the quasiperiodic and chaotic behaviours. All of these phenomena occur in a narrow region of parameter space, complicating the assignment of the single route to chaos.

Contents

Acknowledgements ix

Abstract xiii

List of Figures xix

List of Tables xxi

Symbols and Acronyms xxiii

1 Introduction 1
- 1.1 Consensual revisit of pipe flow experiments . . . 2
- 1.2 The long and winding road . . . 7
  - 1.2.1 Onset of turbulence in time . . . 7
  - 1.2.2 Spread of turbulence in space . . . 11
- 1.3 Objectives and Scope . . . 14
  - 1.3.1 Large-scale flows outside turbulent patches . . . 15
  - 1.3.2 Counter-rotating streamwise vortices inside turbulent patches . . . 15
- 1.4 Outline of the thesis . . . 16

2 Historical survey on the transitional flow regime 17
- 2.1 Overview . . . 17
- 2.2 Transition to turbulence in planar flows . . . 18
  - 2.2.1 Turbulent spots and coherent structures . . . 18
  - 2.2.2 Large-scale quadrupolar flows . . . 21
  - 2.2.3 Transition to turbulence in plane Couette flow . . . 25
- 2.3 Navier-Stokes equations . . . 29
  - 2.3.1 Main difficulties of the Navier-Stokes equations . . . 30
    - 2.3.1.1 Nonlinearity . . . 30
    - 2.3.1.2 Nonintegrability . . . 32
    - 2.3.1.3 Nonlocality . . . 34
  - 2.3.2 Conditions for eliminating nonlinearity . . . 36
    - 2.3.2.1 Laminar flow at low Reynolds numbers . . . 36
    - 2.3.2.2 Weakly perturbed flow near linear instability threshold . . . 37

2.3.2.3 Linear instability analysis I: Orr-Sommerfeld equation . 40
2.3.2.4 Linear instability analysis II: Kelvin mode solution . . . 41
2.3.2.5 Linear instability analysis III: limitation and extension . 43
2.3.2.6 Perturbed flow in rapid distortion limit 45
2.3.2.7 Flow in rotating coordinates 47

3 Quadrupolar flows around spots in internal shear flows 51
3.1 Introduction 51
3.2 Formulation 52
3.2.1 Linearised Navier-Stokes equations 52
3.2.2 Geometric scale separation in plane Couette flow 55
3.2.3 Poloidal-toroidal decomposition 58
3.2.4 Kelvin wake formalism 59
3.2.5 Boundary conditions 61
3.2.6 Forcing selection 63
3.2.6.1 Minimal assumption model for a localised spot 64
3.2.6.2 Parity of the forcing 65
3.3 Analytical solutions for poloidal and toroidal functions 66
3.3.1 Modal solutions 67
3.3.2 Inverse Fourier transform 68
3.4 Large-scale flows 70
3.4.1 Analytical expressions for the wall-normal averaged flow 70
3.4.2 Quadrupolar flow and algebraic asymptote 71
3.4.3 Coexistence of exponential and algebraic decays 72
3.4.3.1 Single-mode model versus two-mode model 73
3.4.3.2 Reversed quadrupolar flow 74
3.4.4 Topological origin of the quadrupolar flow 79
3.5 Conclusions and oulooks 81
3.5.1 The asymptotic decay of the quadrupolar flow is algebraic 82
3.5.2 Existence of an exponentially localised reversed quadrupolar flow 83
3.5.3 Topological origin of the algebraically decaying quadrupolar flow . 83

4 Bifurcation analysis for counter-rotating vortices 85
4.1 Introduction 85
4.2 Formulation 87
4.2.1 Scaling analysis for flows in rotating coordinates 88
4.2.2 Normal form 91
4.3 Bifurcation analysis for flows with rotational symmetry 95
4.3.1 Hopf bifurcation in the phase plane 97
4.3.1.1 Case 1: unbounded periodic orbits 98
4.3.1.2 Case 2: periodic orbits confined within a heteroclinic cycle 99
4.3.2 Heteroclinic tangency in the phase plane 104
4.3.3 Non-chaotic transient 108

4.4 Bifurcation analysis for flows with broken rotational symmetry 111
4.4.1 Quasiperiodicity and circle map 112
4.4.2 Phase locking and torus bifurcation 115
4.4.3 Peculiar devil's staircase 120
4.5 Discussion and conclusions 125

5 Discussion and future works **129**
5.1 General discussion 129
5.2 Quadrupolar flows outside turbulent spot 130
5.3 Bifurcating vortices inside turbulent spot 132

A Quadrupolar flows arising from an external perturbation **135**
A.1 Modal solutions for poloidal and toroidal functions 136
A.1.1 Modal solutions 137
A.1.2 Continued fraction expansion 138
A.2 Large-scale flows 141

B Quadrupolar flows in shear flows between two porous walls **147**
B.1 Governing equations 148
B.1.1 Perturbative expansion 148
B.2 Modal solutions 150
B.3 Analytical solutions 151

C Quadrupolar flows in plane Poiseuille flow **157**
C.1 Governing equations and forcing selection 158
C.2 Solutions for poloidal and toroidal functions 161
C.2.1 Large-scale flows 163

D Method of eigenfunction expansion **167**
D.1 Solutions obtained from method of undetermined coefficients 167
D.1.1 Solutions forced by an even forcing 168
D.1.2 Solutions forced by an odd forcing 168
D.2 Eigenfunction expansion 169
D.2.1 Solutions forced by an even forcing 169
D.2.2 Solutions forced by an odd forcing 170

E Evaluate integrals involving Bessel and rational functions **173**

F Bifurcation analysis for competitively exclusive flows **175**

G List of Author's Publications **179**

Bibliography **181**

List of Figures

1.1 Sum of times cited per year . . . 2
1.2 Setup of the Reynolds' pipe experiment. . . . 3
1.3 Onset of turbulence in pipe flow. . . . 4
1.4 Lifetime of turbulent puffs in pipe flow. . . . 5
1.5 Mean lifetime of a puff before decaying or splitting. . . . 6
1.6 Power spectra of fluid velocities demonstrating quasiperiodicity. . . . 9
1.7 Bifurcation diagrams exhibiting super- and sub-critical behaviours. . . . 10
1.8 Directed percolation and in cylindrical Couette flow. . . . 13

2.1 Turbulent spots in planar shear flows. . . . 19
2.2 Counter-rotating pairs of streamwise vortices. . . . 20
2.3 Large-scale flows in planar shear flows. . . . 23
2.4 Direction fields associated with a $k = 1$ topological defect. . . . 24
2.5 Structurally unstable topological defect. . . . 24
2.6 Experimental apparatus of plane Couette flow. . . . 25
2.7 Bifurcation diagram of transition to turbulence in plane Couette flow. . . . 26
2.8 Exponentially decaying quadrupolar flow. . . . 28
2.9 Tails of quadrupolar flow. . . . 28
2.10 The self-sustaining process. . . . 44
2.11 Morph of exact coherent structures under homotopy. . . . 46

3.1 Schematic representation of forcing arising from an autonomous spot. . . . 65
3.2 Quadrupolar in-plane flow. . . . 75
3.3 Contours of the wall-normal vorticity. . . . 76
3.4 Contours of the velocity components. . . . 77
3.5 Decay of the velocity components. . . . 78
3.6 Contours of the wall-normal averaged pressure. . . . 79

4.1 An illustration of the transition to turbulence in planar shear flows. . . . 86
4.2 An illustration of the phase space. . . . 95
4.3 Unfolding and phase portraits of the planar system: Case 1.1. . . . 99
4.4 Unfolding and phase portraits of the planar system: Case 1.2. . . . 100
4.5 Unfolding and phase portraits of the planar system: Case 1.3. . . . 100
4.6 Unfolding and phase portraits of the planar system: Case 2. . . . 101
4.7 Level curves of the Hamiltonian function. . . . 105

4.8 Phase portraits near the Hopf bifurcation. . . . 107
4.9 Probability density function of the relative helicity density. . . . 109
4.10 Non-chaotic transient. . . . 110
4.11 Invariant two-torus embedded in three dimensions. . . . 113
4.12 Poincaré section for motions on a torus. . . . 114
4.13 Phase locking and period doubling. . . . 116
4.14 Bifurcation scenarios on the Poincaré section. . . . 118
4.15 Bifurcation scenarios on the Poincaré section (continued). . . . 119
4.16 Devil's staircase. . . . 121
4.17 Coexisting torus knot attractors in the phase space. . . . 122
4.18 Coexistence between torus and torus knot attractor in the phase space. . . . 123
4.19 Bifurcation diagram. . . . 124

A.1 Schematic representation of forcing due to two counter-acting water jets. 136
A.2 Leading order approximations for the hyperbolic tangent function. . . . 139
A.3 Test integral and its approximations. . . . 140
A.4 The decay of the streamwise velocity. . . . 142
A.5 Quadrupolar in-plane flow. . . . 143
A.6 Contours of the velocity components. . . . 144
A.7 Contours of the pressure component. . . . 145
A.8 Superposition between the y-averaged wall-normal vorticity and the in-plane directional field. . . . 145

B.1 Quadrupolar in-plane flow with penetrating no-slip boundary conditions. 153
B.2 Velocity contours with penetrating no-slip boundary conditions. . . . 154
B.3 Pressure field with penetrating no-slip boundary conditions. . . . 155

C.1 Superposition between the y-averaged wall-normal vorticity and the in-plane directional field. . . . 165
C.2 Contours of the pressure component. . . . 165
C.3 Contours of the velocity components. . . . 166

F.1 The unfolding of the planar system (F.3). . . . 176
F.2 Qualitative bifurcations of the three-dimensional flow. . . . 177

List of Tables

1.1 Critical exponents of directed percolation in D dimensions. 12

4.1 Classification of fifth-order unfolding terms. 102

Symbols and Acronyms

Navier-Stokes equations	governing equations of the fluid motions, 31.
Reynolds number Re	control parameter of the Navier-Stokes equations, 5.
Directed percolation	propagation of activities through connected space, 11.
Coherent structures	flow structures that persist in space and in time, 14.
Vorticity $\boldsymbol{\omega} = \nabla \times \boldsymbol{u}$	curl of fluid velocity $\boldsymbol{u}$, 32.
Lamb vector $\boldsymbol{u} \times \boldsymbol{\omega}$	nonlinear term in the Navier-Stokes equations, 33.
Helicity density $\boldsymbol{u} \cdot \boldsymbol{\omega}$	measure of coherence, 33.
Coriolis force $-2\boldsymbol{\Omega} \times \boldsymbol{u}$	force due to transform of coordinates, 50.
Centrifugal force $-\boldsymbol{\Omega} \times (\boldsymbol{\Omega} \times \boldsymbol{r})$	force due to transform of coordinates, 50.
Euler force $-\mathrm{d}_t \Omega \times \boldsymbol{r}$	force due to transform of coordinates, 50.
Rossby number ϵ	ratio of inertial to Coriolis forces, 51.
Ekman number ϵRe^{-1}	ratio of viscous to Coriolis forces, 89.
Lubrication theory	scale analysis using disparity of length scales, 57.
Poloidal-toroidal decomposition	representation of incompressible vector fields, 59.
Airy functions Ai & Bi	solutions to the Airy equation, 44.
Bessel functions J_m	solutions to the Bessel equation, 71.
Modified Bessel functions K_m	solutions to the modified Bessel equation, 71.
Fixed points	stationary solutions to differential equations, 97.
Periodic orbits	solutions that repeat themselves in time, 98.
Poincaré section	traces of periodic orbits on a hyperplane, 96.
Saddle points	fixed points with stable and unstable manifolds, 102.
Heteroclinic cycles	connections of different saddle points, 102.
Smale horseshoe	invariant set due to the transverse homoclinicity, 112.

Chapter 1

Introduction

In Eastern languages, e.g. in Chinese (湍流) and in Japanese (紊流), the meaning of turbulence is so intertwined with the concept of chaos that the term "turbulence" comprises two characters: the former signifies "vortical and chaotic" while the later signifies "flow". In western languages, e.g. in English and in French, the term "turbulence" originates from the Latin "turbulentus", meaning "full of commotion, restless, disturbed, boisterous, stormy". Although the term "turbulence" was first introduced into the scientific community describing a certain kind of fluid motion by Lord Kelvin [1] in 1887, it was only popularised by Taylor [2] and Prandtl [3] after World War I.

As suggested by its name, turbulence is characterised by intense swirling motions. These motions lead to increased mixing and transport of mass, momentum, and heat in flows [4, 5]. As a consequence, turbulence homogenises reactants, thereby accelerating chemical reactions and combustion processes on one hand; and causes drag on aircraft wings and in pipelines, thereby being identified as the culprit for energy consumption in flight and in oil and gas transport through pipelines on the other. Therefore, depending on the applications, the practical interest would be to promote or prevent turbulence. However, despite abundant experiments and direct numerical simulations on this account, a fundamental understanding for the problem: "How turbulence becomes turbulent?" is incomplete.

The study of the transition to turbulence in shear flows dates back to the time of Lord Kelvin and Osborne Reynolds. From that time onward, this subject has not only been one of the major topics in hydrodynamics, but has also attracted attentions from such great theoretical physicists as Arnold Sommerfeld, Werner Heisenberg, Andrey Kolmogorov,

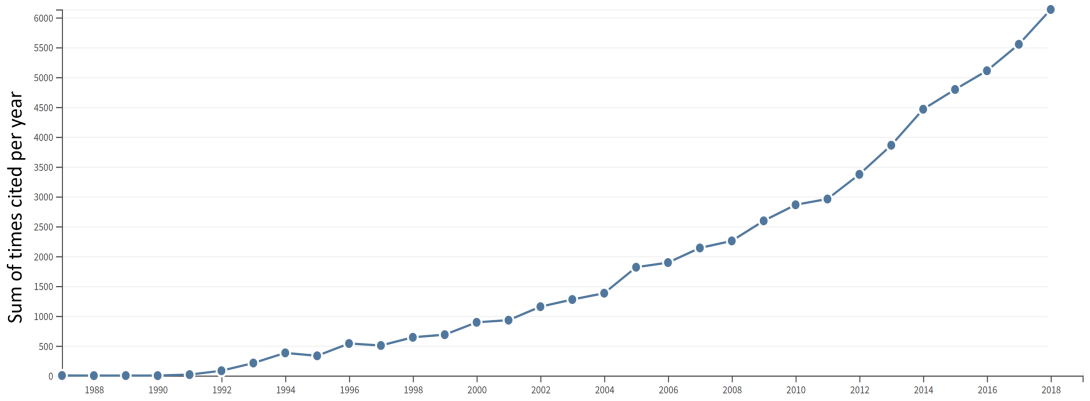

FIGURE 1.1: Sum of times cited per year on topic "transition to turbulence in shear flows".

and Lev Landau. Although temporarily abandoned by the community in favour of the new quantum physics [6], the breakthrough in dynamical systems theory in the late twentieth century has attracted physicists, noticeably Yves Pomeau and Paul Manneville, to consider this old topic in fluid dynamics. According to citation report from Web of Science, there is zero citation on the topic "transition to turbulence in shear flows" before 1990s, and a monotonically increase of citations for each sequential year, as shown in figure 1.1. This "last great unsolved problem of classical physics"[1] has now regained popularity.

Entering the twenty-first century, the rapidly advancing experimental and numerical techniques seem to throw the theoretical approach at disadvantage. It would be reasonable to investigate at this point how far one can achieve by adopting purely theoretical approaches. By providing analytical solutions to localised structures mediating the transition to turbulence in planar shear flows and predictions of new flow phenomena that are overlooked in experiments and simulations over decades, the answer delivered by this thesis is: surprisingly far.

1.1 Consensual revisit of pipe flow experiments

From the geophysical currents under the surface of the ocean to the cumulus clouds at the top of the planetary boundary layer, from a plume of smoke rising from a cigarette to a droplet of ink dispersing in the water, and from the fuel and air mixing in combustion

[1] In a quote that variously attributed to Sommerfeld, Einstein, and Feynman [6], "turbulence is the last great unsolved problem of classical physics."

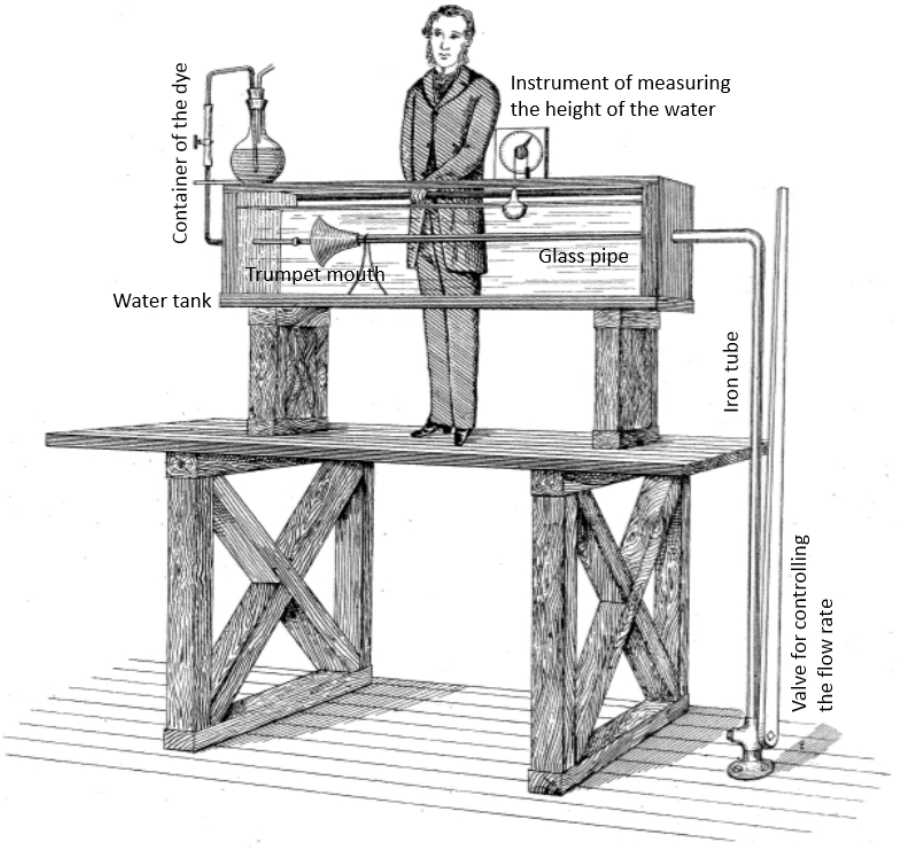

FIGURE 1.2: Setup of the Reynolds' pipe experiment. Figure from: Reynolds [7].

engines to the oil and gas flowing in transmission pipelines, turbulence is ubiquitous in nature, daily life and engineering practice.

Although being ubiquitous in nature, the first systematic study of the transition to turbulence was not available until the end of the nineteenth century. In his pioneering experiment, Reynolds [7] studied the motion of water in a long thin glass pipe with diameter 25mm $\pm$ 0.78mm and length 1.5m, hence the aspect ratio is 60. The pipe is horizontally immersed in a water tank wherein the water is driven by the gravity and enters the pipe through a trumpet mouth made of varnished wood. The fluid motion is visualised by injecting dye at the entrance of the trumpet-shaped mouth. The velocity of the water in the pipe is obtained by measuring the height of the water in the tank, while the flow rate is controlled by tuning the valve mounted at the bottom of a vertical iron tube connecting to the glass pipe. The setup of Reynolds' pipe flow experiment is sketched in figure 1.2.

Despite the lack of linear instability of the laminar pipe flow [8, 9], a transition to turbulence can be observed. Following Reynolds' sketch, which is shown in figure 1.3, the

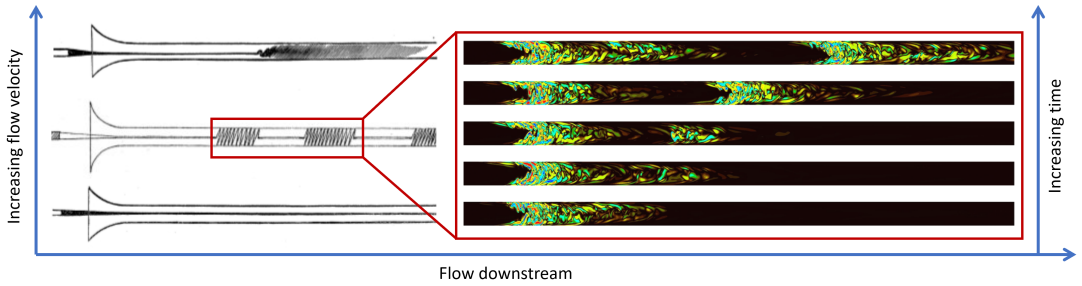

FIGURE 1.3: Reynolds sketch of the onset of turbulence in pipe flow with increasing flow velocity. Bottom: the laminar flow; middle: coexistence of intermittent laminar and turbulent puffs patches at low Reynolds numbers; and top: transition to turbulence from the laminar flow upstream. Figure from: Reynolds [7]. The inset shows a modern direct numerical simulation for the transitional pipe flows, where a localised turbulent puff splits into two with increasing time. Figure from: Avila et al. [10].

dye remains confined to the centre of the pipe when the fluid velocity is low, indicating that the flow is laminar. With increasing flow velocity, turbulence emerge in the form of localised patches of irregular motions called puffs. Since the pipe flow is confined in the radial direction, puffs can only manifest themselves in the axial direction. This leads to an irregular sequence of turbulent puffs advected downstream, as shown in the middle panel of figure 1.3. As the fluid velocity is further increased above a certain critical value, the dye remains laminar for some distance before mixing with the surrounding water downstream, signalling the transition to featureless turbulence in pipe flow.

A systematic continuation of the experiment with pipes of different diameters and water at different temperatures reveals that the generic [2] characteristics of the fluid motion depend only on the relation among (i) the linear dimension of the space occupied by the fluid, (ii) the fluid velocity, and (iii) the physical properties, i.e. density and viscosity, of the fluid. This relation, known as the Reynolds number [3], is given by

$$Re = \frac{ud}{\nu}, \tag{1.1}$$

where, for pipe flow, u is the centre-line velocity, d is the diameter of the pipe, and ν is the kinematic viscosity of the fluid.

[2] Here, "generic" means, as long as the value of Re remains the same, the dynamics of the flows at different scales, e.g. from accretion disk in galaxies [11] to rotating plane Couette flow in laboratories [12], are identical. This observation, commonly known as the Reynolds' similarity principle, has a profound impact on the engineering practice, because it provides a theoretical basis for performing experiments with reduced scale models.

[3] Although the concept was first introduced by George Stokes [13] in 1851, the term "Reynolds number" was invented by Arnold Sommerfeld [14] in 1908, naming after Osborne Reynolds [7] who promoted the idea.

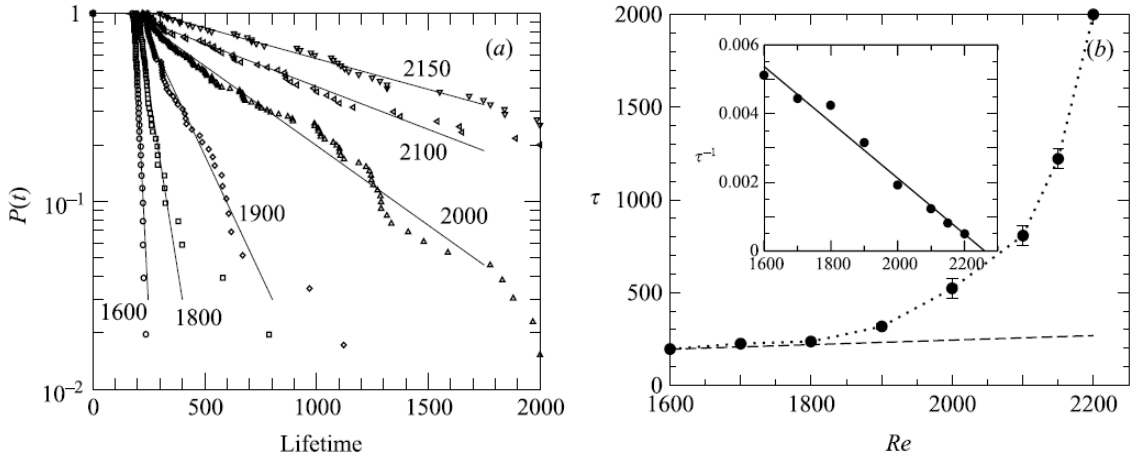

FIGURE 1.4: Lifetime of turbulent puffs in pipe flow. Left: probability $P(t)$ of a puff remaining turbulent after time t; and right: the median lifetime τ of a turbulent puff as a function of Reynolds number. Figure from: Faisst and Eckhardt [19].

Although there is little doubt that Re is the only control parameter characterising the dynamics of the pipe flow, the determination of critical Reynolds number Re_c, at which the transition to turbulence takes place, turns out to be extremely difficult and has been debated ever since Reynolds' experiment in 1883. In literature, the documented critical Reynolds numbers range vastly from 1700 to 3000 [15]. At these Reynolds numbers, puffs decay [16] or split [17, 18], depicting a strong spatiotemporal intermittency, cf. the inset in figure 1.3. Faisst and Eckhardt [19] investigated numerically the lifetime of turbulent puffs and found that (i) the decay of turbulence lifetime is exponential, hence it is a memoryless process [20]; and (ii) the mean turbulence lifetime increases exponentially with Re, indicating that there exists a $Re_c = 2250$ at which the lifetime of a turbulent puff diverges, as shown in figure 1.4. The qualitative feature of diverging lifetime of a turbulent puff at Re_c has been advocated by later experimental (cf. figure 3 in Peixinho and Mullin [21]) and numerical investigations (cf. figure 4 in Willis and Kerswell [22]).

However, in a long pipe with diameter 4 ± 0.01mm and length 15m, hence the aspect ratio 3750, and by tracking experimentally the evolution of turbulent puffs over 8 orders of magnitude in time, Hof et al. [23] concluded a superexponential scaling for the median lifetime as a function of Re. Therefore, opposed to the previous findings [19, 21, 22], they suggested that the turbulence is always transient. Later direct numerical simulation by Avila et al. [10] supported the superexponential scaling, thereby confirming the transient nature of turbulence. In the same paper, Avila et al. [10] defined the critical Reynolds number $Re_c \approx 2040$ as the intersection between the time scale for puff slitting and that for puff decaying, as shown in figure 1.5. That is, although the individual turbulent

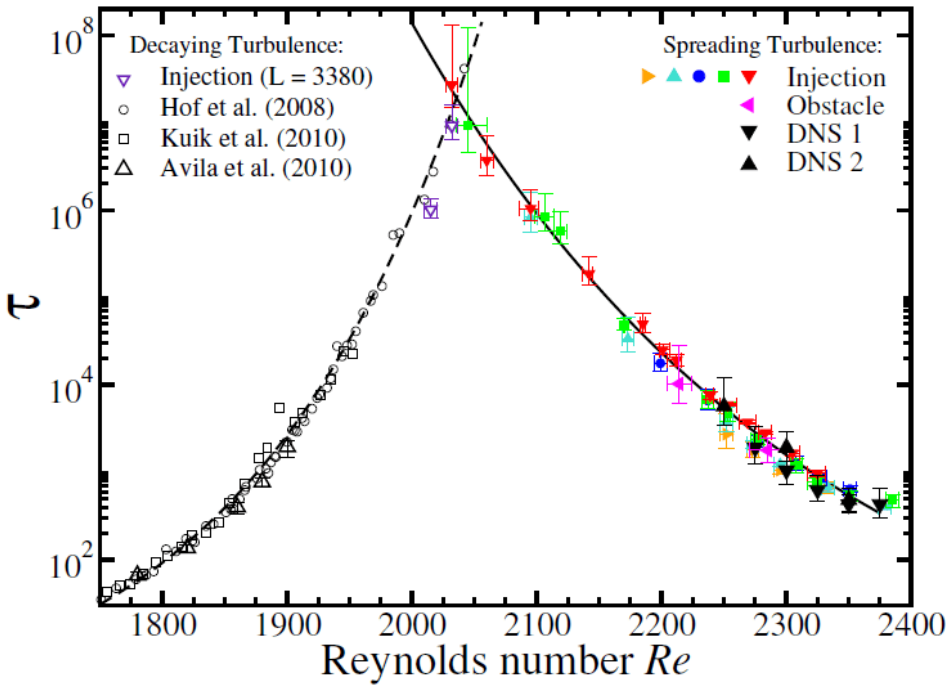

FIGURE 1.5: Mean lifetime of a puff before decaying or splitting. The intersection $Re_c = 2040 \pm 10$ signals the critical Reynolds number at which turbulence is sustained in a statistical sense. Figure from: Avila et al. [10].

puff is always transient, above Re_c the puff slitting process outweighs the puff decaying, signalling a transition to the statistically sustained turbulence in pipe flow. For a theoretical perspective on the route to turbulence in pipe flow, cf. Barkley [24] and references therein.

Although the transient nature of turbulent puffs and the Re_c for pipe flow have eventually been accepted by the community, decades of competitions and controversies in experiments and direct numerical simulations reveal the limitation of purely experimental and numerical approaches. By contrast to theories, experiments and direct numerical simulations do not have any predictive power because they are by themselves a reflection of a particular aspect of nature. Consequently, in order to extract rules from experiments and simulations, e.g. critical Reynolds numbers, extensive statistics are required, cf. figure 1.5. Moreover, since transition to turbulence in shear flows is associated with long transients and is strongly affected by finite size effects [23], in order to eliminate these effects, ever longer observation time and ever larger flow domain are required [15]. Conversely, asymptotic limits in space and time usually lead to plausible simplifications in theory, making the theoretical approach a better option, cf. Chapter 3.

1.2 The long and winding road [4]

According to consensual observations of preceding pipe flow experiments and simulations, the transition to turbulence in wall-bounded shear flows can be roughly divided into two phases:

i the onset of turbulence, which is temporally chaotic but localised in space; and

ii the spread of the spatially localised turbulence over the whole flow domain.

In the following, these two aspects are reviewed with emphases on deficiencies of the existing theories.

1.2.1 Onset of turbulence in time

Observing that the Fourier transform of turbulent velocities comprises, typically, a continuous spectrum of temporal frequencies, Landau [26] envisaged turbulence as complex quasiperiodic motions occurring on an infinite-dimensional torus: with increasing fluid velocity, the stationary laminar state loses stability and is sequentially replaced by first a periodic and then quasiperiodic attractors with an increasing number of incommensurate frequencies [5]. The deficiency of Landau's scenario remains unexplored until 1970s. In fact, quasiperiodic motions as proposed by Landau [26] are not strictly turbulent as they do not

i exhibit sensitive dependence on initial conditions; nor

ii provide sufficient mixing in the phase space,

two fingerprints of turbulence.

Without knowing the work by Lorenz [28], Ruelle and Takens [29] observed that motions on a four-dimensional [6] torus is structurally unstable, thereby cannot occur in the

[4] The title of this section contributes to Pomeau [25], who distinguished between the super- and subcritical transitions to turbulence and initiated the statistical description, i.e. directed percolation, for the transition to turbulence in wall-bounded shear flows.

[5] The same scenario has been proposed by Hopf [27] four years later in 1948, independently.

[6] The condition of dimensionality *four* is further reduced to *three* by Newhouse et al. [30].

generic sense. In contrast to Landau's scenario, chaos immediately sets in after two or three generalised Hopf bifurcations (see below), wherein only a few degrees of freedom is evoked. Ever since, Ruelle and Takens' scenario has been experimentally evidenced in many closed flow systems, most notably in Taylor-Couette flow [31], a rotating layer of fluid driven between co-rotating concentric cylinders, and in Rayleigh-Bénard convection [32], a horizontal layer of fluid heated from below. Figure 1.6 shows the power spectra of typical times series measured in Taylor-Couette flow and Rayleigh-Bénard convection. With increasing values of the control parameter, the system experiences sequentially

i a periodicity, where the power spectra is characterised by a fundamental frequency and its harmonics;

ii a quasiperiodicity, where the power spectra is characterised by two incommensurate frequencies and their linear combination; and eventually

iii chaos, signalled by the emergence of a continuum of frequencies [7].

With the same experimental setup, i.e. the Rayleigh-Bénard convection, Bergé et al. [34] observed that the flow can become turbulent via spatiotemporal intermittency. In the framework of dynamical systems theory, however, the concept of intermittency is limited to a purely temporal sense: the periodic behaviour of a time series is interrupted by irregular segments turbulent motions. In parallel with how attracting fixed points lose stability in one-dimensional mappings, Pomeau and Manneville [35] identified three types of intermittency routes to chaos

i saddle-node bifurcation, where a real eigenvalue of the periodic orbit crosses the unit circle at $+1$;

ii Hopf bifurcation, where two complex conjugate eigenvalues cross the unit circle simultaneously; and

iii flip bifurcation, where a real eigenvalue crosses the unit circle at -1.

According to Pomeau [36], the intermittency occurs because the newly emerged strange attractor keeps memory of the fixed point behaviour such that the trajectory is wandering

[7] When only discrete frequency components are present, although being apparently irregular, the long-term prediction of the system's behaviour is possible; whereas the predictability is lost in the presence of however small "randomness", as evidenced by the broadband frequency component [33]

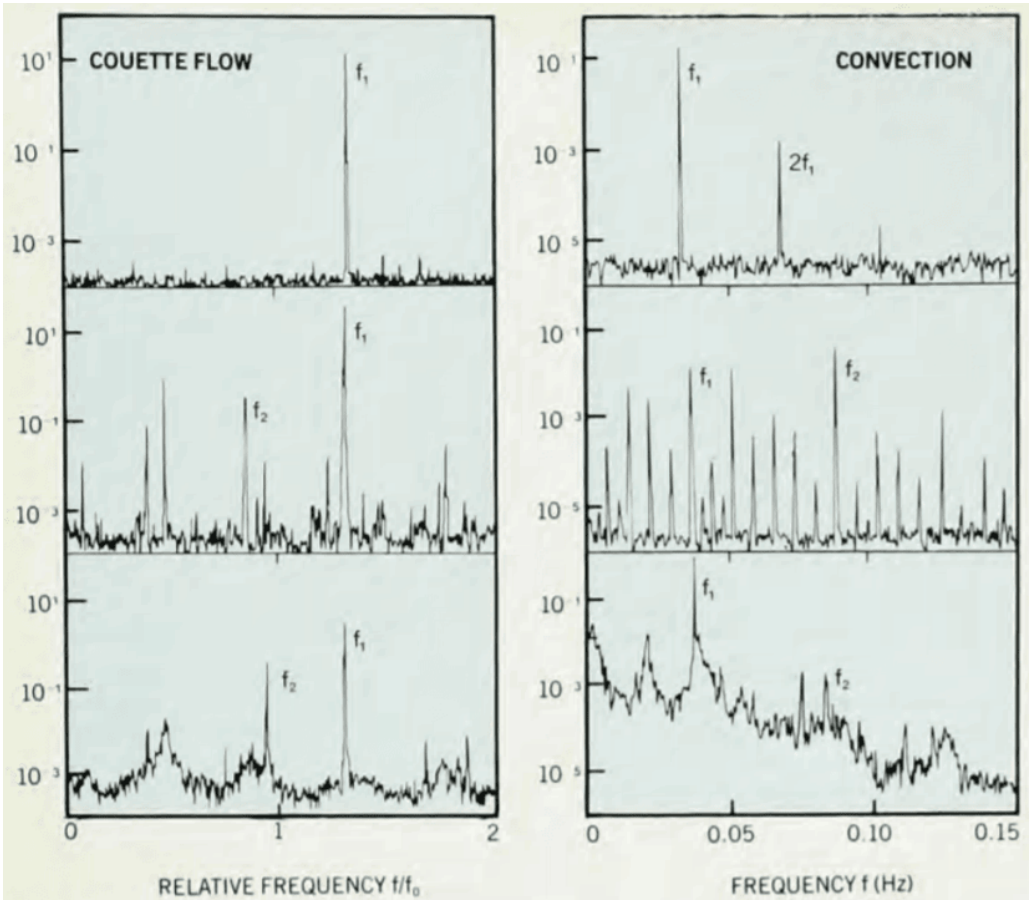

FIGURE 1.6: Power spectra of a typical time series of velocity from left: Taylor-Couette flow and right: Rayleigh-Bénard convection. The upper row corresponds to periodic flows with one fundamental frequency; while the second row the quasiperiodic flows containing two incommensurate frequencies. The bottom row depicts turbulence comprising a continuous spectra of frequencies in addition to few dominant peaks. This figure, which is taken from Swinney and Gollub [32], provides a strong experimental evidence for the scenario proposed by Ruelle and Takens [29].

around the "ghost" of the fixed point on the Poincaré section for a long time. Similar behaviours have also been observed in a bifurcation analysis for coherent structures inside the turbulent patches, cf. Chapter 4.

It should be emphasised that in none of previous cited works has a link been established between the governing equation of incompressible flows, i.e. the Navier-Stokes equations, and the proposed low-dimensional dynamical systems exhibiting quasiperiodicity, intermittency, and chaos, cf. Chapter 1 in [6]. Despite their success in describing routes to turbulence in typical closed systems, e.g. Taylor-Couette flow and Rayleigh-Bénard convection, the preceding scenarios cannot explain the onset of turbulence in wall-bounded shear flow involving pipe flow, plane Couette flow, plane Poiseuille, etc. In previous

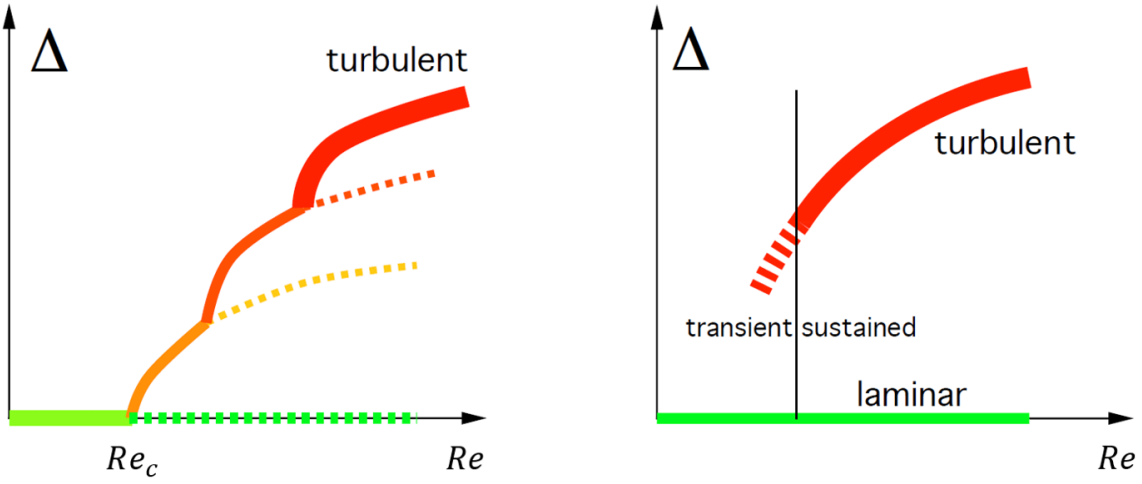

FIGURE 1.7: Bifurcation diagrams exhibiting supercritical (left) and subcritical (right) behaviours. Left: as the control parameter Re increasing past the linear stability threshold Re_c, the laminar state loses stability, as indicated in dashed line, and it is replaced by a cascade of bifurcations where the bifurcating state (solid lines) emerges from the bifurcated state (dashed lines) and remains close to it, signifying a continuous thereby subcritical transition to turbulence. Right: the linearly stable laminar state coexists with a nontrivial bifurcating state (red line) gaining stability at large distances Δ from it, signifying a discontinuous thereby subcritical transition to turbulence. Figure from: Manneville [38].

cases, the volume forces, namely centrifugal force in Taylor-Couette flow and temperature gradient in Rayleigh-Bénard convection [37], acting on the fluid generate various linear instabilities. As a consequence, the laminar state loses stability and gives way to a sequence of bifurcations where the bifurcated state is replaced by the bifurcating states that emerge from and remain close to it, leading to the *supercritical* transition to turbulence.

In the case of shear flows, for instance pipe flows, turbulence first emerges in the form of localised turbulent puffs immersed in the otherwise linearly stable laminar background [7]. Puffs can decay, or else split and thereby proliferate [10, 23]. In this case, the transition to turbulence takes place in the absence of the linear instability and is driven by finite amplitude disturbances. During the transition, two qualitatively different states, i.e. the linearly stable laminar state and the nontrivial bifurcating state (puffs), coexist, depicting a *subcritical* transition to turbulence [39]. At higher Reynolds numbers, localised puffs grow into spatially extending slugs, signalling a transition to featureless turbulence [17, 18, 40]. The main difficulty preventing the application of dynamical systems theory to the subcritical transition to turbulence is associated with the discontinuity. That is, the emerging nontrivial bifurcating state is disconnected with and remains far from the

laminar base state, which makes the normal form analysis from the laminar base state impossible [8]. Conceptual bifurcation diagrams illustrating supercritical and subcritical transitions to turbulence are sketched in figure 1.7.

Finally, the dynamical systems approach is only applicable to the onset of temporal chaos whereas turbulence is a spatiotemporal phenomenon. Therefore, the feasibility of the dynamical systems theory is limited to small aspect-ratio systems where the confinement effect is strong enough to suppress the spatial modulation of the unstable modes. In this case, the instability is purely temporal [38]. For extended systems, the system can be decomposed into a large numbers of mutually interacting elementary cells [9], i.e. minimum flow units [42], hence the research interests shift towards how turbulence spreads over the whole domain.

1.2.2 Spread of turbulence in space

In extended subcritical systems, the spatial modulation leads to the formation of fronts [39]. Fronts divide the physical space into a lattice of cells individually governed by one of the two competing states, namely the linearly stable thereby non-bifurcating laminar state and the nontrivial bifurcating turbulent state arising far from it. Pomeau [39, 43] borrowed ideas from statistical physics and postulated that the dynamics of fronts can be modelled by a purely stochastic process known as directed percolation. In statistical physics, directed percolation describes a stochastic two-state, i.e., active and absorbing, contamination process, hopping in a preferred direction on a lattice. Specifically, a site that is active can spontaneously decay into an absorbing state with probability p_1, whereas an absorbing site is only excited by a contact interaction with active neighbours with probability p_2. Since the decay into an absorbing state is irreversible, the system is envisioned as a $(D+1)$ dimensional lattice, with the preferred orientation "directed" in time. A phase transition takes place if the ratio $P = p_2/p_1$ surpasses a critical value P_c, at which the spreading overpowers the decay. In this case, there is at least one connected path that survives through the direction of percolation, signalling a phase transition

[8] Normal form analysis is essentially a series expansion about an equilibrium solution of the system, whose feasibility is therefore to the neighbourhood of the fixed point.

[9] In quasi-one dimensional systems, e.g. pipe flow, the mutual interaction between these elementary cells is short-ranged [41]; while in quasi-two dimensional systems, e.g. planar Couette flow, it is unknown whether this interaction is short-ranged or long-ranged. The analytical solutions for quadrupolar flows as shown in Chapter 3 provides an incomplete answer to this question.

Scaling	Exponent	$D = 1$	$D = 2$
$\rho \propto (P - P_c)^{\beta}$	β	0.276486	0.583
$\xi_{\perp} \propto (P - P_c)^{-\nu_{\perp}}$	$\nu_{\perp}$	1.096854	0.733
$\xi_{\parallel} \propto (P - P_c)^{\nu_{\parallel}}$	$\nu_{\parallel}$	1.733847	1.295

TABLE 1.1: Critical exponents of directed percolation in D dimensions.

Although the precise value of P_c depends on the details of the system, universality emerges as, near the threshold, the mean density of active sites ρ increases continuously from zero as $\rho \propto (P - P_c)^{\beta}$, while the correlation length $\xi_{\perp}$ and the correlation time $\xi_{\parallel}$ diverge: $\xi_{\perp,\parallel} \propto (P - P_c)^{-\nu_{\perp,\parallel}}$. This scaling-free behaviour is characterised by a universal set of critical exponents β, $\nu_{\perp}$, and $\nu_{\parallel}$, whose values depend only on the dimensionality D of the embedding space. For $D < 3$, the values of the critical exponents are determined numerically [44], as summarised in Table 1.1.

In terms of the transition to turbulence in shear flows, the active and absorbing sites on the lattice correspond to turbulent spots and laminar background. Consequently, the control parameter P and the order parameter ρ translate to the Reynolds number Re and the turbulent fraction, respectively. In order to test Pomeau's conjecture, Lemoult et al. [45] performed experiments and numerical simulations for quasi-one-dimensional subcritical Taylor-Couette flow, with two highly confined spatial directions. Hence the propagation of the laminar-turbulent interface is limited to the azimuthal direction. Figure 1.8 shows a comparison between directed percolation simulation and the transition to turbulence in cylindrical Couette experiments. They do look alike. Moreover, in both experiments and simulations, the turbulent fraction increases continuously above the critical Reynolds number, with critical exponents meet the expectation of directed percolation universality class in $1 + 1D$. These observations support Pomeau's conjecture. In system with two extended directions, Sano and Tamai [46] also confirmed that the transition to turbulence in plane Poiseuille experiments follows directed percolation, but with the reported critical Reynolds number being significantly higher than the one at which turbulent patches sustain [47]. With stress-free boundary condition, Chantry et al. [48] investigated numerically the transition to turbulence in Waleffe flow and found the results are in good agreement with the directed percolation universality class in $2 + 1D$, suggesting that the universal behaviour of the transitional shear flow is independent of the boundary conditions.

This seems to be the end of the story, but not quite. In all cited previous studies, where

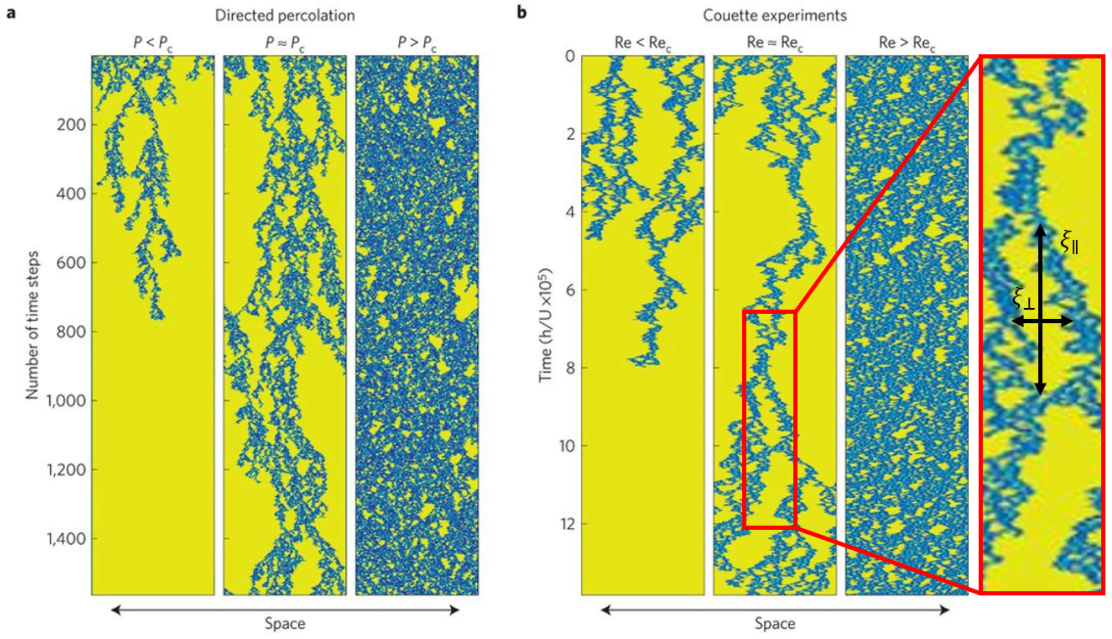

FIGURE 1.8: Spatiotemporal intermittency as visualised in directed percolation simulation (left) and in cylindrical Couette experiment (right), where active (turbulent) sites are shown in blue while the absorbing (laminar) sites are in yellow. The inset illustrates the concept of correlation time $\xi_{\parallel}$ and correlation length $\xi_{\perp}$ in a spatiotemporal pattern. Figure from: Lemoult et al. [45].

the relevance of directed percolation is evidenced, the active state is not the featureless turbulence but the one comprising alternating laminar and turbulent stripes, wherein the turbulent fraction is at most 0.6 [10]. Moreover, given the relevance of directed percolation to the subcritical transition to turbulence, as pointed out by Manneville [38]:

> *"Statistical physics approaches invoking e.g. directed percolation or large deviations are just a compact way to describe the transition with little physical interpretation of the processes at stake."*

Therefore, the implications and limitations of such a purely statistical, thereby stochastic, description for deterministic phenomena, namely the transition to turbulence, must be further explored.

To begin with, in order to interpret a transition as directed percolation, three prerequisites must be fulfilled [49–51]:

i the existence of a unique absorbing state;

[10] This issue was pointed out by Prof. R. Monchaux.

ii the absence of long-range interactions; and

iii the absence of special attributes such as additional symmetries or quenched disorder.

Near their onset, localised turbulent patches comprise coherent structures [11], e.g. streamwise vortices in plane-Couette flow [56–58] and hairpin vortices in pipe flows [59, 60]. The fulfilment of the first condition requires that coherent structures themselves cannot be accounted as an absorbing state and are self-similar [12].

Moreover, there is no reason that the interaction between turbulent patches are short-ranged from the first principal, here the Naiver-Stokes equations. In fact, experiments [61–63] and numerical simulations [64–66] evidence the existence of large-scale circulations around localised turbulent patches. Depending on their far-field decay, these large-scale flows can introduce a long-range interaction[13], thereby conflicting with the second requirement.

1.3 Objectives and Scope

In his monograph in 1971, Bradshaw [68] regarded turbulence as "the most common, the most important, and the most complicated kind of fluid motion." Similar statements were expressed by Lundqvist [69] on award ceremony speech for the 1982 Nobel prize in physics.

[11] Like turbulence, the terminology "coherent structure" has, by far, no precise definition. In fact, the definition of coherent structure evolves in time and is strongly influenced by the availability of visualisation techniques. Pre-1980s, researchers attempted to interpret coherent structures as helical vortices because the suppressed nonlinearity explains the origin of coherent motions, most notably by Keith Moffatt [52] and Arkady Tsinober [53]; from 1980s to 1990s, a new trend evolves as to identify coherent structures as regions fulfilling certain criteria for pressure, leading by Julian Hunt [54] and Fazle Hussain [55]; nowadays, benefited from rapid advances in experimental facilities and numerical power, a wide range of apparently organised motions are observed, and consequently, the definition of coherent structures is generalised to "energy containing structures that is apparently not turbulent nor laminar", e.g. streaks and streamwise vortices, as well as the turbulent spots containing them. The last definition is widely adopted by researchers specialised in transitional wall-bounded shear flows.

[12] The directed percolation is essentially a mean-field theory in the sense that in order to treat turbulent spot as a active state, one needs to performing average over the spot. Hence, the underlying assumptions are: (i) turbulence are coherent structures, i.e. streamwise vortices and streaks; and (ii)coherent structures are self-similar.

[13] In statistical physics, long-range interactions refer to those where the two-body inter-particle potential decays algebraically with power smaller than the dimensionality of the embedding space [67]. Otherwise, it is short-ranged. Despite the lack of formal analogy of interaction potential in fluid mechanics, the rule of thumb is, if the large-scale flows decay exponentially in the far-field, then the spot-spot interaction is short-ranged.

> *"However, there have been a few important exceptions, where the experimental facts have been well known for a long time but where the fundamental theoretical understanding has been lacking and where the early theoretical models have been incomplete or even seriously in error. ...The third classical problem I mentioned, namely turbulence, has not yet been solved, and remains a challenge for the theoretical physicists."*

Now, half a century later, the situation has changed little: despite the rapid advances in experimental and numerical techniques, a theoretical understanding develops slowly. As such, the present thesis is dedicated to a theoretical understanding and a mathematical modelling of:

1.3.1 Large-scale flows outside turbulent patches

Despite their ubiquitous observation in experiments and numerical simulations, the origin of the large-scale quadrupolar flow is still masked by an aura of mathematical mystery. Conventionally, quadrupolar flows are believed to come from the nonlinearity of the Navier-Stokes equations [70] and decay exponentially away from the localised turbulent spot [64, 71].

In the thesis, a qualitatively different point of view is adopted: the emergence of large-scale flows has a linear origin and is characterised by a topological invariant, here the winding number. Moreover, the analytical solution suggests that the asymptotic decay of the quadrupolar flow is algebraic with power-law exponent -3, cf. Chapter 3. Since the present results differ remarkably from customary beliefs, a state of art survey on turbulent spots and large-scale flows around them and the existing theories is provided in Chapter 2.

1.3.2 Counter-rotating streamwise vortices inside turbulent patches

Evidenced by the coexistence between laminar base flow and turbulent spots containing coherent structures, as well as the requirement that coherent structures are not the absorbing state, it is argued that the instability in plane Couette flow bifurcates from the coherent state comprising a pair of counter-rotating streamwise vortices. In this case, although the global instability is subcritical, in the sense that the bifurcating state is

at finite distance to the laminar state at the onset of instability, the bifurcation of the nontrivial solution from the coherent state is expected to be supercritical. Moreover, the linear stability of the laminar flow provides a strong confinement effect that the instability emerging from the coherent structures is not affected by the spatial modulation, thereby purely temporal. These assumptions, together, lead to a drastic reduction of the Navier-Stokes equations to a system comprising three ordinary differential equations, whereby a formal bifurcation analysis is applicable.

1.4 Outline of the thesis

The remaining of the thesis is structured as follows:

Chapter 2 is divided into two parts. The first part reviews the experimental and numerical observations for the spatially localised turbulent patches in various shear flows, with emphases on coherent structures inside and large-scale flows outside these turbulent patches. The second part provides an explanation for why the Navier-Stokes equations are difficult to solve and a historical survey on the existing theories for how to overcome these difficulties. Special attention is given to plane Couette flow, which is the major subject of the present thesis.

Chapter 3 deals with the large-scale flows outside turbulent patches, where an analytical derivation of the far-field for the quadrupolar flows observed generically around turbulent spots is provided. The asymptotic decay of the large-scale flow is obtained and predictions for new flow scenarios are made based exclusively on the analytical solutions we obtain.

Chapter 4 conducts the bifurcation analysis for counter-rotating streamwise vortices inside turbulent patches. By resorting to a linearisation about a counter-rotating pair of streamwise vortices, a three-dimensional dynamical system is derived from the Navier-Stokes equations. With broken rotational symmetry, the system experiences a quasiperiodicity route to chaos, wherein a peculiar devil's staircase is unveiled.

Finally, the results coming out in this thesis and their physical significance are discussed in terms of the perspectives they open in Chapter 5.

Chapter 2

Historical survey on the transitional flow regime

2.1 Overview

Two types of transition to turbulence can be distinguished in incompressible flows [39, 72]. It can be supercritical, characterised by a continuous evolution with increasing complexity as the control parameter, here the Reynolds number, is raised. Or it can be subcritical, characterised by coexistence of laminar and turbulent regions over a finite range of Reynolds numbers. The emergence of localised patches of turbulence on a laminar background [73–75], the formation of peculiar laminar-turbulent patterns in different systems [66, 76–80], and the presence of the large-scale secondary flows around localised turbulence [61, 62, 64, 65] are essential characteristics of this so-called transitional flow regime.

On the other hand, the governing equations of fluid dynamics, i.e. the Navier-Stokes equations, are by themselves a remarkable and canonical problem in mathematics. The difficulty associated with seeking for exact and explicit solutions to the Navier-Stokes equations is legendary. In fact, it is yet unknown whether

> *"in three space dimensions and time, given an initial velocity field, there exists a vector velocity and a scalar pressure field, which are both smooth and globally defined, that solve the Navier–Stokes equations."*

This question, commonly referred to as the existence and smoothness problem of the Navier-Stokes equations, is one of seven millennium prize problems. It is offered a US $\$1,000,000$ by the Clay Mathematics Institute to the first person who proves or disproves it [81].

As such, the review of literature is split into two parts. The first part reviews the phenomenology of the transition to turbulence in subcritical systems with attentions paid to the coherent structures within and the large-scale flows around spatially localised turbulent patches. The focus of the second part is on mathematics, where the difficulties associated with solving the Navier-Stokes equations are summarised and a historical survey of existing theories is provided.

2.2 Transition to turbulence in planar flows

The transition to turbulence in wall-bounded shear flows is subcritical, which occurs in the absence of linear instability of the laminar base flow and is characterised by coexistence of laminar and turbulent regions over the transitional flow regime. At the lowest Reynolds number where turbulence is reported, the laminar-turbulent coexistence takes the form of localised turbulent patches, termed puffs in the quasi-one-dimensional pipe flow and spots in the quasi-two-dimensional planar flows, interspersed amidst otherwise linearly stable laminar base flow. Turbulent puffs were first observed by Reynolds [7] in pipe flow, where the flow is confined in the radial direction and the spatial modulation can manifest itself only along the axial direction. These structures in pipe flow are exponentially localised [82], hence interactions between adjacent two puffs are clearly short-range [41]. As an extension of the quasi-one-dimensional pipe flow, planar shear flows evolve freely in both streamwise and spanwise directions, consequently richer dynamics emerge with underlying mechanisms that are harder to decipher. Therefore, the focus of the thesis shall be on the subcritical transition to turbulence in planar shear flows.

2.2.1 Turbulent spots and coherent structures

Since their discovery by Emmons [73] in a water table study, turbulent spots have been subsequently observed in most incompressible shear flows confined between two walls involving counter-rotating Taylor-Couette flow between two concentric cylinders [76], plane

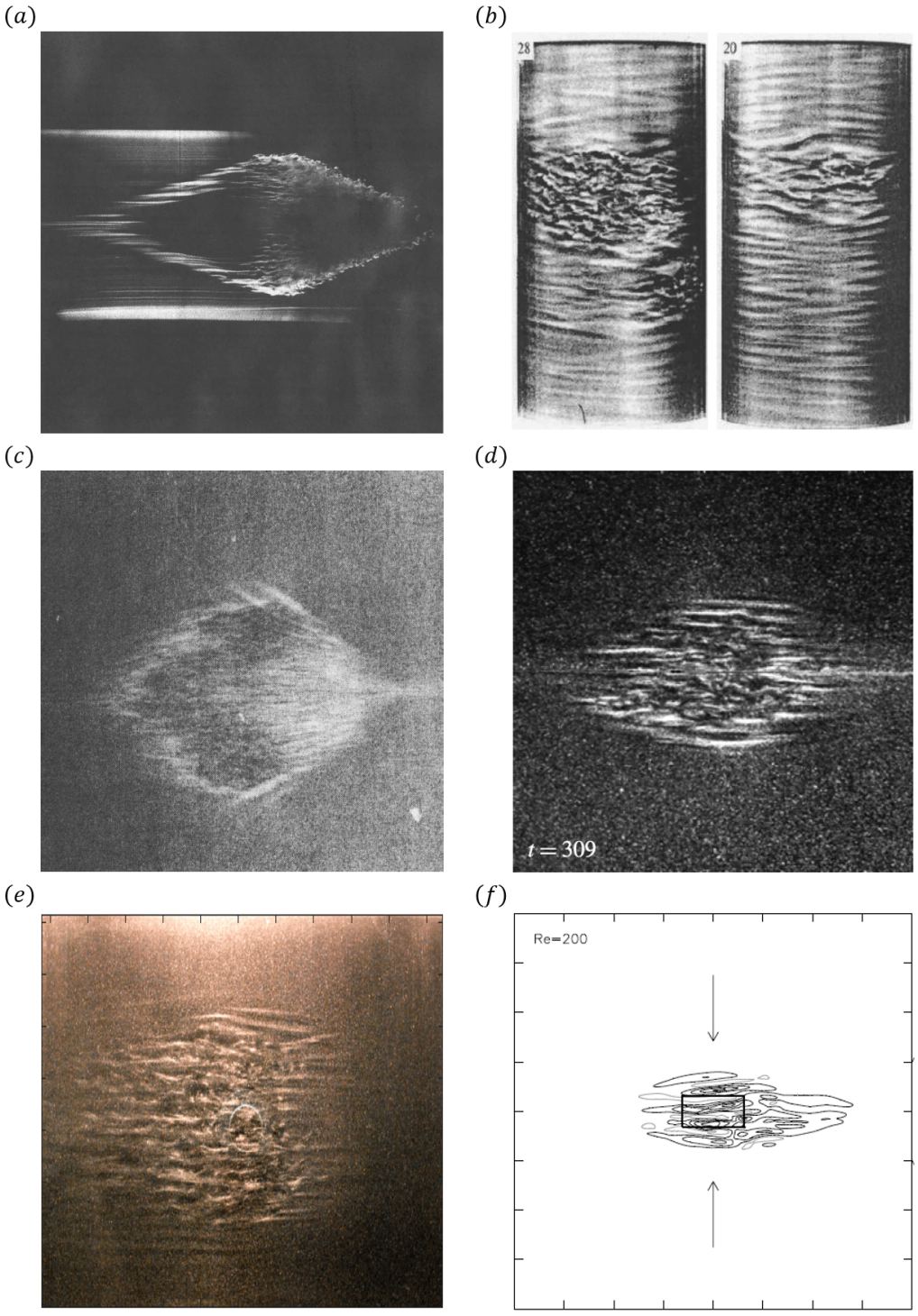

FIGURE 2.1: Turbulent spots in various planar shear flows. (*a*) zero pressure gradient boundary layer, figure from: Gad-El-Hak et al. [83]; (*b*) Taylor-Couette flow, figure from: Prigent et al. [78]; (*c*) plane Poiseuille flow, figure from: Alavyoon et al. [84], (*d*) plane Couette flow, figure from: Couliou and Monchaux [58]; (*e*) Couette-Poiseuille flow, figure from: Klotz et al. [85]; and (*f*) sinusoidal shear flow, figure from: Schumacher and Eckhardt [64].

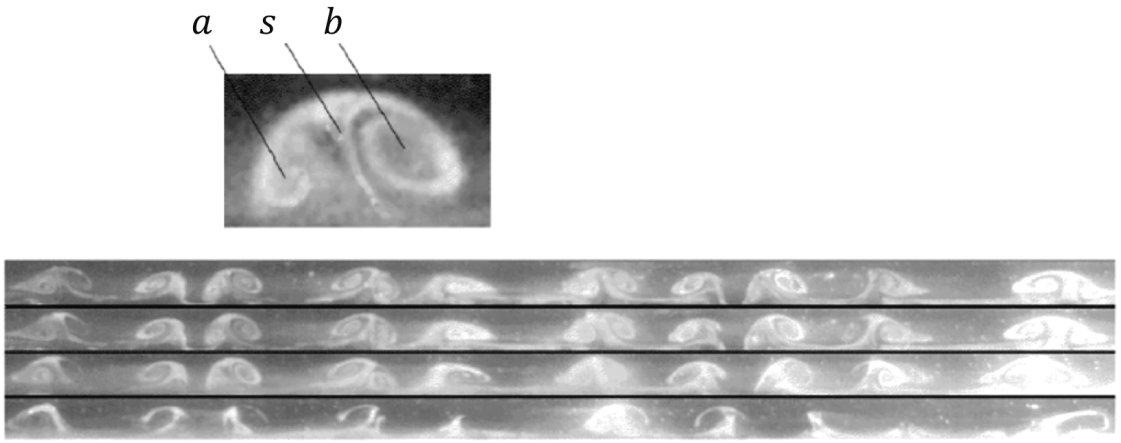

FIGURE 2.2: Visualisation of counter-rotating pairs of streamwise vortices in plane Couette flow. The inset displays coherent structures in the form of two counter-rotating streamwise vortices, i.e. a and b, and a streak s induced by those vortices via the lift-up mechanism. Figure from: Bottin et al. [57].

Poiseuille flow between two stationary plates and driven by a pressure gradient [74, 84], and plane Couette flow sheared between two counter-moving plates [75, 86]. More recently, advances in experimental and numerical techniques have enabled the observation of turbulent spots in Couette-Poiseuille flow [85], in a thin layer of fluid driven by a sinusoidal body force and confined between two surfaces with stress-free boundary conditions [64, 66], and in an annular flow confined between two co-axial cylinders and driven by a pressure gradient in the axial direction [87]. Spots can decay, or spread, exhibiting complex growth dynamics [58, 80, 88]. At Reynolds numbers higher than the onset of turbulence, localised initial conditions lead to turbulent spots quickly invading the whole domain [58, 89, 90].

Despite their apparent difference in shape, turbulent spots feature generic small-scale coherent structures in the form of elongated streamwise velocity streaks maintained by counter-rotating streamwise vortices [56, 57, 91], as shown in figure 2.2. Here, streamwise vortices refer to regions of coherent vorticity aligned with the streamwise direction, which are essentially steady; while the streaks refer to elongated regions of fluid whose speed is higher or lower compared with the mean flow.

In the framework of the linear instability analysis, streamwise vortices are generally referred to as the saturated primary instability of the laminar base flow, upon which streaks grow due to the lift-up effect [92]. With increasing Reynolds numbers, secondary instabilities develop from the modified base flow comprising streamwise vortices and streaks,

which eventually gives rise to the onset of turbulence. Secondary instability calculations have been carried out for various shear flows dominated by streamwise vortices and streaks, e.g. Görtler vortices in boundary layers over a concave wall [93], Dean vortices in curved pipe and channels [94], streamwise vortices and streaks inside boundary layers [95], and all the calculations lead to the similar results [96], indicating that there is a "universality" underlying the transition to turbulence in vortex dominated shear flows.

In the framework of the dynamical systems approach, these recurrent coherent structures can be regarded as attractors in simple dynamical systems, cf. Chapter 2 in Holmes et al. [6]. Hence, for flows dominated by coherent structures, one may build a low-dimensional dynamical system by keeping only the dominant coherent structures, while modelling the inessential features arising from the incoherent parts. The same point of view has been shared by Jiménez [91]: wall-bounded shear flows can be regarded as a high-dimensional dynamical systems comprising interacting coherent structures, whose internal dynamics is autonomous, independent of the incoherent background. As such, the evolution of the flow is largely local, which enables a search for the self-organised solutions that are independent of the global evolution of the base flow. These ideas shall be further exploited in Chapter 4.

At the higher-half of the transitional flow regime, the laminar-turbulent coexistence takes the form of the interlaced laminar and turbulent stripes that are inclined with respect to the streamwise direction. The turbulent regions expand with increasing Reynolds number, signalling the transition to the featureless turbulence and the termination of the transitional flow regime. In this thesis, the focus is on the lower half of the transitional Reynolds number regime wherein turbulent spots, counter-rotating streamwise vortices, and the large-scale quadrupolar flows are ubiquitously observed. For details of turbulent stripes at higher Reynolds numbers, cf. [38, 79, 97–99].

2.2.2 Large-scale quadrupolar flows

The presence of turbulent spots in planar shear flows is always accompanied by the existence of large-scale circulations penetrating deeply into the laminar regions. Here, turbulent spots are extended in the wall-normal direction, thereby filling the gap. Although both turbulent spots and large-scale flows around the spot are three-dimensional, quadrupolar flows are numerically revealed by averaging between the two plates [64, 65] and experimentally measured in the mid-plane [63]. Reported examples include plane

Poiseuille flow [61, 100], plane Couette flow [62, 65, 89], and sinusoidal flow [64, 66]. Despite their different driving mechanisms, symmetries, and boundary conditions, the large-scale flows in these planar systems share several features: The wall-normal velocity features small-scale fluctuations which decay rapidly away from the spot [101]. The large-scale in-plane velocities vary more slowly, they are directed inward along the streamwise direction and outward along the spanwise direction, giving rise to a quadrupolar circulation, as shown in figure 2.3. The generic observation of quadrupolar flows in various planar shear flows suggests that the mechanism underlying their emergence is independent of (i) the boundary conditions at walls; (ii) the details of turbulent spots; and (iii) the driving mechanisms of flow, providing a hint that the origin of quadrupolar flows is topological [102].

Lying outside classic theory of fluid dynamics, two-dimensional systems with broken continuous symmetries admit a certain class of structures, called topological defects. Topological defects comprise a core region where the order is destroyed by thermal fluctuations and a far-field where the slowly varying elastic variable describes the distortion from the spatially uniform ground state [104]. Examples of topological defects include vortices in the xy-model and in the superfluid thin film, charges in two-dimensional Coulomb gas, and dislocations and disclinations in two-dimensional crystals [105]. Therefore, it is tempting to interpret turbulent spots as the topological defect and large-scale flows as the elastic variable[1]. However, there are two caveats.

First, consider a two-dimensional vector in polar coordinates $\boldsymbol{s}(r,\theta)$

$$\boldsymbol{s}(r,\theta) = |s(r,\theta)|(\cos(\varphi),\sin(\varphi)), \tag{2.1}$$

whose magnitude $|s(\boldsymbol{x})|$ is everywhere nonzero and angle variable

$$\varphi = k\theta + \theta_0 \tag{2.2}$$

varies continuously in space. Here, $k = 0, \pm1, \pm2, ...$ is the index of the topological defect and θ_0 is an arbitrary constant, cf. Chapter 9 in Chaikin and Lubensky [104]. Therefore, although a topological defect is solely characterised by its index k, the configuration of the direction field $\varphi(k,\theta_0)$ is not unique.

Figure 2.4 shows three representative direction fields associated with a topological point defect with index $k = 1$. Even though the ubiquitous observation of quadrupolar flows

[1]This analogy is further discussed as perspectives in Chapter 5

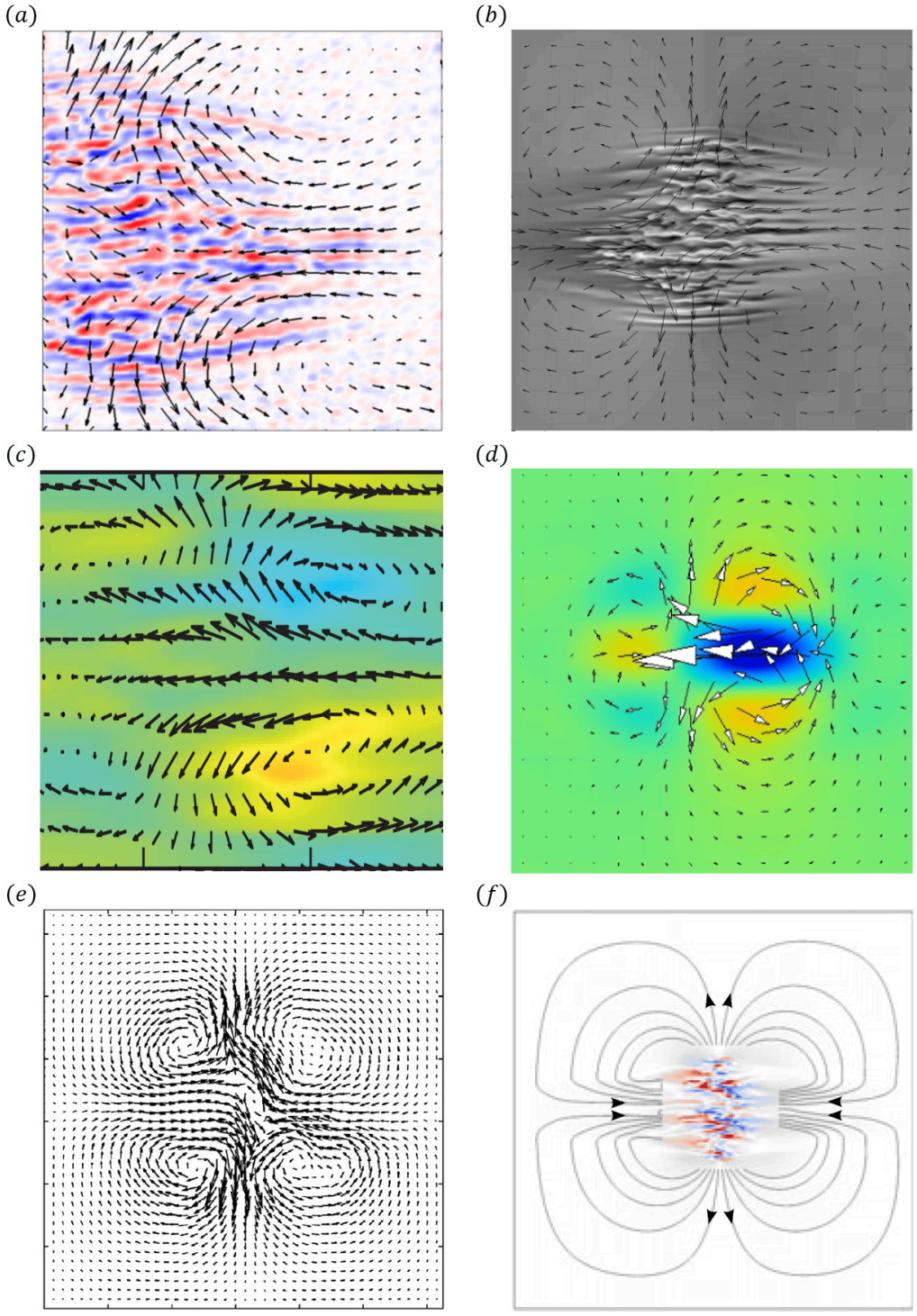

FIGURE 2.3: Large-scale flows in various planar shear flows. (*a*) plane Couette flow (experiment), figure from: Couliou and Monchaux [63]; (*b*) plane Couette flow (DNS), figure from: Duguet and Schlatter [65]; (*c*) plane Poiseuille flow (experiment), figure from: Lemoult et al. [61], (*d*) plane Poiseuille flow, figure from: Tsukahara et al. [103]; (*e*) Modelling with no-slip boundary conditions, figure from: Lagha and Manneville [70]; and (*f*) Modelling with free-slip boundary conditions, figure from: Chantry et al. [66].

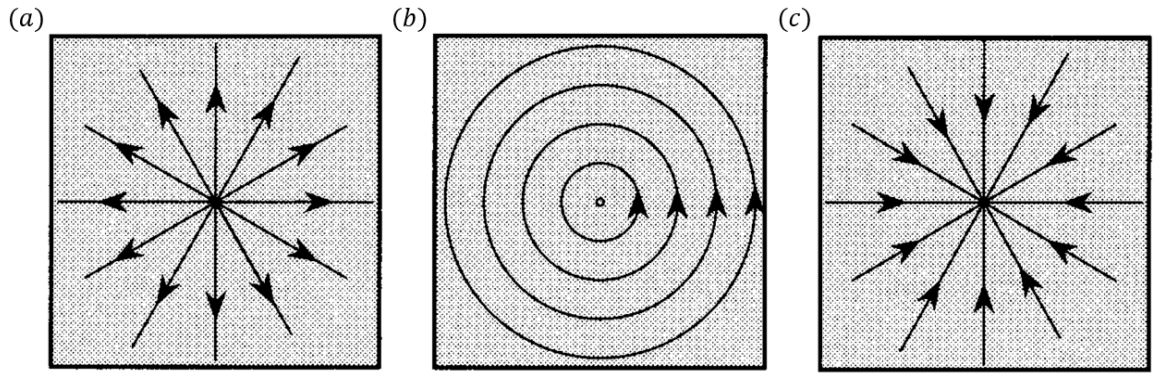

FIGURE 2.4: Direction fields associated with a $k = 1$ topological defect: (a) $\theta_0 = 0$; (b) $\theta_0 = \pi/2$; and (c) $\theta_0 = \pi$. Figure from: Chaikin and Lubensky [104].

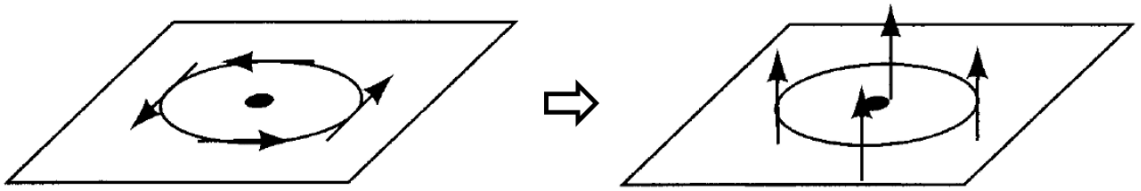

FIGURE 2.5: A structurally unstable topological defect with codimension $d' = 2$ and the dimensionality of the order parameter $n = 3$.

may imply that the index of turbulent spots in various shear flows is unique, the unicity of the quadrupolar flow is far from clear. Thus, there must be a generic mechanism which uniquely determines the value of θ_0.

Second, in the previous discussion, both the dimensionality n of the order parameter $\boldsymbol{s}(r, \theta)$ and the codimension $d' = d - d_s$, where d is the dimensionality of the physical space and d_s is the dimensionality of the core, are 2. Topological defects satisfying $n = d'$ are structurally stable. Conversely, in planar shear flows, although the turbulent spot is topologically equivalent to a point upon wall-normal average such that $d' = 2$. Without apparent evidence of the contrary, the y-averaged velocity field is three-dimensional such that $n > d'$. In this case, there is an escape of spins to the third, i.e. the wall-normal, direction, rendering the topological defect structurally unstable, as shown in figure 2.5.

In boundary layers where the flow is not confined between two walls, despite the presence of localised turbulent spots, no quadrupolar flow has been observed. On the other hand, by restoring the confinement effect with an external forcing, oblique laminar-turbulent interfaces that are typically observed in planar shear flows confined between two walls begin to emerge [106]. This observation implies that the occurrence of localised structures

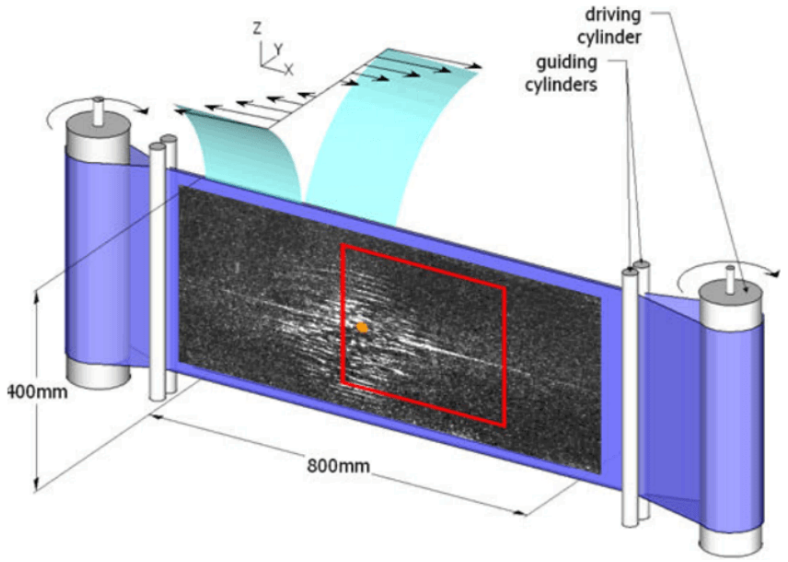

FIGURE 2.6: Schematic drawing of the experimental apparatus of plane Couette flow. The whole apparatus is enclosed in the tank filled by water. Figure from: Couliou and Monchaux [62].

in transitional shear flows depends on the dimensionality of the physical space d, and consequently the codimension d'.

To summarise, in order to evoke the topological argument for emergence of quadrupolar flows, one must

1. identify a mechanism that selects θ_0; and
2. prove that the y-averaged large-scale flow is two-dimensional.

2.2.3 Transition to turbulence in plane Couette flow

Among other planar shear flows, plane Couette flow is known to be linearly stable at all Reynolds number [107], here defined as $Re = Uh/\nu$, where $\pm U$ is the speed of counter-moving plates, h is the half-gap size between them, and ν is the kinematic viscosity of the fluid, and admits a simple analytical expression for the base flow: $U_x(y) = Sy$, where the shear $S = U/h$. The lack of curvature of the base flow leads to plausible mathematical simplifications; while the absence of mean advection makes the long-term tracking of turbulent spots possible. Therefore, plane Couette flow is the canonical system for analytical and experimental studies of localised turbulent spots and for the investigation of the large-scale flows around them.

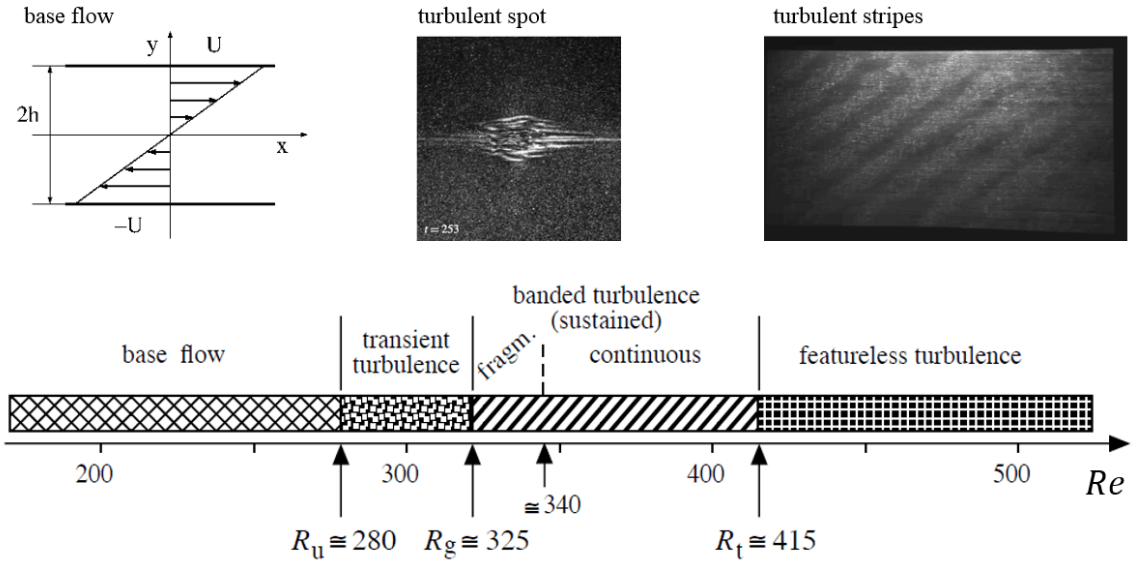

FIGURE 2.7: Bifurcation diagram of transition to turbulence in plane Couette flow with increasing Reynolds number. Figure from: Manneville [38].

Pioneered by Tillmark and Alfredsson [86] and Daviaud et al. [75], plane Couette flow is experimentally achieved by using a transparent plastic belt forming a closed loop driven by two large rotating cylinders and confined by two pairs of smaller guiding cylinders so as to maintain the gap size, as shown schematically in figure 2.6. However, in the absence of the linear instability of the base flow, a perturbation with finite amplitude is required to trigger a constantly growing turbulent spot. The bifurcation diagram of transition to turbulence in plane Couette flow with increasing Reynolds number is sketched in figure 2.7.

Although turbulent spots are observed in plane Couette flows as low as $Re \approx 280$, they remain transient until $Re \approx 325$ [108]. For $Re \geq 325$, turbulent spots become sustained and take a rhombic shape, with the dimension along the streamwise direction being slightly larger than its counterpart in the spanwise direction [56, 75, 86]. During their initial growth, the spot undergoes a spanwise expansion consequent to two distinct mechanisms: the stochastic nucleation of new streaks at the spanwise laminar-turbulent interface [88] and the spreading of turbulence due to the spanwise advection by large-scale flows [58, 63]. At later stages, growing turbulent spots start to distort for and several spots may interact with each other. Two neighbouring spots can approach and merge, forming a single stripe inclined with respect to the streamwise direction [80].

For $Re < 325$ turbulent spots in plane Couette flow are not sustained. However, they can be sustained artificially if they are continuously forced by the presence of a permanent

disturbance, e.g. a transverse jet [75, 86] or a solid obstacle [58, 109]. Even at low Reynolds numbers $Re \leq 10$, a continuous forcing localised in space triggers a permanent response interpretable as a non-turbulent spot [110].

Moreover, large-scale flows introduce modifications to the base flow and depending on their far-field decay, they may contribute to a long-range modulation among turbulent spots [77, 78], leading to the formation of laminar-turbulent banded patterns or labyrinths [79, 80]. Therefore, in order to understand the underlying mechanism for the spreading and suppression of localised turbulence by large-scale flows and to formulate an interaction rule among spots, it is necessary to know how the large-scale flow intensities decay with the distance from the spot.

The physical origin of the large-scale flow is the mismatch of the streamwise flow rates across the laminar-turbulent interface [65]. The mismatch is associated with the presence of overhang regions, where the flow is turbulent near one wall and laminar near the other [76, 89]. However, the scaling behaviour of large-scale flows away from turbulent spots is far from clear and even controversial. Schumacher and Eckhardt [64] have investigated the growth of turbulent spots in a parallel flow confined between two stress-free walls and driven by a sinusoidal body force. By averaging between the two walls, they observed quadrupolar flows apparently similar to those in plane Couette flow with no-slip boundary conditions [63, 65]. In a moderate periodic domain of size $80h\times\ 2h\times\ 80h$, where $2h$ is the gap width, they found that the kinetic energy of the large-scale flow exhibits an exponential decay in space, with a decay rate almost independent of the turbulent fluctuations inside the spot, as shown in figure 2.8 (a). More recently, Brand and Gibson [71] analysed a localised steady solution of plane Couette flow in a periodic domain of size $200h\times\ 2h\times\ 200h$. They found that the quadrupolar flow decays exponentially in both streamwise and spanwise directions, as shown in figure 2.8 (b), thereby supporting the previous observation by Schumacher and Eckhardt [64].

However, a closer examination of the database obtained in Duguet and Schlatter [65] reveals a deviation from the exponential scaling for larger computation domains, but no clear scaling rule can be established. In a periodic domain of size $[500h, 2h, 500h]$, it is possible, in principle, to fit the data to both exponential and power-law scaling, while the power-law seems to be a better description for tails of the large-scale flow, as shown in figure 2.9. In experiments by Couliou and Monchaux [62], no clear scaling has emerged from the data either.

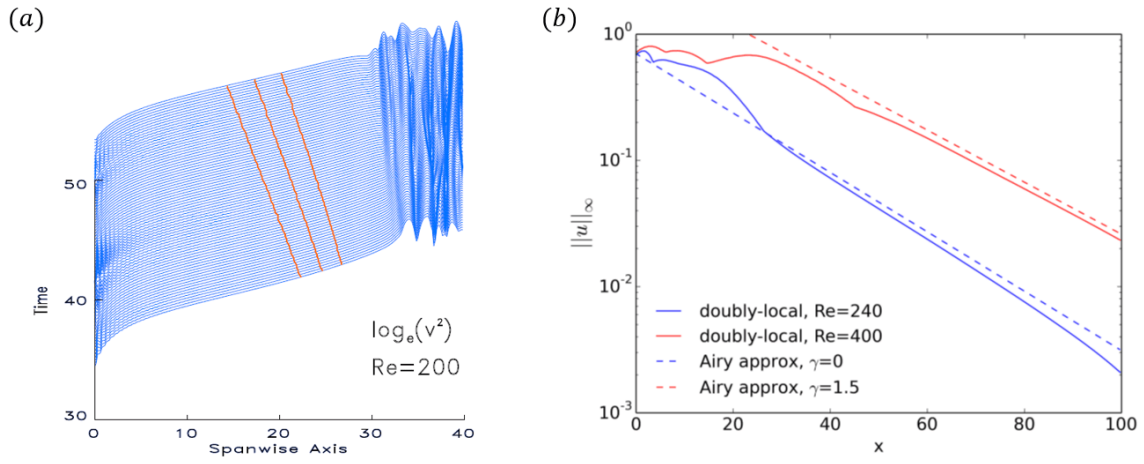

FIGURE 2.8: The exponential decay of quadrupolar flow away from the turbulent spot around (*a*) a localised turbulent spot in sinusoidal flow, figure from: Schumacher and Eckhardt [64]; and (*b*) doubly-localised steady solutions, figure from: Brand and Gibson [71].

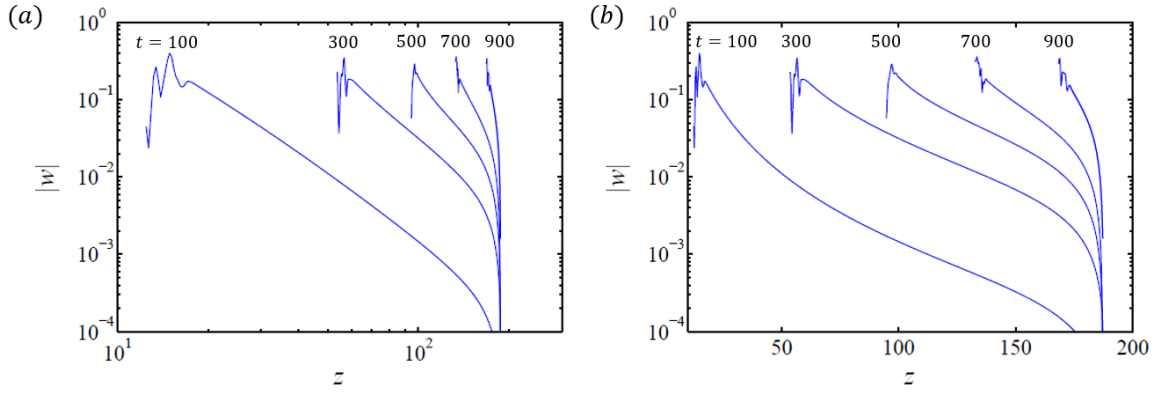

FIGURE 2.9: Tails of the spanwise velocity around a plane Couette spot at times $t = 100, 300, 500, 700, 900$ in both (*a*) log-log; and (*b*) semi-log scaling, where the computation domain is $[375h, 375h]$. Figure from: Schlatter [111].

Despite its ubiquitous observation in experiments and direct numerical simulations, as well as its practical importance in understanding growth dynamics and pattern formation, the origin of quadrupolar flows is still masked by an aura of mathematical mystery. In particular, no analytical solution for quadrupolar flows has been obtained by solving the Navier-Stokes equations. Chapter 3 presents an analytical derivation for quadrupolar circulations in flows with linear laminar profile but confined by free-slip boundary conditions at the walls, instead of no-slip. As we shall see, such a trade-off is a necessary compromise for the analytical approach. The reasons for choosing to accomplish an analytical study are (i) the current technical limitations in addressing experimentally or numerically the prediction of the far-field decay and (ii) the general lack of analytical

studies on spatial localisation in the Navier-Stokes equations and their importance for a genuine understanding of the underlying localisation mechanisms.

2.3 Navier-Stokes equations

The evolution of fluid velocity $\boldsymbol{u}(\boldsymbol{x}, t)$ of an incompressible flow with unity density and constant kinetic viscosity ν is governed by the Navier-Stokes equations

$$\partial_t \boldsymbol{u} + \boldsymbol{u} \cdot \nabla \boldsymbol{u} = -\nabla p + \nu \nabla^2 \boldsymbol{u}, \tag{2.3}$$

$$\nabla \cdot \boldsymbol{u} = 0, \tag{2.4}$$

where $p(\boldsymbol{x}, t)$ is the pressure. Eq. (2.3) was independently discovered by Navier [112] in 1823 and Stokes [113] in 1845, which now carries their names. The evolution of $(\boldsymbol{u}, p)$ as described by the Navier-Stokes equations is parabolic in time and the corresponding stationary problem is elliptical in space. Consequently, a complete description of the fluid motions requires supplementation with initial and boundary conditions. For simplicity, only the stationary boundary conditions [2], e.g. the no-slip boundary condition where velocity vanishes at walls, are considered.

The Navier-Stokes equations are simply a restatement of the Newton's second law of fluid motion, namely forces equal mass times acceleration. The left hand side of equation (2.3) is the acceleration, while the right hand side is the sum of the volume forces, i.e. the pressure gradient and the viscous force. In the absence of viscosity, i.e. $\nu = 0$, the momentum equation (2.3) reduces to the Euler equations

$$\partial_t \boldsymbol{u} + \boldsymbol{u} \cdot \nabla \boldsymbol{u} = -\nabla p, \tag{2.5}$$

which was first derived by Leonhard Euler in 1755 [37]. Since the Euler equations do not contain the second order derivatives in $\boldsymbol{u}$, different boundary conditions must be supplemented. This implies that, even in the limit $\nu \to 0$, solutions to the Navier-Stokes equations are different from those to the Euler equations [5].

[2] Here, stationary boundary conditions are those which are independent of time. Note that, this does not mean that the boundaries are themselves at rest. Well-known examples are, fluid flows sheared between two concentric cylinders rotating with prescribed constant speeds, namely Taylor-Couette flow; and between two parallel plates translating with opposite yet constant velocities, namely plane Couette flow. For flows driven by external forces such as pressure gradient in pipe flow and body force in sinusoidal flow, the stationary boundary condition translates to the requirement that the external forces are time-independent.

2.3.1 Main difficulties of the Navier-Stokes equations

At present, it is possible to obtain the fully resolved solution of the Navier-Stokes equations at moderate Reynolds numbers, known as the directed numerical simulation. However, this does not solve the problem of turbulence. Observing the evolution of numerical results, which are not in the analytic form, does not contribute to a fundamental understanding of the physics behind the phenomenology.

But why the Navier-Stokes equations, a set of *apparently* simple equations arising from an *assuredly* simple mechanism, is hard. In his monograph, Tsinober [114] summarised the main difficulties of the Navier-Stokes equations into three N's, i.e. nonlinearity, nonintegrability, and nonlocality.

2.3.1.1 Nonlinearity

It must be emphasised that both the velocity $\boldsymbol{u}(\boldsymbol{x},t)$ and the pressure $p(\boldsymbol{x},t)$ given in the Navier-Stokes (2.3) and the Euler (2.5) equations are of fluid at a fixed point in space, and they are not associated with a fixed fluid particle [37]. Therefore, the nonlinearity $\boldsymbol{u}\cdot\nabla\boldsymbol{u}$ arises due to the particle trajectory mapping [115], which is a homeomorphism from the co-moving Lagrangian (or material) frame with a fluid particle to the Eulerian frame which is fixed in space. More specifically, the velocity $\boldsymbol{u}(\boldsymbol{x},t)$ is a function of both position $\boldsymbol{x}(t)$ and time t. Sine the spatial variable is itself a function of time, using the chain rule

$$\frac{\mathrm{D}\boldsymbol{u}(\boldsymbol{x},t)}{\mathrm{D}t}=\frac{\partial\boldsymbol{u}(\boldsymbol{x},t)}{\partial t}+\frac{\partial\boldsymbol{u}(\boldsymbol{x},t)}{\partial\boldsymbol{x}}\frac{\partial\boldsymbol{x}(t)}{\partial t}=\partial_t\boldsymbol{u}+\boldsymbol{u}\cdot\nabla\boldsymbol{u}. \tag{2.6}$$

For this reason, the operator $\mathrm{D}_t=(\partial_t+\boldsymbol{u}\cdot\nabla)$ is commonly referred to as the material time derivative, so as to distinguish with the ordinary time derivative d_t. In fact, one can avoid the difficulty associated with the nonlinearity by working in the Lagrangian frame attached to a moving fluid particle. However, in this case, the difficulty translates into determining the trajectories along which fluid particles evolve from a given set of initial conditions, making the problem even more intractable.

The suppression of the nonlinearity by the so-called helicity $\boldsymbol{u}\cdot\boldsymbol{\omega}$ is one of the most fascinating property of the Navier-Stokes equations [52, 116, 117]. Denote $\boldsymbol{\omega}=\nabla\times\boldsymbol{u}$

the vorticity of the fluid and using the vector identity

$$\frac{1}{2}\nabla \boldsymbol{u}^2 = \boldsymbol{u} \times \boldsymbol{\omega} + \boldsymbol{u} \cdot \nabla \boldsymbol{u}, \tag{2.7}$$

the Navier-Stokes equations can be expressed in the Stokes form

$$\partial_t \boldsymbol{u} = -\nabla(p + \frac{1}{2}\boldsymbol{u}^2) + \boldsymbol{u} \times \boldsymbol{\omega} + \nu \nabla^2 \boldsymbol{u}, \tag{2.8}$$

where the nonlinearity stemming from the Lamb vector $\boldsymbol{u} \times \boldsymbol{\omega}$ is skew-symmetric and quadratic, and the Bernoulli function $p + \frac{1}{2}\boldsymbol{u}^2$ is of the dimension of energy. Observing from the trigonometric identity

$$(\boldsymbol{u} \times \boldsymbol{\omega})^2 + (\boldsymbol{u} \cdot \boldsymbol{\omega})^2 = |\boldsymbol{u}|^2 |\boldsymbol{\omega}|^2, \tag{2.9}$$

regions with high helicity, which is defined as

$$H = \int_{\mathbb{R}^3} \boldsymbol{u} \cdot \boldsymbol{\omega} \mathrm{d}^3 \boldsymbol{x}, \tag{2.10}$$

are expected to have small contributions from the Lamb vector $\boldsymbol{u} \times \boldsymbol{\omega}$, and vice versa. The suppression of nonlinearity, thereby reduced energy cascade and energy dissipation, by helicity density has led many [116, 118–121] to speculate that helical structures, wherein the velocity and vorticity vectors are nearly aligned or anti-aligned, have long life times, hence coherent. However, early directed numerical simulations on homogeneous turbulence and channel flows reported no clear correlation between helicity and dissipation [122]. This apparent controversy may be due to that the helicity density is defined on a spatial point, measuring the relative alignment between velocity and vorticity at that point, while coherent structures signifies the correlated velocity and vorticity over a finite space and a long time. Therefore, the instantaneous helicity for coherent structures, e.g. streamwise vortices, is best interpreted as the inner product between the space averaged vorticity over the coherent structure and the translation velocity $\boldsymbol{U}$ experienced by the it at each time instance

$$\boldsymbol{U} \cdot \int_{\mathbb{R}^3} \boldsymbol{\omega} \mathrm{d}^3 \boldsymbol{x}, \tag{2.11}$$

which is clearly different from the previous definition of helicity integral (2.10).

2.3.1.2 Nonintegrability

Although the nonlinearity is often accused as the source of complexity, it should be pointed out that not all nonlinear partial differential equations are as notoriously difficult as the Navier-Stoke equations. Completely integrable systems, e.g. nonlinear Schrodinger equation and Korteweg–de Vries (KdV) equation, admit explicit and analytic solutions evolving from an arbitrary set of initial conditions [123]. In these systems, chaos stems from the stochasticity of the initial and boundary conditions. By contrast, turbulence is autonomous, suggesting that the Navier-Stokes equations are not integrable. In fact, stemming from the Newton's second law, the Navier-Stokes equations reduce all kinds of fluid motions to a single point analysis and, as pointed out by Lagrange in his monograph *mécanique analytique* (quoted from Tsinober [114])

> *"...if the equations involved were integrable, one could determine completely, in all cases, the motion of a fluid moved by any forces."*

Although there is no universally accepted definition of integrability for partial differential equations, the rule of thumb is [124]

i the ability to give explicit solutions;

ii the presence of algebraic geometry; and

iii the existence of many conserved quantities.

To begin with, obtain an explicit solution to the Navier-Stokes equation is hopeless, and the geometry associated with turbulence is, in general, fractal and multifractal [125], thereby not algebraic. Although the Euler equations possess a limited group of conserved global quantities such as momentum, energy, helicity, and angular momentum [3], many of the conservation laws are broken in the presence of viscosity and even become controversial [126–128]. A complete list of conserved quantities in Euler equations and their proofs can be found in Majda and Bertozzi [115], hence omitted here.

In the following, the conservation of the kinetic energy and the helicity is revisited. To avoid technicalities, it is assumed that both $\boldsymbol{u}$ and p decay sufficiently fast in the infinity.

[3] Due to the slow decay of $|\boldsymbol{u}|$ in the infinite, the conservation of angular momentum $\int_{\mathbb{R}^3} \boldsymbol{x} \times \boldsymbol{u} \mathrm{d}^3\boldsymbol{x}$ is usually replaced by the conservation of fluid impulse $\int_{\mathbb{R}^3} \boldsymbol{x} \times \boldsymbol{\omega} \mathrm{d}^3\boldsymbol{x}$.

Multiplying equation (2.8) with $\boldsymbol{u}$ and using the vector identity

$$\boldsymbol{u} \cdot \nabla^2 \boldsymbol{u} = \nabla \cdot (\boldsymbol{u} \times \boldsymbol{\omega}) - \boldsymbol{\omega}^2, \tag{2.12}$$

yielding

$$(\partial_t + \boldsymbol{u} \cdot \nabla) \frac{1}{2} \boldsymbol{u}^2 = -\nabla \cdot (\boldsymbol{u} p + \nu \boldsymbol{u} \times \boldsymbol{\omega}) - \nu \boldsymbol{\omega}^2. \tag{2.13}$$

Integrating the preceding equation over $\mathbb{R}^3$ and using the divergence theorem, the evolution of the kinetic energy solves the following ordinary differential equation

$$\frac{\mathrm{d}}{\mathrm{d}t} \int_{\mathbb{R}^3} \boldsymbol{u}^2 \mathrm{d}^3 \boldsymbol{x} = -2\nu \int_{\mathbb{R}^3} \boldsymbol{\omega}^2 \mathrm{d}^3 \boldsymbol{x}. \tag{2.14}$$

Here, the viscosity acts as a sink, monotonically transferring the kinetic energy into heat. It is interesting to note that, if the pressure is time independent, i.e. $\partial_t p = 0$, the conservation of kinetic energy can be expressed in terms of the Bernoulli function

$$\frac{\mathrm{d}}{\mathrm{d}t} \int_{\mathbb{R}^3} \left(\frac{1}{2} \boldsymbol{u}^2 + p \right) \mathrm{d}^3 \boldsymbol{x} = -\nu \int_{\mathbb{R}^3} \boldsymbol{\omega}^2 \mathrm{d}^3 \boldsymbol{x}. \tag{2.15}$$

This implies that the Bernoulli function is conserved over $\mathbb{R}^3$ or along the particle trajectory [115] in the inviscid limit. In this case, one recovers the Bernoulli equation.

There are exceptions where the viscosity can act as a source. Combining the vorticity equation, which is obtained by taking the curl of equation (2.8), and the momentum equation (2.3), the transport equation for the helicity density reads

$$(\partial_t + \boldsymbol{u} \cdot \nabla) \boldsymbol{u} \cdot \boldsymbol{\omega} = -\nabla \cdot \left[\boldsymbol{\omega} \left(p - \frac{1}{2} \boldsymbol{u}^2 \right) \right] + \nu \left(\boldsymbol{\omega} \nabla^2 \boldsymbol{u} + \boldsymbol{u} \nabla^2 \boldsymbol{\omega} \right). \tag{2.16}$$

Using the vector identity

$$\nabla \cdot [\boldsymbol{u} \times (\nabla \times \boldsymbol{\omega})] = \boldsymbol{\omega} \cdot \nabla \times \boldsymbol{\omega} + \boldsymbol{u} \cdot \nabla^2 \boldsymbol{\omega}, \tag{2.17}$$

$$\nabla \cdot [\boldsymbol{\omega} \times (\nabla \times \boldsymbol{u})] = \boldsymbol{\omega} \cdot \nabla \times \boldsymbol{\omega} + \boldsymbol{\omega} \cdot \nabla^2 \boldsymbol{u}, \tag{2.18}$$

and note that the divergence terms vanish upon an integration over $\mathbb{R}^3$, we obtain

$$\frac{\mathrm{d}}{\mathrm{d}t} \int_{\mathbb{R}^3} \boldsymbol{u} \cdot \boldsymbol{\omega} \mathrm{d}^3 \boldsymbol{x} = -2\nu \int_{\mathbb{R}^3} \boldsymbol{\omega} \cdot \nabla \times \boldsymbol{\omega} \mathrm{d}^3 \boldsymbol{x}. \tag{2.19}$$

By contrast to equation (2.14), the vector product $\boldsymbol{\omega} \cdot \nabla \times \boldsymbol{\omega}$, commonly referred to as the super-helicity density [129], is sign indefinite. That is, depending on the relative alignment between the helicity and the super-helicity densities, their product can be negative, leading to a production of the helicity density by viscosity.

In general, the helicity and the super-helicity can be interpreted as a measure for the lack of reflection symmetry at the large- and small-scales, respectively [128]. Note that, equation (2.19) implies that the breaking of reflectional symmetry in large scales is subsequent to the lack of symmetry in small scales. The finite growth of helicity requires a nonlocal coupling between scales that the symmetry breaking (resp. restoring) in large scales enforces a restoring (resp. breaking) of the symmetry in small scales. In order to investigate the symmetry breaking/restoring in smaller scales, one may continue to write down the transport equation for the super-helicity

$$\frac{\mathrm{d}}{\mathrm{d}t} \int_{\mathbb{R}^3} \boldsymbol{\omega} \cdot (\nabla \times \boldsymbol{\omega}) \mathrm{d}^3\boldsymbol{x} = 2 \int_{\mathbb{R}^3} \nabla \times \boldsymbol{\omega} \cdot \nabla (\boldsymbol{u} \times \boldsymbol{\omega}) \mathrm{d}^3\boldsymbol{x} - 2\nu H_h, \tag{2.20}$$

leading to an ever smaller-scale hyper-helicity

$$H_h = \int_{\mathbb{R}^3} \nabla \times \boldsymbol{\omega} \cdot (\nabla \times \nabla \times \boldsymbol{\omega}) \mathrm{d}^3\boldsymbol{x}, \tag{2.21}$$

and so on so forth. The chain is endless, resulting in an infinite regression.

2.3.1.3 Nonlocality

Complete integrable systems are clearly exceptional. Most nonlinear differential equations arising from physics do not admit explicit formulae for solutions, thereby non-integrable. Classical examples include Van der Pol's equations, Duffing's equations, and the Lorenz equations. Despite the nonlinearity and the nonintegrability, the onset of chaos in these systems can be approached in terms of the dynamical systems theory [130]. As summarised in Chapter 1, the spatial modulation prevents us from interpreting the transition to turbulence in an extended flow domain from a pure dynamical system point of view. Mathematically, this modulation is linked with the nonlocality of the Navier-Stokes equations.

Note that, the Navier-Stokes equations do not include the time-derivative of p, hence if the pressure can be expressed in terms of velocity, i.e. $p(\boldsymbol{u})$, it can be explicitly eliminated from the Navier-Stokes equations. Taking the divergence operator to the Navier-Stokes

equations, one obtains the Poisson equation for pressure

$$-\nabla^2 p = \frac{\partial u_i}{\partial x_j}\frac{\partial u_j}{\partial x_i}. \tag{2.22}$$

The solution to the Poisson equation can be expressed formally as

$$p = -\nabla^{-2}\frac{\partial u_i}{\partial x_j}\frac{\partial u_j}{\partial x_i}, \tag{2.23}$$

up to an additive constant. Consequently, the fluid pressure $p(\boldsymbol{x}, t)$ can be regarded as an auxiliary variable, namely at each moment t, it is determined by the incompressibility constraint up to an "inessential" constant [27]. It is noteworthy that the expression (2.23) involves an inverse of the Laplace operator ∇^{-2}, which is nonlocal in the sense that the solution for p at each space point requires the entire information of $\boldsymbol{u}$ over $\mathbb{R}^3$. If p is eliminated by substitution, the Navier-Stokes equation can be expressed as an integro-differential space-time system for $\boldsymbol{u}$ only

$$(\partial_t + \boldsymbol{u}\cdot\nabla)\boldsymbol{u} = \nabla\nabla^{-2}\frac{\partial u_i}{\partial x_j}\frac{\partial u_j}{\partial x_i} + \nu\nabla^2\boldsymbol{u}, \tag{2.24}$$

where the nonlocality is explicitly present.

Note that, this nonlocality is an inherent property of the Navier-Stokes equations and cannot be eliminated through successive linear operations. For instance, although the pressure term can be eliminated by taking the curl operator of equation (2.8), giving rise to the equation for vorticity

$$\partial_t\boldsymbol{\omega} = \nabla\times(\boldsymbol{u}\times\boldsymbol{\omega}) + \nu\nabla^2\boldsymbol{\omega}. \tag{2.25}$$

In order to express this equation in terms of $\boldsymbol{\omega}$ alone, we need to substitute the following Poisson equation for velocity

$$\nabla^2\boldsymbol{u} = -\nabla\times\boldsymbol{\omega}, \tag{2.26}$$

into the vorticity equation (2.25), yielding

$$\partial_t\boldsymbol{\omega} = -\nabla\times\left[\nabla^{-2}(\nabla\times\boldsymbol{\omega})\times\boldsymbol{\omega}\right] + \nu\nabla^2\boldsymbol{\omega}, \tag{2.27}$$

where the same nonlocal operator ∇^{-2} reappears in the vorticity formalism (2.27).

2.3.2 Conditions for eliminating nonlinearity

The three aforementioned difficulties of the Navier-Stokes equations, i.e. nonlinearity, nonintegrability, and nonlocality, are not three individual entities but intertwined, leading to a hard nut to crack. Therefore, in order to tackle the problem, (reasonable) assumptions that break the links among these difficulties are necessary. For instance, linear stability analysis [8, 96] linearises the Navier-Stokes equations about the base flow, thereby eliminating the nonlinearity; while the one-dimensional Burgers [131] equation keeps the nonlinearity but eliminates the pressure terms and reduces the dimensionality, hence the resulting system is completely integrable and local [114]. Based on data obtained from direct numerical simulations of plane Couette flow, Brand and Gibson [71] performed a drastic reduction of the Navier-Stokes equations by dropping the time derivative, linearising about the base flow, and eliminating the pressure term. The resulting equation for the streamwise velocity takes the form of the one-dimensional Airy equation, which is linear, integrable, and local.

Identifying the nonlinearity as the prime difficulty of the Navier-Stokes equation [114], it is reasonable to consider: how far one can achieve without it? Various conditions permitting linearisation are summarised and discussed in the following.

2.3.2.1 Laminar flow at low Reynolds numbers

Denote U and L the characteristic velocity and length scales of the flow, the inertial and viscous terms in the Navier-Stokes equations (2.3) have dimensions U^2/L and $\nu U/L^2$, respectively. Their ratio gives rise to a dimensionless parameter, namely the Reynolds number

$$Re = \frac{\text{inertial force}}{\text{viscous force}} = \frac{U^2/L}{\nu U/L^2} = \frac{UL}{\nu}. \tag{2.28}$$

For $Re \ll 1$, the inertial force is negligible in comparison with the viscous force, hence can be discarded.

For instance, let us consider a steady flow, i.e. $\partial_t \boldsymbol{u} = 0$, by dropping the inertial terms, Eq. (2.3) reduces to the following Stokes equations

$$\nu \nabla^2 \boldsymbol{u} - \nabla p = 0, \tag{2.29}$$

depicting an exact balance between the pressure gradient and the viscous force. For a steady motion of a viscous fluid between two infinite, oppositely moving plates with speed $\pm U$, the Stokes equations (2.29) reduce to

$$\nu \partial_y^2 u_x = \partial_x p, \tag{2.30}$$

where x-axis is aligned with the direction of the shearing, and y-axis is normal to the plates such that the plates locate at $y = \pm h$. Eq. (2.30) is supplemented with the no-slip boundary conditions

$$u_x|_{y=\pm h} = (y/h)U \quad \text{and} \quad u_y|_{y=\pm h} = u_z|_{y=\pm h} = 0. \tag{2.31}$$

Note that, Eq. (2.30) is valid only if both sides of the equation are constant

$$\partial_x p = \text{const.} \tag{2.32}$$

Consequently, the laminar profile, which is commonly referred to as Couette-Poiseuille flow, is given by

$$u_x = \frac{\partial_x p}{2\nu} y^2 + Sy + b, \tag{2.33}$$

where the coefficients

$$b = -\frac{h^2 \partial_x p}{2\nu}, \quad S = U/h, \tag{2.34}$$

are determined from the no-slip boundary conditions (2.31).

For flows with vanishing pressure gradient, one recovers the linear laminar profile of plane Couette flow

$$u_x = Sy, \quad u_y = 0, \quad u_z = 0. \tag{2.35}$$

For flows between two motionless plates driven by the pressure gradient, one obtains plane Poiseuille flow

$$u_x = \frac{\partial_x p}{2\nu}(y^2 - h^2), \quad u_y = 0, \quad u_z = 0. \tag{2.36}$$

2.3.2.2 Weakly perturbed flow near linear instability threshold

For flows admitting a well-defined laminar base flow, it is customary to decompose the instantaneous flow field $(\boldsymbol{u}, p)$ into the base flow, denoted here by $(\boldsymbol{U}, P)$, in addition to

a perturbation $(\tilde{\boldsymbol{u}}, \tilde{p})$, that is

$$\boldsymbol{u} = \boldsymbol{U} + \tilde{\boldsymbol{u}}, \quad p = P + \tilde{p}. \tag{2.37}$$

Substituting the decomposition into the Navier-Stokes equations (2.3), and note that the base flow is itself a solution to the Navier-Stokes equations, thereby being subtracted. These lead to an apparently more complex equation characterising the evolution of the perturbation

$$\partial_t \tilde{\boldsymbol{u}} + \boldsymbol{U} \cdot \nabla \tilde{\boldsymbol{u}} + \tilde{\boldsymbol{u}} \cdot \nabla \boldsymbol{U} + \tilde{\boldsymbol{u}} \cdot \nabla \tilde{\boldsymbol{u}} = -\nabla \tilde{p} + \nu \nabla^2 \tilde{\boldsymbol{u}}. \tag{2.38}$$

On the left hand side, there are three terms arising from the advective nonlinearity of the instantaneous flow field. They are: (i) $\boldsymbol{U} \cdot \nabla \tilde{\boldsymbol{u}}$, which is linear, representing the advection of the perturbed velocity by the base flow; (ii) $\tilde{\boldsymbol{u}} \cdot \nabla \boldsymbol{U}$, which is linear, representing the "stretching" of the perturbed velocity by the shear of the base flow [4]; and (iii) $\tilde{\boldsymbol{u}} \cdot \nabla \tilde{\boldsymbol{u}}$, which is nonlinear, representing the self-interaction of the perturbed flow. Note that, the nonlinearity, which is quadratic in $\tilde{\boldsymbol{u}}$, is negligible if the intensity separation between $\tilde{\boldsymbol{u}}$ and $\boldsymbol{U}$ is sufficient, i.e. $|\tilde{\boldsymbol{u}}| \ll |\boldsymbol{U}|$, leading to a linearisation about the base flow

$$\partial_t \tilde{\boldsymbol{u}} + \boldsymbol{U} \cdot \nabla \tilde{\boldsymbol{u}} + \tilde{\boldsymbol{u}} \cdot \nabla \boldsymbol{U} = -\nabla \tilde{p} + \nu \nabla^2 \tilde{\boldsymbol{u}}. \tag{2.39}$$

It should be emphasised that the decomposition (2.37) and the resulting equation (2.38) are valid for all flows; while the linearised equation (2.39) is applicable only when the quadratic nonlinear term is negligible in comparison.

For plane Couette flow, the base flow is given by equation (2.35), and substitution into Eqs. (2.39) gives componentwise

$$(\partial_t + Sy\partial_x)\,\tilde{u}_x = -\partial_x \tilde{p} + \nu \nabla^2 \tilde{u}_x - S\tilde{u}_y, \tag{2.40a}$$

$$(\partial_t + Sy\partial_x)\,\tilde{u}_y = -\partial_y \tilde{p} + \nu \nabla^2 \tilde{u}_y, \tag{2.40b}$$

$$(\partial_t + Sy\partial_x)\,\tilde{u}_z = -\partial_z \tilde{p} + \nu \nabla^2 \tilde{u}_z, \tag{2.40c}$$

where the perturbed pressure solves

$$\nabla^2 \tilde{p} = -2S\partial_x \tilde{u}_y, \tag{2.41}$$

[4] According to Prof. B. Eckhardt, this term may be interpreted alternatively as the advection of the base flow by turbulence, thereby "inessential". As it shall be reviewed in §2.3.2.4, the inclusion of this term changes the eigenfunctions of the differential operator from trigonometric functions to Airy functions.

so as to satisfy the incompressibility constraint. The preceding equations are subjected to the no-slip boundary conditions

$$\tilde{u}_x = \tilde{u}_y = \tilde{u}_z = 0, \tag{2.42}$$

at walls and at the infinity. Taking the divergence operator to Eq. (2.40b) and using the Poisson equation (2.41), one obtains a decoupled equation for the wall-normal velocity $\tilde{u}_y$ only

$$\left[\left(\partial_t + Sy\partial_x\right)\nabla^2 - \nu\nabla^4\right]\tilde{u}_y = 0. \tag{2.43}$$

In order to form a complete description for the three-dimensional flow field, besides Eq. (2.43), another equation, which provides information on $\tilde{u}_x$ and $\tilde{u}_z$, is required. Taking the curl operator to equation (2.40), one obtains the linearised equation for the perturbed vorticity

$$\left(\partial_t + Sy\partial_x\right)\tilde{\omega}_x = \nu\nabla^2\tilde{\omega}_x, \tag{2.44a}$$

$$\left(\partial_t + Sy\partial_x\right)\tilde{\omega}_y = \nu\nabla^2\tilde{\omega}_y - S\partial_z\tilde{u}_y, \tag{2.44b}$$

$$\left(\partial_t + Sy\partial_x\right)\tilde{\omega}_z = \nu\nabla^2\tilde{\omega}_z - S\partial_z\tilde{u}_z. \tag{2.44c}$$

It is seen that the equation for $\tilde{\omega}_x$ is homogeneous taking the form of the advection-diffusion equation, while equations for $\tilde{\omega}_y$ and $\tilde{\omega}_z$ are inhomogeneous forced by the spanwise inhomogeneity of corresponding perturbed velocities $\tilde{u}_y$ and $\tilde{u}_z$, respectively. Here, the equation for $\tilde{\omega}_x$does not provides sufficient information for $\tilde{u}_x$ and the equation for $\tilde{\omega}_z$ does not provide information of $\tilde{u}_z$.

According to Schmid and Henningson [96], when supplemented by the proper boundary conditions

$$\tilde{u}_y = \partial_y\tilde{u}_y = \tilde{\omega}_y = 0, \tag{2.45}$$

at walls and at the infinity [5], the system comprising equations for $\tilde{u}_y$ and $\tilde{\omega}_y$

$$\left[\left(\partial_t + Sy\partial_x\right)\nabla^2 - \nu\nabla^4\right]\tilde{u}_y = 0, \tag{2.46a}$$

$$\left[\left(\partial_t + Sy\partial_x\right) - \nu\nabla^2\right]\tilde{\omega}_y = -S\partial_z\tilde{u}_y, \tag{2.46b}$$

[5]This is an example of the no-slip boundary conditions where $\tilde{u}_y = 0$ specifies that there is no penetration at walls; while the combination $\partial_y\tilde{u}_y = \tilde{\omega}_y = 0$ translates to that $\tilde{u}_x$ and $\tilde{u}_z$ are identically zero at walls and in the infinity, thereby no-slip.

provides a complete description for the evolution of an arbitrary weak perturbation in plane Couette flow. More specifically, with solutions for $\tilde{u}_y$ and $\tilde{\omega}_y$, the streamwise and spanwise velocity components can be recovered by solving:

$$(\partial_x^2 + \partial_z^2)\tilde{u}_x = +\partial_z\tilde{\omega}_y - \partial_x\partial_y\tilde{u}_y, \tag{2.47}$$

$$(\partial_x^2 + \partial_z^2)\tilde{u}_z = -\partial_x\tilde{\omega}_y - \partial_z\partial_y\tilde{u}_y, \tag{2.48}$$

with the Dirichlet boundary conditions

$$\tilde{u}_x|_{x,z\to\infty} = \tilde{u}_x|_{x,z\to\infty} = 0. \tag{2.49}$$

2.3.2.3 Linear instability analysis I: Orr-Sommerfeld equation

For historical reasons [14, 132, 133], Eqs. (2.46) were first derived to determine whether the particular type of laminar base flow is linearly stable, here the plane Couette flow. For planar shear flows with two homogeneous directions, this consists of two steps: (i) substituting the travelling wave ansatz

$$\tilde{u}_y(x,y,z,t) = \hat{u}_y(y)e^{\mathrm{i}(k_x x + k_z z - k_x c t)}, \tag{2.50a}$$

$$\tilde{\omega}_y(x,y,z,t) = \hat{\omega}_y(y)e^{\mathrm{i}(k_x x + k_z z - k_x c t)}, \tag{2.50b}$$

where k_x and k_z are the streamwise and spanwise wavenumbers, respectively, and c denotes the phase speed, into Eqs. (2.46)

$$\left[(-\mathrm{i}k_x c + \mathrm{i}k_x S y)(\partial_y^2 - k_x^2 - k_z^2) - \nu(\partial_y^2 - k_x^2 - k_z^2)^2\right]\hat{u}_y = 0, \tag{2.51a}$$

$$\left[(-\mathrm{i}k_x c + \mathrm{i}k_x S y) - \nu(\partial_y^2 - k_x^2 - k_z^2)\right]\hat{\omega}_y = -\mathrm{i}k_z S\hat{u}_y, \tag{2.51b}$$

and (ii) seek for unstable eigenvalues. These equations are supplemented with the Fourier transformed Dirichlet boundary conditions

$$\hat{u}_y = \partial_y\hat{u}_y = \hat{\omega}_y = 0, \tag{2.52}$$

at walls and at the infinity. Since the coefficients of preceding equations are real, all complex eigenvalues appear in conjugate pairs. Thus, seeking for unstable eigenvalues is equivalent to look for complex k_x, k_z, and c. In particular, the choice $c \in \mathbb{C}$ and $k_x, k_z \in \mathbb{R}$ depicts a temporal problem, where the amplitude of the wave grows or decays

exponentially in time, while the structure of the wave is preserved in space. On the other hand, the choice $c \in \mathbb{R}$ and $k_x, k_z \in \mathbb{C}$ is referred to as a spatial problem that the amplitude of the wave grows or decays in space, while its frequency remains constant [96].

The equation for the wall-normal velocity $\hat{u}_y$ is first derived by Orr [132] in 1907 and independently by Sommerfeld [14] in 1908, which now bears their names and are commonly referred to as the Orr-Sommerfeld equation. While the equation for the wall-normal vorticity $\hat{\omega}_y$ was discovered almost 30 years later by Squire [133], hence the Squire equation. For inviscid flows, where $\nu = 0$, the Orr-Sommerfeld equation (2.51a) reduces to the Rayleigh equation [134, 135]. For plane Couette flow, the Rayleigh equation becomes

$$(Sy - c)(\partial_y^2 - k_x^2 - k_z^2)\hat{u}_y = 0, \tag{2.53}$$

with the boundary conditions $\hat{u}_y = 0$ at the walls and at infinity.

For sufficiently small values of Re, the viscosity has a purely destabilising effect [136]. In this limit, Southwell and Chitty [137] investigated in details the Orr-Sommerfeld equation for plane Couette flow, namely Eq. (2.51a), but they failed to answer the question whether the base flow is linearly stable or unstable. In the other limit of where $Re \to \infty$, Case [138] and Dikii [139] applied the Fourier-Laplace method, i.e. taking Fourier transform with respect to x and Laplace transform with respect to t, to the linearised equation (2.46a), and it was found that an arbitrary initial perturbation vanishes as $1/\sqrt{x^2 + y^2}$ or faster in space. Hence, the inviscid plane Couette flow is linearly stable. The stability of the viscous plane Couette flow is partially evidenced by Dikii [140] that, all standing waves with $c = 0$ are stable, and finally proved by Romanov [107] in 1973. It was shown that all normal modes decays for $k_x \geq 0$ and $Re \geq 0$.

2.3.2.4 Linear instability analysis II: Kelvin mode solution

Despite being the starting point of the linear stability analysis for planar shear flows, the Orr-Sommerfeld equation is notoriously difficult to solve. Analytically, investigations lead to various different asymptotic regimes in the $Re - k_x$ plane, where nothing but absolute stability is reported [141]. The difficulties associated with solving the Orr-Sommerfeld equations numerically arise from the sensitive dependence on discretisation schemes [96] and on truncation errors [142].

The Orr-Sommerfeld equation for plane Couette flow is a (i) fourth order ordinary differential equation with (ii) various coefficient containing the spatial variable y. The origins underlying these mathematical difficulties can be easily understood. To begin with, the involvement of high-order derivatives originates from the non-vanishing pressure gradient $\partial_y p$ in the momentum equation for $\tilde{u}_y$. That is, if $\partial_y p$ is identically zero, the Orr-Sommerfeld equation for a two-dimensional perturbation $\hat{u}(x, y)$ reduces to a second order differential equation

$$\left[(-\mathrm{i}k_x c + \mathrm{i}k_x S y) - \nu(\partial_y^2 - k_x^2)\right] \hat{u}_y = 0, \tag{2.54}$$

which takes the form of the generalised Airy equation, whose general solutions consist of a superposition of the Airy functions Ai and Bi as

$$\hat{u}_y = c_1 \mathrm{Ai}\left(\frac{\left(\sqrt{3} - \mathrm{i}\right)\left[(c - Sy)k_x + \mathrm{i}\nu k_x^2\right]}{2\nu^{\frac{1}{3}} S^{\frac{2}{3}} k_x^{\frac{2}{3}}}\right) + c_2 \mathrm{Bi}\left(\frac{\left(\sqrt{3} - \mathrm{i}\right)\left[(c - Sy)k_x + \mathrm{i}\nu k_x^2\right]}{2\nu^{\frac{1}{3}} S^{\frac{2}{3}} k_x^{\frac{2}{3}}}\right), \tag{2.55}$$

for $k_x \in \mathbb{R}$. The coefficients c_1 and c_2 are determined from the boundary conditions. However, since the order of the differential equation is reduced, the boundary condition has to be modified accordingly, cf. Chapter 3.

On the other hand, if the mean flow advection is negligible, one avoids the difficulties associated with the variable coefficients. Based on these ideas, Marcus and Press [143] exploited the translational symmetry in Lagrangian coordinates so as to eliminate the advection term. More specifically, the laminar plane Couette flow is invariant with respect to a spatial translation in the homogeneous directions and a central inversion about y; these boost to a co-moving Lagrangian coordinates

$$x_L = x - Syt, \quad y_L = y, \tag{2.56}$$

where the subscript $_L$ denotes the spatial variables in the Lagrangian coordinates.

Instead of the equation for $\tilde{u}_y$, Marcus and Press [143] took advantage of the simplicity of the equation for the streamwise vorticity $\tilde{\omega}_x$. Taking Fourier transform in the streamwise x_L and wall-normal y_L directions, or equivalently substituting the ansatz

$$\tilde{\omega}_x(x, y, t) = \hat{\omega}_x(t) e^{\mathrm{i}k_x x_L + \mathrm{i}k_y y_L} = \hat{\omega}_x(t) e^{\mathrm{i}k_x x + \mathrm{i}(k_y - Sk_x t)y} \tag{2.57}$$

into equation (2.44a), yielding

$$\partial_t \hat{\omega}_x = -\nu \left[k_x^2 + (k_y + S k_x t)^2 \right] \hat{\omega}_x, \tag{2.58}$$

and a direct integration implies that the streamwise vorticity decays as

$$\hat{\omega}_x \propto e^{-\frac{1}{3}\nu S^2 y^2 t^3}, \tag{2.59}$$

at large time, thereby linearly stable. The ansatz (2.57) was first proposed by Lord Kelvin [1] in solving the V-shaped wave pattern in the far-field behind a constantly moving ship, hence the solution obtained by using ansatz (2.57) is generally referred to as the Kelvin mode solution. It shall be seen in Appendix C that the quadrupolar flow is such a solution for plane Couette flow.

Note that, taking the Fourier transform in the wall-normal direction is justified only when the flow is unbounded in this direction, and in order to match the boundary conditions at walls, method of images, which was originally introduced by Lord Kelvin in 1848, can be used. Without knowing the work of Marcus and Press [143], Dubrulle and Knobloch [11] applied the Kelvin ansatz (2.57) to the compressible rotating plane Couette flow and, to avoid technicalities associated with the method of images, they proved that the flow under consideration is stable to infinitesimal perturbations in an unbounded domain.

2.3.2.5 Linear instability analysis III: limitation and extension

Although there is no doubt that plane Couette flow is stable against an infinitesimal perturbation, it is first pointed out by Lord Rayleigh [144] that, it may be unstable subjected to finite amplitude disturbances. As such, a linearisation achieved by discarding the quadratic nonlinearity $\tilde{\boldsymbol{u}} \cdot \nabla \tilde{\boldsymbol{u}}$ is no longer justified. Confronting this difficulty, two different points of view have been proposed: one seeks for an extension of the linearised framework

> *"It is not the process of linearization that limits insight. It is the nature of the state we choose to linearize about."* (E. T. Eady [145])

and interprets the transition as a consequence of the secondary instabilities [145–147]; while the other advocates for a closer examination of the nonlinearity [148].

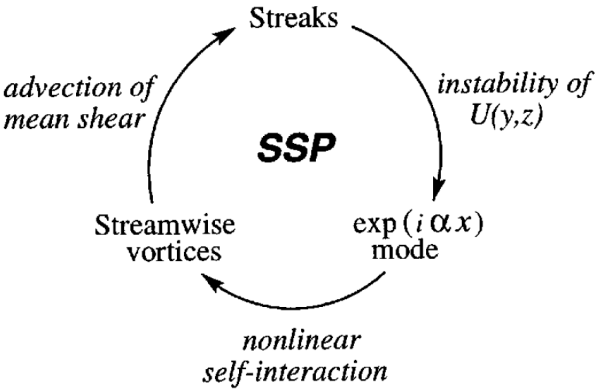

FIGURE 2.10: The self-sustaining process proposed by Waleffe and his colleagues. Starting from the streamwise vortices, (i) which generate streaks via the lift-up effect, i.e. advection of mean flow by streamwise vortices; (ii) streaks are suffered from the inflectional instabilities and breakdown; and (iii) nonlinear self-interactions regenerate streamwise vortices. Figure from: Waleffe [151].

In many cases, a finite amplitude disturbance does not drive the flow directly into turbulence. Instead, it is saturated [6], establishing a new steady or quasi-steady base flow. Subjected to infinitesimal perturbations, a linear instability can develop upon the modified base flow, and eventually drives the flow into turbulence. The instability evolved from the modified base flow is referred to as the secondary instability. In terms of the transitional planar shear flows, the modified base flow comprises velocity streaks arising from the counter-rotating pairs of streamwise vortices. In this case, a linearisation about the vortices is justified [149]. This idea is further explored in Chapter 4.

Despite the success of the secondary instability theory, an unavoidable question is how an infinitesimal perturbation reaches a finite amplitude with the purely linear formulations. Trefethen et al. [150] found that, due to the existence of the off-diagonal coupling terms, the linear operator associated with the Orr-Sommerfeld equation is non-normal, i.e. cannot be projected onto a set of mutual orthogonal eigenfunctions. Although all eigenvalues are negative, kinetic energy can grow transiently, eliciting nonlinear effects. In this sense, the modal instabilities associated with each individual eigenfunctions is incomplete.

Since early 1990s, advances in computational techniques allow for a direct numerical searching for the fully nonlinear invariant solutions of the Navier-Stokes equations [152]. By a continuation of solutions bifurcating from the two-dimensional streaky flow $U(y, z)$ with streamwise vortices externally maintained by the prescribed body force, a family of steady state and travelling wave solutions are numerically obtained [153, 154]. These

[6] The saturation of finite amplitude disturbances is due to the nonlinearity of the Navier-Stokes equations, cf. Waleffe [148].

numerical solutions look similar to coherent structures educed from direct numerical simulation of various shear flows, hence referred to as the exact coherent structures [154]. These invariant structures are the building block of turbulence and are believed to capture many, not only structural but also statistical, properties of the subcritical transition. Note that, exact coherent structures do not necessarily connect, directly (i.e. via the primary instability) or indirectly (i.e. via the secondary instability), to the laminar solution [92, 148, 151], and since they are typically unstable, the transition to turbulence is then a matter of existing nonzero basins of attraction wherein the solution trajectories are bouncing among these invariant structures [91].

Physically, exact coherent structures are maintained by a nonlinear self-sustaining process as shown in figure 2.10. Rather than the instability of laminar flows, the self-sustaining process arises from a study of the transition *from* turbulence [155]. Consequently, exact coherent structures are best understood as the residue of fully developed turbulence that survives down to the critical Reynolds numbers, below which turbulence relaminarises. Borrowing ideas from algebraic topology, Waleffe [153, 156] investigated the morph of exact coherent structures under homotopy from Couette to Poiseuille flows and from free-slip to no-slip boundary conditions. He found they look similar to one another as shown in figure 2.11, indicating that the coherent structures are homotopy equivalence. Ever since, exact coherent structures of similar kinds have been numerically [157, 158] and experimentally [159] identified in pipe flow and in annular pipe flow under a homotopy of various aspect ratios [160].

2.3.2.6 Perturbed flow in rapid distortion limit

For fully developed turbulence, although the amplitude of the perturbed flow is no longer infinitesimal, a linearisation can still be justified under the framework of the rapid distortion theory [161, 162]. The rapid distortion theory describes the response of turbulence transiting through a region with strong mean flow shear. A linearisation can be established when the distortion by the mean flow $\tilde{\boldsymbol{u}} \cdot \nabla \boldsymbol{U}$ takes place so rapidly that nonlinear self-interaction of the distorted turbulence $\tilde{\boldsymbol{u}} \cdot \nabla \tilde{\boldsymbol{u}}$ has insufficient time to modify the flow [163].

For flows subjected to a pure shearing, e.g. plane Couette flow, the inertial dynamics is characterised by two competing processes. The nonlinear cascade of kinetic energy characterised by an eddy turnover time $\tau_e = \lambda/U$, where λ and U are the characteristic

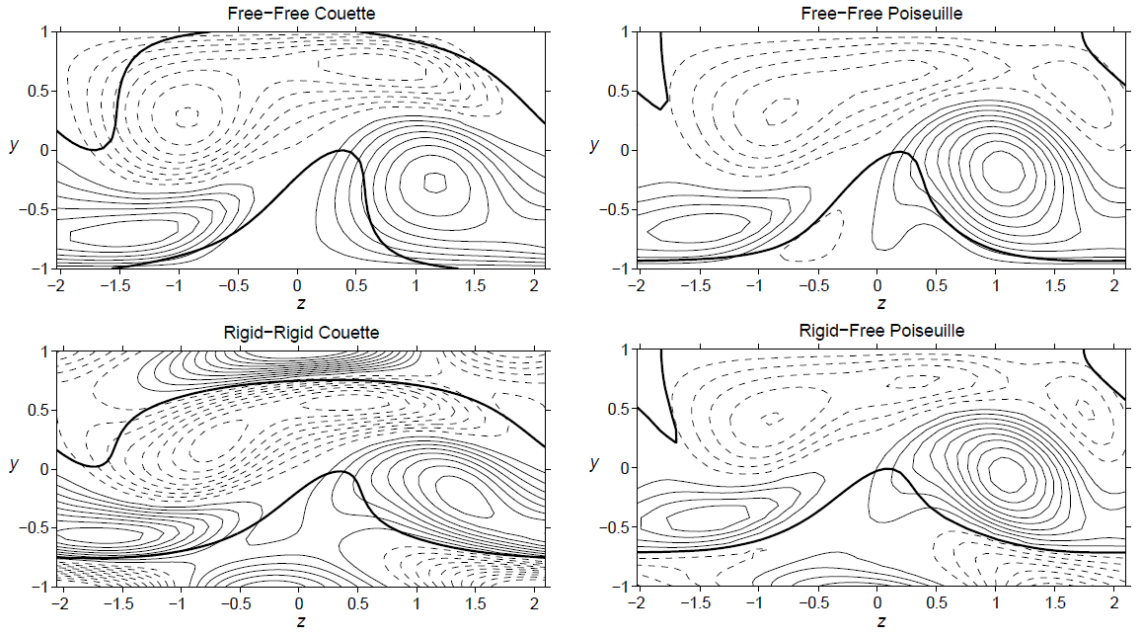

FIGURE 2.11: Morph of exact coherent structures under homotopy from Couette to Poiseuille flows (horizontal) and from free-slip to no-slip boundary conditions (vertical). Exact coherent structures are visualised as contours of streamwise vorticity. This picture is taken from Waleffe [156].

length and velocity of the distorted perturbation; and the differential stretching of eddies characterised by a shear straining time $\tau_s = 1/S$. In the case $\tau_s > \tau_e$, except for a geometric distortion, the nonlinear interaction of perturbed flow is essentially unaffected by the presence of the flow shear [163]. On the other hand, if $\tau_e > \tau_s$, a large-scale structure has insufficient time to transfer its energy to successively smaller scales before losing coherence, thereby preserving features of their initial state [162].

Denote by λ the length scale[7] associated with the large-scale flow. The geometric scale separation inscribed in all planar shear flows ensures the existence of a small parameter

$$\eta = h/\lambda, \tag{2.60}$$

which, in turn, translates into the rapid distortion limit

$$\tau_s/\tau_e = \eta \ll 1, \quad \tau_s = h/U. \tag{2.61}$$

That is, the large-scale perturbations entering the transitional plane Couette flow are so rapidly distorted that the nonlinear interaction has essentially no effect. In this limit,

[7] As we shall see in Chapter 3, this length scale diverges, i.e. $\lambda \to \infty$.

terms that are scaled with S are dominant and all others are negligible in comparison. Thus, equation (2.38) reduces to the rapid distortion equations [5]

$$\partial_t \tilde{\boldsymbol{u}} + \boldsymbol{U} \cdot \nabla \tilde{\boldsymbol{u}} + \tilde{\boldsymbol{u}} \cdot \nabla \boldsymbol{U} = -\nabla \tilde{p}. \tag{2.62}$$

By contrast to linear stability analysis [96], whose validity relies on the intensity separation, thereby limited to the weak perturbations at large distances from a localised turbulent spot, the rapid distortion equations are due to the scale separation typically found in all planar shear flows, hence they are applicable in describing both the rapid distortion of large-scale flows over the entire flow domain, as well as the long-term evolution in the far-field.

2.3.2.7 Flow in rotating coordinates

The Navier-Stokes equations, which stems from the Newton's second law of motion, depicts the rate of change of the momentum in an inertial reference frame equals to the sum of forces acting on the fluid. For flows where the effect of the rotation is dominant, e.g. Taylor-Couette and geophysical flows, the description of fluid motions requires a transformation for the material derivative of an arbitrary vector, say $\boldsymbol{B}$, from inertial to rotating [8] coordinates, which reads [164]

$$\left(\frac{\mathrm{D}\boldsymbol{B}}{\mathrm{D}t}\right)_i = \left(\frac{\mathrm{D}\boldsymbol{B}}{\mathrm{D}t}\right)_r + \boldsymbol{\Omega} \times \boldsymbol{B}, \tag{2.63}$$

where the subscript $_i$ and $_r$ indicate inertial and rotating frames, respectively, and $\boldsymbol{\Omega}$ is the angular velocity of the rotating frame. Thus, the relative velocity observed from the rotational frame is

$$\boldsymbol{u}_r = \boldsymbol{u}_i - \boldsymbol{\Omega} \times \boldsymbol{r}, \tag{2.64}$$

where $\boldsymbol{r}$ is the position vector for a fluid particle in the rotating frame. Substituting (2.64) into (2.63) and using the chain rule gives

$$\left(\frac{\mathrm{D}\boldsymbol{u}_i}{\mathrm{D}t}\right)_i = \left(\frac{\mathrm{D}\boldsymbol{u}_r}{\mathrm{D}t}\right)_r + \left(\frac{\mathrm{D}\boldsymbol{\Omega}}{\mathrm{D}t}\right)_r \times \boldsymbol{r} + 2\boldsymbol{\Omega} \times \boldsymbol{u}_r + \boldsymbol{\Omega} \times (\boldsymbol{\Omega} \times \boldsymbol{r}). \tag{2.65}$$

[8] Rotating coordinates involve acceleration in the radial direction, thereby non-inertial.

The equation states that the acceleration in an inertial frame is equal to the rate of change of the relative motion in a rotating frame in additional to (i) the Euler acceleration $(\mathrm{D}_t\boldsymbol{\Omega})_r \times \boldsymbol{r}$, arising from the temporal variation of the rotation rate $\boldsymbol{\Omega}$; (ii) the Coriolis acceleration $2\boldsymbol{\Omega} \times \boldsymbol{u}_r$, which acts perpendicular to both the relative velocity $\boldsymbol{u}_r$ and to $\boldsymbol{\Omega}$, representing a linear mimic of the nonlinear Lamb vector; and (iii) the centripetal acceleration $\boldsymbol{\Omega} \times (\boldsymbol{\Omega} \times \boldsymbol{r})$, [9] arising from the curvature effect of the particle trajectory. Although being commonly referred to as fictitious, these forces (per unit mass), i.e. Euler, Coriolis, and centrifugal, are necessities to make the Newton's second law hold in the rotating frame, and they should be treated like real forces [166].

Substituting the Navier-Stokes equations (2.3) into (2.65) and expressing the flow characteristics in terms of the relative variables, the fluid motion in steadily rotating coordinates, i.e. $\partial_t\boldsymbol{\Omega} = 0$, is governed by

$$\partial_t\boldsymbol{u} + (\boldsymbol{u}\cdot\nabla)\boldsymbol{u} + \boldsymbol{\Omega} \times (\boldsymbol{\Omega} \times \boldsymbol{r}) = -\nabla p + 2\boldsymbol{u} \times \boldsymbol{\Omega} + \nu\nabla^2\boldsymbol{u}, \tag{2.66}$$

where the subscripts $_r$ are omitted. Denote by

$$\epsilon = \frac{\Omega^{-1}}{L/U} = \frac{U}{\Omega L}, \tag{2.67}$$

the Rossby number, which is the ratio between the time scale associated with rotation Ω^{-1} and that associated with the relative motion L/U. Analogous to the rapid distortion theory reviewed in the previous section, for $\epsilon \gg 1$, the fluid can hardly sense the effect of rotation over the time scale of the relative motion. On the other hand, for $\epsilon \ll 1$, the effect of rotation dominates.

If the interest is on the slow evolution of the relative motion, let us scale the time variable by L/U, and in the absence of a scale separation in length scales, a complete scaling relation is given by [10],

$$t = (L/U)t^*, \quad \boldsymbol{u} = U\boldsymbol{u}^*, \quad \boldsymbol{\Omega} = \Omega\boldsymbol{\Omega}^*, \quad p = Pp^*, \quad \boldsymbol{x} = L\boldsymbol{x}^*, \quad \boldsymbol{r} = L\boldsymbol{r}^*. \tag{2.68}$$

Substituting the scaling relations into equations (2.66), yielding

$$\epsilon\left[\partial_{t^*} + (\boldsymbol{u}^*\cdot\nabla)\right]\boldsymbol{u}^* + \epsilon^{-1}\boldsymbol{\Omega}^* \times (\boldsymbol{\Omega}^* \times \boldsymbol{r}^*) = -\frac{\epsilon P^*}{U^{*2}}\nabla p^* + 2\boldsymbol{u}^* \times \boldsymbol{\Omega}^* + \epsilon Re^{-1}\nabla^2\boldsymbol{u}^*. \tag{2.69}$$

[9] Note that the acceleration is centripetal, meaning centre seeking; whereas the corresponding force, which points in the opposite direction, is centrifugal, meaning centre fleeting [165].

[10] Otherwise, the shorter length scale must be used.

It is seen that, despite the relative motion is of finite amplitude, the quadratic nonlinearity can be safely discarded if either the rotation is sufficiently strong or if the length scale of the relative motion is large such that $\epsilon \ll 1$ [167]. For applications where the Reynolds number is large, the Ekman number is negligible, then the relative motion in rotating coordinates reduces to a balance between the centrifugal force, the pressure gradient, and the Coriolis force:

$$\epsilon^{-1}\boldsymbol{\Omega}^* \times (\boldsymbol{\Omega}^* \times \boldsymbol{r}^*) = -\frac{\epsilon P}{U^2}\nabla p^* + 2\boldsymbol{u}^* \times \boldsymbol{\Omega}^*. \tag{2.70}$$

Depending on the selection of the scaling P, various idealised flows, for instance,

i geostrophic flow: $P = O(U\Omega L)$;

ii cyclostrophic flow: $P = O(\Omega^2 L^2)$;

iii inertia flow: $P = O(U^2)$;

can be achieved. That is, the selection for P depends on identifying the predominant mechanism for generating pressure gradient in the rotating flow. This idea shall be further explored in Chapter 4.

Before ending this chapter, it should be re-emphasised that the difficulty associated with solving the Navier-Stokes equations is legendary and, as pointed out in "A First Course in Turbulence" by Tennekes and Lumley [4]

> *"The success of attempts to solve problems in turbulence depends strongly on the inspiration involved in making the crucial assumption."*

The central assumption made throughout this thesis is presence of scale separations

1. the geometric scale separation inscribed in all planar shear flows; and
2. the intensity separation near the onset of the secondary instability.

which justifies (i) an elimination of terms that are too small; and (ii) a perturbative expansion about the associated small parameter.

The successful application of these simplifications leads to (i) an analytical solution for the quadrupolar flows outside turbulent spots in Chapter 3; and (ii) a bifurcation analysis for counter-rotating vortices inside turbulent spots in Chapter 4.

Chapter 3

Quadrupolar flows around spots in internal shear flows

3.1 Introduction

Turbulent spots occur in shear flows confined between two walls, and are surrounded by robust quadrupolar flows. Such large-scale flows may play a role in the long-range interaction between turbulent spots, with strong consequences on the laminar-to-turbulent transition. Whether the far-field decay is exponential or algebraic remains controversial. We address this problem theoretically, by considering an isolated pointwise spot in a plane shear flow with free-slip boundary conditions at both walls. Within these assumptions and by exploiting the geometric scale separation, a set of differential equations governing the large-scale flows is derived from the Navier-Stokes equations and solved for analytically. By averaging the flow between the two walls, it is found that the wall-normal velocity is exponentially localised in the plane while the in-plane velocity field is quadrupolar, featuring a superposition of algebraic and exponential decay. At leading order, the decay exponent is -3. Closer examination of the obtained analytical solutions reveals that the quadrupolar angular dependence stems from (i) the shearing of the streamwise velocity and (ii) the breaking of the spanwise homogeneity. Near the point source, exponentially decaying solutions can generate reversed quadrupolar flows. The algebraically decaying velocity field is two-dimensional and harmonic, suggesting a topological origin to the quadrupolar flow.

The plan of the chapter is as follows: a derivation of equations governing the large-scale flow is given in §3.2, in additional to a modelling of turbulent spots based on symmetry arguments. In §3.3, the proposed governing equations for the poloidal and toroidal functions are supplemented with free-slip boundary conditions and solved analytically. The characteristics of the large-scale flow are recovered from the poloidal and toroidal functions in §3.4, along with a brief argument for the possible topological origin of quadrupolar circulation in planar shear flows. Finally, conclusions drawn from the present study are given in §3.5.

3.2 Formulation

In this section, we present a derivation for a linearised model characterising the spatial distribution of the large-scale flow. Throughout the derivation, two assumptions have been exploited: (i) the intensity separation between the large-scale flow in the far-field and the relative speed of counter-moving plates in §3.2.1 and §3.2.4; and (ii) the scale separation between the wall-normal and the homogeneous directions in §3.2.2. In order to solve the derived model, boundary conditions are discussed in §3.2.5 and the forcing term representing the presence of a localised turbulent spot is modelled in §3.2.6.

3.2.1 Linearised Navier-Stokes equations

Turbulent spots in plane Couette flow are limited to a bounded region in two homogeneous directions, but extend all the way across the gap. Localised distribution of the small-scale turbulent fluctuations inside the spot leads to the large-scale flow penetrating deeply into the laminar regions. At large distances from the spot, the decaying large-scale flow contributes to a weak deviation from the laminar base flow. Following Li and Widnall [168], we consider a decomposition of the instantaneous flow characteristics, i.e. the velocity $\boldsymbol{u}$ and the pressure p, into a base flow $(\boldsymbol{U}, P)$, turbulent fluctuations $(\boldsymbol{u}', p')$ inside the turbulent spot, and a perturbation $(\tilde{\boldsymbol{u}}, \tilde{p})$ representing the large-scale flow

$$\boldsymbol{u} = \boldsymbol{U} + \boldsymbol{u}' + \tilde{\boldsymbol{u}}, \quad p = P + p' + \tilde{p}, \tag{3.1}$$

where, denoting by overbar the ensemble averaging, the large-scale flow is given by

$$\tilde{\boldsymbol{u}} = \overline{\boldsymbol{u} - \boldsymbol{U}}, \quad \tilde{p} = \overline{p - P}. \tag{3.2}$$

By taking the ensemble average of the Navier-Stokes equations, in Cartesian coordinates, where the axes x, y, and z are aligned with the streamwise, wall-normal, and spanwise directions, the large-scale flow $(\tilde{\boldsymbol{u}}, \tilde{p})$ is governed by:

$$\partial_t \tilde{\boldsymbol{u}} + \boldsymbol{U} \cdot \nabla \tilde{\boldsymbol{u}} + \tilde{\boldsymbol{u}} \cdot \nabla \boldsymbol{U} + \overline{\boldsymbol{u}' \cdot \nabla \boldsymbol{u}'} = -\rho^{-1} \nabla \tilde{p} + \nu \nabla^2 \tilde{\boldsymbol{u}}, \tag{3.3}$$

$$\nabla \cdot \tilde{\boldsymbol{u}} = 0, \tag{3.4}$$

where ρ is the fluid density. In Eq. (3.3), terms that are quadratic in $\tilde{\boldsymbol{u}}$ are neglected, reflecting the observation that the large-scale flow is a weak perturbation on the background laminar shear flow, that is $|\tilde{\boldsymbol{u}}| \ll U$. The preceding equations are supplemented by the Dirichlet boundary conditions

$$\boldsymbol{U} = \boldsymbol{u}' = \tilde{\boldsymbol{u}} = 0, \tag{3.5}$$

at the walls $y = \pm h$ and at infinity, i.e. $|x|, |z| \to \infty$.

By applying the divergence operator to Eq. (3.3) and using Eq. (3.4), the Poisson equation for pressure is

$$\rho^{-1} \nabla^2 \tilde{p} = -2S \partial_x \tilde{u}_y - \nabla \cdot \overline{\boldsymbol{u}' \cdot \nabla \boldsymbol{u}'}. \tag{3.6}$$

It is seen that the perturbed pressure comes from two distinct origins: (i) the spatial variation of the perturbed velocity, and (ii) the divergence of the Reynolds stresses. Consequently, the perturbed pressure can be further decomposed into

$$\tilde{p} = \tilde{p}^{(\mathrm{i})} + \tilde{p}^{(\mathrm{ii})}, \tag{3.7}$$

where $\tilde{p}^{(\mathrm{ii})}$ is denoted, up to an additive constant, by

$$\rho^{-1} \nabla^2 \tilde{p}^{(\mathrm{ii})} = -\nabla \cdot \overline{\boldsymbol{u}' \cdot \nabla \boldsymbol{u}'}. \tag{3.8}$$

It is seen from Eq. (3.8) that, since the Reynolds stresses are not divergence-free, the divergence of the Reynolds stresses will always generate a corresponding pressure field

$\tilde{p}^{(\mathrm{ii})}$ so as to make the sum

$$\boldsymbol{q}_{\tilde{\boldsymbol{u}}} = -\overline{\boldsymbol{u}' \cdot \nabla \boldsymbol{u}'} - \rho^{-1} \nabla \tilde{p}^{(\mathrm{ii})}, \tag{3.9}$$

satisfy the incompressible condition

$$\nabla \cdot \boldsymbol{q}_{\tilde{\boldsymbol{u}}} = 0. \tag{3.10}$$

This observation reflects the mathematical fact that, for incompressible flows, the role of the pressure is to project the compressible nonlinear terms onto the subspace of divergence-free flow fields. Therefore, we interpret $\boldsymbol{q}_{\tilde{\boldsymbol{u}}}$ as a forcing term mimicking the presence of an autonomous turbulent spot.

By using (3.9) and dropping the superscript $^{(\mathrm{i})}$ denoting the origin, the momentum equation (3.3) can be expressed as

$$\partial_t \tilde{\boldsymbol{u}} + \boldsymbol{U} \cdot \nabla \tilde{\boldsymbol{u}} + \tilde{\boldsymbol{u}} \cdot \nabla \boldsymbol{U} = -\rho^{-1} \nabla \tilde{p} + \nu \nabla^2 \tilde{\boldsymbol{u}} + \boldsymbol{q}_{\tilde{\boldsymbol{u}}}, \tag{3.11}$$

where the incompressibility constraint (3.4) leads to the following Poisson equation

$$\rho^{-1} \nabla^2 \tilde{p} = -2S \partial_x \tilde{u}_y. \tag{3.12}$$

Due to the presence of the variable part of the pressure gradient in Eq. (3.9), the forcing term need not vanish at the walls. However, in order to simplify the algebra, we impose the Dirichlet boundary conditions for the forcing

$$\boldsymbol{q}_{\tilde{\boldsymbol{u}}}|_{y=\pm h} = 0, \tag{3.13}$$

complementary to the boundary conditions (3.5). Alternatively, Li and Widnall [168] and Lagha and Manneville [70] have modelled an isolated turbulent spot as a Gaussian distribution of Reynolds stresses in the homogeneous directions with prescribed vertical variations, deviating from the current approach.

Note that the condition 3.13 is selected so as to simplify the problem. In fact, stemming from the boundary conditions 3.5, the Reynolds stresses vanish at the walls, but the boundary conditions for the pressure gradient is undetermined such that

$$\boldsymbol{q}_{\tilde{\boldsymbol{u}}}|_{y=\pm 1} = -\rho^{-1} \nabla \tilde{p}|_{y=\pm 1} \neq 0. \tag{3.14}$$

As it shall be discussed in detail in Appendix A that the mismatch between the boundary conditions for the perturbed velocities and for the forcing term gives rising to the complementary solutions involving hyperbolic trigonometric functions, causing difficulties for recovering the flow variables from the modal solutions.

3.2.2 Geometric scale separation in plane Couette flow

Conventionally, the Poisson equation (3.12) is combined with the momentum equation (3.11) to eliminate $\tilde{p}$, resulting in a fourth-order differential equation with variable coefficients in y which, unfortunately, is "uncooperative" [143]. However, if the order of the involved differential operators is reduced and if the coefficients are constant, the equation can be solved without difficulty. On the other hand, a distinguishing feature of the planar flows is that, unlike localised turbulent fluctuations, the large-scale flow is spatially extended in the homogeneous directions, whereas highly confined in the wall-normal direction due to the presence of walls. Since the large-scale flows do not present an obvious well-defined length scale, let us denote by λ the distance from a localised turbulent spot to where the large-scale flow is measured. The geometry of planar flows entails the existence of a small parameter

$$\eta = h/\lambda \ll 1. \tag{3.15}$$

This slenderness is associated with a separation of geometric scales. Due to the confinement by the walls, the perturbed flow occurs at length scales $\approx h$ in the wall-normal direction, while it is extended in the homogeneous directions. In a periodic box of size $[500h, 2h, 500h]$, for instance, the large-scale flow is observed at scales $\lambda \approx 100h$, cf. figure 3 in Duguet and Schlatter [65]. For this particular case, $\eta \approx 10^{-2}$ measures the separation between the small and large scales.

In this study, we suggest to exploit this geometric scale separation. We thus rescale the homogeneous coordinates x and z by λ, and the wall-normal coordinate y by h

$$x = \lambda x^*, \quad y = h y^*, \quad z = \lambda z^*, \tag{3.16}$$

where the superscript * denotes rescaled dimensionless variables, in which the walls are now located at $y = \pm 1$. We choose to rescale in-plane velocities by U (such that S becomes unity). The incompressibility constraints (3.4) and (3.10) lead to the following

substitution for the velocity components

$$\tilde{u}_x = U\tilde{u}_x^*, \quad \tilde{u}_y = \eta U\tilde{u}_y^*, \quad \tilde{u}_z = U\tilde{u}_z^*, \tag{3.17}$$

and for the forcing

$$q_{\tilde{u}_x} = \left(\nu U/h^2\right) q_{\tilde{u}_x}^*, \quad q_{\tilde{u}_y} = \eta\left(\nu U/h^2\right) q_{\tilde{u}_y}^*, \quad q_{\tilde{u}_z} = \left(\nu U/h^2\right) q_{\tilde{u}_z}^*, \tag{3.18}$$

where the scaling for the forcing terms is selected so as to balance the viscous dissipation. Similarly, the scaling for the pressure, as in lubrication theory [169]

$$\tilde{p} = \rho(\nu U\lambda/h^2)\tilde{p}^*, \tag{3.19}$$

is built on a balance between the pressure gradients and the dominant viscous terms in the homogeneous directions. The scaling (3.19) is justified provided that the reduced Reynolds number α is small, where

$$\alpha = \eta Re \ll 1. \tag{3.20}$$

This condition is satisfied as soon as the scale separation η^{-1} sufficiently large, cf. Eq. (3.15), and it shall be assumed henceforth.

Finally, we scale the time variable by a time scale associated with the large-scale flow, which reads

$$t = (\lambda/U)t^*. \tag{3.21}$$

Substituting the preceding scaling relations into Eq. (3.11), the rescaled non-dimensional Navier-Stokes equations are:

$$\left(\eta^2\partial_{x^*}^2 + \partial_{y^*}^2 + \eta^2\partial_{z^*}^2\right)\tilde{u}_x^* - \alpha\left(\partial_{t^*} + y^*\partial_{x^*}\right)\tilde{u}_x^* = \partial_{x^*}\tilde{p}^* + \alpha\tilde{u}_y^* - q_{\tilde{u}_x}^*, \tag{3.22a}$$

$$\left(\eta^2\partial_{x^*}^2 + \partial_{y^*}^2 + \eta^2\partial_{z^*}^2\right)\tilde{u}_y^* - \alpha\left(\partial_{t^*} + y^*\partial_{x^*}\right)\tilde{u}_y^* = \eta^{-2}\partial_{y^*}\tilde{p}^* - q_{\tilde{u}_y}^*, \tag{3.22b}$$

$$\left(\eta^2\partial_{x^*}^2 + \partial_{y^*}^2 + \eta^2\partial_{z^*}^2\right)\tilde{u}_z^* - \alpha\left(\partial_{t^*} + y^*\partial_{x^*}\right)\tilde{u}_z^* = \partial_{z^*}\tilde{p}^* - q_{\tilde{u}_z}^*, \tag{3.22c}$$

and the Poisson equation (3.12) becomes:

$$\left(\partial_{x^*}^2 + \eta^{-2}\partial_{y^*}^2 + \partial_{z^*}^2\right)\tilde{p}^* = -2\alpha\partial_{x^*}\tilde{u}_y^*. \tag{3.23}$$

By contrast to lubrication theory, wherein the Laplace operator reduces to a second-order derivative with respect to y^*, the full operator is retained here, signifying the geometric scale separation.

We observe from Eq. (3.22b) that the vertical pressure gradient is larger, by a factor η^{-2}, than remaining terms in the equation, hence it cannot be balanced. The formal procedure consists of expanding the perturbed pressure as

$$\tilde{p}^* = \tilde{p}^{*(0)} + \eta^2 \tilde{p}^{*(1)} + O(\eta^4). \tag{3.24}$$

Substituting the expansion into Eqs. (3.22) and collecting powers of η^{-2} reveals that

$$\partial_{y^*} \tilde{p}^{*(0)} = 0. \tag{3.25}$$

This means that, due to the confinement by the walls, the leading order pressure $\tilde{p}^{*(0)}$ is only effective in generating large-scale flows in the homogeneous directions. The first order correction $\tilde{p}^{*(1)}$ enters Eq. (3.22b), generating small-scale vertical motions of $O(h)$, but has negligible effect on generating the large-scale in-plane flows of $O(\lambda)$. Since Eqs. (3.22) are linear and since we are interested in the angular dependence and scaling characteristics of the large-scale flows, we filter out the irrelevant small-scale vertical motions by truncating the perturbative expansion (3.24) to the lowest order:

$$\tilde{p}^* = \tilde{p}^{*(0)}. \tag{3.26}$$

Substituting the truncation (3.26) into Eqs. (3.22) and using (3.25), we obtain:

$$\left(\eta^2 \partial_{x^*}^2 + \partial_{y^*}^2 + \eta^2 \partial_{z^*}^2\right) \tilde{u}_x^* - \alpha \left(\partial_{t^*} + y^* \partial_{x^*}\right) \tilde{u}_x^* = \partial_{x^*} \tilde{p}^* + \alpha \tilde{u}_y^* - q_{\tilde{u}_x}^*, \tag{3.27a}$$

$$\left(\eta^2 \partial_{x^*}^2 + \partial_{y^*}^2 + \eta^2 \partial_{z^*}^2\right) \tilde{u}_y^* - \alpha \left(\partial_{t^*} + y^* \partial_{x^*}\right) \tilde{u}_y^* = -q_{\tilde{u}_y}^*, \tag{3.27b}$$

$$\left(\eta^2 \partial_{x^*}^2 + \partial_{y^*}^2 + \eta^2 \partial_{z^*}^2\right) \tilde{u}_z^* - \alpha \left(\partial_{t^*} + y^* \partial_{x^*}\right) \tilde{u}_z^* = \partial_{z^*} \tilde{p}^* - q_{\tilde{u}_z}^*. \tag{3.27c}$$

For completeness, the perturbed pressure can be recovered by solving the following two-dimensional Poisson equation

$$\left(\partial_{x^*}^2 + \partial_{z^*}^2\right) \tilde{p}^* = -2\alpha \partial_{x^*} \tilde{u}_y^*, \tag{3.28}$$

as soon as the wall-normal velocity is determined.

3.2.3 Poloidal-toroidal decomposition

In order to guarantee that the validity of the incompressible constraints (3.4) and (3.10) is not effected by the truncation (3.26), we represent the perturbed velocity $\tilde{\boldsymbol{u}}$ using the poloidal-toroidal decomposition

$$\tilde{\boldsymbol{u}}^* = \nabla^* \times (\tilde{\psi}^* \boldsymbol{e}_y) + \nabla^* \times \nabla^* \times (\tilde{\phi}^* \boldsymbol{e}_y), \tag{3.29}$$

where $\nabla^* = (\eta\partial_{x^*}, \partial_{y^*}, \eta\partial_{z^*})$ is now the scaled gradient operator, $\tilde{\phi}^*$ and $\tilde{\psi}^*$ are the poloidal and toroidal functions, respectively, and $\boldsymbol{e}_y$ is the unit vector pointing towards positive y. Similarly, the forcing term $\boldsymbol{q}^*_{\tilde{\boldsymbol{u}}}$ can be expressed in terms of the poloidal $q^*_{\tilde{\phi}}$ and the toroidal $q^*_{\tilde{\psi}}$ components as

$$\boldsymbol{q}^*_{\tilde{\boldsymbol{u}}} = \nabla^* \times (q^*_{\tilde{\psi}} \boldsymbol{e}_y) + \nabla^* \times \nabla^* \times (q^*_{\tilde{\phi}} \boldsymbol{e}_y). \tag{3.30}$$

Hence, rather than working with the three-dimensional velocity field, we pursue in this paper the poloidal-toroidal formulation à la Marqués [170]:

$$\mathcal{L}\,\tilde{\phi} = -q_{\tilde{\phi}}, \tag{3.31a}$$

$$\mathcal{L}\,\tilde{\psi} = -q_{\tilde{\psi}} + \eta\alpha\partial_z\tilde{\phi}, \tag{3.31b}$$

where the the superscript * denoting rescaled dimensionless variables is now dropped for simplicity and the differential operator is given by

$$\mathcal{L} = \left(\eta^2\partial_x^2 + \partial_y^2 + \eta^2\partial_z^2\right) - \alpha\left(\partial_t + y\partial_x\right). \tag{3.32}$$

Here, Eq. (3.31a) is obtained by substituting the decomposition (3.29) and (3.30) into Eq. (3.27b), while Eq. (3.31b) is obtained by taking the curl of Eqs. (3.27) and projecting onto the $\boldsymbol{e}_y$ component. In order to simplify the expression, the two-dimensional Laplace operator $(\partial_x^2 + \partial_z^2)$ has been removed from both sides of Eqs. (3.31). Consequently, $\tilde{\phi}$ and $\tilde{\psi}$ are determined only up to an additive function $h_{\tilde{\phi}}(x, z)$ and $h_{\tilde{\psi}}(x, z)$ satisfying the two-dimensional Laplace equations

$$(\partial_x^2 + \partial_z^2)h_{\tilde{\phi}}(x, z) = (\partial_x^2 + \partial_z^2)h_{\tilde{\psi}}(x, z) = 0. \tag{3.33}$$

Stemming from the Dirichlet boundary conditions (3.5), Eq. (3.33) is supplemented with boundary conditions

$$h_{\tilde{\phi}}(x,z)|_{|x|,|z|\to\infty} = h_{\tilde{\psi}}(x,z)|_{|x|,|z|\to\infty} = 0, \tag{3.34}$$

such that $h_{\tilde{\phi}}(x,z)$ and $h_{\tilde{\psi}}(x,z)$ are identically zero:

$$h_{\tilde{\phi}}(x,z) = h_{\tilde{\psi}}(x,z) = 0. \tag{3.35}$$

Therefore, $\tilde{\phi}$ and $\tilde{\psi}$ are uniquely determined by the second-order differential equations (3.31). Similarly, combining Eqs. (3.28) and (3.29) and taking out the two-dimensional Laplace operator $(\partial_x^2 + \partial_z^2)$, the perturbed pressure becomes

$$\tilde{p} = 2\eta^2\alpha\partial_x\tilde{\phi}. \tag{3.36}$$

3.2.4 Kelvin wake formalism

In the absence of the forcing, Eq. (3.31a) is homogeneous, and its solutions include a superposition of Airy functions as shown by Brand and Gibson [71], Dubrulle and Zahn [171], Zammert and Eckhardt [172]. However, Eq. (3.31b) is inhomogeneous, forced by the spanwise inhomogeneity of $\tilde{\phi}$. In the presence of the forcing terms, both Eqs. (3.31a) and (3.31b) are inhomogeneous, and solutions to these equations involve integrals containing Airy functions, complicating the theoretical treatment.

In order to get around the difficulty arising from the variable coefficients and from the finiteness of the Reynolds number, we consider a change of coordinates by exploiting the symmetry of the base flow. The linear profile of the plane Couette flow is invariant with respect to a spatial translation in homogeneous directions and a central inversion about y. These lead to a co-moving Lagrangian frame defined by the new variables

$$t_L = t, \quad x_L = x - yt, \quad y_L = y, \quad z_L = z, \tag{3.37}$$

where the subscript $_L$ denotes variables in the Lagrangian frame. Using the chain rule, the partial derivatives are expressed in the Lagrangian frame as

$$\partial_t = \partial_{t_L} - y\partial_{x_L}, \quad \partial_x = \partial_{x_L}, \quad \partial_y = \partial_{y_L} - t\partial_{x_L}, \quad \partial_z = \partial_{z_L}. \tag{3.38}$$

This transformation of coordinates was first introduced by Kelvin to solve the steady wake pattern behind a constantly moving ship [173] and to demonstrate the linear stability of unbounded plane Couette flow [1]. The Kelvin's approach has been constantly revisited in the context of linear stability analysis and subsequently generalised to incorporate the effects of confinement by the walls [143], density stratification [174], compressibility and rotation [11], and coupling with a magnetic field [175]. For a comprehensive review regarding the historical perspectives, applications, and validity of the Kelvin's approach, see Craik and Criminale [176] and references therein.

Substituting the transformation (3.38) into Eqs. (3.31), we obtain

$$(\triangle_L - \alpha\partial_{t_L})\,\tilde{\phi} = -q_{\tilde{\phi}}, \tag{3.39a}$$

$$(\triangle_L - \alpha\partial_{t_L})\,\tilde{\psi} = -q_{\tilde{\psi}} + \eta\alpha\partial_{z_L}\tilde{\phi}, \tag{3.39b}$$

where the time dependence explicitly present in the differential operator

$$\triangle_L = \eta^2\partial_{x_L}^2 + (\partial_{y_L} - t\partial_{x_L})^2 + \eta^2\partial_{z_L}^2, \tag{3.40}$$

signifies a continuous tilting of the co-moving Lagrangian frame [11]. At $t = 0$, the Lagrangian and the Eulerian frames coincide. In this formalism, the effect of the base flow advection is lumped into the temporal evolution in the co-moving Lagrangian frame.

Since large-scale flows decay away from the turbulent spot, the velocity of the translating Lagrangian frame is expected to be much greater than that of the large-scale flow at large distances from the spot. Assuming localised turbulent spots are frozen in the Eulerian frame and following Taylor [177], we expect that the large-scale flow is frozen in the co-moving Lagrangian coordinates, i.e. its temporal evolution is negligible

$$\partial_{t_L}\tilde{\phi} = \partial_{t_L}\tilde{\psi} = 0. \tag{3.41}$$

Substituting the Taylor's hypothesis (3.41), which is justified by the intensity separation in the far-field, into Eqs. (3.39), and reverting the transformation (3.38), the governing equations for large-scale flows in the Eulerian frame are eventually

$$\left(\eta^2\partial_x^2 + \partial_y^2 + \eta^2\partial_z^2\right)\tilde{\phi} = -q_{\tilde{\phi}}, \tag{3.42a}$$

$$\left(\eta^2\partial_x^2 + \partial_y^2 + \eta^2\partial_z^2\right)\tilde{\psi} = -q_{\tilde{\psi}} + \eta\alpha\partial_z\tilde{\phi}. \tag{3.42b}$$

By seeking invariant solutions in the Lagrangian frame (3.37) as in Kelvin [173] (see also Chapter 3 in Lighthill [178] and Chapter 23 in Howison [169]), the advection term is exactly balanced by the time derivative, reducing the operator $\mathcal{L}$ to the scaled Laplace operator in the Eulerian frame. Consequently, the difficulty associated with the variable coefficients in y is removed. The preceding equations can be solved classically using Fourier transforms as soon as the boundary conditions as well as the forcing terms $q_{\tilde{\phi}}$ and $q_{\tilde{\psi}}$ are specified.

Before proceeding to a discussion of the boundary conditions in §3.2.5 and a modelling of the forcing terms in §3.2.6, it is instructive to compare the proposed model (3.42) with the existing ones. Brand and Gibson [71] performed a direct numerical analysis of dominant terms in the Navier-Stokes equations for a steady doubly-localised solution. When expressed in our notations, the leading order terms in the equation for $\tilde{u}_x$ depicts a balance between the two-dimensional Laplacian and the advection by the base flow (cf. their equation (3.2)):

$$\left(\partial_y^2 + \eta^2 \partial_z^2\right) \tilde{u}_x = \alpha y \partial_x \tilde{u}_x. \tag{3.43}$$

The preceding equation takes the form of the generalised Airy equation and has solutions that decay exponentially in both streamwise and spanwise directions. On the contrary, by solving Eqs. (3.42), we seek for invariant solutions translated by the base flow, i.e. the Kelvin wake "behind" a localised turbulent spot, where the advection term has essentially no effect. As shall be seen in §3.4.2, solutions to Eqs. (3.42) decay algebraically in the far-field, suggesting that the tails of the large-scale flow are *not* characterised by the leading order terms, i.e. the advection terms, in the linearised Navier-Stokes equations.

3.2.5 Boundary conditions

The original boundary conditions for the plane Couette problem are no-slip (3.5), which can be expressed in terms of the wall-normal components of the velocity and vorticity as

$$\tilde{u}_y|_{y=\pm 1} = \partial_y \tilde{u}_y|_{y=\pm 1} = \tilde{\omega}_y|_{y=\pm 1} = 0. \tag{3.44}$$

Stemming from the poloidal-toroidal decomposition (3.29), there is a correspondence between the velocity-vorticity and poloidal-toroidal formulations:

$$\tilde{u}_y = -\eta^2 \left(\partial_x^2 + \partial_z^2\right) \tilde{\phi}, \tag{3.45}$$

$$\tilde{\omega}_y = -\eta^2 \left(\partial_x^2 + \partial_z^2\right) \tilde{\psi}. \tag{3.46}$$

Hence, the preceding no-slip boundary condition (3.44) can be rewritten in terms of the poloidal and toroidal functions as

$$\tilde{\phi}|_{y=\pm 1} = \partial_y \tilde{\phi}|_{y=\pm 1} = \tilde{\psi}|_{y=\pm 1} = 0. \tag{3.47}$$

Here, the constraints on $\partial_y \tilde{\phi}$ and $\tilde{\psi}$ together ensure that the tangential velocities vanish at the walls. Note that there are four boundary conditions imposed on $\tilde{\phi}$, compatible with the presence of the fourth-order differential operator ∇^4 in the original momentum equation for $\tilde{\phi}$, cf. Eq. (14*b*) in Marqués [170]. In this work, however, the removal of the vertical pressure gradient, which arises as a natural consequence of the geometric scale separation (3.15), does not only filter out irrelevant small-scale motions driven by the vertical pressure gradient, but also leads to mathematical simplifications by reducing the fourth-order differential equation with respect to y to a second-order one. Therefore, Eq. (3.42a) can support only two boundary conditions at the walls. This observation implies that the filtered small-scale motions must play a dominant role in satisfying the no-slip boundary conditions (3.47). Consequently, by removing them, we have to relax the no-slip boundary conditions to free-slip boundary conditions in order to ensure that the resulting problem is mathematically well-posed. The full problem supplemented by the no-slip boundary conditions will be treated in a future work together with comparisons with direct numerical simulations.

Numerical simulations of Waleffe flow with *stress-free* boundary conditions (as considered by [64] and [48, 66])

$$\tilde{u}_y|_{y=\pm 1} = \partial_y^2 \tilde{u}_y|_{y=\pm 1} = \partial_y \tilde{\omega}_y|_{y=\pm 1} = 0, \tag{3.48}$$

suggest that the presence of slip at the walls does not affect the generic properties of the large-scale flow. The stress free boundary conditions can be expressed in terms of $\tilde{\phi}$ and $\tilde{\psi}$ as

$$\tilde{\phi}|_{y=\pm 1} = \partial_y^2 \tilde{\phi}|_{y=\pm 1} = \partial_y \tilde{\psi}|_{y=\pm 1} = 0, \tag{3.49}$$

where vanishing $\partial_y^2\tilde{\phi}|_{y=\pm1}$ and $\partial_y\tilde{\psi}|_{y=\pm1}$ ensure that the tangential stresses are zero at the walls. However, since the linear laminar profile of plane Couette flow does not satisfy the stress-free boundary conditions, one needs to modify the base flow by, for instance, the inclusion of a sinusoidal body force. Moreover, similar to the no-slip boundary conditions, there are four constraints imposed on $\tilde{\phi}$, incompatible with the second-order differential equation (3.42a). Therefore, in general, the stress-free boundary conditions (3.49) cannot be satisfied, unless $\tilde{\phi}$ solves

$$\partial_y^2\tilde{\phi} = c\tilde{\phi}, \tag{3.50}$$

up to a multiplying constant c. In this case, the two types of boundary conditions for $\tilde{\phi}$ are simultaneously satisfied. Prominent examples include trigonometric and hyperbolic trigonometric functions.

As a compromise between the number of boundary conditions that can be imposed on Eq. (3.31a) and the compatibility with the linear base flow, we consider in this paper a flow with mixed boundary conditions as in Eckhardt and Pandit [101]. More specifically, we require that the laminar profile satisfies the no-slip boundary conditions (3.5) of the full Navier-Stokes equations, whereas the perturbation satisfies the following *free-slip* boundary conditions:

$$\tilde{\phi}\,|_{y=\pm1} = 0 \quad \text{and} \quad \partial_y\tilde{\psi}\,|_{y=\pm1} = 0. \tag{3.51}$$

Here, the constraint on $\tilde{\phi}$ signifies that there is no penetration at the walls, while the constraint on $\tilde{\psi}$ is borrowed from the stress-free boundary conditions (3.49). It is demonstrated in §3.3.1 that the perturbed flow field obtained in this paper also satisfies the stress-free boundary conditions (3.49), while the generality of the proposed free-slip boundary conditions (3.51) is discussed from a topological point of view in §3.4.4.

3.2.6 Forcing selection

In this section, we perceive large-scale flows as arising from the blockage effect of localised turbulent spots, compatible with the Kelvin wake formalism in §3.2.4. This leads to a formulation of the forcing terms by making the minimal assumption in §3.2.6.1. Based on the parity analysis of Eqs. (3.42), we conclude in §3.2.6.2 that the formation of

quadrupolar flows is associated with the forcing components that are symmetric with respect of the mid-plane $y = 0$.

3.2.6.1 Minimal assumption model for a localised spot

In order to solve Eqs. (3.42), we must specify an analytical form for the forcing $(q_{\tilde{\phi}}, q_{\tilde{\psi}})$, yet the selection must not predetermine the large-scale flow. As such, we make the minimal assumption by modelling a localised turbulent spot as an obstacle located in the xy-plane, that will deflect the streamwise velocity into vertical momentum, without imposing wall-normal vorticity distribution in the xz-plane. By virtue of the conservation of angular momentum, the vertical momentum will alternate sign on each side of the obstacle, resembling a pinwheel located in the xy-plane, rotating about its spanwise axis and driven by the mean flow, cf. 3.1. Assuming that the vertical momentum is concentrated on a mathematical filament along the y-axis which terminates at the walls, the minimal forcing is:

$$q_{\tilde{\phi}} = -Ag(y)\delta'(x)\delta(z), \tag{3.52}$$

$$q_{\tilde{\psi}} = 0. \tag{3.53}$$

Here, A is the amplitude of the forcing and the prime denotes derivative with respect to the scaled x-axis, i.e. $\eta\partial_x$, which arises as a consequence of opposite vertical momentum. Note that the poloidal forcing (3.52) imposes a counter-rotating pair of streamwise circulations in the yz-plane. The form factor

$$g(y)|_{y=\pm 1} = 0, \tag{3.54}$$

is adjusted so as to satisfy the Dirichlet boundary condition (3.13).

The sign of A remains undetermined, and it shall be concluded by comparing the analytic solution with previous experimental and numerical results in §3.4.2. Denoting the integral

$$G = \int_{-1}^{1} g(y)\,\mathrm{d}y. \tag{3.55}$$

For $AG > 0$, the forcing term (3.52) introduces an overall spanwise vorticity which is opposite in sign to that of the base flow; whereas for $AG < 0$, the spanwise vorticity associated with the spot is aligned with that of the base flow.

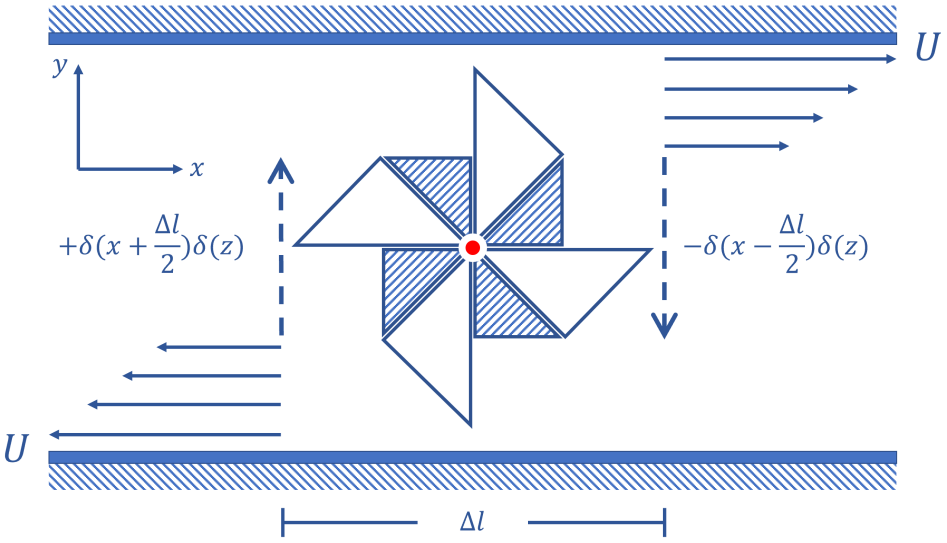

FIGURE 3.1: Schematic of a forcing induced by a pinwheel driven by the mean flow, i.e. the superposition of base flow and turbulent fluctuations inside the spot (solid line). The forcing comprises two anti-aligned vertical momentum in the poloidal field (dashed line), contributing to a spanwise rotation proportional to the vorticity of the mean flow.

3.2.6.2 Parity of the forcing

Although the characteristics of turbulent spots, as well as of the large-scale flows around them, are strongly three-dimensional, the quadrupolar circulation is usually revealed numerically after applying the y-average, denoted by

$$\langle\,\cdot\,\rangle = \frac{1}{2}\int_{-1}^{1} \cdot\,\mathrm{d}y, \tag{3.56}$$

to the perturbed in-plane flow $\langle\tilde{\boldsymbol{u}}_{2D}\rangle = (\langle\tilde{u}_x\rangle, \langle\tilde{u}_z\rangle)$. Here, the y-averaged in-plane velocities

$$\langle\tilde{u}_x\rangle = -\eta\partial_z\langle\tilde{\psi}\rangle + \eta\partial_x\langle\partial_y\tilde{\phi}\rangle, \tag{3.57}$$

$$\langle\tilde{u}_z\rangle = +\eta\partial_x\langle\tilde{\psi}\rangle + \eta\partial_z\langle\partial_y\tilde{\phi}\rangle, \tag{3.58}$$

can be decomposed into a divergence-free component characterised by the stream function $\langle\tilde{\psi}\rangle$ and a curl-free component characterised by the velocity potential $\langle\partial_y\tilde{\phi}\rangle$. The latter is identically zero with the Dirichlet boundary conditions (3.51)

$$\langle\partial_y\tilde{\phi}\rangle = \frac{1}{2}\left(\tilde{\phi}|_{y=+1} - \tilde{\phi}|_{y=-1}\right) = 0. \tag{3.59}$$

Therefore, the in-plane flow $\langle \tilde{\boldsymbol{u}}_{2D} \rangle$ is divergence-free, arising from the non-vanishing $\langle \tilde{\psi} \rangle$.

Since the differential operator in Eqs. (3.42) is strictly second-order, the parity of the poloidal and toroidal functions is uniquely determined by the parity of the forcing. More specifically, the odd component of $q_{\tilde{\phi}}$ leads to $\tilde{\psi}$ vanishing upon y-averaging. Since $q_{\tilde{\psi}}$ is identically zero by assumption, the quadrupolar flow must stem from the even part of the forcing. Accordingly, we restrict ourselves to the case where $g(y)$ is an even function of y.

Let $g(y)$ be an arbitrary even function satisfying the Dirichlet boundary condition (3.54), it can be expanded using Fourier series as

$$g(y) = \sum_{n=1}^{\infty} a_n \cos(\xi_n y), \tag{3.60}$$

where a_n denote the Fourier coefficients and the wavenumbers are discretised:

$$\xi_n = \left(n - \frac{1}{2}\right)\pi \quad \text{for} \quad n = 1, 2, 3... \tag{3.61}$$

In this model, the index n signifies that there are n mutually counter-rotating vortices stacking along the y-axis. Based on the minimal assumption meant to model a localised filament-like spot, the present analysis can be applied to not only the transitional flows with $Re \approx 300$ but to all regimes with $Re > 0$ down to the Stokes regime.

3.3 Analytical solutions for poloidal and toroidal functions

In this section, the modal solutions for the poloidal and toroidal functions are presented in §3.3.1 and their inverse Fourier transform are evaluated in §3.3.2. Due to the presence of hyperbolic trigonometric functions in modal solutions, the wall-normal average is applied to simplify the expression. Moreover, the origin of the quadrupolar angular dependence and the algebraic decay in the toroidal function is uncovered in §3.3.1 and §3.3.2, respectively.

3.3.1 Modal solutions

The homogeneity in x and z justifies the use of Fourier transform in the corresponding directions with wavenumbers K_x and K_z. For any function $\tilde{f}$, let $\hat{f}$ be denoted by

$$\tilde{f}(x,y,z) = \frac{1}{2\pi\eta}\iint_{-\infty}^{\infty} \hat{f}(y,K_x,K_z)e^{\mathrm{i}(K_x x+K_z z)/\eta}\mathrm{d}K_x\mathrm{d}K_z, \tag{3.62}$$

where the presence of η in the basis function signifies the smallness of wavenumbers $K_x, K_z \sim O(\eta)$ associated with the large-scale motion. Expanding the potential functions $\tilde{\phi}$ and $\tilde{\psi}$, as well as the forcing terms $q_{\tilde{\phi}}$ and $q_{\tilde{\psi}}$, using (3.62) and substituting the expansions into (3.42) gives

$$\left(\partial_y^2 - K^2\right)\hat{\phi} = \mathrm{i}\frac{A\,K_x}{2\pi\eta}\sum_{n=1}^{\infty} a_n\cos(\xi_n y_L), \tag{3.63a}$$

$$\left(\partial_y^2 - K^2\right)\hat{\psi} = \mathrm{i}\alpha K_z\hat{\phi}, \tag{3.63b}$$

where $K = \sqrt{K_x^2 + K_z^2}$ is the radial wavenumber. The preceding equations are supplemented with the Fourier-transformed free-slip boundary conditions

$$\hat{\phi}\,|_{y=\pm1} = 0 \quad \text{and} \quad \partial_y\hat{\psi}\,|_{y=\pm1} = 0. \tag{3.64}$$

Using the method of undetermined coefficients, Eqs. (3.63) are solved recursively, yielding

$$\hat{\phi} = -\mathrm{i}\frac{A\,K_x}{2\pi\eta}\sum_{n=1}^{\infty}\frac{a_n\cos(\xi_n y)}{K^2+{\xi_n}^2}, \tag{3.65}$$

$$\hat{\psi} = -\frac{\alpha A\,K_x K_z}{2\pi\eta}\sum_{n=1}^{\infty}\frac{a_n}{(K^2+{\xi_n}^2)^2}\left[\cos(\xi_n y) + \xi_n\sin(\xi_n)\frac{\cosh(Ky)}{K\sinh(K)}\right], \tag{3.66}$$

where the complementary solutions involving hyperbolic trigonometric functions arise so as to satisfy the corresponding boundary conditions at the walls. Note that the modal solution $\hat{\phi}$ has vanishing second-order derivatives

$$\partial_y^2\hat{\phi}|_{y=\pm1} = 0, \tag{3.67}$$

at the walls. Therefore, the obtained solutions (3.65) and (3.66) satisfy, upon inverse Fourier transforms, not only the free-slip boundary conditions (3.51) but also the stress-free boundary conditions (3.49).

Upon averaging in y, the modal solutions (3.65) and (3.66) become

$$\langle\hat{\phi}\rangle = -\mathrm{i}\frac{A\,K_x}{2\pi\eta}\sum_{n=1}^{\infty}\frac{b_n}{K^2+\xi_n^2}, \tag{3.68}$$

$$\langle\hat{\psi}\rangle = -\frac{\alpha A\,K_xK_z}{2\pi\eta K^2}\sum_{n=1}^{\infty}\frac{b_n}{K^2+\xi_n^2}, \tag{3.69}$$

where the hyperbolic trigonometric functions arising from the complementary solutions cancel by averaging and

$$b_n = a_n\sin(\xi_n)/\xi_n, \tag{3.70}$$

are the modified Fourier coefficients.

Let us introduce the polar decomposition for the wavenumbers:

$$K_x = K\cos(\varphi), \quad K_z = K\sin(\varphi). \tag{3.71}$$

The quadrupolar nature of the solution stems from the angle dependence of the product

$$K_xK_z = \frac{1}{2}K^2\sin(2\varphi), \tag{3.72}$$

which generates second azimuthal harmonics in the xz-plane. The presence of K_xK_z in Eq. (3.69) is inscribed in the obstacle interpretation of the forcing (3.52) and the structure of the toroidal equation (3.63b), hence it is independent of the particular choice of the boundary conditions. Moreover, the $1/K^2$ denominator in Eq. (3.69) arises from the wall-normal averaging of the complementary solutions in Eq. (3.66). This prefactor is exactly balanced by K^2 in the numerator. As seen in the next subsection, this exact balance leads to the algebraic decay upon inverse Fourier transform through the appearance of Bessel functions of the first kind.

3.3.2 Inverse Fourier transform

After obtaining the modal solutions, we still face the task of inverting the Fourier transform. Let us introduce polar coordinates via

$$x^\diamond = r^\diamond\cos\theta, \quad z^\diamond = r^\diamond\sin\theta, \tag{3.73}$$

where the spatial coordinates are re-scaled as $x^\diamond = x/\eta$ and $z^\diamond = z/\eta$, so that the spatial coordinates are normalised by the half-gap size h, cf. Eq. (3.15). Dropping the superscript $^\diamond$, the inverse Fourier transform for the y-averaged poloidal and toroidal functions can be expressed in polar coordinates as

$$\langle\tilde{\phi}\rangle = \frac{1}{2\pi\eta}\int_0^\infty\int_0^{2\pi}\langle\hat{\phi}\rangle e^{\mathrm{i}Kr\cos(\varphi-\theta)}K\mathrm{d}K\mathrm{d}\varphi \tag{3.74}$$

$$= -\frac{A}{4\pi^2\eta^2}\sum_{n=1}^{\infty}\int_0^\infty\frac{b_n\,K^2}{K^2+\xi_n^2}\mathrm{d}K\int_0^{2\pi}\mathrm{i}\cos(\varphi)e^{\mathrm{i}Kr\cos(\varphi-\theta)}\mathrm{d}\varphi, \tag{3.75}$$

and

$$\langle\tilde{\psi}\rangle = \frac{1}{2\pi\eta}\int_0^\infty\int_0^{2\pi}\langle\hat{\psi}\rangle e^{\mathrm{i}Kr\cos(\varphi-\theta)}K\mathrm{d}K\mathrm{d}\varphi \tag{3.76}$$

$$= -\frac{\alpha A}{8\pi^2\eta^2}\sum_{n=1}^{\infty}\int_0^\infty\frac{b_n\,K}{K^2+\xi_n^2}\mathrm{d}K\int_0^{2\pi}\sin(2\varphi)e^{\mathrm{i}Kr\cos(\varphi-\theta)}\mathrm{d}\varphi. \tag{3.77}$$

Since integrands involving the angular variables are decoupled from those with wavenumbers, they can be evaluated independently, yielding

$$\int_0^{2\pi}\mathrm{i}\cos(\varphi)e^{\mathrm{i}Kr\cos(\varphi-\theta)}\mathrm{d}\varphi = -2\pi\cos(\theta)J_1(Kr), \tag{3.78}$$

$$\int_0^{2\pi}\sin(2\varphi)e^{\mathrm{i}Kr\cos(\varphi-\theta)}\mathrm{d}\varphi = -2\pi\sin(2\theta)J_2(Kr), \tag{3.79}$$

where $J_m(Kr)$ denotes the m^{th} order Bessel function of the first kind. Substitution gives

$$\langle\tilde{\phi}\rangle = \frac{A\cos(\theta)}{2\pi\eta^2}\sum_{n=1}^{\infty}b_n\int_0^\infty\frac{K^2\,J_1(Kr)}{K^2+\xi_n^2}\mathrm{d}K = \frac{A\cos(\theta)}{2\pi\eta^2}\sum_{n=1}^{\infty}b_n\xi_nK_1(\xi_nr), \tag{3.80}$$

$$\langle\tilde{\psi}\rangle = \frac{\alpha A\sin(2\theta)}{4\pi\eta^2}\sum_{n=1}^{\infty}b_n\int_0^\infty\frac{K\,J_2(Kr)}{K^2+\xi_n^2}\mathrm{d}K = \frac{\alpha A\sin(2\theta)}{2\pi\eta^2}\sum_{n=1}^{\infty}b_n\left[(\xi_nr)^{-2}-\frac{1}{2}K_2(\xi_nr)\right], \tag{3.81}$$

where $K_m(\xi_nr)$ is m^{th} order modified Bessel function of the second kind. The integral (3.80) is given by Eq. (6.565.4) in Gradshteyn and Ryžhik [179]. The integral (3.81) is not elementary, therefore a special treatment is required, see Appendix E. The occurrence of the term $1/(\xi_nr)^2$ in the y-averaged toroidal field in Eq. (3.81) is at the root of the algebraic decay of the in-plane velocity components. The mathematical origin of that term can be traced to the recurrence relation of the Bessel function $J_2(Kr)$, cf. Eq. (E.3) and the integral (E.7) in the Appendix E.

3.4 Large-scale flows

In this section we present the full analytical expressions for the main flow components after wall-normal averaging in §3.4.1, as well as their asymptotic behaviour in the far-field in §3.4.2. We also uncover in §3.4.3 an unexpected property of the flow circulation at intermediate distances from the spot, and eventually explain in §3.4.4 the origin of the quadrupolar flow from a topological point of view.

Note that, the quantities α, A and η only appear in Eq. (3.80) and (3.81) as amplitudes, not as arguments, they do not affect the angular dependence and the scaling characteristics of the large-scale flow, only its strength. Consequently, the qualitative features of the large-scale flow depend only on the Fourier coefficients a_n of the forcing.

3.4.1 Analytical expressions for the wall-normal averaged flow

From the analytical solutions for the poloidal and toroidal functions, various y-averaged flow variables can be recovered, yielding

$$\begin{aligned}\langle\tilde{u}_x\rangle &= -\left[\sin(\theta)\partial_r + \cos(\theta)r^{-1}\partial_\theta\right]\langle\tilde{\psi}\rangle \\ &= -\frac{ARe\cos(3\theta)}{\pi\eta}\sum_{n=1}^{\infty} b_n\xi_n\left[(\xi_n r)^{-3} - \frac{1}{8}K_1(\xi_n r) - \frac{1}{2}(\xi_n r)^{-1}K_2(\xi_n r)\right] \\ &\quad - \frac{ARe\cos(\theta)}{8\pi\eta}\sum_{n=1}^{\infty} b_n\xi_n K_1(\xi_n r),\end{aligned} \tag{3.82}$$

for the streamwise velocity,

$$\begin{aligned}\langle\tilde{u}_z\rangle &= +\left[\cos(\theta)\partial_r - \sin(\theta)r^{-1}\partial_\theta\right]\langle\tilde{\psi}\rangle \\ &= -\frac{ARe\sin(3\theta)}{\pi\eta}\sum_{n=1}^{\infty} b_n\xi_n\left[(\xi_n r)^{-3} - \frac{1}{8}K_1(\xi_n r) - \frac{1}{2}(\xi_n r)^{-1}K_2(\xi_n r)\right] \\ &\quad + \frac{ARe\sin(\theta)}{8\pi\eta}\sum_{n=1}^{\infty} b_n\xi_n K_1(\xi_n r),\end{aligned} \tag{3.83}$$

for the spanwise velocity,

$$\langle\tilde{u}_y\rangle = -\left[\partial_r^2 + r^{-1}\partial_r + r^{-2}\partial_\theta^2\right]\langle\tilde{\phi}\rangle = -\frac{A\cos(\theta)}{2\pi\eta^2}\sum_{n=1}^{\infty} b_n\xi_n^3 K_1(\xi_n r), \tag{3.84}$$

for the wall-normal velocity,

$$\begin{aligned}\langle\tilde{\omega}_y\rangle &= -\left[\partial_r^2 + r^{-1}\partial_r + r^{-2}\partial_\theta^2\right]\langle\tilde{\psi}\rangle \\ &= \frac{ARe\sin(2\theta)}{4\pi\eta}\sum_{n=1}^{\infty} b_n\xi_n^2\left[K_0(\xi_n r) + 2(\xi_n r)^{-1}K_1(\xi_n r)\right],\end{aligned} \tag{3.85}$$

for the wall-normal vorticity, and eventually

$$\begin{aligned}\langle\tilde{p}\rangle &= 2\eta\alpha\left[\cos(\theta)\partial_r - \sin(\theta)r^{-1}\partial_\theta\right]\langle\tilde{\phi}\rangle \\ &= -\frac{ARe\cos(2\theta)}{2\pi}\sum_{n=1}^{\infty} b_n\xi_n^2\left[K_0(\xi_n r) + 2(\xi_n r)^{-1}K_1(\xi_n r)\right] - \frac{ARe}{2\pi}\sum_{n=1}^{\infty} b_n\xi_n^2 K_0(\xi_n r),\end{aligned} \tag{3.86}$$

for the pressure, where the spatial derivatives ∂_x and ∂_z have been expressed in polar coordinates. Note that, while the scaling of the flow variables $\langle\tilde{u}_y\rangle$, $\langle\tilde{\omega}_y\rangle$, and $\langle\tilde{p}\rangle$ is solely characterised by the modified Bessel functions of various orders, the in-plane velocities $\langle\tilde{u}_x\rangle$ and $\langle\tilde{u}_z\rangle$ feature a superposition of algebraic power law functions $1/r^3$ and modified Bessel functions $K_m(\xi_n r)$. Therefore, a qualitatively different asymptotic behaviour is expected for $\langle\tilde{u}_x\rangle$ and $\langle\tilde{u}_z\rangle$.

3.4.2 Quadrupolar flow and algebraic asymptote

Since, independently of its order m, the modified Bessel function $K_m(\xi_n r)$ decays faster than exponential in the asymptotic limit, cf. Eq. (9.7.2) in Abramowitz and Stegun [180]

$$K_m(\xi_n r) = \sqrt{\frac{\pi}{2}}\frac{e^{-\xi_n r}}{\sqrt{\xi_n r}}\left[1 + O(\frac{1}{\xi_n r})\right], \quad \text{as} \quad r \to \infty, \tag{3.87}$$

the wavenumber ξ_n can be regarded as the inverse of a screening length over which contributions from $K_m(\xi_n r)$ are negligible. Consequently, the asymptotic behaviour of the large-scale flow must be characterised by the slower algebraic decay. It is seen from Eqs. (3.82) and (3.83) that, in the absence of the modified Bessel functions, each Fourier

mode contributes to the same algebraic asymptote:

$$\langle \tilde{u}_x \rangle = -\frac{ARe\cos(3\theta)}{\pi\eta} \sum_{n=1}^{\infty} b_n \xi_n^{-2}\, r^{-3}, \tag{3.88}$$

$$\langle \tilde{u}_z \rangle = -\frac{ARe\sin(3\theta)}{\pi\eta} \sum_{n=1}^{\infty} b_n \xi_n^{-2}\, r^{-3}, \tag{3.89}$$

provided that $r \gg 1/\xi_1$. In other words, unlike previous findings by Schumacher and Eckhardt [64] and Brand and Gibson [71], we find that the far-field decay of the large-scale in-plane flow is algebraic, whose power-law exponent is -3. In particular, for

$$A \sum_{n=1}^{\infty} b_n \xi_n^{-2} > 0, \tag{3.90}$$

the angular dependence of the asymptotic solutions (3.88) and (3.89) entails a quadrupolar angular dependence with streamwise inflow and spanwise outflow, consistently with previous experimental and numerical observations. We, therefore, conclude that the localised perturbation in Eqs. (3.52) and (3.53) gives rise to the algebraically decaying quadrupolar in-plane flows in the far-field.

Featuring modified Bessel functions, the flow variables $\langle \tilde{u}_y \rangle$, $\langle \tilde{\omega}_y \rangle$, and $\langle \tilde{p} \rangle$ decay faster than exponentially and are thereby referred to in the following as *exponentially localised*. Consequently, we define a spot as exponentially localised if and only if both $\langle \tilde{u}_y \rangle$ and $\langle \tilde{\omega}_y \rangle$ are exponentially localised. It shall be discussed in detail in §3.4.4 that, independently of the boundary conditions at the walls and details of the base flows, the angular dependence and the scaling characteristics of the large-scale in-plane flow around an exponentially localised turbulent spot are unique and given by Eqs. (3.88) and (3.89), in the asymptotic limit.

3.4.3 Coexistence of exponential and algebraic decays

Although the asymptotic solutions (3.88) and (3.89) capture the angular dependence and scaling characteristics of the large-scale in-plane flows in the far-field, as one approaches the origin from infinity, the first Fourier mode with wavenumber ξ_1 comes into play at scales of $O(1/\xi_1)$, followed by the second Fourier mode with wavenumber ξ_2 at scales of $O(1/\xi_2)$, and so forth. From Eq. (3.81), the exponentially decaying components $K_2(\xi_n r)$ have the same angular dependence but with opposite sign as compared to the algebraically

decaying components $(\xi_n r)^{-2}$, constituting an exponentially localised reversed quadrupolar flow. Since exponential functions decay faster than algebraic ones, we may expect situations where the exponential decay takes over the algebraic decay near the turbulent spot, thus revealing the reversed quadrupolar flow.

3.4.3.1 Single-mode model versus two-mode model

We restrict ourselves to a minimal forcing with only the first two Fourier modes, implying a single-vortex and a triple-vortex configurations, respectively. In this case, there remains two free parameters in the solutions, namely the amplitude of the forcing A and the ratio between the first two Fourier coefficients, denoted by

$$\gamma = a_2/a_1. \tag{3.91}$$

For small values of γ, the y-dependence of the forcing is dominated by the lowest Fourier mode $n = 1$. An increase in γ signals a shift towards the second Fourier mode.

Without loss of generality, the coefficient of the first Fourier mode is selected to be $a_1 = 1$ such that the first two modified Fourier coefficients are given by

$$b_1 = \frac{2}{\pi} \quad \text{and} \quad b_2 = -\frac{2}{3\pi}\gamma. \tag{3.92}$$

Consequently, Eq. (3.90) reduces to

$$A\sum_{n=1}^{2} b_n \xi_n^{-2} = \frac{8A}{\pi^3}\left(1 - \frac{\gamma}{27}\right) > 0. \tag{3.93}$$

There are two parameter combinations that can lead to the experimentally observed quadrupolar flows with streamwise inflow and spanwise outflow: (i) $A > 0$ and $\gamma < 27$; and (ii) $A < 0$ and $\gamma > 27$. Note that the latter depicts two counter-clockwise spanwise circulations near the walls, separated by a negative spanwise vorticity at the centre of a localised spot, and similarly for the case: $A > 0$ and $\gamma < 0$. Since these configurations have not been reported in previous studies, we therefore focus on the parameter regime:

$$A > 0 \quad \text{and} \quad 0 \leq \gamma < 27. \tag{3.94}$$

More specifically, for the single-mode model: $A > 0$ and $\gamma = 0$, the poloidal forcing imposes a uniform spanwise circulation in the xy-plane that counter-acts the base flow. For the two-mode model: $A > 0$ and $0 < \gamma < 27$, the forcing term signifies a three-vortex configuration with three mutually counter-rotating spanwise vortices stacking along the y-axis, wherein both vortices near the walls rotate with the base flow.

With this choice, the integral (3.55) reduces to

$$G = \int_{-1}^{1} \left[\cos\left(\frac{1}{2}\pi y\right) + \gamma \cos\left(\frac{3}{2}\pi y\right) \right] \mathrm{d}y = -\frac{4}{3\pi}(\gamma - 3). \tag{3.95}$$

Following the discussion in §3.2.6, for $0 \leq \gamma < 3$, the forcing term is dominated by the circulating cell in the centre, resulting in an overall spanwise vorticity which is opposite in sign to that of the base flow. On the other hand, for $3 < \gamma < 27$, two circulating cells near the walls become dominant, hence the induced spanwise vorticity by the poloidal forcing is align with the base flow. In order to highlight these two distinct cases and their impact on the large-scale flow, two representative ratios: $\gamma = 0$ (single-mode model) and $\gamma = 15$ (two-mode model), are considered. As we shall see in §3.4.3.2, the flow configuration is insensitive to the precise values of γ in parameter regime: $\gamma \in (3, 27)$.

3.4.3.2 Reversed quadrupolar flow

In order to highlight the flow topology, we show in figure 3.2 the directional field for the in-plane velocities, defined as the vector $\langle \tilde{\boldsymbol{u}}_{2D} \rangle(x, z) = (\langle \tilde{u}_x \rangle, \langle \tilde{u}_z \rangle)$ normalised by its length $|\langle \tilde{\boldsymbol{u}}_{2D} \rangle|(x, z)$, so that all vectors have unit length. In both cases $\gamma = 0$ and $\gamma = 15$, the directional field outside the square box exhibits generic quadrupolar angular dependence, hence it is referred to as the far-field. Conversely, the directional field inside the box exhibits a dependence on γ and it is referred to as the core region. For $\gamma = 0$, the streamlines, visualised as level curves of the toroidal function $\langle \tilde{\psi} \rangle$, are homoclinic to the origin, forming an ideal quadrupole. For $\gamma = 15$, the large-scale flow features a reversed quadrupole centred at the origin, surrounded by four large vortices. Since the precise value of each contour depends on the product ARe/η and the ratio γ, the colour bars are best interpreted as indicators for relative magnitudes only. It should be re-emphasised that, in the present study, the turbulent spot is assumed to be infinitesimally small, whereas it is of finite size in reality.

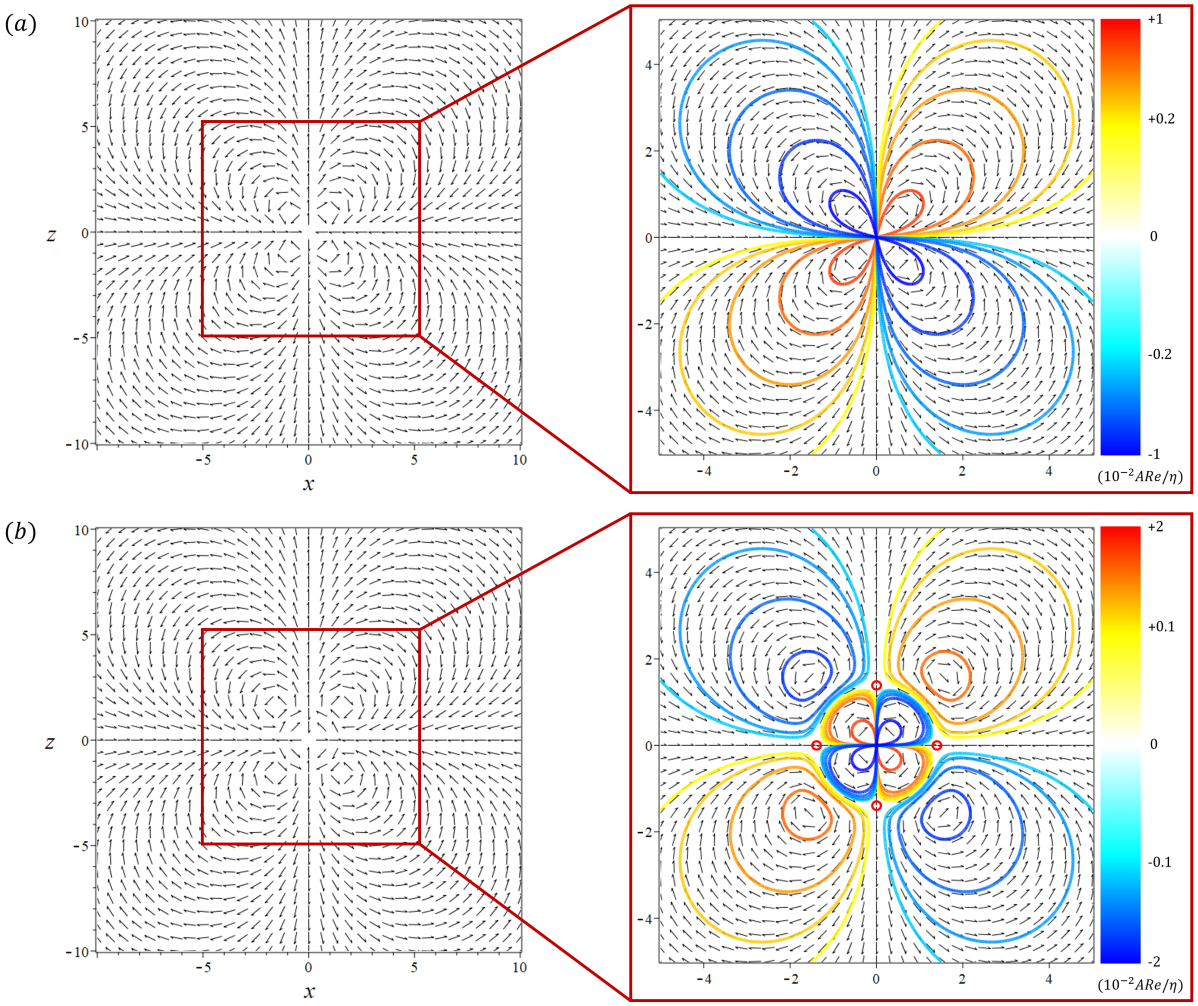

FIGURE 3.2: Directional field for the y-averaged in-plane velocities $\langle\tilde{\boldsymbol{u}}_{2D}\rangle$, defined as $\langle\tilde{\boldsymbol{u}}_{2D}\rangle/|\langle\tilde{\boldsymbol{u}}_{2D}\rangle|$, exhibiting quadrupolar angular dependence, i.e. with inflow along the streamwise x-axis and outflow along the spanwise z-axis, cf. Eqs. (3.82) and (3.83). Despite the difference in the forcing (a) $\gamma = 0$ and (b) $\gamma = 15$, the flow field (left) outside the inset (right) remains essentially unchanged. The streamlines shown in the insets are visualised as level curves of the toroidal function $\langle\tilde{\psi}\rangle$, increasing from blue to red (colour online). In the case $\gamma = 15$, the streamlines reveal the coexistence of a reversed quadrupolar flow centred at the origin and four vortices separated by the invariant manifolds of four hyperbolic saddle points, denoted by red circles.

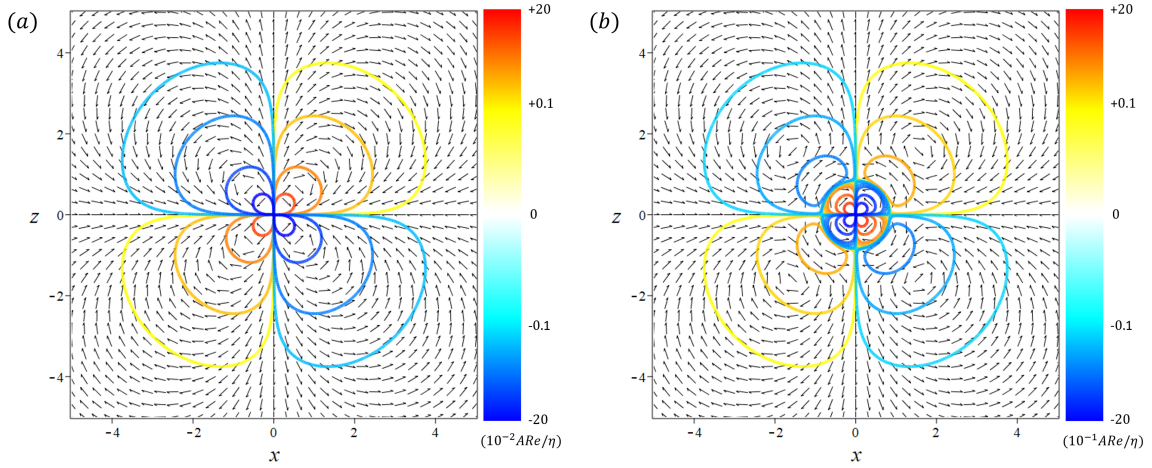

FIGURE 3.3: Superposition between the contour plots of the y-averaged wall-normal vorticity $\langle\tilde{\omega}_y\rangle$, where (a) $\gamma = 0$ and (b) $\gamma = 15$, and the in-plane directional field, cf. Eq. (3.85). Note that the exponentially decaying $\langle\tilde{\omega}_y\rangle$ takes opposite signs of the circulation direction of the two-dimensional vector field $\langle\tilde{\boldsymbol{u}}_{2D}\rangle$, indicating that the algebraically decaying component of the quadrupolar flows is irrotational.

Figure 3.3 displays a superposition between the contours of the wall-normal vorticity $\langle\tilde{\omega}_y\rangle$ and the quadrupolar directional field from figure 3.2. It is seen that in both cases, i.e. the single-mode and two-mode models, the predominant wall-normal vorticity $\langle\tilde{\omega}_y\rangle$ corresponds to a quadrupolar angular dependence with streamwise outflow and spanwise inflow, opposite in sign to the in-plane circulation in figure 3.2. These reversed quadrupolar flows arise from the exponentially localised components of the toroidal function $\langle\tilde{\psi}\rangle$, consistently with the irrotational property of the quadrupolar flow in the far-field. Since the wall-normal vorticity $\langle\tilde{\omega}_y\rangle$ is obtained by taking the curl of the large-scale in-plane flow $\langle\tilde{\boldsymbol{u}}_{2D}\rangle$, it is independent of turbulent motions inside the spot.

Following the pioneering direct numerical simulation by Lundbladh and Johansson [89], we present in figure 3.4 the contours for the y-averaged velocity components. For $\gamma = 0$, the contours of the in-plane velocity components $\langle\tilde{u}_x\rangle$ and $\langle\tilde{u}_z\rangle$ are homoclinic to the origin, forming sextupoles; while those for the wall-normal velocity $\langle\tilde{u}_y\rangle$ form a dipole corresponding to a spanwise vorticity in accord with that of the base flow. In the case $\gamma = 15$, the symmetry associated with the sextupole of the qualitative in-plane velocity components is broken, accompanied by a reversal of the wall-normal velocity $\langle\tilde{u}_y\rangle$ in the core, cf. figure 3.4 $(b,$ right column).

In order to understand the symmetry breaking observed in figure 3.4, we display in figure 3.5 (a) and (b) the decay of velocity components: $|\langle\tilde{u}_x\rangle|$ and $|\langle\tilde{u}_y\rangle|$ along the streamwise x-axis. The decay of the wall-normal vorticity $|\langle\tilde{\omega}_y\rangle|$ and the pressure $|\langle\tilde{p}\rangle|$ is also included

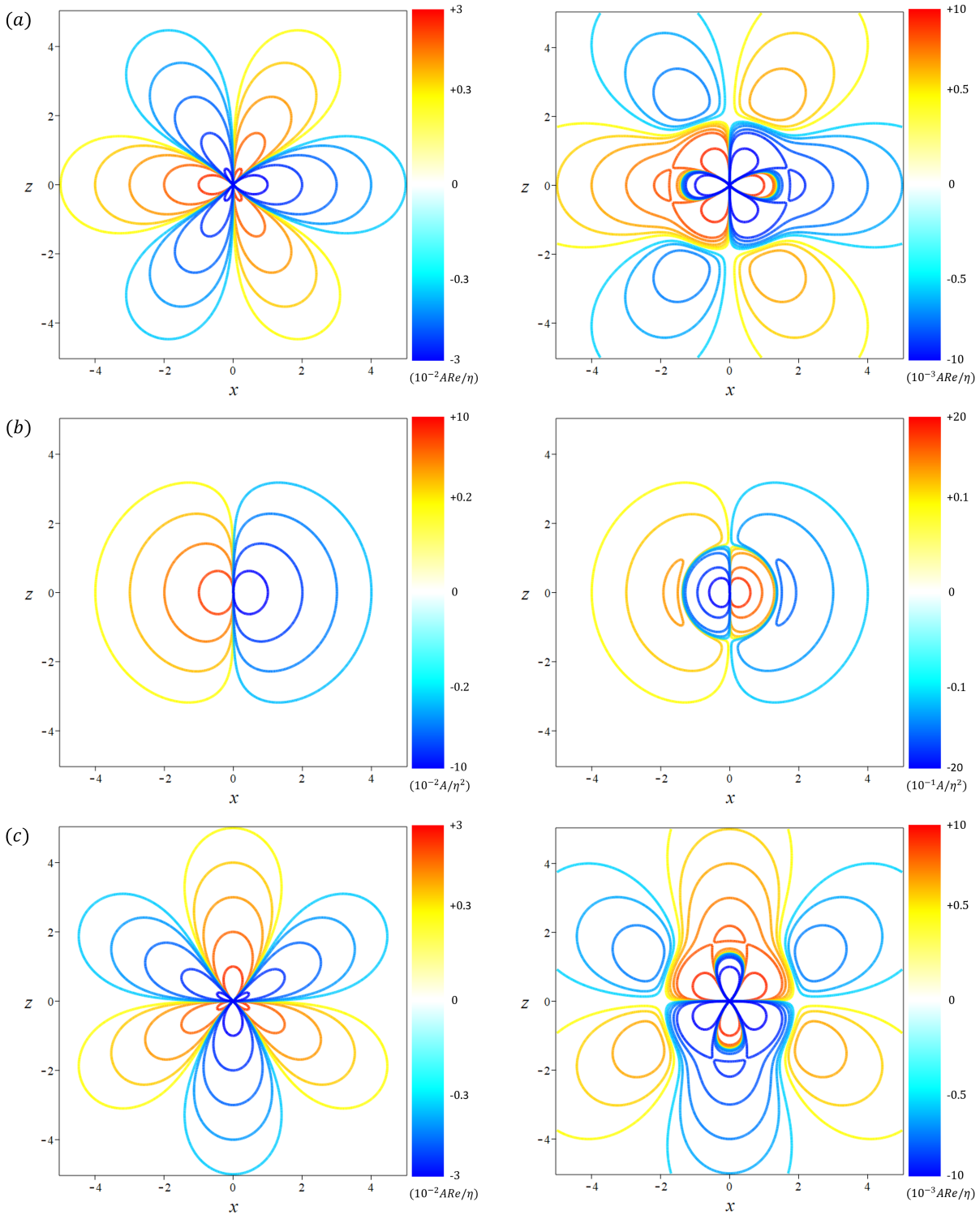

FIGURE 3.4: Contour plots for the y-averaged (*a*) streamwise velocity $\langle\tilde{u}_x\rangle$, cf. Eq. (3.82); (*b*) wall-normal velocity $\langle\tilde{u}_y\rangle$, cf. Eq. (3.84) and; (*c*) spanwise velocity $\langle\tilde{u}_z\rangle$, cf. Eq. (3.83). The left and right columns correspond to the cases of $\gamma = 0$ and $\gamma = 15$, respectively.

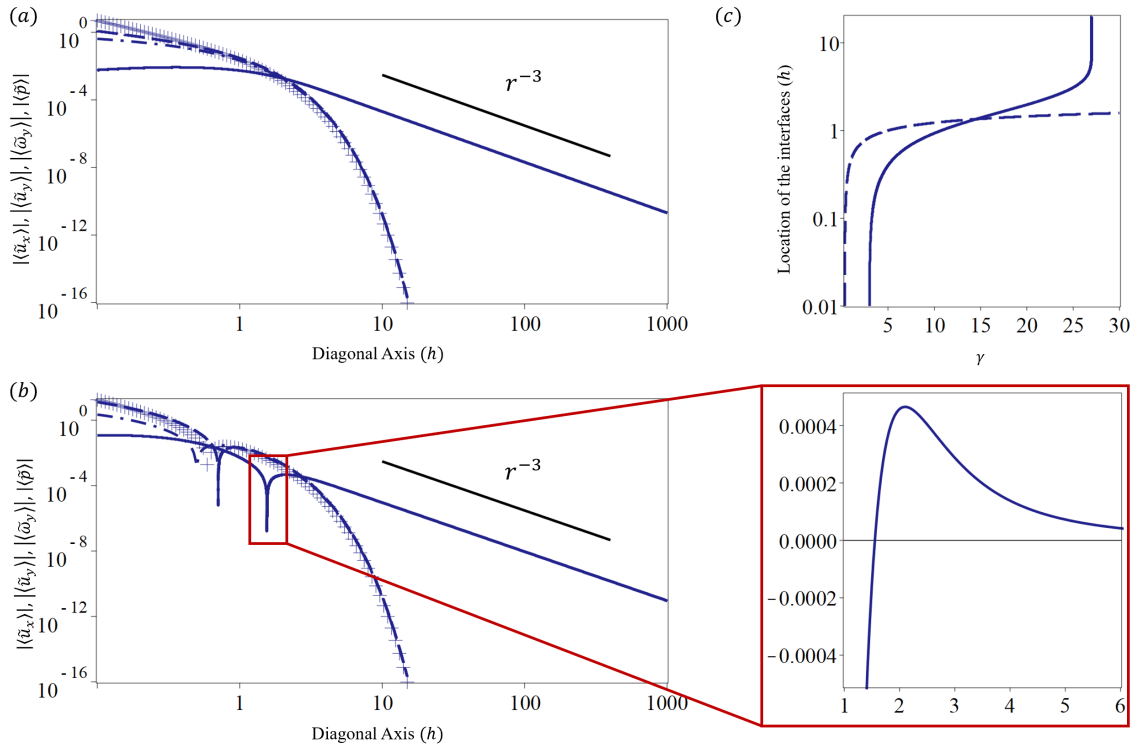

FIGURE 3.5: Decay of flow variables along the diagonal axis. In order to establish a comparison, the flow variables $|\langle\tilde{u}_x\rangle|$ (solid line), $|\langle\tilde{u}_y\rangle|$ (dashed line), $|\langle\tilde{\omega}_y\rangle|$ (crosses), and $|\langle\tilde{p}\rangle|$ (dash-dot line) are normalised by their amplitudes ARe/η, A/η^2, ARe/η, and ARe, respectively. While $|\langle\tilde{u}_y\rangle|$, $|\langle\tilde{\omega}_y\rangle|$, and $|\langle\tilde{p}\rangle|$ decay exponentially, $|\langle\tilde{u}_x\rangle|$ scales algebraically in the far-field, with a power-law exponent -3, independent of the ratio: (a) $\gamma = 0$ and (b) $\gamma = 15$. The inset reveals that the interface in (b) is where the velocity component $\langle\tilde{u}_x\rangle$ flips sign. (c) Location of the interfaces for $\langle\tilde{u}_x\rangle$ (solid line) and $\langle\tilde{u}_y\rangle$ (dashed line) along the streamwise x-axis for $\gamma = a_1/a_2 \in [0, 30]$.

as a reference. In both cases $\gamma = 0$ and $\gamma = 15$, the in-plane velocity components are dominated by the algebraic decay, whose power-law exponent is -3, in the limit $r \to \infty$. For $\gamma = 15$, the decay of flow variables are characterised by the presence of interfaces at which they flip sign. In particular, the location of the interfaces for $\langle\tilde{u}_x\rangle$ and $\langle\tilde{u}_y\rangle$ along the x-axis is plotted in figure 3.5 (c) as a function of γ. The interface for $\langle\tilde{u}_x\rangle$ appears first as γ increases past $\gamma = 3$ and quickly shifts towards infinity at $\gamma = 27$. For $\gamma > 27$, the flow field is characterised by an experimentally unobserved anti-quadrupolar flow with streamwise outflow and spanwise inflow, consistent with the expectation (3.93). On the other hand, the interface for $\langle\tilde{u}_y\rangle$ appears as soon as the second Fourier mode comes into play, i.e. $\gamma > 0$. With increasing values of γ, the interface for $\langle\tilde{u}_y\rangle$ persists and is almost independent of γ. Therefore, within the framework of the linear theory of large-scale flows, the second Fourier mode ξ_2 is a necessity in order to capture the reversal observed in figure 3.4 $(b, \text{right column})$.

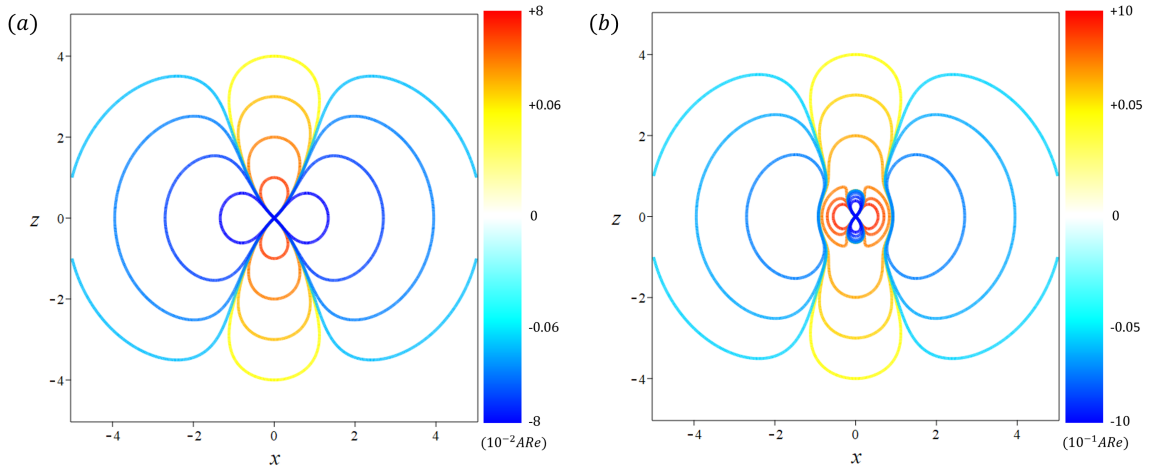

FIGURE 3.6: Contours of the y-averaged pressure $\langle\tilde{p}\rangle$: (a) $\gamma = 0$ and (b) $\gamma = 15$, cf. Eq. (3.86).

For completeness, the contours of the y-averaged pressure are shown in figure 3.6. For $\gamma = 0$, the y-averaged pressure $\langle\tilde{p}\rangle$ is exponentially localised with negative branches aligned with the streamwise direction and with the positive branches along the spanwise direction, consistent with a streamwise inflow and a spanwise outflow as shown in figure 3.2. For $\gamma = 15$, the symmetry of the pressure field is broken by the emergence of the reversed pressure in the core region, linked to the interface observed in figure 3.5 (b).

3.4.4 Topological origin of the quadrupolar flow

We discuss in this section the consequence of an exponentially localised turbulent spot, where both $\langle\tilde{u}_y\rangle$ and $\langle\tilde{\omega}_y\rangle$ decay exponentially. Since $\langle\tilde{\omega}_y\rangle$ is exponentially localised, the algebraically decaying component of the y-averaged in-plane flow $\langle\tilde{\boldsymbol{u}}_{2D}\rangle$ must be irrotational. Recalling from Eq. (3.59) that the y-averaged in-plane flow field between two walls is incompressible, we conclude that the algebraically decaying component of $\langle\tilde{\boldsymbol{u}}_{2D}\rangle$ is harmonic, i.e. both divergence-free and curl-free. To summarise, the algebraically decaying components of the y-averaged in-plane flow are harmonic if the y-averaged wall-normal vorticity is exponentially localised. This observation can be extended to all planar shear flows confined between two walls.

Since $\langle\tilde{u}_y\rangle$ is also exponentially localised, the y-averaged large-scale flow $\langle\tilde{\boldsymbol{u}}\rangle$ can be decomposed into a two-dimensional algebraically decaying harmonic component $\langle\tilde{\boldsymbol{u}}\rangle^H$ and

a three-dimensional exponentially decaying component $\langle\tilde{\boldsymbol{u}}\rangle^E$ such that

$$\langle\tilde{\boldsymbol{u}}\rangle = \langle\tilde{\boldsymbol{u}}\rangle^H + \langle\tilde{\boldsymbol{u}}\rangle^E, \tag{3.96}$$

where $\langle\tilde{\boldsymbol{u}}\rangle^H$ and $\langle\tilde{\boldsymbol{u}}\rangle^E$ both satisfy the Dirichlet boundary conditions

$$\langle\tilde{\boldsymbol{u}}\rangle^H \to 0, \quad \langle\tilde{\boldsymbol{u}}\rangle^E \to 0 \quad \text{as} \quad r \to \infty. \tag{3.97}$$

In the framework of algebraic topology, we interpret such an exponentially localised turbulent spot as an isolated zero of the two-dimensional vector field bounded by the Dirichlet boundary conditions at infinity. Denote by $\mathcal{C}$ any simple closed curve enclosing the isolated zero and $p = (r_p, \theta_p)$ a point on $\mathcal{C}$. Let p travel along $\mathcal{C}$ counterclockwise, the corresponding vector $\langle\tilde{\boldsymbol{u}}\rangle^H(r_p, \theta_p)$ attached to the point rotates continuously. Upon returning to its original position, it rotates by an angle $2k\pi$ for some integer k, [see, e.g. Chapter 9 in 104]. We define by k the Poincaré index of the exponentially localised turbulent spot after averaging between the two walls. It can be shown that k is a topological invariant solely determined by the characteristics of the turbulent spot inside $\mathcal{C}$. It is independent of the exact form of $\mathcal{C}$ [130]. According to the Hodge decomposition theorem [see, e.g. Theorem 2.2.1 in 181], such a harmonic field $\langle\tilde{\boldsymbol{u}}\rangle^H$ is unique per Poincaré index, and it is independent of boundary conditions of the $\tilde{\boldsymbol{u}}$ at the walls. The exponentially decaying component $\langle\tilde{\boldsymbol{u}}\rangle^E$, however, depends on details such as the boundary conditions at walls, the base flow profile, and the forcing. These contributions lead to a deviation from the canonical harmonic flow given by Eqs. (3.88) and (3.89). This deviation is however localised in the core region only. In the asymptotic limit where the contribution from $\langle\tilde{\boldsymbol{u}}\rangle^E$ is negligible, the large-scale flow around an isolated turbulent spot is characterised by the harmonic component $\langle\tilde{\boldsymbol{u}}\rangle^H$, which is uniquely determined by the index of the turbulent spot and independent of the boundary conditions at the walls.

According to the Poincaré-Hopf theorem [see, e.g. 182], the index of an isolated turbulent spot is also unique and characterised by the Euler characteristics of the planar geometry. The index of an isolated turbulent spot can be extracted from figure 3.2. For $\gamma = 0$, the directional field has one fixed point, namely the quadrupole, with index $+3$; while for $\gamma = 15$, the directional field possesses nine fixed points including a quadrupole with index $+3$, four vortices with index $+1$ each, and four saddles with index -1 each, such that the total sum of the indices is $+3$ and remains unchanged. Therefore, we conclude without any proof that the index of an isolated turbulent spot in planar shear flow satisfying the Dirichlet boundary conditions (3.97) is uniquely equal to $+3$.

The uniqueness of the harmonic vector field, which is ensured by the Hodge decomposition theorem, and the uniqueness of the index of an isolated turbulent spot, which is ensured by the Poincaré-Hopf theorem, together imply that the topology of the harmonic vector field $\langle\tilde{\boldsymbol{u}}\rangle^H$ is uniquely determined by the planar geometry, namely, the two-dimensional plane with Dirichlet boundary conditions at infinity and a simple isolated zero at the origin. Therefore, we expect that the y-averaged large-scale flow around an exponentially localised turbulent spot confined between two walls is generically quadrupolar and decays algebraically with power-law exponent -3 in the asymptotic limit $r \to \infty$. In other words, the origin of the ubiquitously observed quadrupolar circulations around turbulent spots in planar shear flows is topological.

3.5 Conclusions and oulooks

Using scale analysis and symmetry argument, we have derived a set of linear second-order differential equations for the poloidal and toroidal functions characterising the spatial evolution of large-scale flows around an isolated spot, namely Eqs. (3.42).

Scale analysis reveals that the variable part of the vertical pressure gradient does not contribute to the large-scale velocity field in the homogeneous directions. It is therefore neglected. Physically, this corresponds to a filtering of the smallest-scale wall-normal flows driven by the vertical pressure gradient, as well as the corresponding in-plane motions so as to satisfy the incompressibility constraint. Mathematically, the elimination of the vertical pressure gradient reduces the poloidal equation from a fourth-order differential equation with respect to the wall-normal variable y to a second-order one. Hence the no-slip boundary conditions, which require both the poloidal function and its derivative along the vertical direction to vanish at the walls, cannot be satisfied. Consequently we relaxed the no-slip conditions to the free-slip boundary conditions. It is noteworthy that the obtained poloidal functions have vanishing second-order derivatives at the walls, hence the perturbed flow presented in this paper satisfies not only the free-slip but also the stress-free boundary conditions.

Since the large-scale flow decays, as long as the far-field is of concern, the intensity separation justifies seeking invariant solutions in the co-moving Lagrangian frame, namely the Kelvin wake pattern named after Kelvin [173]. With this formalism, we get around of the difficulty associated with the variable coefficients in y, a typical feature of all shear flows.

Comparing the obtained solutions with experimental and numerical observations, we conclude that the quadrupolar flows are the stationary wake pattern "behind" a localised spot in planar shear flows. In this sense, large-scale flows arise as a consequence to the blockage effect of localised structures in shear flows, rather than the detailed turbulent dynamics inside the spot.

Since these simplifications rely only on (i) the scale separation between wall-normal and homogeneous directions; and (ii) the intensity separation between the large-scale flow in the far-field and the characteristic velocity scale of the base flow, we expect them to be readily applicable to any planar shear flows confined between two walls. The proposed governing equations have been solved analytically using the method of undetermined coefficients. By averaging the solutions between two walls and inverting the Fourier transform, we have recovered quadrupolar flows similar to previous experimental and numerical observations.

A closer examination of the analytical solutions leads to the following three main predictions:

3.5.1 The asymptotic decay of the quadrupolar flow is algebraic

While the wall-normal velocity component is exponentially localised, the in-plane velocities feature a superposition between an algebraic and an exponential decay. That is, the decay of the in-plane velocity components is exponential near an isolated turbulent spot and it is algebraic with a power-law exponent -3 in the far-field. Note that, this observation does not contradict previously reported exponential decay in moderately-sized systems by Schumacher and Eckhardt [64] and Brand and Gibson [71], where no algebraic decay was found. The algebraic decay can be masked by the exponential decay near the turbulent spot and unveil itself only at larger distances than computed in these numerical investigations. Note that algebraic decay of the large-scale flow implies that the associated length scale diverges, namely $\lambda \to \infty$, hence the scale-separation criterion (3.20) for large-scale flows is always valid, independent of the Reynolds number.

3.5.2 Existence of an exponentially localised reversed quadrupolar flow

The existence of reversed quadrupolar flow is a robust outcome of the proposed model (3.42) but it has never been reported explicitly in the literature. As soon as the negative spanwise vorticity is generated near the walls inside the spot and becomes dominant, the exponentially localised reversed quadrupolar flow emerges. This reversed quadrupolar flow leads to four large circulating cells in the xz-plane and a spanwise circulation that counteracts the base flow in the xy-plane. The predicted flow resembles those with similar patterns observed within turbulent spots in previous experiment [62] and numerical simulation [89]. However, since the spot is pointwise in our model, this resemblance can be fortuitous. On the other hand, instead of the in-plane velocities, the existence of the reversed quadrupolar flow, hence the validity of the linearised theory, can be unambiguously tested by investigating the wall-normal vorticity. We expect that, independently of the domain size and the resolution, the wall-normal vorticity dispays quadrupolar contours and is of opposite sign to the direction of quadrupolar circulation in the far-field. Since these reversed solutions are exponentially localised, their presence does not affect the algebraically decaying large-scale flow in the asymptotic limit $r \to \infty$.

3.5.3 Topological origin of the algebraically decaying quadrupolar flow

By exploiting the exponential localisation of the wall-normal components of velocity and vorticity fields, as well as the non-penetrating boundary conditions at the walls, we have uncovered a topological origin for quadrupolar circulations in planar shear flows. More specifically, the algebraically decaying component of the large-scale flow is two-dimensional and harmonic, which is uniquely determined by the index of the y-averaged turbulent spots. For planar shear flows confined between two walls, the index of an isolated turbulent spot is unique and equals $+3$. Therefore, independently of the details of the driving mechanism and of the boundary conditions at the walls, we conclude that the presence of quadrupolar circulations around localised turbulent spots in planar shear flows confined between two walls, e.g. plane Couette, plane Poiseuille, Couette-Poiseuille, and Waleffe flows, is generic.

Many other questions remain open and deserve verification using either experimental or numerical means. In particular, with the increase in computer memory, a direct numerical simulation of the fully-resolved nonlinear Navier-Stokes equations with no-slip boundary conditions, in domains large enough to unambiguously verify the present predictions about decay exponent, is currently becoming feasible. Similarly, the minimal assumption adopted in the present modelling to mimic a localised turbulent spot by a filament-like obstacle can be compared with the nonlinear simulations and tested. Alternatively, the linearised model (3.42) can give the Green's function, see e.g. Blake [183], Liron and Mochon [184], Grenier and Nguyen [185], which could be used to derive the response to any vorticity distribution mimicking an actual spot or band. Finally, a generalisation of the present derivation to arbitrary boundary conditions at the wall, to pressure-driven flows such as Poiseuille or Couette-Poiseuille flows, to even to non-planar geometries and even to external boundary-layer flows would be welcome.

Chapter 4

Bifurcation analysis for counter-rotating vortices

4.1 Introduction

Turbulent spots are not homogeneous patches of turbulence but consist of generic coherent structures in the form of counter-rotating streamwise vortices and velocity streaks arising from those elongated vortices. The complete self-sustaining process (as reviewed in §2.3.2.5) has been described by a 8-mode model by Waleffe [148, 151] and a 9-mode model by Eckhardt and his collaborators [186, 187]. These models are obtained by projecting the numerical data onto judiciously chosen modes using the Galerkin method and are believed to capture the main features of turbulence in shear flows. However, given their high dimensionality, these models are impossible to study analytically. Moreover, in the chaotic region of these models, one does not know which mechanism would correspond to a strange attractor possibly observed in the phase space. On the other hand, the interaction between streamwise vortices and inviscid waves has been investigated by Hall and Sherwin [188] in the asymptotic limit $Re \to \infty$, thereby deviating from the endeavour of route to turbulence at moderate Reynolds numbers.

The major difficulty associated with interpreting the transition to turbulence as a dynamical system is the lack of instability. As such, a linear stability analysis about the base flow cannot describe the onset of turbulence in planar shear flows. On the other hand, although the onset of turbulence is disconnected to laminar base flow, it bifurcates from and remains close to the nontrivial branch, cf. figure 4.1. Therefore, it would be justified

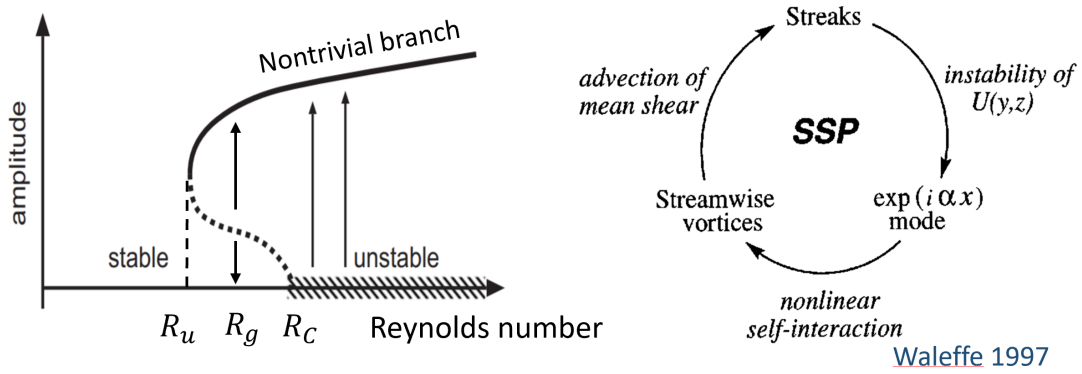

FIGURE 4.1: An illustration of the transition to turbulence in planar shear flows. Figure adapted from Waleffe [151].

to perform a bifurcation analysis about the nontrivial branch. Since the nontrivial branch is attracting, it must corresponds to one of the observable in experiments. Starting from a featureless turbulence and gradually reducing the Reynolds number, the self-sustaining process is the last nontrivial process which survives below the global threshold R_g. Hence, the self-sustaining process reflects essentially an interaction between the laminar base flow and the nontrivial branch. In between the nontrivial branch and the laminar base flow, there exists an unstable branch which gains existence at the moment of the saddle-node bifurcation and separates the basins of attraction of the nontrivial branch and the laminar base flow. As such, in order to enable an interaction between the laminar base flow and the nontrivial branch, a solution trajectory must overcomes an energy barrier associated with the unstable branch.

Let us revisit the self-sustaining process and start from the streaks, which are merely the modified base flow by counter-rotating vortices, and consequently has a linear origin. Streaks undergo a transient growth and pick up a streamwise instability, provided that the amplification is sufficient. Since the transient growth is associated with the non-orthogonality of the shear and has a linear origin, we conclude

1. the shear of the base flow will not affect the eigenvalues of the linearised equations;
2. the role of the shear is to provide a linear amplification to overcome the energy barrier associated with the unstable branch; and
3. the nontrivial branch, which has a nonlinear origin, must corresponds to counter-rotating vortices.

Therefore, by contrast to the conventional Galerkin method, in this chapter, a low-dimensional dynamical system is derived by resorting to the scale analysis and the symmetry arguments. More specifically, the focus is on the bifurcation analysis for flows dominated by a pair of counter-rotating rigid vortices. As long as the asymptotic limit $t \to \infty$ is of concern, the shear of the base flow can be neglected. The feature of existing two counter-rotating vortices forming a pair is reflected by requiring that the helicity integral is conserved.

The dynamical system featuring a pair of counter-rotating vortices is derived in §4.2. The resulting model consists of a set of three ordinary differential equations signifying the $\mathbb{Z}_2$-symmetric pitchfork/Hopf problem. The relevance of this model to the transition to turbulence was conjectured without proof by Iooss and Langford [189] 40 years ago. Therefore, the present work complements their conjecture by bridging the dynamical system from a purely mathematical origin to the governing equations of fluid mechanics. The bifurcation analysis for fixed points and periodic orbits are undertaken in §4.3 for system with the preserving rotational symmetry and in §4.4 for system with the broken rotational symmetry, respectively. Note that, for the proposed model, the rotational symmetry limits the effective dimension of the phase space to two, thereby precluding the existence of chaos. In both cases, we observe the emergence of a conjugate pair of fixed points that may be linked with the finite amplitude velocity streak aligned or anti-aligned with the vortex axis. Lastly, the limitation of the model are highlighted and discussed in §4.5.

4.2 Formulation

The Navier-Stokes equations in a constantly rotating coordinate system are [37]

$$\partial_t \boldsymbol{u} = -\nabla P + \boldsymbol{u} \times (2\boldsymbol{\Omega} + \boldsymbol{\omega}) + \nu \nabla^2 \boldsymbol{u}, \tag{4.1}$$

where the fluid density is taken to be constant, i.e. $\rho = 1$, and Eq. (4.1) is supplemented with the Dirichlet boundary conditions: $\boldsymbol{u} = 0$, at the boundaries. Here, by using the vector identity

$$\boldsymbol{\Omega} \times (\boldsymbol{\Omega} \times \boldsymbol{r}) = -\frac{1}{2} \nabla \left(\boldsymbol{\Omega} \times \boldsymbol{r} \right)^2, \quad \boldsymbol{u} \cdot \nabla \boldsymbol{u} = \frac{1}{2} \nabla \boldsymbol{u}^2 - \boldsymbol{u} \times \boldsymbol{\omega}, \tag{4.2}$$

the centrifugal force $\boldsymbol{\Omega} \times (\boldsymbol{\Omega} \times \boldsymbol{r})$ and the kinetic energy $\boldsymbol{u}^2/2$ have been absorbed into the pressure gradient, giving rise to the effective pressure

$$P = p + \frac{1}{2}\boldsymbol{u}^2 - \frac{1}{2}\left(\boldsymbol{\Omega} \times \boldsymbol{r}\right)^2 . \tag{4.3}$$

The presence of rotation introduces a second set of length, time and velocity scales, respectively, the radius of the fluid trajectory R, the inverse of the angular velocity Ω^{-1}, where $\Omega = |\boldsymbol{\Omega}|$, and the tangential velocity of the rotation ΩR, in additional to the characteristic length L, time τ and velocity U scales of the relative motion $(\boldsymbol{u}, p)$. Unlike Chapter 3 where the formulation is built upon the scale separation between the wall-normal and the homogeneous length scales, in this chapter, no explicit scale separation is assumed. That is, $L \sim O(R)$. Instead, we propose to take advantage of the intensity separation between U and ΩR.

4.2.1 Scaling analysis for flows in rotating coordinates

Near the onset of the secondary instability, the magnitude of the relative velocity $|\boldsymbol{u}|$ is infinitesimal as compared with the tangential velocity ΩR of the rotating frame, hence the Rossby number is small

$$\epsilon = \frac{U}{\Omega R} \ll 1. \tag{4.4}$$

It should be pointed out that, by contrast to the geostrophic balance where $\epsilon \ll 1$ is ensured by the small curvature of flow trajectories (cf. Chapter 1 in Pedlosky [167]), i.e. $R \to \infty$, in the present application, the validity of the relation (4.4) is due to the intensity separation underlying the linear instability analysis.

In order to exploit the disparity in the characteristic velocities, let us consider a rescaling achieved by [1]

$$\boldsymbol{u} = U\boldsymbol{u}^*, \quad t = \Omega^{-1}t^*, \quad \boldsymbol{\Omega} = \Omega\boldsymbol{\Omega}^*, \quad \boldsymbol{r} = R\boldsymbol{r}^*, \quad \boldsymbol{x} = R\boldsymbol{x}, \quad P = (\Omega R)^2 P^*, \tag{4.5}$$

where, by contrast to the lubrication theory considered in Chapter 3, the scaling for the effective pressure is selected to balance the inertial terms, reflecting the physical intuition that, in rotation dominated or vortex dominated flows, the pressure arises so as to balance the centrifugal force due to the rotation. Hence, this scaling is valid only if the reduced

[1] It is pointed out for clarity, although they did not show it explicitly, the same scaling relations have been exploited in deriving Eq. (14.3) in the textbook by Landau and Lifshitz [37].

Reynolds number, or the inverse Ekman number, is large

$$\epsilon^{-1}Re = \frac{\Omega R^2}{\nu} \gg 1. \tag{4.6}$$

This condition is satisfied either if the Rossby number ϵ is sufficiently small, or if the Reynolds number is sufficiently large. The former is justified by the assignment of the secondary instability analysis, while the later reflects the observation that turbulent spots occur at Reynolds numbers that are greater than unity.

Substituting the preceding scaling relations into equation (4.1) and dropping the superscript * denoting the rescaled dimensionless variables, we have

$$\partial_t \boldsymbol{u} = -\epsilon^{-1}\nabla P + 2\boldsymbol{u} \times \boldsymbol{\Omega} + \epsilon\left(\boldsymbol{u} \times \boldsymbol{\omega} + Re^{-1}\nabla^2 \boldsymbol{u}\right). \tag{4.7}$$

Since ϵ is chosen small, the explicit appearance of powers of ϵ in Eq. (4.7) implies the following perturbative expansions for P:

$$P = P^{(0)} + \epsilon P^{(1)} + \epsilon^2 P^{(2)} + O(\epsilon^3). \tag{4.8}$$

Substituting the preceding expansions into Eq. (4.7) and collecting powers of ϵ leads to a sequence of differential equations

$$O(\epsilon^{-1}): \quad \nabla P^{(0)} = 0, \tag{4.9a}$$

$$O(\epsilon^{0}): \quad \partial_t \boldsymbol{u} = -\nabla P^{(1)} + 2\boldsymbol{u} \times \boldsymbol{\Omega}, \tag{4.9b}$$

$$O(\epsilon^{+1}): \quad \nabla P^{(2)} = \boldsymbol{u} \times \boldsymbol{\omega} + Re^{-1}\nabla^2 \boldsymbol{u}. \tag{4.9c}$$

At the leading order $O(\epsilon^{-1})$, Eq. (4.9a) depicts a cyclostrophic balance, where the pressure gradient is completely balanced by the centripetal acceleration arising from the curvature effect [164]. Cyclostrophic balance is widely observed in geophysical flows, e.g. tornadoes [190], waterspout [191] and dust devils [192], and is applied in computational fluid dynamics as a criterion for identifying coherent vortices [54, 55]. Thus, Eq. (4.9a) depicts a base flow dominated by a single rigid vortex upon which the secondary instability arises at the subsequent orders.

At the order $O(\epsilon^0)$, Eq. (4.9b) characterises the temporal evolution of an infinitesimal disturbance deviating from the cyclostrophic balance. Since the quadratic nonlinearity of the Navier-Stokes equation and the viscous dissipation enter only at the higher orders

$O(\epsilon)$, they are negligible provided that the criterion (4.6) is fulfilled. Note that, the Coriolis force is skew-symmetric. Acting orthogonally to solution trajectories, the Coriolis force is energy conservative: it does not create nor dissipate energy, but merely distributes the energy among the different scales. Moreover, taking the divergence of Eq. (4.9b), the effective pressure $P^{(1)}$ solves

$$\nabla^2 P^{(1)} = 2\boldsymbol{\omega} \cdot \boldsymbol{\Omega}, \tag{4.10}$$

where the nonzero $P^{(1)}$ arises from the alignment between the angular velocity $\boldsymbol{\Omega}$ and the vorticity of the perturbed velocity $\boldsymbol{\omega}$.

In terms of the dynamical systems theory (cf. Chapter 7 in Guckenheimer and Holmes [130]), ordinary differential equations with skew-symmetric Jacobian matrix is degenerated in the sense that the inclusion of a finite amplitude perturbation can produce multiple repelling and attracting tori and heteroclinic orbits. For vector fields possessing the rotational symmetry, the heteroclinic orbits that occur are necessarily degenerated. If the nonlinear unfolding is not axisymmetric, the flow is likely to be chaotic, i.e. contain transversal heteroclinic orbits.

Note the $\nabla P^{(1)}$ vanishes for $\boldsymbol{u} = 0$ and since $\boldsymbol{u}$ is infinitesimal, formally, the effective pressure gradient can be expanded in powers of $\boldsymbol{u}$, yielding

$$\nabla P^{(1)} = \boldsymbol{\mu}\boldsymbol{u} + O(\boldsymbol{u}^2), \tag{4.11}$$

and to the leading order, the perturbation matrix $\boldsymbol{\mu}$ is given by

$$\boldsymbol{\mu} = \begin{bmatrix} \mu_{11} & \mu_{12} & \mu_{13} \\ \mu_{21} & \mu_{22} & \mu_{23} \\ \mu_{31} & \mu_{32} & \mu_{33} \end{bmatrix}. \tag{4.12}$$

In order to exploit the existing dynamical system theory and the bifurcation analysis, we seek for solutions of the form

$$\boldsymbol{u} = \hat{\boldsymbol{u}}(t) e^{\mathrm{i}\boldsymbol{k}\boldsymbol{x}}. \tag{4.13}$$

As such, the linearised equation (4.9b) takes the form

$$\mathrm{d}_t \hat{\boldsymbol{u}} = (\boldsymbol{\mu} + \boldsymbol{A})\hat{\boldsymbol{u}}, \tag{4.14}$$

where the matrix

$$\boldsymbol{A} = \begin{bmatrix} 0 & +2\Omega_z & -2\Omega_y \\ -2\Omega_z & 0 & +2\Omega_x \\ +2\Omega_y & -2\Omega_x & 0 \end{bmatrix}, \tag{4.15}$$

is skew-symmetric and the incompressibility constraint $\nabla \cdot \boldsymbol{u} = 0$ is replaced by the following orthogonality condition:

$$\hat{\boldsymbol{u}} \cdot \boldsymbol{k} = 0. \tag{4.16}$$

4.2.2 Normal form

In order to reduce the variables Ω_x, Ω_y, and Ω_z into one

$$\Omega = \sqrt{\Omega_x^2 + \Omega_y^2 + \Omega_z^2}, \tag{4.17}$$

we introduce a special orthogonal transformation:

$$\boldsymbol{B} = \boldsymbol{S}^{-1}\boldsymbol{A}\boldsymbol{S} \quad \text{and} \quad \hat{\boldsymbol{v}} = \boldsymbol{S}^{-1}\hat{\boldsymbol{u}}, \tag{4.18}$$

where

$$\boldsymbol{S} = \frac{1}{\sigma}\begin{bmatrix} \Sigma\Omega_x/\Omega^2 - 1 & (\Omega_z - \Omega_y)/\Omega & \sigma\Omega_x/\Omega \\ \Sigma\Omega_y/\Omega^2 - 1 & (\Omega_x - \Omega_z)/\Omega & \sigma\Omega_y/\Omega \\ \Sigma\Omega_z/\Omega^2 - 1 & (\Omega_y - \Omega_x)/\Omega & \sigma\Omega_z/\Omega \end{bmatrix}, \tag{4.19}$$

with

$$\sigma = \frac{\sqrt{(\Omega_x - \Omega_y)^2 + (\Omega_y - \Omega_z)^2 + (\Omega_x - \Omega_z)^2}}{\Omega}, \quad \Sigma = \Omega_x + \Omega_y + \Omega_z, \tag{4.20}$$

provided that $\sigma \neq 0$. Otherwise, the transformation (4.18) is singular; and in this case, the transformation matrix (4.19) is replaced by

$$\boldsymbol{S} = \frac{1}{\sigma}\begin{bmatrix} -1/\sqrt{6} & -1/\sqrt{2} & +1/\sqrt{3} \\ +2/\sqrt{6} & 0 & +1/\sqrt{3} \\ -1/\sqrt{6} & +1/\sqrt{2} & +1/\sqrt{3} \end{bmatrix}. \tag{4.21}$$

Substitution gives

$$\mathrm{d}_t\hat{\boldsymbol{v}} = \left(\boldsymbol{S}^{-1}\boldsymbol{\mu}\boldsymbol{S} + \boldsymbol{B}\right)\hat{\boldsymbol{v}}, \tag{4.22}$$

where

$$\boldsymbol{B} = \begin{bmatrix} 0 & +2\Omega & 0 \\ -2\Omega & 0 & 0 \\ 0 & 0 & 0 \end{bmatrix}. \tag{4.23}$$

Although the special orthogonal transformation does not affects the eigenvalues of the linearised system, the perturbation matrix $\boldsymbol{S}^{-1}\boldsymbol{\mu}\boldsymbol{S}$ is quite complex now. Therefore, instead of calculating the precise values of the perturbation matrix, we consider a general perturbation.

In the absence of the perturbation $\boldsymbol{\mu} = 0$, the system (4.22) is degenerated with a simple zero, and a pair of purely imaginary eigenvalues $\pm\mathrm{i}\Omega$. Subjected to an arbitrary perturbation, the simple zero will remain real; whereas the pair of purely imaginary eigenvalues will remain complex conjugate. Moreover, since the perturbation $\boldsymbol{\mu}$ stems from an effective pressure gradient and since the curl of a gradient is identically zero, the perturbation cannot contribute to a rotation of the system. Lastly, as long as the asymptotic behaviour is of concern, the off-diagonal terms can be neglected. As such, we concluded that an arbitrary perturbation of gradient type to the system (4.22) has only two degrees of freedom such that

$$\boldsymbol{\mu} = \begin{bmatrix} \mu_1\hat{u}_x \\ \mu_1\hat{u}_y \\ \mu_2\hat{u}_z \end{bmatrix}. \tag{4.24}$$

Consequently, Eq. (4.22) can be expressed in terms of the matrix form as:

$$\begin{bmatrix} \mathrm{d}_t\hat{u}_x \\ \mathrm{d}_t\hat{u}_y \\ \mathrm{d}_t\hat{u}_z \end{bmatrix} = \begin{bmatrix} \mu_1\hat{u}_x \\ \mu_1\hat{u}_y \\ \mu_2\hat{u}_z \end{bmatrix} + \begin{bmatrix} 0 & +2\Omega & 0 \\ -2\Omega & 0 & 0 \\ 0 & 0 & 0 \end{bmatrix} \begin{bmatrix} \hat{u}_x \\ \hat{u}_y \\ \hat{u}_z \end{bmatrix}. \tag{4.25}$$

The system is linearly stable for $\mu_i < 0$ and unstable for $\mu_i > 0$, respectively. The off-diagonal components are skew-symmetric, underlying the normal form of the dynamical systems. For $\mu_i = 0$, namely, when the centrifugal force is exactly balanced by the pressure gradient, the Jacobian matrix depicts an equivariance of the vector field with respect to the axis of rotation associated with the purely imaginary eigenvalues $\pm\mathrm{i}\Omega$.

With the inclusion of higher order nonlinear terms, a sequence of bifurcations can take place, depicting a route to chaos in vortex dominated flows.

Introducing the cylindrical coordinates

$$\hat{u}_x = r\cos(\varphi), \quad \hat{u}_y = r\sin(\varphi), \quad \hat{u}_z = h, \tag{4.26}$$

Eq. (4.25) can be rewritten as

$$\mathrm{d}_t r = +\mu_1 r, \tag{4.27a}$$
$$\mathrm{d}_t h = +\mu_2 h, \tag{4.27b}$$
$$\mathrm{d}_t \varphi = -2\Omega. \tag{4.27c}$$

Note that, arising from the non-zero rotation of the coordinates, the state variables

$$r = |\hat{\boldsymbol{u}} \times \boldsymbol{\Omega}|/\Omega \quad \text{and} \quad h = \hat{\boldsymbol{u}} \cdot \boldsymbol{\Omega}/\Omega, \tag{4.28}$$

resemble the linear counterparts of the normalised Lamb vector magnitude and helicity density by the angular velocity $\Omega \neq 0$, respectively.

So far, what we have been obtained are just the linear part of the normal form, and in order to consider the successive bifurcation from the nontrivial branch, we need to take into account all possible nonlinear unfolding. Note that, the equation for angular variable (4.27c) is decoupled from the rest as long as the rotational symmetry is preserved. And if this is the case, it would be sufficient to consider the planar system spanned by r and h. Since the origin representing the vortex flow must be a trivial fixed point, the most general expansion constitutes a power series of $(r + h)$, namely

$$\mathrm{d}_t r = +\mu_1 r + r(a_1 r + a_2 h + a_3 r^2 + a_4 r h + a_5 h^2) + O\left(|r, h|^4\right), \tag{4.29a}$$
$$\mathrm{d}_t h = +\mu_2 h + h(b_1 r + b_2 h + b_3 r^2 + b_4 r h + b_5 h^2) + O\left(|r, h|^4\right). \tag{4.29b}$$

Note that, the variable r is an absolute value by definition, imposing a reflectional symmetry with respect to r; and since the system possesses a pair of counter-rotating vortices, a perturbation will simultaneous feel the presence of both vortices, imposing a reflectional symmetry with respect to h:

$$(r, h, \varphi) \to (-r, -h, \varphi). \tag{4.30}$$

Taken preceding symmetry into consider, we have

$$a_1 = a_2 = a_4 = b_1 = b_2 = b_4 = 0. \tag{4.31}$$

With a proper scaling of the state variables

$$r = \tilde{r}/\sqrt{|a_2|}, \quad h = \tilde{h}/\sqrt{|b_4|}, \quad \Omega = -\tilde{\Omega}/2, \tag{4.32}$$

and dropping the tilde, the normal form (4.29a) reduces to the following well-posed $\mathbb{Z}_2$-symmetric pitchfork/Hopf problem underlying the onset of the secondary instability in flows dominated by a pair of counter-rotating vortices

$$\mathrm{d}_t r = r\left(\mu_1 + ar^2 + bh^2\right), \tag{4.33a}$$
$$\mathrm{d}_t h = h\left(\mu_2 + cr^2 + dh^2\right), \tag{4.33b}$$
$$\mathrm{d}_t \varphi = \Omega. \tag{4.33c}$$

Here the equations are truncated up to $O\left(|r,h|^3\right)$ and the coefficients

$$a = \pm 1, \quad b = a_3/|b_4|, \quad c = b_3/|a_2|, \quad d = \pm 1, \tag{4.34}$$

depend on the details of the nonlinear unfolding.

Note that, the system (4.33) possesses both the reflectional symmetry associated with h and the rotational symmetry associated with φ, while the solution of which may possess part or none of these symmetries. That is, these symmetries can be broken during the evolution of the system. Such symmetry breaking may arise externally from the imposition of boundary conditions, or from driving forces, or it may happen spontaneously [193]. In the case of spontaneous symmetry breaking, the symmetric state is unstable so that the system spontaneously evolves towards stable states by breaking the symmetry.

Before moving onto the bifurcation analysis, it should be pointed out that the relevance between the system (4.33) and the transition to turbulence via bifurcations has been conjectured by Iooss and Langford [189] half 40 years ago. However, to the best of the author's knowledge, no link between the normal form (4.33) and the Navier-Stokes equations has been established previously.

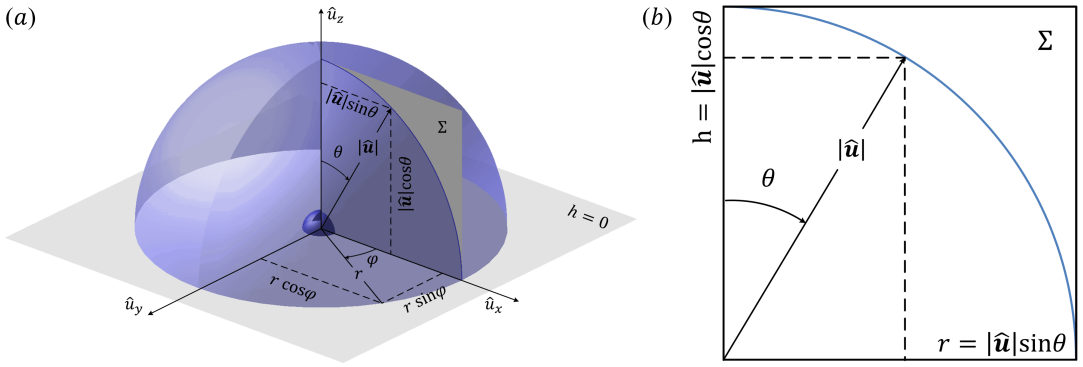

FIGURE 4.2: An illustration of the phase space: (a) the flow in the three-dimensional phase space is bounded by a sphere of radius $|\hat{\boldsymbol{u}}|$; and (b) the planar phase space contained in the Poincaré section $\Sigma = \{(r, \varphi, z) \in \mathbb{R}^2 \times S^1 \,|\varphi = 0\}$. The three-dimensional phase space is symmetrical to the plane $h = 0$ representing the complex-lamellar state, with the negative half of the phase space mirroring the positive half shown.

4.3 Bifurcation analysis for flows with rotational symmetry

For systems which preserve the rotational symmetry, the equation for φ is decoupled from those for r and h. Consequently, the system (4.33) can be reduced to a two-dimensional problem by considering a projection on a global cross section $\Sigma = \{(r, \varphi, z) \in \mathbb{R}^2 \times S^1 \,|\varphi = 0\}$, the so-called Poincaré section, as shown in figure 4.2. The reduced planar system on Σ is given by

$$\mathrm{d}_t r = r\left(\mu_1 + ar^2 + bh^2\right), \quad a = \pm 1, \tag{4.35a}$$

$$\mathrm{d}_t h = h\left(\mu_2 + cr^2 + dh^2\right), \quad d = \pm 1, \tag{4.35b}$$

where the r- and h-axes are invariant

$$\mathrm{d}_t r = \mu_1 r + ar^3 \quad \text{and} \quad \mathrm{d}_t h = \mu_2 h + dh^3, \tag{4.36}$$

resembling the complex-lamellar and the Beltrami flows, respectively. Here, invariant means that, initiated with complex-lamellar or helical conditions, solutions to Eqs. (4.36) remain complex-lamellar or helical conditions for infinite time.

Let $\theta \in [0, \pi]$ be an angle between the velocity $\hat{\boldsymbol{u}}$ and the axis of rotation $\boldsymbol{\Omega}$, hence the state variables r and h can be expressed as

$$r = |\hat{\boldsymbol{u}}| \sin(\theta) \quad \text{and} \quad h = |\hat{\boldsymbol{u}}| \cos(\theta). \tag{4.37}$$

Since the planar system (4.35) has reflectional symmetry with respect to the r-axis and since $r \geqslant 0$ by definition, it is sufficient to consider only the first quadrant. Within the first quadrant, the system (4.35) has up to four coexisting fixed points

$$(r_0, h_0) = (0, 0) \qquad \text{for} \quad \mu_1, \mu_2 \in \mathbb{R}, \tag{4.38a}$$

$$(r_1, h_1) = (\sqrt{-\mu_1/a}, 0) \qquad \text{for} \quad \mu_1 a < 0, \tag{4.38b}$$

$$(r_2, h_2) = (0, \sqrt{-\mu_2/d}) \qquad \text{for} \quad \mu_2 d < 0, \tag{4.38c}$$

$$(r_3, h_3) = \left(\sqrt{\frac{b\mu_2 - d\mu_1}{ad - bc}}, \sqrt{\frac{c\mu_1 - a\mu_2}{ad - bc}}\right) \qquad \text{for} \quad \frac{b\mu_2 - d\mu_1}{ad - bc} > 0, \ \frac{c\mu_1 - a\mu_2}{ad - bc} > 0. \tag{4.38d}$$

For $\Omega \neq 0$, the trivial [2] fixed point (r_0, z_0) corresponds to the base flow where the relative velocity $\hat{\boldsymbol{u}}$ vanishes. Crossing the line $\mu_1 = 0$, a pitchfork bifurcation occurs from the origin (r_0, z_0) in the one-dimensional centre manifold given by the coordinate axis $z = 0$, creating the fixed point (r_1, z_1). The fixed point (r_2, z_2) is created in the same manner on the line $\mu_2 = 0$. The fixed point (r_3, z_3) gains its appearance through a pitchfork bifurcation occurring from either the fixed point (r_1, z_1) on the line $\mu_2 = c\mu_1/a$, or from (r_2, z_2) on the line $\mu_2 = d\mu_1/b$. Located on the invariant r- and h-axes, the fixed points (r_1, h_1) and (r_2, h_2) can be referred to as the complex-lamellar and the helical modes, respectively. More specifically, since $\Omega \neq 0$ by definition, fixed points on the h-axis correspond to enhanced velocities aligned or anti-aligned with the axis of rotation. Consequently, these helical modes may be phenomenologically linked with the presence of velocity streaks coexisting with the counter-rotating vortices.

As long as a Hopf bifurcation does not take place from the fixed point (r_3, h_3), these equilibrium solutions remain non-interactive. That is, although up to four distinct fixed points can coexist in the phase plane Σ, they compete for presence. Starting from an arbitrary initial condition, the solution trajectory converges monotonically to one of the four fixed points; an observer cannot but perceive the existence of only one fixed point

[2] Here, "trivial" means that, independent of the coefficients: a, b, c, and d, and the bifurcation parameters: μ_1 and μ_2, the fixed point (r_0, h_0) is always present.

by observing a single solution trajectory. Borrowing ideas from ecology [194], this non-interactive situation is referred to as the competitive exclusion state and we remark that: competitively exclusive flows cannot be chaotic. For the bifurcation analysis of this case, see Appendix F.

On the other hand, during the Hopf bifurcation, periodic orbits emerge from the fixed point (r_3, z_3), wherein the mode dominance is no longer a singular event. As trajectories circulate in the phase space, the flow undergoes a self-sustaining process involving successive changes in energy and coherence. Analogously, we refer to this situation as the competitive coexistence state, and in this situation more complicated dynamics are expected to emerge. Therefore, the coefficients in Eqs. (4.35) are selected as so to allow the occurrence of the Hopf bifurcation.

4.3.1 Hopf bifurcation in the phase plane

In order to determine the occurrence of the Hopf bifurcation, it is prerequisite to evaluate the Jacobian of the system (4.35) linearised at the fixed point (r_3, z_3)

$$\boldsymbol{J}|_{(r_3,z_3)} = \begin{bmatrix} 2a\dfrac{b\mu_2 - d\mu_1}{ad-bc} & 2b\sqrt{\dfrac{b\mu_2 - d\mu_1}{ad-bc}}\sqrt{\dfrac{c\mu_1 - a\mu_2}{ad-bc}} \\ 2c\sqrt{\dfrac{b\mu_2 - d\mu_1}{ad-bc}}\sqrt{\dfrac{c\mu_1 - a\mu_2}{ad-bc}} & 2d\dfrac{c\mu_1 - a\mu_2}{ad-bc} \end{bmatrix}, \tag{4.39}$$

with the trace

$$\mathrm{tr}(\boldsymbol{J})|_{(r_3,z_3)} = \frac{2(cd\mu_1 - ad\mu_1 + ab\mu_2 - ad\mu_2)}{ad-bc}, \tag{4.40}$$

and the determinant

$$\det(\boldsymbol{J})|_{(r_3,z_3)} = \frac{4(b\mu_2 - d\mu_1)(c\mu_1 - a\mu_2)}{ad-bc}. \tag{4.41}$$

Combining the occurrence condition of the Hopf bifurcation $\mathrm{tr}(\boldsymbol{J})|_{(r_3,z_3)} = 0$ and $\det(\boldsymbol{J})|_{(r_3,z_3)} > 0$ with the existence condition of the fixed point (r_3, z_3) given by equation (4.38d), it is found that the Hopf bifurcation occurs on the line

$$\mu_2 = \frac{a-c}{d-b}\mu_1, \tag{4.42}$$

in the parameter space, provided that

$$ad = -1 \quad \text{and} \quad bc < -1. \tag{4.43}$$

Almost randomly, the coefficients for a and d are selected as

$$a = -1 \quad \text{and} \quad d = 1, \tag{4.44}$$

such that for $\mu_1 = \mu_2 = 0$, the trivial fixed points (r_0, h_0) is a saddle with inflow along the r-axis and outflow along the h-axis. Substituting (4.44) into (4.42), the Hopf bifurcation occurs on the line:

$$\mu_2 = k_H \mu_1 \quad \text{with} \quad k_H = \frac{c+1}{b-1}, \tag{4.45}$$

in the parameter space. Depending on the combination of coefficients b and c, thereby the sign of the slope k_H, as well as the presence of fixed points (r_1, h_1) and (r_2, h_2) at the moment of the Hopf bifurcation, two qualitatively different cases can be distinguished.

4.3.1.1 Case 1: unbounded periodic orbits

For $b > 1$ and $c < -1$, hence $k_H < 0$, the unfolding is shown in figure 4.3. It is seen that, although the Hopf bifurcation occurs in the second quadrant of the parameter space, the pitchfork bifurcations, which give rise to the fixed point (r_3, h_3), take place in the first and the third quadrants, respectively. At the the moment of the Hopf bifurcation, the fixed points (r_2, h_2) and (r_3, h_3) are absent. Therefore, these periodic orbits generated at the Hopf bifurcation are unbounded in the sense that, as they grow in size, they fill the entire phase plane.

For $b > 1$ and $-1 < c < 1/b$ and $< -1/c < b < 1$ and $c < -1$, besides the trivial fixed point (r_0, h_0) and the off-axis fixed point (r_3, h_3), at the moment of the Hopf bifurcation, the phase plane has another nontrivial fixed point on the invariant axis. For instance, for $b > 1$ and $-1 < c < 1/b$, the stable manifold $W^s(r_2, h_2)$ of the fixed point (r_2, h_2) divides the phase plane into two basins of attraction. For perturbations initiated below $W^s(r_2, h_2)$, the solution trajectories converge towards the trivial fixed point (r_0, h_0) representing the base flow comprising counter-rotating vortices. For perturbations initiated above $W^s(r_2, h_2)$, the dynamics of the solution trajectories are characterised by the periodic orbits arising from the Hopf bifurcation. Despite the presence of invariant

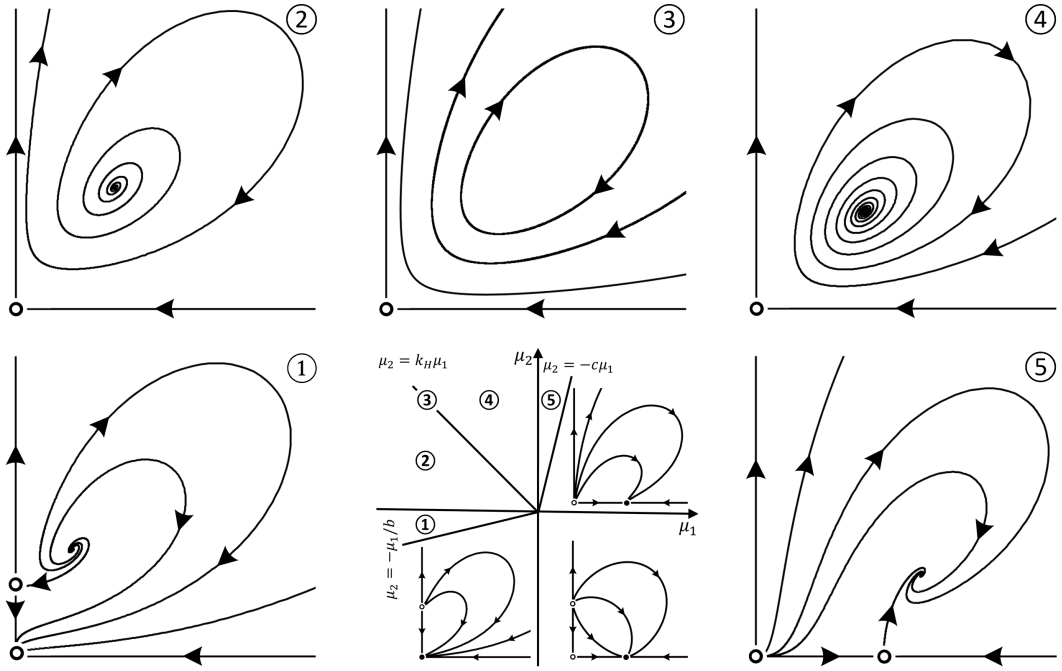

FIGURE 4.3: Unfolding and phase portraits of the planar system (4.35), where $a = -1$, $d = 1$, $b > 1$ and $c < -1$, where the periodic orbits emerged at the moment of the Hopf bifurcation are unbounded. Henceforth, solid circles indicate stable fixed points and the hollow ones indicate instability.

manifolds dividing the phase plane, periodic orbits emerging at the Hopf bifurcation are unbounded, they leave the local neighbourhood of the origin. In these cases, the use of the normal form analysis, which is only applicable to an arbitrarily small neighbourhood of a single fixed point [130], is no longer justified. That is, a complete unfolding for unbounded periodic orbits requires global analysis, which, except for a few exceptions, is not available [195].

Note that, physically, the presence of unbounded periodic orbits in the phase plane implies that the energy associated with the corresponding solution trajectories diverge. While, mathematically, this divergence is reflected in the fact that the trace of the Jacobian of the planar system (4.35) is not zero. That is, the energy is not conserved in the present case, thereby contradicting the energy conserving nature of the nonlinearity $\boldsymbol{u} \times \boldsymbol{\omega}$ in Eq. (4.1).

4.3.1.2 Case 2: periodic orbits confined within a heteroclinic cycle

For $b < 0$ and $c > 0$, hence $k_H < 0$, the fixed point (r_3, z_3) exists in a wedge-shaped region $\mu_2 \in (-c\mu_1, \mu_1/b)$ in the parameter space. At the moment of the Hopf bifurcation, besides

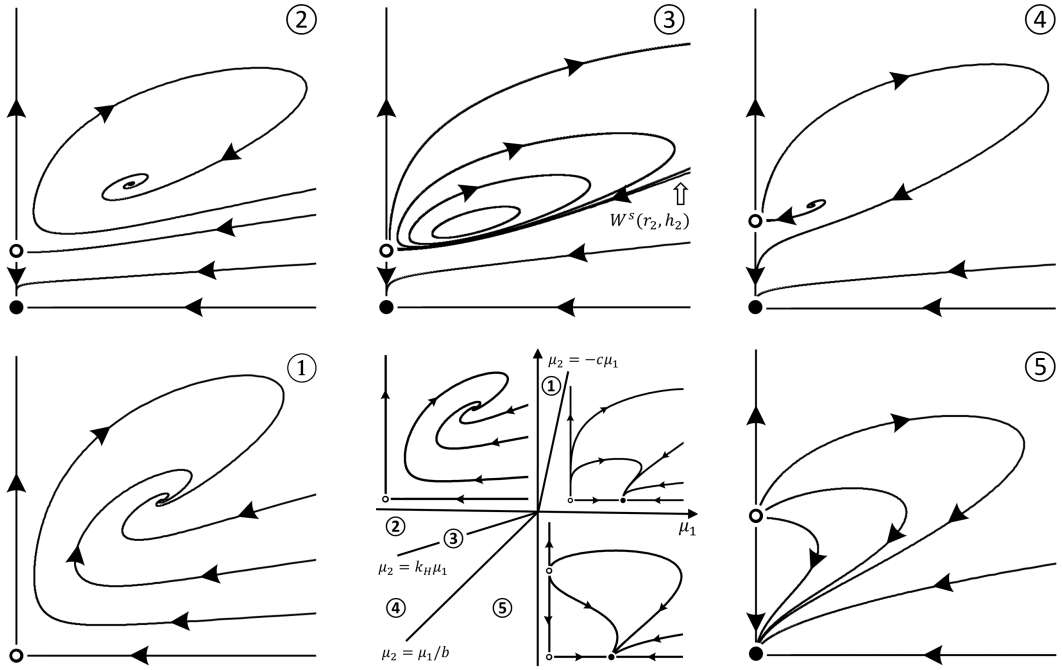

FIGURE 4.4: Unfolding and phase portraits of the planar system (4.35), where $a = -1$, $d = 1$, $b > 1$ and $1- < c < -1/b$, where the periodic orbits emerged at the moment of the Hopf bifurcation are unbounded.

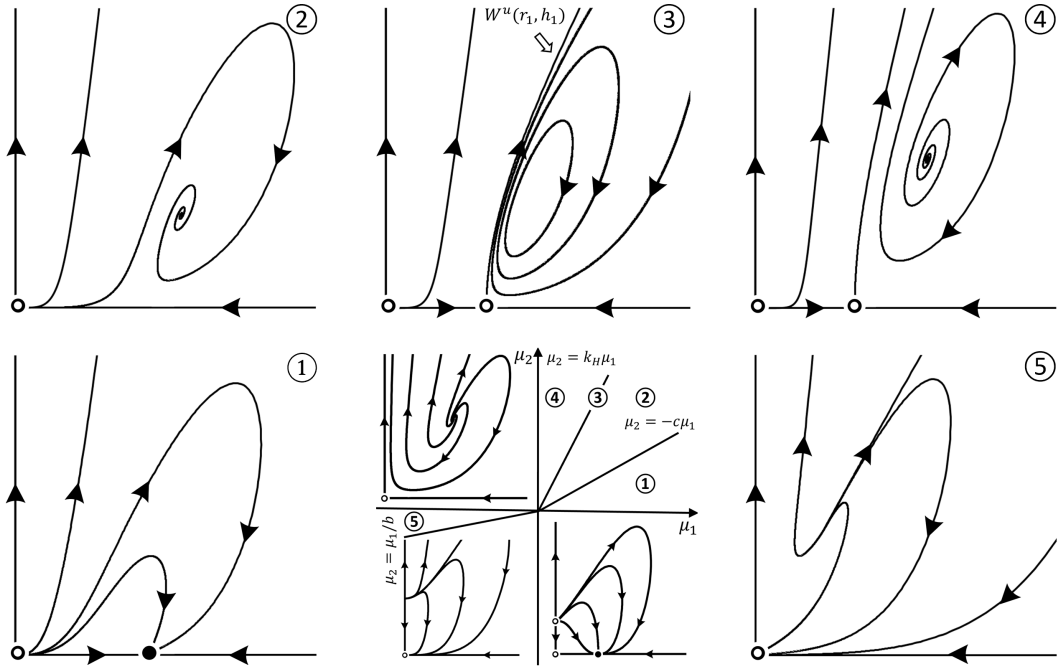

FIGURE 4.5: Unfolding and phase portraits of the planar system (4.35), where $a = -1$, $d = 1$, $-1/c < b < 1$ and $c < -1$, where the periodic orbits emerged at the moment of the Hopf bifurcation are unbounded.

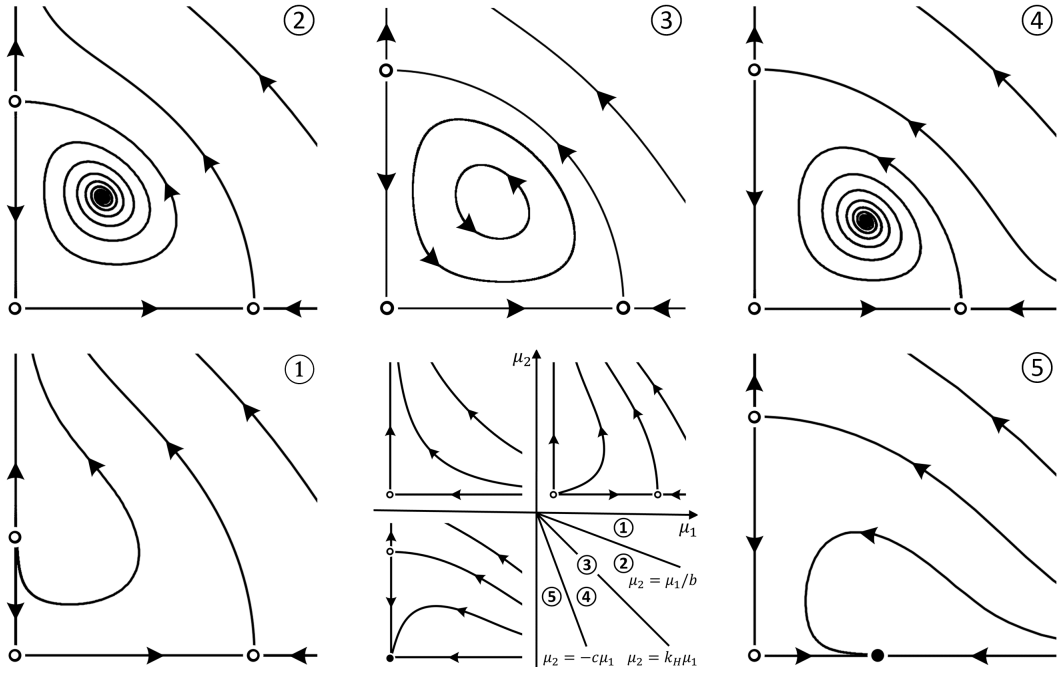

FIGURE 4.6: Unfolding and phase portraits of the planar system (4.35), where $a = -1$, $d = 1$, $b < -1$ and $c > 1$, where the periodic orbits emerged at the moment of the Hopf bifurcation are bounded within the heteroclinic cycle connecting fixed points (r_0, h_0), (r_1, h_1), and (r_2, h_2).

a family of periodic orbits, a heteroclinic cycle connecting saddle points (r_0, z_0), (r_1, z_1), and (r_2, z_2) is born, as shown in figure 4.6. In terms of the dynamical systems, the presence of the heteroclinic cycle can be regarded as a source of complexity. Here, by contrast to the previous cases, the family of periodic orbits are now bounded within the heteroclinic cycle. Note that, as the parameters μ_1 and μ_2 crossing the line $\mu_2 = k_H\mu_1$, the phase portraits as shown in figure 4.6 are not homeomorphic because the phase plane looses the family of period orbits created at the Hopf bifurcation. Since the quantity and the topology of the saddles (r_0, h_0), (r_1, h_1), (r_2, h_2) and the foci (r_3, h_3) remain unchanged, a global bifurcation must occur, perhaps, in the form of a coalescence between the periodic orbits and the heteroclinic cycle.

In order to stabilise the degenerate Hopf bifurcation and to determine the fate of the corresponding heteroclinic cycle, one must restore the truncated fifth-order terms back to the normal form (4.35). Up to a change of the coordinate system, it is possible to add only a single term to Eq. (4.35b), cf. Chapter 7.5 in Guckenheimer and Holmes [130]. However, depending on the preserving and breaking of the reflectional symmetry $z \to -z$

	Symmetry preserving	Symmetry breaking
Invariance preserving	$\gamma_1 h^5, \gamma_2 r^2 h^3, \gamma_3 r^4 h$	$\gamma_4 r h^4, \gamma_5 r^3 h^2$
Invariance breaking	—	$\gamma_6 r^5$

TABLE 4.1: Classification of fifth-order unfolding terms.

and the r-axis invariance

$$\mathrm{d}_t h = 0 \quad \text{as long as} \quad h = 0, \tag{4.46}$$

there are four distinct cases, as categorised in Table 4.1.

Clearly, it is not trivial to choose which individual fifth-order terms and their linear combination to be restored. Among homogeneous terms, the term $\gamma_1 h^5$ can introduce a pair of stable fixed points $(r_4, \pm h_4)$ on the h-axis for suitable values of γ_1 and μ_2, signifying a coexistence of the heteroclinic cycle and the coherent mode representing, phenomenologically, the velocity streaks. As long as the r-axis invariance of the system is preserved, trajectories initiated in the positive half (resp. negative half) of the phase space are restricted in the corresponding half-plane. Hence, the monotonic symmetry breaking terms $\gamma_4 r h^4$ and $\gamma_5 r^3 h^2$ can lead to no new fixed point nor new bifurcation phenomenon. For $\gamma_6 \neq 0$, both the reflectional symmetry and the r-axis invariance are simultaneously broken, hence the generation of helicity in an initially helicity-free flow is then possible. However, remembering $r \geq 0$, the crossing of $h = 0$ is one-way as long as the circular symmetry is preserved, with the crossing direction determined by the sign of γ_6.

In the following, we limit ourselves to the inclusion of a single fifth-order homogeneous term $\gamma_1 h^5$, where $\gamma_1 \neq 0$. Consequently, Eqs. (4.35) become:

$$\mathrm{d}r = r\left(\mu_1 - r^2 + bz^2\right), \tag{4.47a}$$

$$\mathrm{d}h = h\left(\mu_2 + cr^2 + z^2\right) + \gamma_1 h^5. \tag{4.47b}$$

In order to study the possible global bifurcation occurring in the vicinity of the Hopf bifurcation line: $\mu_2 = k_H \mu_1$, one considers the following replacement for the bifurcation parameters:

$$\mu_1 = Re^{-1}\tilde{\mu}_1, \quad \mu_2 = Re^{-1} k_H \tilde{\mu}_1 + Re^{-2}\tilde{\mu}_2, \tag{4.48}$$

in additional to a rescaling of the state variables and the time by a dissipative coefficient $Re \gg 1$ [3]:

$$r = Re^{-1/2}\tilde{r}, \quad h = Re^{-1/2}\tilde{h}, \quad t = Re\tilde{t}. \tag{4.49}$$

Substituting the preceding scaling relations into Eqs. (4.47) and dropping the tilde, Eqs. (4.47) become:

$$\mathrm{d}_t r = r\left(\mu_1 - r^2 + bh^2\right), \tag{4.50a}$$

$$\mathrm{d}_t h = h\left(k_H\mu_1 + cr^2 + h^2\right) + Re^{-1}h\left(\mu_2 + \gamma_1 h^4\right). \tag{4.50b}$$

Inspired by the energy conservation of the inviscid fluid dynamics, the coefficients b and c are determined by requiring that the planar system (4.50) is conservative in the limit $Re \to \infty$. More specifically, this requirement is achieved by solving

$$\begin{aligned} \text{trace} &= \partial_r\left[r\left(\mu_1 - r^2 + bh^2\right)\right] + \partial_h\left[h\left(k_H\mu_1 + cr^2 + h^2\right)\right] \\ &= \mu_1 - 3r^2 + bh^2 + k_H\mu_1 + cr^2 + 3h^2 \\ &= 0, \end{aligned} \tag{4.51}$$

hence the coefficients are given by

$$b = -3, \quad c = 3, \quad k_H = -1. \tag{4.52}$$

Substituting (4.52) back into (4.50) leads to an autonomous system with two degrees of freedom but four parameters, i.e. μ_1, μ_2, Re, and γ_1. Note that, $\mu_1 > 0$ when the Hopf bifurcation occurs, it can be eliminated by considering the following rescaling

$$r = \sqrt{\mu_1}\tilde{r}, \quad h = \sqrt{\mu_1}\tilde{h}, \quad t = \tilde{t}/\mu_1, \quad Re = \mu_1\tilde{Re}, \quad \mu_2 = \mu_1^2\tilde{\mu}, \quad \gamma_1 = \tilde{\gamma}. \tag{4.53}$$

Finally, substituting the coefficients (4.52) and the scaling relations 4.53 into Eqs. (4.50), and dropping the tilde denoting the rescaled variables, the planar system considered in this section becomes

$$\begin{bmatrix} \mathrm{d}_t r \\ \mathrm{d}_t h \end{bmatrix} = \begin{bmatrix} r\left(+1 - r^2 - 3h^2\right) \\ h\left(-1 + 3r^2 + h^2\right) \end{bmatrix} + Re^{-1}\begin{bmatrix} 0 \\ h\left(\mu + \gamma h^4\right) \end{bmatrix}. \tag{4.54}$$

[3] Depending on the applications, Re can be interpreted as the (reduced) Reynolds number, the square root of the Taylor number, or the inverse of the Ekman number. That is, the Re dependence here is best regarded as a trend rather than the precise value of Reynolds number at with a particular bifurcation takes place.

For $\gamma < 0$, the inclusion of the fifth-order term introduces a pair of symmetric conjugate stable fixed points

$$(r_4, \pm h_4) = (0, \pm\sqrt{-Re/\gamma_1}) + O(Re^{-1}), \tag{4.55}$$

such that the kinetic energy associated with these solutions increases linearly with Re. With a proper rescaling of Re, the presence of the pair of symmetry conjugate fixed points (r_4, h_4) may provide an understanding for the generation of high-energy velocity streaks from low-energy counter-rotating vortices.

4.3.2 Heteroclinic tangency in the phase plane

Note that, in the limit $Re \to \infty$, the planar system (4.54) is Hamiltonian, with the Hamiltonian function

$$H(r, h) = rh(1 - r^2 - h^2), \tag{4.56}$$

such that the planar system (4.54) can be expressed as

$$\begin{bmatrix} \mathrm{d}_t r \\ \mathrm{d}_t h \end{bmatrix} = \begin{bmatrix} +\partial_h H \\ -\partial_r H \end{bmatrix} + Re^{-1} \begin{bmatrix} 0 \\ h\,(\mu + \gamma h^4) \end{bmatrix}. \tag{4.57}$$

Since $H(r, h)$ does not explicitly depend on time, using the chain rule, the time derivative of the Hamiltonian function is

$$\mathrm{d}_t H(r, h) = \frac{\partial H}{\partial r}\frac{\mathrm{d}r}{\mathrm{d}t} + \frac{\partial H}{\partial h}\frac{\mathrm{d}h}{\mathrm{d}t} = 0. \tag{4.58}$$

That is, $H(r, h)$ is conserved along the solution trajectory and, in a rough sense, it can be referred to as the energy of the system (4.57).

The level curves of the Hamiltonian function, denoted by

$$\Gamma_K : \quad H(r, h) = K \tag{4.59}$$

are shown in figure 4.7(a). As evident from the figure, there exists a continuous family of periodic orbits encircling the centre (r_3, h_3). As the value of K decreases, the amplitude of periodic orbits increases. Until at $K = 0$, the periodic orbit born at the Hopf bifurcation disappears when it simultaneously collides with the saddles (r_0, h_0), (r_1, h_1), and (r_2, h_2), forming a heteroclinic cycle Γ_0. The heteroclinic cycle separates the planar phase space

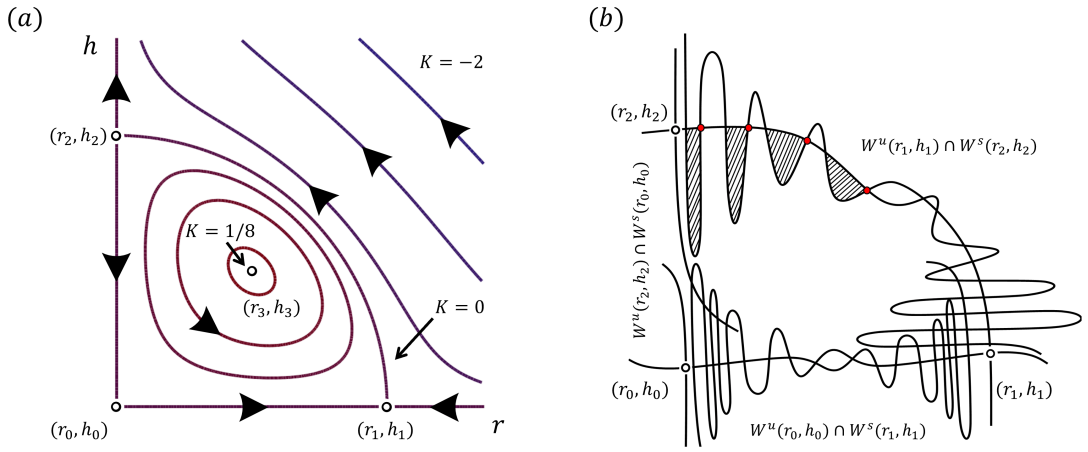

FIGURE 4.7: (a) The unperturbed level curves of the Hamiltonian energy function $\Gamma_K : H(r,h) = K$, where the red colour indicates higher values of K and the blue colour indicates the opposite; and (b) the qualitative structure of the perturbed Hamiltonian system by an axis asymmetric forcing, where the intersections between the stable and unstable manifolds $W^u(r_0,h_0) \cap W^s(r_1,h_1)$, $W^u(r_1,h_1) \cap W^s(r_2,h_2)$ and $W^s(r_0,h_0) \cap W^u(r_2,h_2)$ are nonempty and transversal. There exists a operation M mapping $s \in W^u(r_0,h_0) \cap W^s(r_1,h_1)$ to $M(s) \in W^u(r_0,h_0) \cap W^s(r_1,h_1)$. Repeating the operation reveals a countable infinity of periodic points (indicated with red) intersecting both the stable and the unstable manifolds. The lobes (shaded region) are successively stretched and folded, terminating in an accumulation of a fractal series of lobes near the fixed points.

into two regions. For trajectories initiated outside Γ_0, the velocity spontaneously aligns with the axis of rotation and increases in amplitude, reminiscent of streaks. While the region inside Γ_0 is filled with a family of periodic orbits with periods varying continuously with the energy level K. At the heteroclinic cycle Γ_0, the associated period diverges. Note that, the flow within the cycle Γ_0 exhibits a competitive coexistence. That is, a single solution trajectory visits sequentially the fixed points representing the base flow (r_0,h_0), the coherent mode (r_2,h_2), and the incoherent mode (r_1,h_1), reminiscent of the Lotka-Volterra predator-prey model [196, 197].

Note that, the configuration involving a continuum of periodic orbits as we see in figure 4.7(a) is structurally unstable in the sense that it cannot survive under arbitrarily small perturbations. The addition of the axis-symmetric fifth-order term γh^5 stabilises the Hamiltonian system by replacing the continuum of concentric periodic orbits by a single limit cycle. On the other hand, if the perturbation is axis-asymmetric, the heteroclinic cycle may split into transversely intersecting stable and unstable manifolds, as shown in figure 4.7(b). These transversely intersecting orbits inevitably lead to the heteroclinic tangle with no defined destination, which is now a well-known source of chaotic

behaviours.

In order to determine the occurrence of the heteroclinic cycle in the parameter space, the Melnikov method is considered in the following. According to Theorem 4.5.4 in Guckenheimer and Holmes [130], the heteroclinic tangency occurs as long as the Melnikov function $M(\mu)$ vanishes. Since the system (4.57) is Hamiltonian in the limit $Re \to \infty$ and since the dissipative term does not explicitly depend on time for finite Re, the Melnikov function is defined as (cf. Eq. 4.5.15 in Guckenheimer and Holmes [130])

$$\begin{aligned} M(\mu) &= \iint_{\Gamma_0} \text{trace} \begin{bmatrix} 0, & 0 \\ 0, & \partial_h \left[h \left(\mu + \gamma h^4 \right) \right] \end{bmatrix} \mathrm{d}r\mathrm{d}h \\ &= \iint_{\Gamma_0} (\mu + 5\gamma_1 h^4) \mathrm{d}r\mathrm{d}h, \end{aligned} \tag{4.60}$$

where the integral is conducted along the heteroclinic circle:

$$\Gamma_0 : \quad r^2 + h^2 = 1 \quad \text{for} \quad r \geqslant 0, \quad h \geqslant 0. \tag{4.61}$$

The integral can be conveniently evaluated by introducing the polar coordinates

$$r = u \sin(\theta) \quad \text{and} \quad h = u \cos(\theta), \tag{4.62}$$

and substitution gives

$$M(\mu) = \int_{\pi/2}^{0} \int_{0}^{1} (\mu + 5\gamma u^4 \cos^4(\theta)) u \mathrm{d}u \mathrm{d}\theta = -\frac{\pi}{4} \left(\frac{5}{8}\gamma + \mu \right). \tag{4.63}$$

As such, the bifurcation curve for the heteroclinic cycle is obtained by solving $M(\mu) = 0$, yielding

$$\mu = -\frac{5}{8}\gamma. \tag{4.64}$$

Note that the Melnikov function computed here is time-independent. Hence, by contrast to the conventional application of the Melnikov theory, wherein the isolated zeros of the Melnikov functions $M(t_0) = 0$ predicts the point-wise tangency of stable and unstable manifolds at some time t_0. Here, however, $M(\mu_0) = 0$ implies a full overlapping of the stable and unstable manifolds at $\mu = \mu_0$. Therefore, unlike figure4.7(b), the heteroclinic cycle obtained in this section has no lobe, no tangle, hence no chaos, and it is therefore referred to as the heteroclinic tangency.

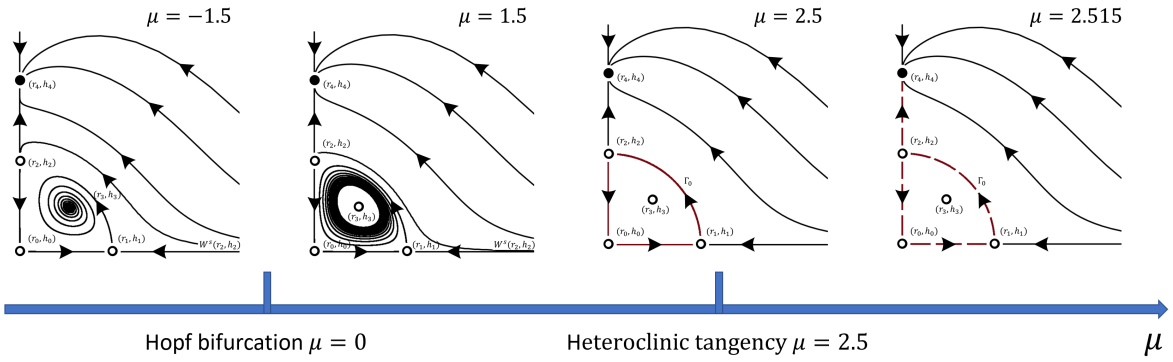

FIGURE 4.8: Phase portraits near the Hopf bifurcation, where for $\gamma = -4$, the Hopf bifurcation takes place at $\mu = 0$ and the heteroclinic tangency occurs at $\mu = 2.5$. For $\mu > 2.5$, the heteroclinic cycle is broken, as visualised by the dashed line. In this case, all solution trajectories eventually converge towards the stable fixed point (r_4, h_4),

Applying the perturbation theory, it can be verified that the fixed point (r_2, h_2) is now located at

$$(r_2, h_2) = (0, 1 - \frac{3\gamma_1}{16} Re^{-1}) + O(Re^{-2}), \tag{4.65}$$

hence the stability of the heteroclinic cycle is determined by considering the saddle quantity [198]

$$\sum_{i=0}^{2} \mathrm{tr}(\boldsymbol{J})|_{(r_i,h_i)} = \frac{25\gamma_1}{8} Re^{-1} + O(Re^{-2}). \tag{4.66}$$

Thus, the heteroclinic cycle Γ_0 is internally stable (resp. unstable) if $\gamma < 0$ (resp. $\gamma > 0$). The stability of the Hopf bifurcation is determined by evaluating the divergence of the right-hand side of Eq. (4.54) on the Hopf bifurcation line: $\mu_2 = 0$. It can be verified that the Hopf bifurcation is supercritical (resp. subcritical) if $\gamma < 0$ (resp. $\gamma > 0$). To this end, the bifurcation analysis suggests that the emergence of complexity (i.e., the heteroclinic cycle) in the phase space and its stability are independent of Re, as long as Re is sufficiently large.

Without loss of generality, γ are chosen to be:

$$\gamma = -4, \tag{4.67}$$

such that the heteroclinic bifurcation occurs at

$$\mu = 2.5. \tag{4.68}$$

Figure 4.8 completes the phase portraits in the vicinity of the Hopf bifurcation. For

$\mu < 0$, the first quadrant of the phase plane has five fixed points, wherein (r_3, h_3) and the new fixed point (r_4, h_4) introduced by the addition of the fifth-order dissipative term are attracting, while fixed points (r_0, h_0), (r_1, h_1), and (r_2, h_2) are of the saddle type. Here, stable manifold of (r_2, h_2), denoted here by $W^s(r_2, h_2)$ divides the phase plane into two basins of attraction, signifying a bi-stability. Solution trajectories initiated below $W^s(r_2, h_2)$ will spiral in to (r_3, h_3); otherwise, they converge towards the streak mode (r_4, h_4). As μ crosses $\mu = 0$ increasing, (r_3, h_3) loses stability at the Hopf bifurcation, giving rise to a stable limit cycle as visualised by the dense orbits in figure 4.8. The limit cycle increases in size as μ increases. At the moment $\mu = 2.5$, the limit cycle overlaps with the heteroclinic cycle Γ_0, signalling the heteroclinic tangency. For $\mu > 2.5$, the limit cycle created at the Hopf bifurcation is destroyed, remaining a single stable steady solution (r_4, h_4) in the first quadrant of the phase plane. However, just beyond $\mu = 2.5$, solution trajectories can circulating on the ghost of Γ_0 for a long time before eventually settling down at (r_4, h_4), resulting in a long transient.

4.3.3 Non-chaotic transient

In order to investigate the distribution of solution trajectories in the phase plane, the evolution of trajectories initiated from a pair of symmetric conjugate initial conditions $(r(0), \pm h(0))$ inside Γ_0 are tracked for a long time. At each time step, the angle variable θ is recorded, cf. Eq. (4.62). The probability density function for $\cos(\theta)$ is plotted in figure 4.9. Since θ is the angle between the velocity vector and the axis of the rotation, following Rogers and Moin [122], $\cos(\theta)$ may be referred to as the relative helicity density measuring the coherence of the flow. In all cases, the probability density function distributes symmetrically about $\cos(\theta)$, compatible with the reflectional symmetry imposed onto the normal form of the planar system, cf. Eq. (4.30). Starting with asymmetric initial conditions and if the simulation time is sufficiently long, the probability density of $\cos\theta$ eventually evolves into a distribution resembling figure 4.9, and therefore is omitted here.

In between the Hopf bifurcation and the heteroclinic tangency, i.e. $0 < \mu_2 < 2.5$, the probability distribution is separated into two disconnected pieces distinguished by weak peaks at $\cos\theta = \pm 0.24$. This observation reflects the presence of a pair of conjugate limit cycles in the first and fourth quadrants of the phase plane. At the moment of the heteroclinic tangency $\mu = 2.5$, the probability density function is characterised by the

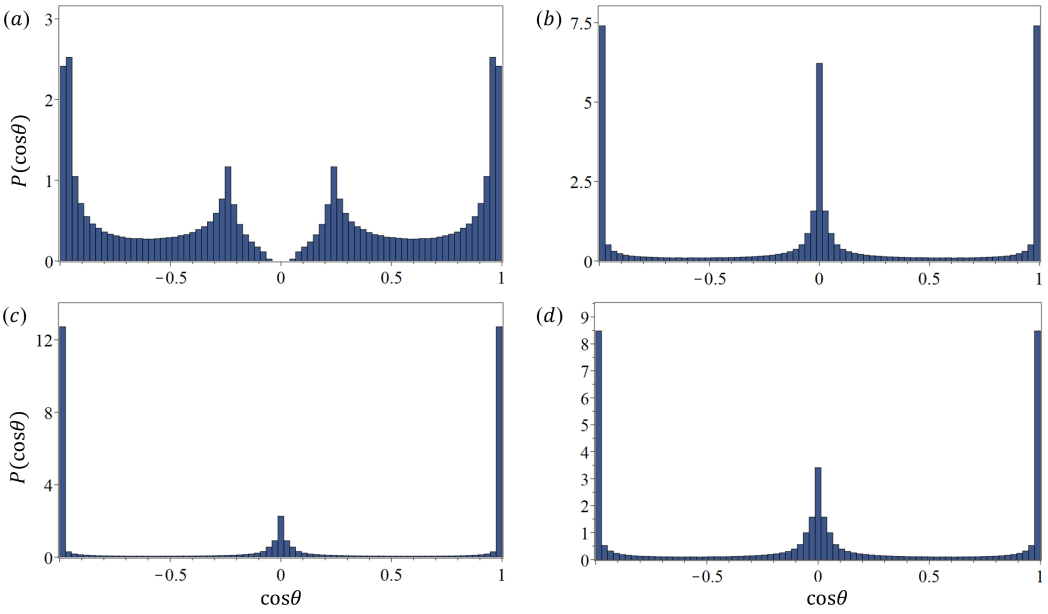

FIGURE 4.9: Probability density function $P(\cos\theta)$ of the relative helicity density $\cos\theta$: (a) before the heteroclinic tangency with $\mu = 1.75$ and $Re = 1000$; (b) at the moment of the heteroclinic tangency with $\mu = 2.5$ and $Re = 1000$; (c) slightly past the heteroclinic tangency with $\mu = 2.515$ and $Re = 1000$; and (d) the same as in (c) except for $Re = 2000$. Notice the different scales in each panel and the maximal integration time is limited to $t_{max} = 4500$ dimensionless units in the simulation.

simultaneous appearance of three sharp peaks located at $\cos\theta = \pm 1$ and $\cos\theta = 0$, signifying the exact competitive coexistence. A solution trajectory sequentially visits (r_0, h_0), (r_1, h_1), and (r_2, h_2), trapped by each saddle point for a long time before rapidly moving towards the next one. The simultaneous appearance of three peaks in the probability density function of the relative helicity density was reported in a direct numerical simulation for Taylor-Green vortex flow [199]. Note that, for μ being slightly above the heteroclinic tangency, the peak at $\cos\theta = 0$ remains albeit with decreased intensity. Since after the heteroclinic tangency, there remains only a pair of stable fixed point $(r_4, \pm h_4)$ located on the h-axis, i.e. with $\cos(\theta) = \pm 1$. The presence of a peak at $\cos(\theta) = 0$ implies that the solution trajectory does not immediately converge towards (r_4, h_4), but travelling on the ghost of the heteroclinic cycle Γ_0 for a long time. Figure 4.9 (d) reveals that, with increasing Re, the peak at $\cos(\theta)$ increases in amplitude, signifying an increase of transient lifetime with Re.

Figure 4.10 (a) and (b) compares the transient lifetime for two different Reynolds number $Re = 1000$ and $Re = 2000$ slightly passing the heteroclinic tangency, where the state variable r is plotted as a function of time. In both cases, the solution trajectories follow periodic motions with small modulations in amplitudes before suddenly collapsing to

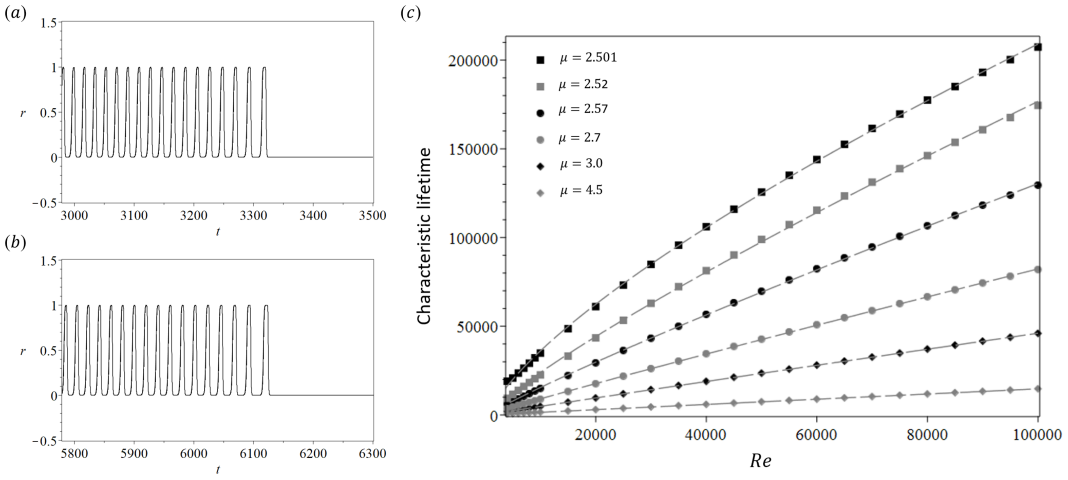

FIGURE 4.10: Non-chaotic transient observed slightly passing the heteroclinic tangency $\mu = 2.515$. (a) For $Re = 1000$, the solution trajectory collapse at $t \approx 3386$; and (b) for $Re = 2000$, the collapse occurs at $t \approx 6274$. (c) transient lifetime plotted as a function of μ and Re.

$r = 0$. The collapse is because the stable limit cycle is destroyed via the heteroclinic bifurcation, leaving a single stable fixed point (r_4, h_4) in the upper phase plane. Figure 4.10 (c) records the lifetime of the transient for given values of Re and $\mu > 2.5$. It is seen that the transient lifetime increases almost linearly with Re, while it decreases with increasing μ. However, due to the limit of the computational power, it is not clear if the transient lifetime will converge to an asymptote in the infinite limit of $Re \to \infty$.

Since the angular variable φ is decoupled from the planar system (4.54), the phase space is essentially two-dimensional until the rotational symmetry is destroyed. According to the Poincaré-Bendixson theorem, there is no chaos in two dimensions such that the transient observed in figure 4.10 must be non-chaotic.

On the other hand, if the perturbation is not axisymmetry, chaos likely occur. Note that, the heteroclinic cycle Γ_0 connecting adjacent saddles (r_0, h_0), (r_1, h_1), and (r_2, h_2) is structurally unstable in the sense that there exists an arbitrarily small non-axisymmetric perturbation that splits it into transversely intersecting two-manifolds as shown in figure 4.7(b). The existence of transverse intersections implies, by the Smale-Birkhoff theorem, that there exists a chaotic invariant set Λ, the famous Smale horseshoe, in the neighbourhood of each intersection. This set consists of a countable infinity of periodic orbits, an uncountable set of aperiodic orbits, and a dense aperiodic orbit, terminating at each intersection. All orbits are of saddle type, namely possess stable and unstable manifolds, and are dense in Λ. These unstable orbits continuously repel any trajectories passing

near Λ, and consequently the trajectories are chaotic because they must diverge endlessly away from all periodic orbits yet remain bounded for a presumably long time. As a corollary, trajectories with arbitrarily close initial conditions eventually diverge, rendering the long-term prediction impossible. Therefore, subsequent to the appearance of Λ, chaos must be present. Since the heteroclinic transversality persists under perturbations, Λ is structurally stable, and it follows that the chaos originated from Λ prevails for a wide range of parameter conditions. However, as emphasised by Kaplan and Yorke [200] and Yorke and Yorke [201], the chaos associated with the system possessing a heteroclinic cycle is not attracting, replacing the non-chaotic transient observed in figure 4.10 by a long chaotic transient.

4.4 Bifurcation analysis for flows with broken rotational symmetry

Although both the Coriolis force $2\boldsymbol{u}\times\boldsymbol{\Omega}$ and the Lamb vector $\boldsymbol{u}\times\boldsymbol{\omega}$ are skew-symmetric, the rotational symmetry is broken as long as the axes of $\boldsymbol{\Omega}$ and $\boldsymbol{\omega}$ are not aligned or anti-aligned. In order to investigate the effect of the broken rotational symmetry on the route to chaos, let us restore the decoupled rotational variable φ and consider the inclusion of a symmetry breaking fifth-order term [4]

$$-kh^4\begin{bmatrix} r\sin(2\varphi) \\ 0 \\ \cos(2\varphi) \end{bmatrix}, \tag{4.70}$$

[4]It was pointed out by Prof. B. Eckhardt after this work that the fifth-order symmetry-breaking term (4.70) is topologically equivalent to

$$-kh^{2N}\begin{bmatrix} r\sin(2\varphi) \\ 0 \\ \cos(2\varphi) \end{bmatrix}, \quad \text{for} \quad N=1,2,3..., \tag{4.69}$$

and, for the problem of fluid dynamics, a better option would be $N=1$. A numerical investigation reveals that, for the cases $N=1$ and $N=2$, the qualitatively features of the bifurcation scenarios remain unchanged. Therefore, only results for $n=2$ are present in the following.

where k measures the strength of the symmetry breaking nonlinearity. That is, the planar system (4.54) becomes

$$\begin{bmatrix} \mathrm{d}_t r \\ \mathrm{d}_t h \\ \mathrm{d}_t \varphi \end{bmatrix} = \begin{bmatrix} r\left(+1 - r^2 - 3h^2\right) \\ h\left(-1 + 3r^2 + h^2\right) \\ \Omega \end{bmatrix} + Re^{-1} \begin{bmatrix} 0 \\ h\left(\mu_2 - 4h^4\right) \\ 0 \end{bmatrix} - kh^4 \begin{bmatrix} r\sin(2\varphi) \\ 0 \\ \cos(2\varphi) \end{bmatrix}. \tag{4.71}$$

Note that, in nonlinear oscillators, the frequency of the oscillator, here the angular velocity Ω associated with the rigid rotation of the counter-rotating vortices, depends on the amplitude the motion [202]. Consequently, in general, it is expected that Ω varies as the control parameter of the system, here Re, changes. On this account, the following functional dependence between Ω and Re is assumed [5]:

$$\Omega = 0.1\sqrt{Re}. \tag{4.72}$$

The selection is based on an order of magnitude consideration that when $Re = 1000$, the angular velocity is of order of unity.

In three dimensions, while the fixed points on the invariant h-axis, i.e. (r_0, h_0), (r_2, h_2), and (r_4, h_4) remain fixed points, those off the h-axis, i.e. (r_1, h_1) and (r_3, h_3), correspond to limit cycles in three dimensions. Consequently, the limit cycle bifurcating from (r_3, h_3) translates into an invariant two-torus of the same stability type. The emerging bifurcation is known as the Neimark-Sacker bifurcation of periodic orbits. Analogous to the Hopf bifurcation, the Neimark-Sacker bifurcation can be either supercritical or subcritical, giving rise to a stable or an unstable torus as the parameter passes through the bifurcation curve. Since the dimensionality of the invariant torus is smaller than the dimension of the phase space, the invariant torus is unlikely to be observed unless itself is attracting. Similar to the previous case, γ is taken to be $\gamma = -4$ fixed.

4.4.1 Quasiperiodicity and circle map

For $k = 0$ and independent of values of Re, the system admits a pair of stable reflectional symmetric two-tori within the parameter range $\mu \in [0.2.5]$, as shown in figure 4.11. The torus grows in size as μ increases. At the moment $\mu = 2.5$, the torus overlaps with the

[5] Note that a different relation can be selected, for instance a linear relation. The selection affects the precise value at which particular bifurcation scenario takes place and the lifetime of the transient dynamics, but it does not affect the bifurcation scenarios.

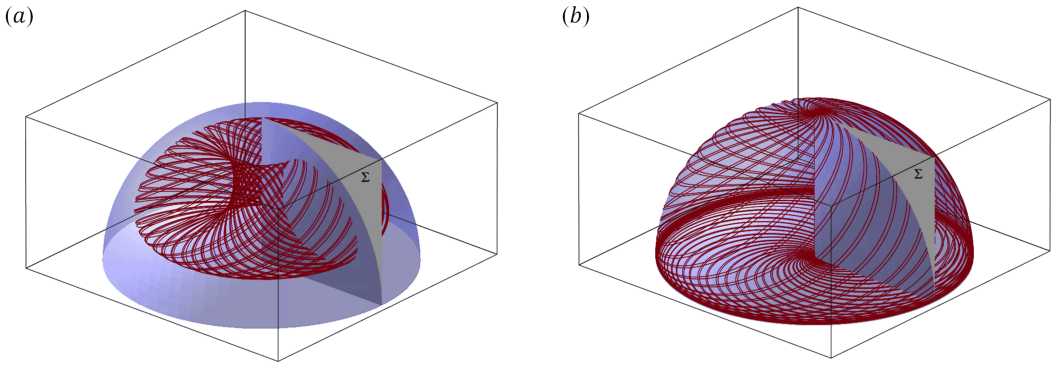

FIGURE 4.11: Invariant two-torus embedded in the three-dimensional phase space: (a) before the heteroclinic tangency with $\mu < 2.5$, where the invariant two-torus signifies the quasiperiodicity and the hemisphere spanned by Γ_0 implies the basin of attraction of the torus; and (b) at the moment of the heteroclinic tangency with $\mu = 2.5$, the invariant torus grows in size and overlaps with Γ_0, filling the hemisphere with heteroclinic orbits.

hemisphere spanned by the heteroclinic cycle Γ_0, depicting a heteroclinic tangency in three dimensions, see figure 4.11 (b). For $\mu > 2.5$, the torus is destroyed through the heteroclinic bifurcation, such that trajectories move off of the surface of the tori, exhibiting three-dimensional dynamics, involving chaos. The precise details of torus breakdown: how it interacts with nearby periodic orbits, loses its differentiability, and is destroyed remain to a great extent obscure [130, 203].

Note that, the flow on the torus is doubly periodic, with the natural oscillation frequency Ω inherent from the rigidly rotating vortices and with a modulation Ω_1 arising from the Neimark-Sacker bifurcation. Consequently, the motions on the torus can be characterised by the ratio between those two frequencies, defined here as the rotational number

$$Ro = \Omega_1/\Omega \quad \text{modulo} \quad 1, \tag{4.73}$$

where the modulo operator retains only the fractional part of the ratio. For Ro being irrational, the torus is filled in by aperiodic orbits, while it locks onto a periodic orbit provided that Ro is rational. The former is referred to as the quasiperiodicity because the flow is characterised by two incommensurable fundamental frequencies Ω_0 and Ω_1, and their linear combinations. The later is referred to as the phase locking because the rational value of Ro is preserved over a finite region of parameters.

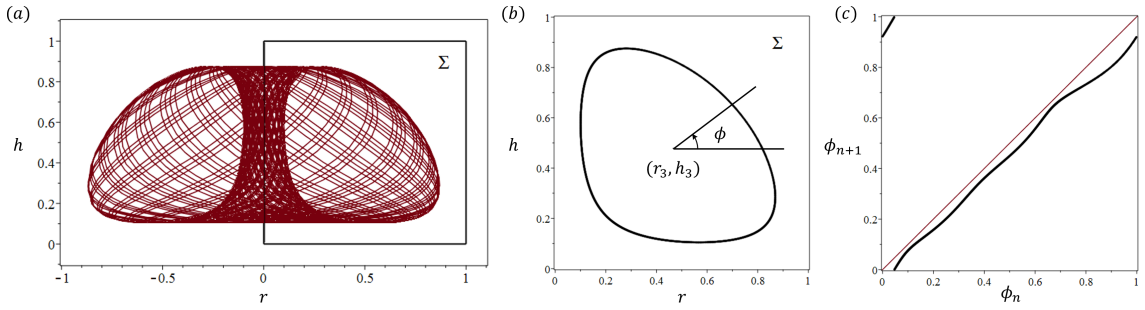

FIGURE 4.12: Poincaré section (b) for phase space motion on a invariance two-torus (a). In (c), the angle variable ϕ_{n+1} is plotted as a function of ϕ_n.

Note that, the trace of torus on the Poincaré section Σ is homeomorphic to a unit circle, see figure 4.12. Following Hilborn [202], let us introduce an angle variable ϕ_n defined as

$$\phi_n = \frac{1}{2\pi}\left[\arctan\left(\frac{h_n - h_3}{r_n - r_3}\right) + \frac{\pi}{2}\text{sign}(r_n - r_3)\right] + \frac{1}{2}, \tag{4.74}$$

measuring the location of trajectories on the circle as they piercing through the Poincaré section, then the motions on the torus can be reduced to the following iterated circle map:

$$\phi_{n+1} = f(\phi_n; k, Re, \mu), \tag{4.75}$$

for points on Σ. By this convention, the phase angle ϕ_n is modulo by 1. That is, $\phi_n = 1$ corresponds to a complete revolution around the closed curve in Σ. Consequently, the rotational number introduced in Eq. (4.73) can be evaluated numerically by considering the following limit

$$Ro = \lim_{N\to\infty} \frac{1}{N}\sum_{n=1}^{N}(\phi_{n+1} - \phi_n), \tag{4.76}$$

where the limit is taken so as to allow transients, as in [202].

In figure 4.12 (c), the circle map (4.75) is constructed numerically by plotting ϕ_{n+1} as a function of ϕ_n. The constructed map resembles the Arnold's sine circle map under criticality, namely it is one-dimensional and invertible. In the absence of nonlinear coupling $k = 0$, two segments are almost parallel to the first bisectrix $\phi_{n+1} = \phi_n$, indicated in figure 4.12 (c) as the red diagonal line. Starting from an arbitrary initial condition, numerical iteration reveals an infinite hopping between the first bisectrix and the circle map, compatible with the quasiperiodic motions on the surface of the torus. Consequently, one may expect to observe similar bifurcation scenarios as k is increased from zero: the system possesses a non-zero measure of phase locking regions, the so-called Arnold tongues, for

$k \neq 0$, which increase in size as the nonlinear coupling k increases. For a given value of k, these phase locking regions occur at the Farey fractions and are organised in the form of the devil's staircases as the control parameter is increased, cf, e.g. figure 1 in [204]. However, as we shall see in the following two subsections, the sine circle does not provide a complete description for the rich dynamics observed here. The bifurcation scenarios within a single phase locking region is tracked numerically in §4.4.2, wherein a Neimark-Sacker bifurcation of torus knots, a period doubling, and a global bifurcations involving torus breakdown are observed. The general bifurcation scenarios are studied in §4.4.3, wherein a peculiar devil's staircases with unusual ordering sequence are uncovered.

4.4.2 Phase locking and torus bifurcation

Note that, the circle map (4.75) involves three control variables k, Re, and μ_2. To begin with, let us keep $k = 0.15$ and $Re = 150$ fixed, and let μ_2 vary. Figure 4.13 displays three numerical integrals for $\mu = 1.8$, $\mu = 1.9$, and $\mu = 2.0$, wherein the first 5000 iterations are discarded so as to eliminate the transient behaviours. In all cases, the rotational number has been calculated using Eq. (4.76), yielding

$$Ro \approx \frac{2}{3}, \tag{4.77}$$

Eq. (4.77) implies that the system is in the phase locking region over the range of parameters under consideration. For $\mu = 1.8$, the phase space has a period one $(2, 3)$ torus knot, as evidenced by the presence of three stable fixed points on the Poincaré section and in the circle map. For $\mu = 1.9$, a period doubling bifurcation is detected: the period one $(2, 3)$ torus knot loses stability as the parameter μ is increased, giving rise to a period two torus knot with the same rotational number in the phase space. As μ is further increased to $\mu = 2.0$, the torus knot is dense and the corresponding circle map loses invertibility, as shown in figure 4.13 (c). That is, there are multiple values of ϕ_n for each values of ϕ_{n+1}. This lack of invertibility is associated with a folding of the solution trajectories, which, in turn, may lead to the chaotic behaviours, cf. Chapter 6 in [202]. However, a closer look at the Poincaré section reveals a spiral in to the period two fixed points. Finally, a drastic increase in simulation time reveals that the asymptotic behaviour for the case $\mu = 2.0$ is periodic, masked by a long transient.

Note that, for $\mu = 2.0$, the period two fixed points on the Poincaré section have imaginary eigenvalues, which may undergo a supercritical Hopf bifurcation, leading to a pair of

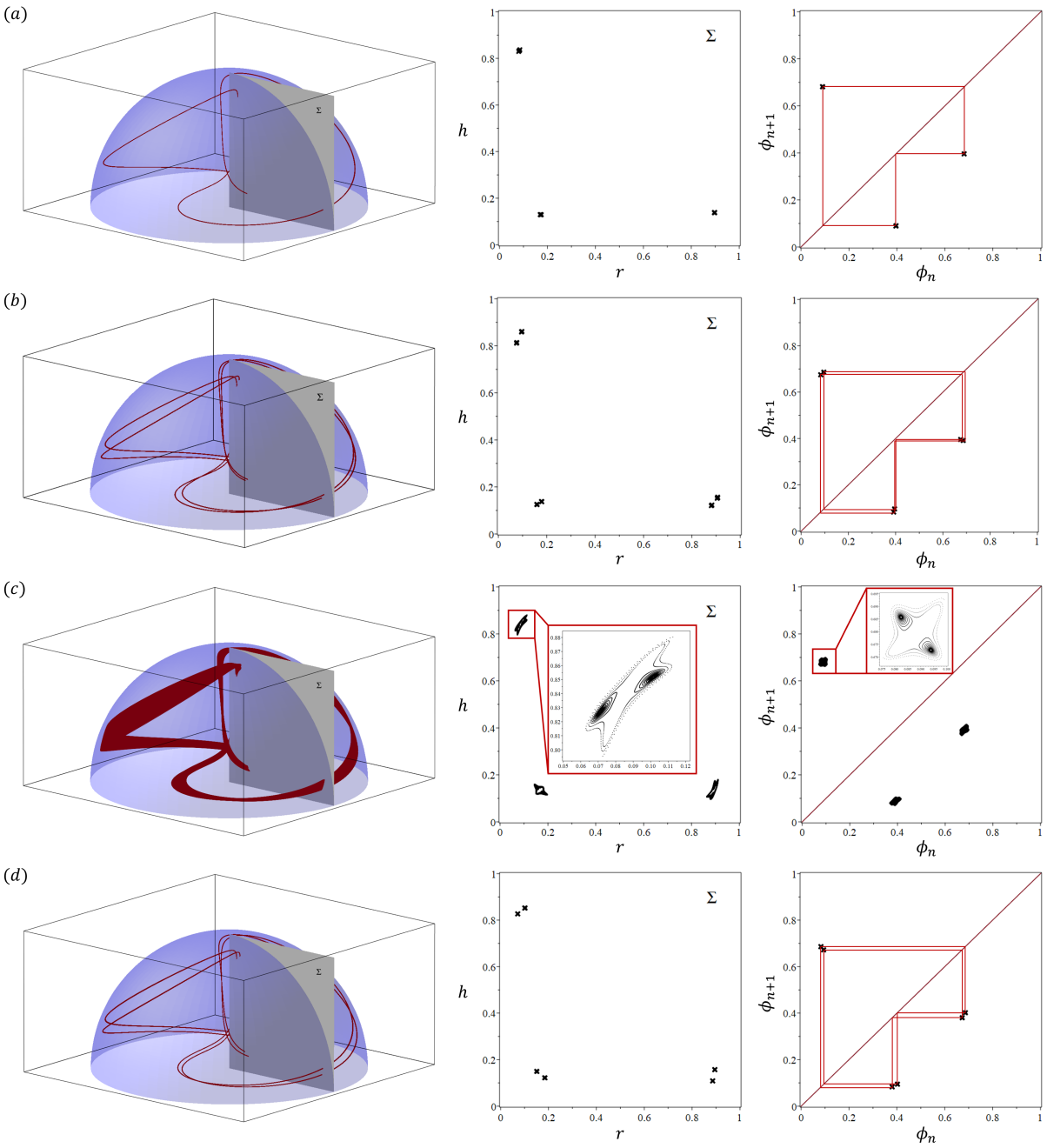

FIGURE 4.13: Phase locking and period doubling. (*a*) $\mu = 1.8$; (*b*) $\mu = 1.9$; and (*c*) $\mu = 2.0$, where the integration time is from $t \in [5000, 50000]$ dimensionless units. (*d*) Same as *c* but with the integration time window chosen to be $t \in [50000, 75000]$. From left to right: the three-dimensional phase space revealing a periodic torus knot, the corresponding Poincaré section and the circle map.

period two limits cycles on Σ. Moreover, as it is seen in the insets of figure 4.13 (c), those period two fixed points reside in a cross-shaped envelope. It is reasonable to conjecture that there exits another pair of period two fixed points located at the up-down tips of the envelope. Last but not least, the emergence of the cross-shaped enveloped may be associated with the Hopf bifurcation of the period one $(2, 3)$ torus knot, giving rise to a $(2, 3)$ torus.

In order to test these conjectures, let us instead keep $\mu = 2.0$ and $Re = 150$ fixed in the following, and let k vary. Figures 4.14 and 4.15 highlights some key features of the bifurcation scenarios as k is increased. For $k = 0.1$, the Poincaré section reveals three stable spirals, implying that the $(2, 3)$ torus knot has complex eigenvalues with negative real part. As k is increased beyond $k = 0.148$, the $(2, 3)$ torus knot undergoes a Hopf bifurcation in the Poincaré section, creating a stable limit cycle as visualised by the dense orbits in figure 4.14 (b). Note that, the emergence of a limit cycle on the Poincaré section corresponds to the creation of a torus in the form of the $(2, 3)$ torus knot in the three-dimensional phase space. This explains the observation of dense orbits in figure 4.13 (c). For $k = 0.14925$, the limit cycle created at the Hopf bifurcation is distorted into a cross shape. Two trajectories are seeded inside the limit cycle, whose initial conditions are marked by crosses. It is seen from the inset of the Poincaré section that, all trajectories converge monotonically towards the cross-shaped limit cycle, implying the absence of stable equilibrium solutions inside the stable limit cycle. However, the peculiar shape the stable limit cycle is associated with the presence of two pairs of unstable periodic-two fixed points at each tip of the cross-shaped stable limit cycle.

For $k = 0.14935$, the unstable fixed points at the tips of the cross-shaped limit cycle gain stability, signifying the coexistence between the stable limit cycle and two pairs of stable periodic-two fixed points bounded within. As k increases towards $k = 0.14945$, solution trajectories initiated outside the cross-shaped envelope, marked by black cross, converge to the one of the periodic-two fixed points, signalling the destruction of the cross-shaped stable limit cycle. This corresponds to a torus breakdown in three dimensions and, by contrast to the previous case with preserving rotational symmetry, chaos must be present. For $k = 0.1625$, the traces on the Poincaré section feature a complicated pattern that is hard to decipher. In particular, solution trajectories initiated from point $(r, h, \varphi) = (0.167, 0.132, 0)$, visualised in figure 4.15 (f) as blue dots, undergoes an extremely long, presumably chaotic, transient motions before eventually converging to a period

$$3 \times 2 \times 7 \times 3 = 126 \tag{4.78}$$

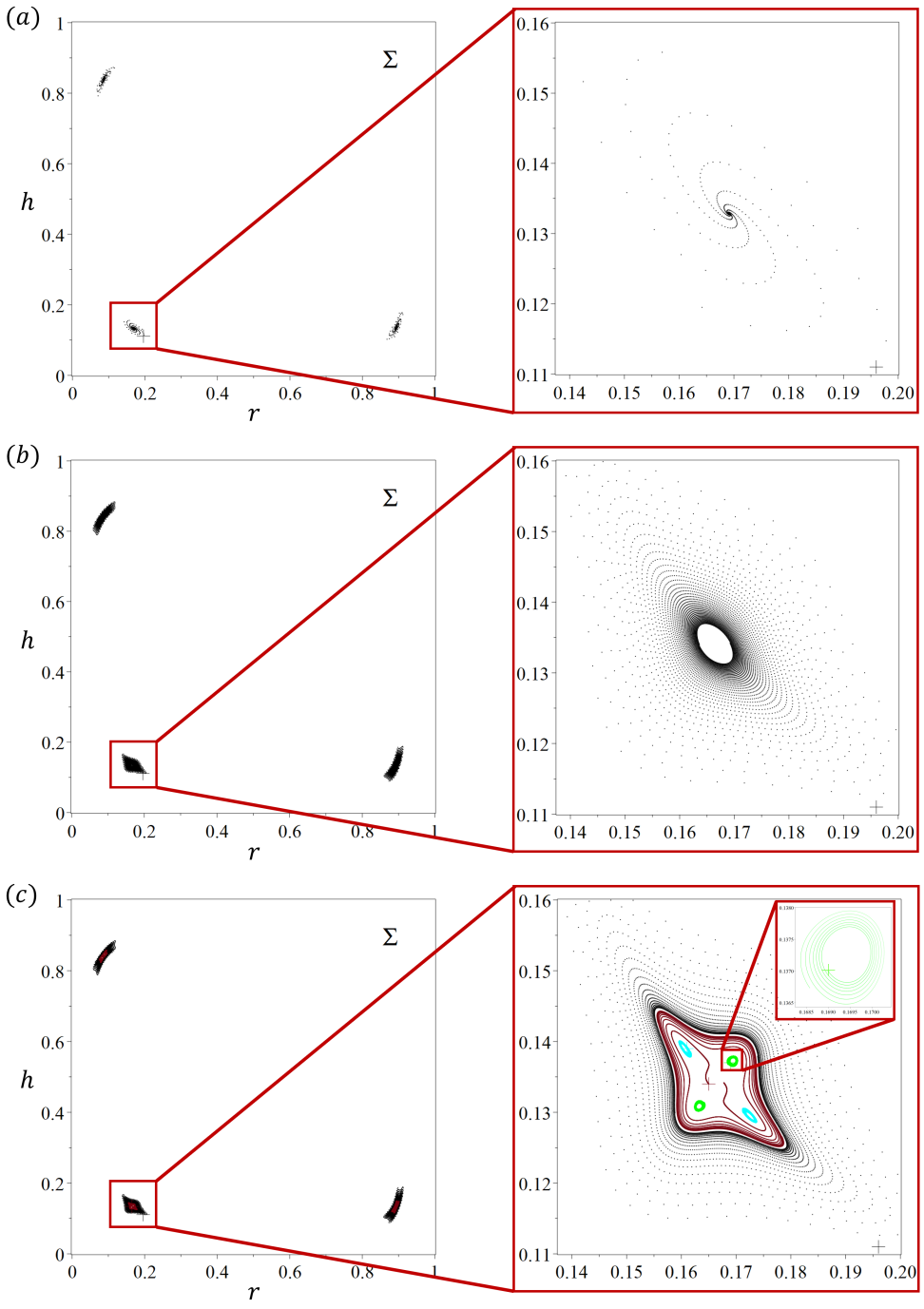

FIGURE 4.14: Bifurcation scenarios on the Poincaré section. (a) $k = 0.1$; (b) $k = 0.148$; and (c) $k = 0.14925$, where the cross symbol denotes the location of the initial condition.

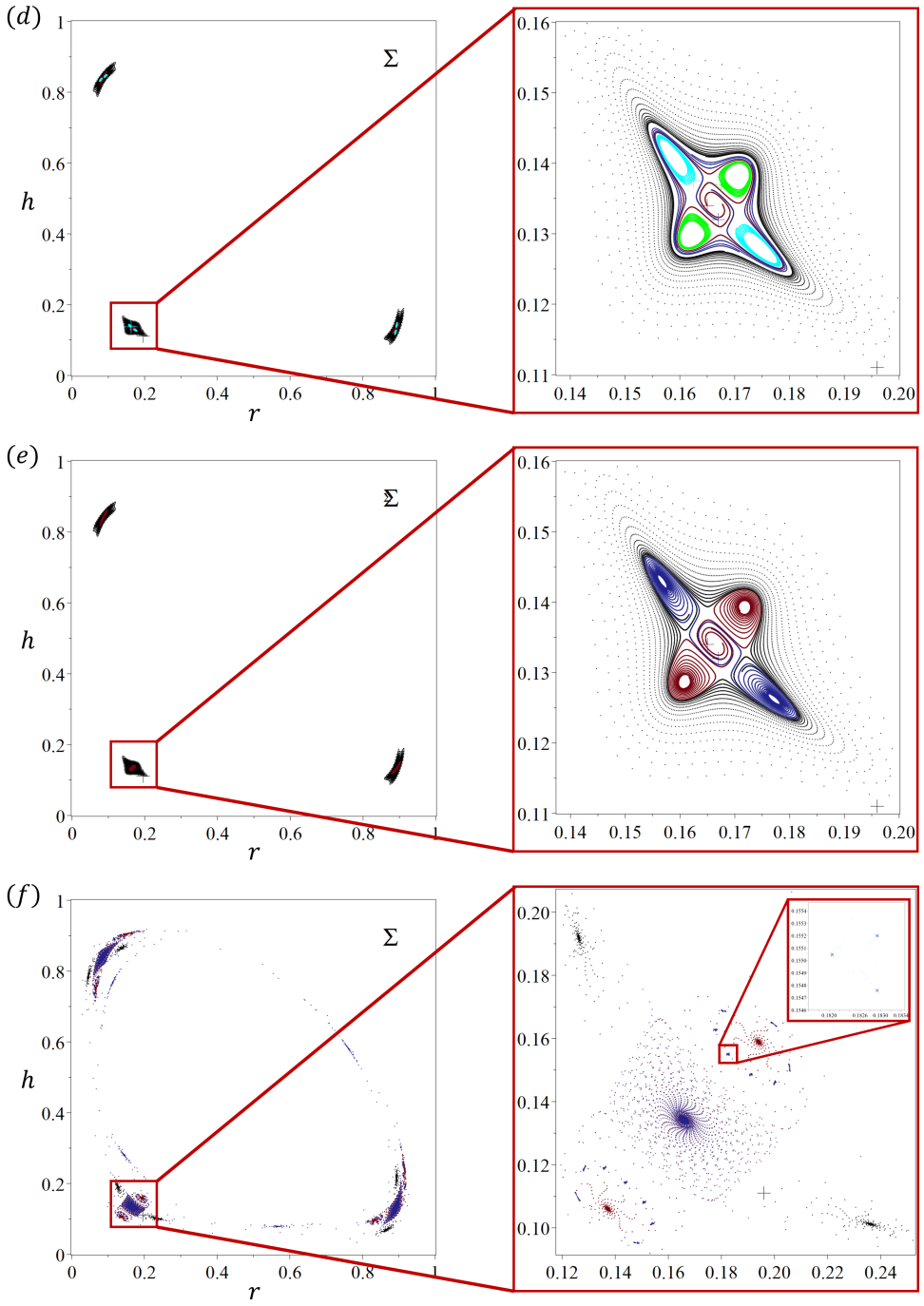

FIGURE 4.15: Bifurcation scenarios on the Poincaré section (continued). (d) $k = 0.14935$; (e) $k = 0.14945$; and (f) $k = 0.1625$, where the cross symbol denotes the location of the initial condition. Note that, in order to obtain (f), the maximal integration time is up to 1.5 million dimensionless units in the simulation. While in other plots, the maximal integration time is truncated at $t_{max} = 150000$.

orbits after 1.5 million dimensionless time units. The distribution of fixed points on the Poincaré section implies that, within the parameter region $k \in [0.14945, 0.1625]$, there may exist a cascade of alternating Neimark-Sacker bifurcation of torus knot and saddle-node bifurcation on the torus.

4.4.3 Peculiar devil's staircase

Figure 4.16 displays two devil's staircases obtained by plotting the rotational number Ro as a function of Re for $k = 0.025$ and $k = 0.05$, respectively. By contrast to the conventional devil's staircases constructed with the sine circle map, the devil's staircase present in this chapter are unique for several reasons.

Among which, the most striking feature is the overlaps among different phase-locking plateaus and the quasiperiodic diagonal line. Such overlaps signify a multi-stability. As Re varies continuously, a trajectory would either remain in the same phase-locking plateau, or climb down along the quasiperiodic thread, or hop between adjacent phase-locking plateaus. As k increases, the quasiperiodic thread scatters to fill the finite intervals along the phase-locking plateaus. Physically, the phase-locking occurs whenever the resonance interaction of harmonics surpasses the tendency of phase drift. An increasing coupling as implied by a greater value of k strengthens the resonance interaction, resulting in a broader range of phase locking intervals observed in figure 4.16(b). Mathematically, the phase locking and the emergence of the corresponding plateaus are associated with the saddle-node bifurcations on Σ. Consequently, the invariant torus is typically destroyed at the moment of the phase locking, featuring a connected but non-overlapping devil's staircase as in the sine circle map. Therefore, the coexistence between the phase locking and quasiperiodic regions obscures the origin of those torus knot attractors.

Remembering that the Hamiltonian system (4.57) possesses a continuum of periodic orbits at the moment of the Hopf bifurcation, they correspond to a family of tori in three dimensions. With preserving rotational symmetry, the addition of the viscous dissipation stabilises one torus and leave an infinite many of unstable tori. Consequently, the conjecture is: the inclusion of the symmetry breaking terms does not destroy the stable torus as shown in figure 4.11 but trigger a saddle-node bifurcations on the unstable tori. Another possibility is that the phase locking indeed occurs on the stable torus, while one of the unstable torus simultaneously gains stability through, perhaps, the boundary crisis

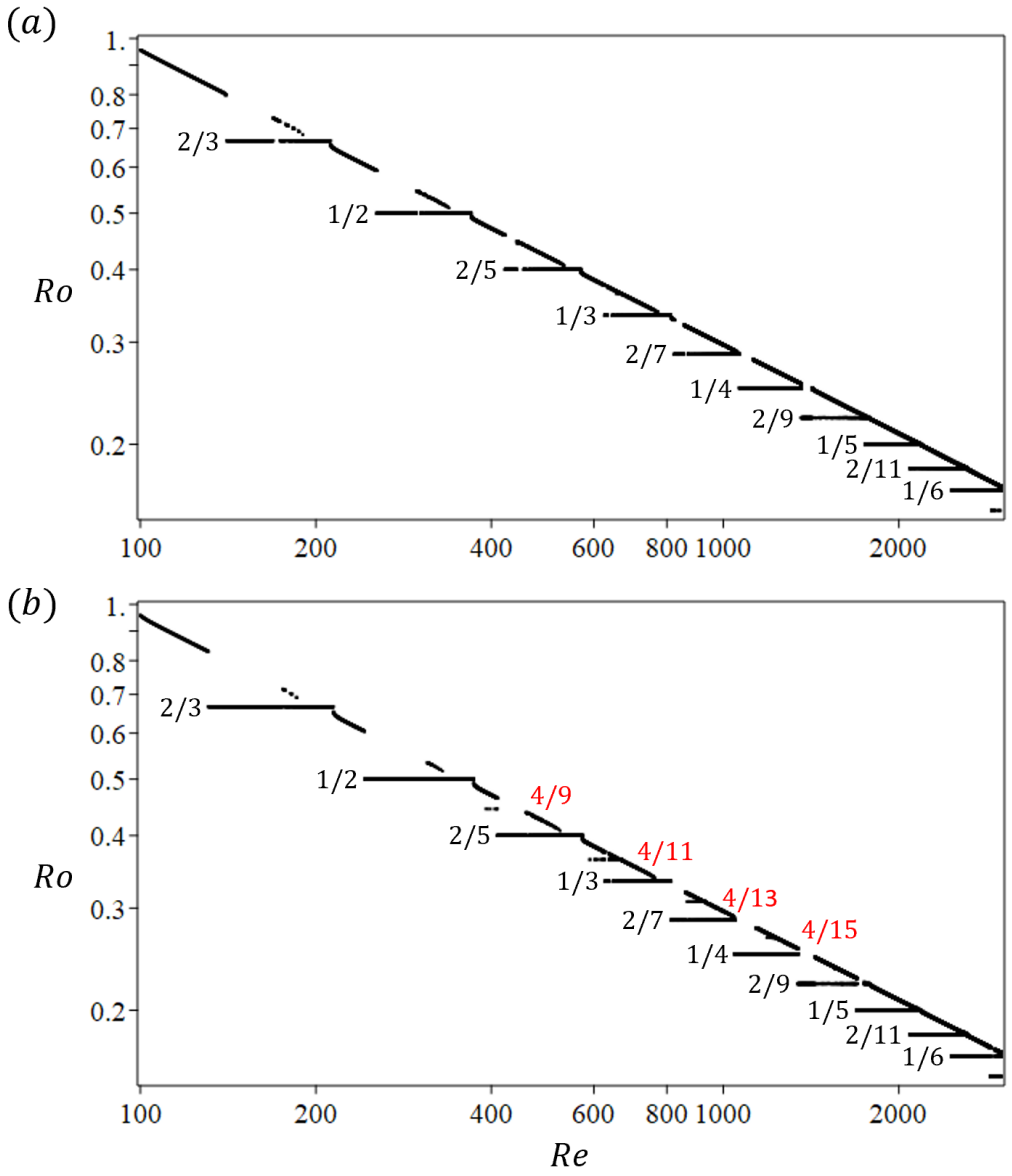

FIGURE 4.16: Devil's staircase, which is obtained by plotting the rotational number Ro as a function of Re: (a) $k = 0.025$; and (b) $k = 0.05$. The diagonal line represents quasiperiodic motions on the surface of the invariant torus, while the plateaus represent phase locking regions with the corresponding rotational number. The plots are in the log-log scales.

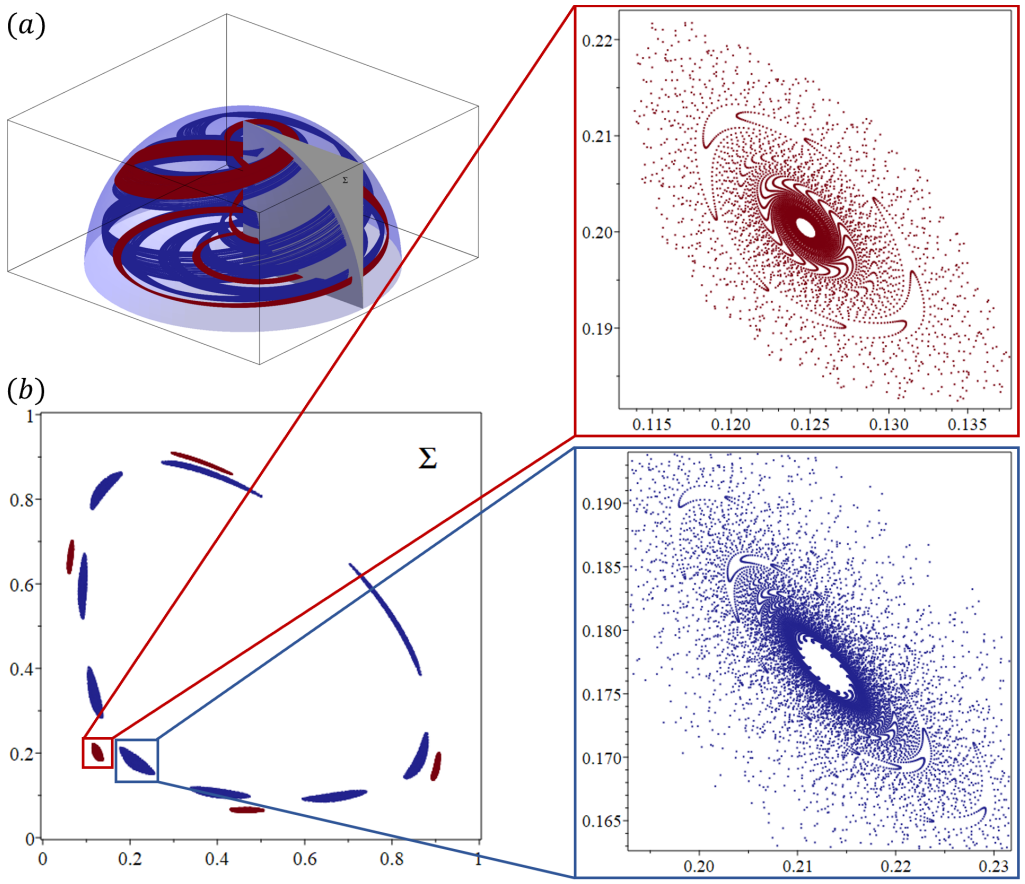

FIGURE 4.17: Coexisting $(1,5)$ torus knot (red) and $(2,9)$ torus knot attractors in the phase space for $Re = 1750$ and $k = 0.45$. The traces of torus knot attractors on the Poincaré section exhibits a multifractal scaling.

[205]. However, the coexistence of several phase locking plateaus at higher values of Re suggests that the former seems to provide a better explanation.

To test these conjectures, the following numerical experiment is conducted. To begin with, for $Re = 1750$ and $k = 0.45$, coexisting $(1,5)$ and $(2,9)$ torus knot attractors are visualised from two different initial conditions, as shown in figure 4.17. Starting from a different initial condition, the coexisting torus attractor has been identified, but since in the present case, the torus is compatible in size with the torus knot attractors, it is therefore omitted for a clearer representation. The traces of the torus knot attractors on the Poincaré section feature an asymptotic spiral-in and foldings of solution trajectories during the transient. Note that, the stable torus increases in size as μ increases towards $\mu = 2.5$. Consequently, if the torus knot attractors arise from the saddle-node bifurcation on the stable torus, then the size of the torus knot attractor is expected to decrease with decreasing μ. The saddle-node bifurcation implies that there exists a torus knot repeller

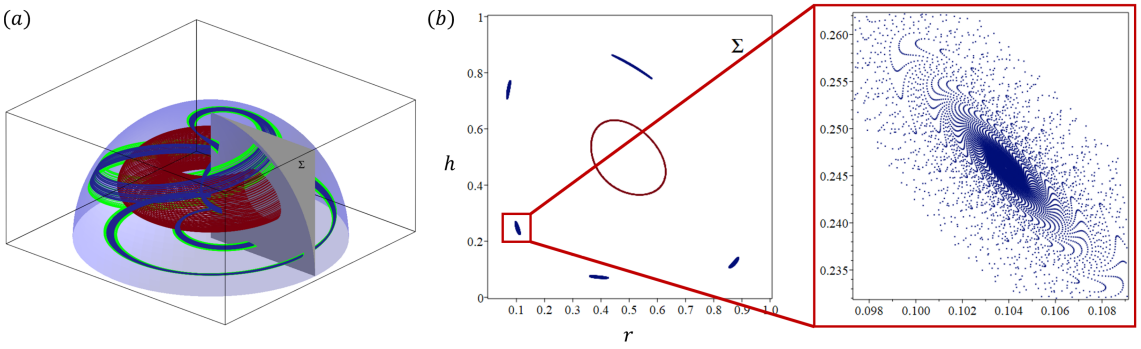

FIGURE 4.18: Coexisting torus (red) and $(1,5)$ torus knot attractor (blue) in the phase space for $Re = 1750$ and $k = 0.45$, but with $\mu = 0.25$. A reverse integration for $t = -4500.. - 4750$ reveals a torus knot repeller (green) coexisting with the attractor. The traces of torus knot attractors on the Poincaré section are similar to those observed in figure 4.17.

of the same topology in the neighbourhood of the attractor. In figure 4.18, simulation is conducted for $Re = 1750$ and $k = 0.45$ as in figure 4.17, but with μ being lowered to $\mu = 0.25$. It is seen that, although the size of the torus is significantly reduced, the $(1,5)$ torus knot attractor is compatible in size with that in figure 4.17. Moreover, a reverse integration visualised a coexisting $(1,5)$ torus knot repeller in the neighbourhood of the attractor, providing an evidence that the torus knot attractors arise from the saddle-node bifurcation on the unstable tori.

Moreover, the devil's staircases in figure 4.16 are displayed in the log-log plots, implying that the rotational number of the associated attractor in the phase space decreases algebraically with Re. A direct consequence is, at large Re, the number of the fixed points of the corresponding torus knot on the Poincaré section increases.

Last but not least, by contrast to the conventional devil's staircase, where Ro associated with each phase locking plateau varies as the Farey sequence

$$\left\{ \cdots, \frac{2}{3}, \frac{3}{5}, \frac{1}{2}, \frac{2}{5}, \frac{1}{3}, \frac{1}{4}, \frac{1}{5}, \cdots \right\}. \tag{4.79}$$

Here, for $k = 0.025$, the steps decrease in value following presumably the Apollonian circle packing sequence [6]

$$\left\{ \cdots, \frac{2}{3}, \frac{1}{2}, \frac{2}{5}, \frac{1}{3}, \frac{2}{7}, \frac{1}{4}, \frac{2}{9}, \frac{1}{5}, \cdots \right\}. \tag{4.80}$$

[6]The relevance of the circle packing sequence was pointed out by Prof. D. Sullivan.

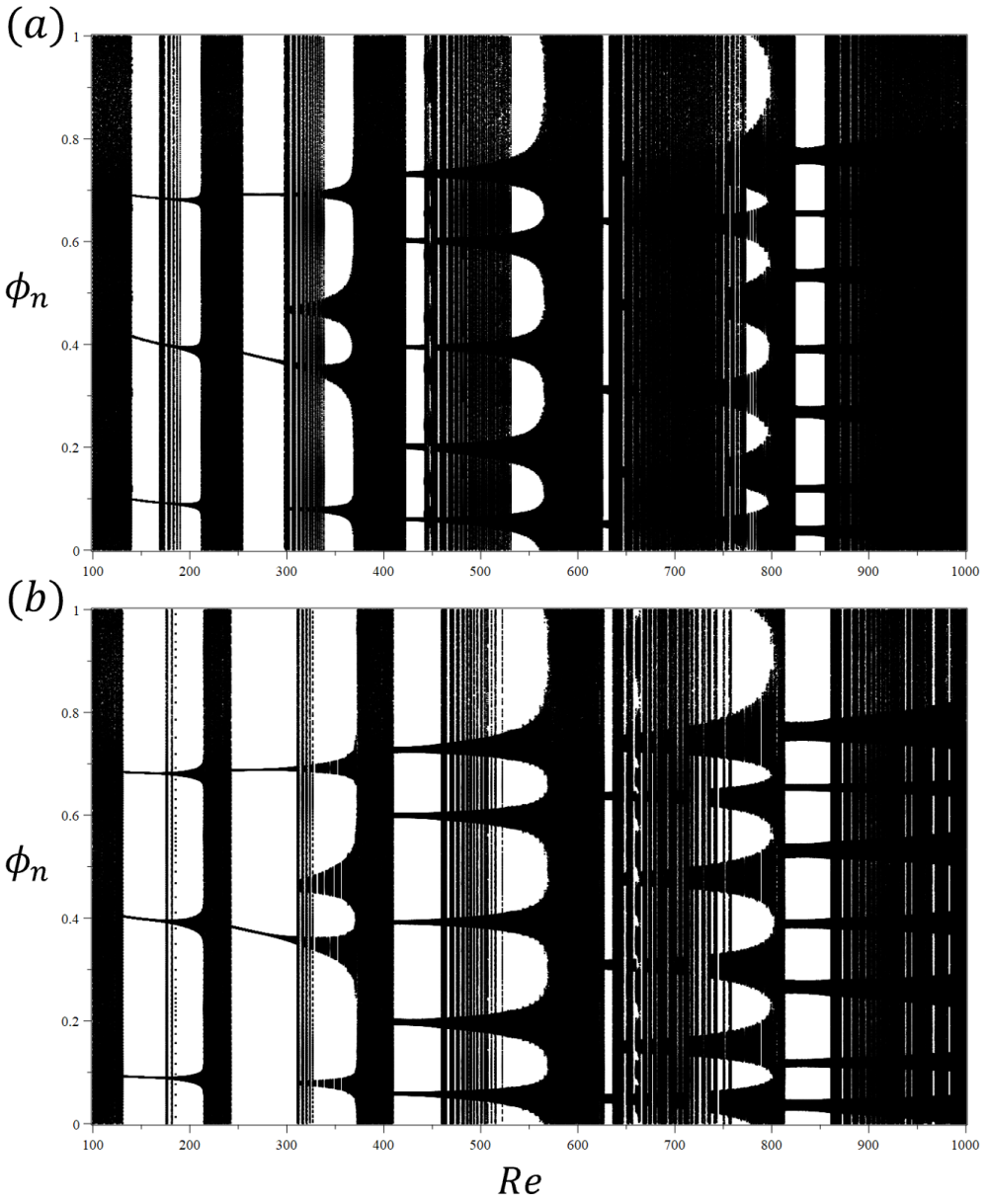

FIGURE 4.19: Bifurcation diagram, which is obtained by plotting the angle variable ϕ_n as a function of Re. (a) k=0.025; and (b) k=0.05.

An increase in k up to $k = 0.05$ reveals the emergence of the secondary phase locking plateaus interspersed between the primary ones

$$\left\{ \cdots \frac{1}{2}, \frac{4}{9}, \frac{2}{5}, \frac{4}{11}, \frac{1}{3}, \frac{4}{13}, \frac{2}{7}, \frac{4}{15}, \frac{1}{4}, \cdots \right\}. \tag{4.81}$$

However, the origin of preceding sequences and their physical significance remain to be explored.

The transition between quasiperiodic, periodic, and presumably chaotic dynamics are

summarised in figure 4.19, wherein the instantaneous value of angle variable ϕ_n is plotted as a function of Re. Due to the computational limitations, the bifurcation diagram is generated by an adiabatically increasing of $Re \in [100, 1000]$ only. The initial transients are omitted. Consequently, if there exists several coexisting attractors in the phase space, only one is shown. For $k = 0.025$, the bifurcation diagram features a filled band for $Re \lessapprox 140$, representing the stable quasiperiodic motions on the surface of the two-torus; while the lines from $Re \in [140, 170]$ represent the periodic motions characterised by the $(2, 3)$ torus knot. The discontinuous transition from the quasiperiodic to the periodic motions at $Re \approx 140$ implies that the $(2, 3)$ torus knot does not bifurcate supercritically from the invariant two-torus. This observation is compatible with the conclusions in §4.4.3 that the birth of the torus knot attractors is disconnected from the torus. With increasing Re, the lines presenting the torus knot attractors penetrate through the quasiperiodic and increase in thickness. The former signifies a bi-stability, while the later corresponds to the Hopf bifurcation of fixed points on Σ. Since most of the bifurcation scenarios observed in figures 4.14 and 4.15 take place in localised regions on Σ and are accompanied by long transients, they cannot be captured by the bifurcation diagram as shown in figure 4.19. Finally, with increasing nonlinear coupling k, quasiperiodic regions shrink in size, in agreement with the elongation of the phase locking plateaus observed in figure 4.16 (b).

4.5 Discussion and conclusions

The subcritical transition to turbulence is a long-standing problem with puzzling phenomenology hard to decipher. Owing to the recent advance in experimental and computational techniques and to the development of mathematical and statistical tools, the knowledge and understanding on this problem have been significantly improved. The word "subcritical" characterises the problem. In the transitional flow regime, the Reynolds number is too low to excite the linear instability so that the laminar base flow remains a non-vanishing stable equilibrium, yet it is sufficiently high to sustain a self-sustaining process, permitting the existence of nontrivial solutions in the form of chaotic saddles in the phase space or turbulent spots in the physical space. Since turbulent spots are spatially localised and have counter-rotating pairs of streamwise vortices embedded within, the dynamics of the perturbed flow around these vortices can be reduced to a strictly temporal evolution characterised by low-dimensional dynamical systems.

Conventionally, the low-dimensional dynamical system is obtained through a Galerkin projection of the Navier-Stokes equations onto a set of orthogonal eigenfunctions that carry most of the energy. However, this method suffers from several limitations. Firstly, these eigenfunctions are not known a priori. They are usually extracted from the database of direct numerical simulation using a proper orthogonal decomposition, hence the obtained dynamical system is applicable only for the specific type of flows that are computed. That is, the generality of the Navier-Stokes equations is lost during the truncation. Secondly, the resulting dynamical system consists of, in general, a set of $4 - 100$ ordinary differential equations. Although this is drastic reduction of the infinitely dimensional phase space associated with the Navier-Stokes equation, the resulting dynamical system is almost impossible to analysed theoretically. Thirdly, in most dynamical systems proposed for flows experiencing a subcritical transition to turbulence, the trivial fixed point, usually the origin, represents the linearly stable laminar state. Therefore, the first bifurcation is expected to be the saddle-node bifurcation which creates a nontrivial stable solution disconnected from the laminar state. This disconnectedness signifies the difficulty. Since the laminar state is a non-bifurcating solution, one cannot expect to linearise the flow about the laminar base flow and perform the normal form analysis on a centre manifold of the laminar state which only apply locally. On the other hand, observing that the chaotic behaviour apparently bifurcates from the nontrivial solution, which gains stability at the saddle-node bifurcation, one may instead consider a linearisation of the flow about the nontrivial solution. In planar shear flows, the nontrivial solution corresponds to a counter-rotating pair of streamwise vortices.

In order to overcome the preceding deficiencies, the Navier-Stokes equation is linearised about a rigid rotating vortex, and the counter-rotating characteristic is recovered by imposing a reflectional symmetry with respect to the complex-lamellar mode. With Fourier transform in three spatial directions, one arrives at a set of three linear ordinary equations. Note that, the Jacobian matrix of the system has a pair of purely imaginary eigenvalues and a simple zero, depicting a well-posed $\mathbb{Z}_2$-symmetric pitchfork/Hopf problem. However, by resorting to the normal form, one considers a problem with specific linearity but general nonlinearity. Therefore, by contrast to the previous Galerkin projection, the specific of the Navier-Stokes equations is lost. Therefore, the main goal of this study is not to reproduce quantitatively the results of a direct numerical simulation but to understand qualitatively how the presence of a counter-rotating pair of streamwise vortices can affect the transition to turbulence. For this purpose, the flow shear and the

associated the transient growth are considered to be secondary because they do not affect the asymptotic behaviours $t \to \infty$.

Bifurcation analysis for fixed points and periodic orbits of the proposed three-dimensional model is undertaken. With preserving rotational symmetry and in the limit $Re \to \infty$, the system is Hamiltonian by construction. At the moment of the Hopf bifurcation, the planar system possesses a continuum of periodic orbits bounded by a heteroclinic cycle connecting three saddle points. The inclusion of the viscous dissipation stabilises one periodic orbit which corresponds to an invariant two-torus in the phase space. The torus grows in size as the bifurcation parameter is raised and it eventually overlaps with the heteroclinic cycle. The heteroclinic tangency is calculated using the Melnikov method. As the bifurcation parameter increases pass the heteroclinic tangency, the invariant two-torus is destroyed, giving arising to a long transient which increases in lifetime as Re increases. However, as long as the rotational symmetry is preserved, the system is essentially two-dimensional, and consequently the transient is non-chaotic.

With the inclusion the symmetry breaking nonlinear terms, the phase space is three-dimensional, hence more complex dynamics involving chaos can emerge. The dynamics of the attractor is investigated numerically by following the intersections of the attractor on the Poincaré section Σ, omitting the initial transient. If Σ traces discrete set of points, the corresponding solution to the full equations is periodic; if Σ traces a closed orbit, the corresponding solutions are quasiperiodic motions on the surface of the torus; chaotic motions are reflected by more complex patterns on Σ. Within the quasiperiodicity region, several bifurcation scenarios, involving phase-locking, period doubling, Neimark-Sacker bifurcation of torus knot, and torus breakdown, are identified as the nonlinear coupling k is gradually increased from zero. By plotting the rotational number as a function of Re with k fixed, a peculiar devil's staircase is revealed. By contrasted to the convectional devil's staircase, which takes the form of the Cantor function, here the phase locking and the quasiperiodic regions overlap, implying a coexistence of invariant torus and torus knot attractors in the phase space. At each phase locking plateau, there resides a torus knot attractor with cross sections of increasing complexity as k increases. Moreover, it is noteworthy that the rotational number associated with each phase locking plateaus does not order in the Farey sequence, but in presumably the circle packing sequence. However, despite a drastic reduction of the dynamical system to three dimensions, the fate of the stable and unstable tori, as well as the consequent bifurcation scenarios with $k \neq 0$, are to a great extent unknown.

Finally, it is noteworthy that the bifurcation scenarios and the traces on the Poincaré sections observed in §4.4 resemble those in a nine-mode model for the sinusoidal shear flow obtained using the Galerkin method [187]. This resemblance[7] provides a hint that the counter-rotating pair of coherent vortices do indeed play an important role in characterising the transition to turbulence inside the spatially localised turbulent spot.

[7]The resemblance between these two models was pointed out by Prof. B. Eckhardt.

Chapter 5

Discussion and future works

5.1 General discussion

Partly because its ubiquity and immense practical importance, and partly because its inherent difficulty and tremendous intellectual fascination, the study of transition to turbulence has attracted research efforts in theory, experiment, and numerics. Since late 18^{th} century, there are two school of thoughts emerged in regard to the mechanism which triggers the laminar-to-turbulent transition. One school considers that the transition to turbulence is due to the linear instability, namely, an infinitesimal perturbation grows exponentially; while the other school considers that the laminar motion is definitely stable and transition to turbulence is triggered only by a disturbance of finite amplitude. Nevertheless, both schools agree that the working fluid can be considered as incompressible, whose motion is characterised by the Navier-Stokes equations. The historical aspects regarding these two school of thoughts has been nicely discussed in Lin [136]. Based on the classification firstly proposed by Landau [26], and later promoted by Pomeau [39], these two school of thoughts are now accepted as the two sides of the same coin, commonly referred to as the supercritical and subcritical transition to turbulence, respectively.

The focus on this thesis is on plane Couette flow where the transition to turbulence is subcritical. The theory of subcritical transition to turbulence dates back to Reynolds [7] and Lord Kelvin [1]. Although temporarily abandoned by much of the community in

favour of the supercritical transition turbulence [1], the advance in experimental facilities and numerical techniques [2] is now drawing physicists back. Pioneered by researchers at Stockhom, Sweden (Lundbladh and Johansson [89], Tillmark and Alfredsson [86]) and at Saclay, France (Daviaud et al. [75], Bottin et al. [57]), accumulating experimental and numerical facts have been reported. To sum up, at the lowest Reynolds number where turbulence organises itself in the form of spatially localised turbulent spots, there are

i counter-rotating streamwise vortices inside the spot; and

ii large-scale quadrupolar flows outside the spot.

Various theories have been proposed to explain origin of these flow structures and their role in the subcritical transition to turbulence, cf. Chapter 2 for a historical survey. Among which, the most successful one is the self-sustaining process proposed by Waleffe [148]. This process bridges plausibly several key ingredients, namely streamwise vortices, velocity streaks, and nonlinearity, of the transitional shear flows. The self-sustaining process, unfortunately, is phenomenological in nature in the sense that it is *identified* from data of direct numerical simulations rather than *derived* from the Navier-Stokes equations. As to the large-scale flows, except for their frequent observation and the robust quadrupolar angular dependence, almost nothing is known.

Therefore, the aim of this thesis is to provide, partially, a theoretical understanding and a mathematical modelling for (i) the stationary quadrupolar flows outside the spot, cf. Chapter 3; and (ii) the bifurcating streamwise vortices inside the spot, cf. Chapter 4. In the following, the obtained results are summarised with additional emphases on their physical significance and potential consequence to the subcritical transition to turbulence.

5.2 Quadrupolar flows outside turbulent spot

In Chapter 3, the governing equations for large-scale flows around turbulent spots have been derived from the Navier-Stokes equations by resorting to the geometric scale analysis inscribed in all planar shear flows. Moreover, the forcing term, which has been identified as constituting of the Reynolds stresses of turbulent fluctuations inside the spot and

[1] This trend may be due to the pattern formation in closed flow systems, in particular the Taylor-Couette flow observed by Swinney and Gollub [32], and the breakthrough in chaos and dynamical systems theory.

[2] As well as the bottleneck associated with the dynamical system theory.

the corresponding pressure gradient that arises so as to compensate the divergence of the Reynolds stresses, is modelled using a symmetry argument. The proposed governing equations were solved analytically, providing, to the author's knowledge, the first analytical solution of the far-field for the quadrupolar flows observed generically around turbulent spots. Based exclusively on analytical solutions, three main predictions has been highlighted in Chapter 3:

1. The quadrupolar flow is found to decay algebraically with power-law exponent -3 at large distances away from the spot;

2. The existence of an exponentially localised reversed quadrupolar flow centred at the turbulent spot; and

3. The quadrupolar flow has a topological origin linked to the Hodge theorem for two-dimensional harmonic fields.

Note that, the present results differ considerably from the common beliefs. To begin with, direct numerical simulations by Schumacher and Eckhardt [64] and Brand and Gibson [71] reported that the quadrupolar flows decay exponentially and no algebraic decay has been identified. Moreover, by investigating the dominant terms in the Navier-Stokes equations, Brand and Gibson [71] proposed a simplified model for the decay of the streamwise velocity in the streamwise direction. By solving their proposed model with an exponentially decaying ansatz, they concluded the exponentially decay of quadrupolar flow [3]. In direct numerical simulations by Duguet and Schlatter [65] and experiments by Couliou and Monchaux [62], unfortunately, no algebraic decay can be concluded neither. Inspired by the early work of Li and Widnall [168], Lagha and Manneville [70] investigated the origin of the quadrupolar flow around an isolated turbulent spot in plane Couette flow, wherein the spot is modelled as a localised distribution of Reynolds stresses. They recovered the quadrupolar angular dependence and obtained similar velocity contours to those in an early direct numerical simulation by Lundbladh and Johansson [89]. Note that, although the observation of reserved circulation inside the turbulent spot has been mentioned in [70], their work tends to give the impression that the occurrence of the quadrupolar flow is due the spatially localised Reynolds stresses generating a reversed spanwise vorticity which counteracts the laminar base flow, contradictory to the present results.

[3]The approached used in [71], namely using the exponentially decaying ansatz to conclude exponential decay, has been opposed by Barnett et al. [206] soon after the original paper by Brand and Gibson [71].

On the other hand, after the work on the quadrupolar flows [207] and up to the thesis submission, the following numerical and experimental evidences are accumulated supporting the preceding predictions. To begin with, a new set of direct numerical simulations has been conducted for plane Couette flow in a very large domain by P. Kashyap and Y. Duguet at LIMSI, Orsay, France. A convergence towards an algebraic decay with power-law exponent -3 is clearly identified with increasing domain size. A post processing for the obtained data reveals that the y-averaged wall-normal vorticity decays faster than exponential and has contours resemble those in figure 3.3 (b), supporting the existence of the exponentially localised reversed quadrupolar flow. In their simulations, the y-averaged wall-normal velocity is also exponentially localised, supporting that the y-averaged large-scale flow is two-dimensional and harmonic. Lastly, quadrupolar flow has been recently observed in Couette-Poiseuille experiments conducted by J. E. Wesfreid's research group at ESPCI, Paris, France, supporting the topological origin of the quadrupolar flow.

Since the present work deals only with quadrupolar flows around turbulent spots in planar shear flows with linear laminar profile and free-slip boundary conditions at the walls. In order to find out how the large-scale flows behave as the pressure gradient and the relative motion of the plates are varied, it would be interesting to consider Couette-Poiseuille flow, which is derived in Chapter 2, with Robin boundary conditions, when expressed in terms of the poloidal and toroidal function

$$(1-\beta)\tilde{\phi} + \beta\partial_y\tilde{\phi} = \beta\tilde{\psi} + (1-\beta)\partial_y\tilde{\psi} = 0, \tag{5.1}$$

at the boundaries. Here, $\beta \in [0,1]$ is the weighting parameter characterising a homotopy from the non-penetrating free-slip boundary conditions, i.e. $\beta = 0$ as in Chapter 3, to the penetrating no-slip boundary conditions, i.e. $\beta = 1$ as in Appendix C. The Robin boundary conditions (5.1) signifies the edge of the boundary layer where the perturbed velocity has equal magnitudes in directions parallel and perpendicular to the boundaries.

5.3 Bifurcating vortices inside turbulent spot

The theory on quadrupolar flows outside the turbulent spot can only be pushed to a point where the nonlinear effects begin to appear. The limitation of the proposed linear theory motivates the bifurcation analysis for counter-rotating vortices inside turbulent spots (Chapter 4), where nonlinearity play an important role.

The application of the dynamical system approach to the transition to turbulence dates back to Landau [26] and Hopf [27] and is popularised by Ruelle and Takens [29]. However, in none of these work was a clear link being bridged between the Navier-Stokes equations and the abstract low-dimensional dynamical system exhibiting quasiperiodicity and chaos [6].

The present work aims to provide such a bridge. Traditionally, the derivation of low-dimensional dynamical systems proposed for the subcritical transition to turbulence is based on a linearisation performed about the linearly stable laminar base flow, hence the first bifurcation that gives rise to the nontrivial solution is the saddle-node bifurcation. Conversely, the dynamical systems derived in Chapter 4 is based on the experimental observation and symmetry arguments. More specifically, in order to get around the difficulty associated with the subcricality, namely the nontrivial solution branch does not manifest itself in a small neighbourhood of the laminar attractor, in Chapter 4, the linearisation is performed about the frequently observed streamwise vortices in shear flows. Since streamwise vortices typically occurs in the form of counter-rotating pairs, the reflectional symmetry with respect to the complex-lamellar state is imposed, resulting in a three-dimensional dynamical system in the Fourier space which depicts a $\mathbb{Z}_2$-symmetric pitchfork/Hopf problem. The relevance of the derived dynamical system to the transition to turbulence in fluid dynamical has been conjectured by Iooss and Langford [189] 40 years ago. To the best of the author's knowledge, Chapter 4 serves as the first proof. However, the bifurcation analysis present in Chapter 4 also shows that the results can give only very little qualitatively understanding to the real fluid. This is because,

1. although the linearity of the dynamical system is derived from the Navier-Stokes equations, the nonlinearity which selects the bifurcation scenarios is postulated; and
2. the understanding for global bifurcation of periodic orbits in dynamical systems with dimensionality greater than two is incomplete.

Therefore, unlike the suggesion by Manneville [38]:

> *"The key word 'universality' was inscribed in relevant normal forms controlling a few specific transition scenarios, the well-known sub-harmonic, quasiperiodic, and intermittency routes,"*

despite a drastic reduction of the state variables into three, the bifurcating periodic orbits can experience a very complicated dynamics with long transient behaviour. Whether these attribute to the breakdown of an invariant torus, a period doubling cascade, or a heterclinic tangency of a periodic orbit will depend upon details. More than one of these phenomena could occur in the system, complicating the assignment of a single route to chaos.

Appendix A

Quadrupolar flows arising from an external perturbation

Experimentally, turbulent spots are triggered in a controlled manner by two types of perturbations : (i) an impulsive perturbation localised both in space and in time, e.g. a water jet piercing through the base flow for a short duration [75, 86, 90]; and (ii) an external obstacle localised in space while permanent in time, e.g. a wire [57, 109] or a bead [62, 63]. In this work, instead of a localised distribution of Reynolds stresses arising from an autonomous turbulent spot, we interpret $\boldsymbol{q}_{\tilde{\boldsymbol{u}}}$ as an external forcing stemming from two oppositely pumping water jets with an off-set in the streamwise direction, as shown in figure A.1. The net effect of these water jets is to introduce a spanwise vorticity in accordance with that if the base flow, hence following the symmetry arguments in §3.2.6, the forcing is expressed in terms of the poloidal and toroidal components as

$$q_{\tilde{\phi}} = -A\cos(\xi_1 y)\delta'(x)\delta(z) \quad \text{and} \quad q_{\tilde{\psi}} = 0, \tag{A.1}$$

where, for simplicity, only a single Fourier mode is considered in this Appendix. Since the presence of such water jets piercing through the boundaries obviously breaks locally the Dirichlet boundary conditions, as opposed to the Dirichlet boundary conditions considered in Chapter 3, the forcing $\boldsymbol{q}_{\tilde{u}}$ satisfies no boundary conditions at the walls henceforth. Consequently, the wavenumbers are no longer discretised, but featuring continuous variation of so as to compensate the crudeness of the modelling (A.1). Moreover, as long as the external perturbation sustains, the constraint $Re \gtrsim 325$ associated with the presence of autonomous turbulent spots can be substantially lowered, accordingly.

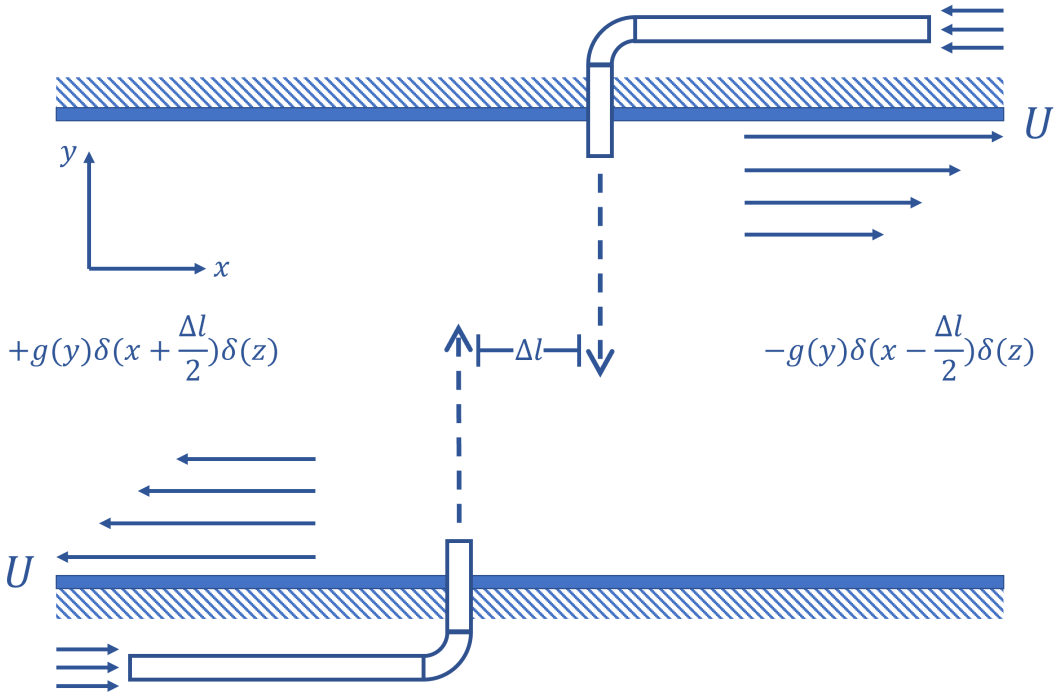

FIGURE A.1: Schematic of a forcing induced by two counter-acting water jets. The net effect of these water jets is to introduce two anti-aligned vertical momentum in the poloidal field (dashed line).

A.1 Modal solutions for poloidal and toroidal functions

Expanding (A.1) onto the Fourier basis introduced in Eq. (3.62)

$$q_{\tilde{\phi}} = -\mathrm{i}\frac{A\,K_x}{(2\pi)^2}\cos(\xi_1 y)\iint_{-\infty}^{\infty} e^{\mathrm{i}(K_x x+K_z z)/\eta}\mathrm{d}K_x\mathrm{d}K_z, \tag{A.2}$$

and replacing the corresponding terms in Eqs. (3.63) gives

$$\left(\partial_y^2 - K^2\right)\hat{\phi} = \mathrm{i}\frac{A\,K_x}{2\pi}\cos(\xi_1 y), \tag{A.3a}$$

$$\left(\partial_y^2 - K^2\right)\hat{\psi} = \mathrm{i}(K_x/\eta)y\hat{\psi} + \mathrm{i}(K_z/\eta)\hat{\phi}, \tag{A.3b}$$

supplemented with the Fourier transformed free-slip boundary conditions (3.64).

A.1.1 Modal solutions

Similar to Chapter 3, Eqs. (A.3) can be solved by resorting to the method of undetermined coefficients, yielding

$$\hat{\phi} = -\mathrm{i}\frac{A\,K_x}{2\pi(K^2+\xi_1^2)}\left[\cos(\xi_1 y) - \cos(\xi_1)\frac{\cosh(Ky)}{\cosh(K)}\right], \tag{A.4}$$

for the poloidal function; and

$$\begin{aligned}\hat{\psi} = &-\frac{A\,K_x K_z\cos(\xi_1)}{4\pi\eta K(K^2+\xi_1^2)}\left[\frac{y\sinh(Ky)}{\cosh(K)} - \frac{\cosh(Ky)}{\sinh(K)} - \frac{\cosh(Ky)}{K\cosh(K)}\right]\\ &-\frac{A\,K_x K_z}{2\pi\eta(K^2+\xi_1^2)^2}\left[\cos(\xi_1 y) + \xi\sin(\xi_1)\frac{\cosh(Ky)}{K\sinh(K)}\right],\end{aligned} \tag{A.5}$$

for the toroidal function. It is seen that, additional terms involving $\cos(\xi_1)$ as coefficients arise from the unsatisfactory of the Dirichlet boundary conditions for $q_{\hat{\phi}}$ at the walls [1]. These additional terms compensate the inhomogeneity of the forcing at the walls such that the boundary conditions (3.64) for the poloidal and toroidal functions are identically satisfied.

Note that, as in Chapter 3, the preceding solutions can be greatly simplified by averaging between two walls, yielding

$$\langle\hat{\phi}\rangle = -\mathrm{i}\frac{A\,K_x}{2\pi(K^2+\xi_1^2)}\left[\xi_1^{-1}\sin(\xi_1) - \cos(\xi_1)K^{-1}\tanh(K)\right], \tag{A.6}$$

$$\langle\hat{\psi}\rangle = -\frac{\alpha A\,K_x K_z}{2\pi\eta K^2(K^2+\xi_1^2)}\left[\xi_1^{-1}\sin(\xi_1) - \cos(\xi_1)K^{-1}\tanh(K)\right]. \tag{A.7}$$

Comparing the modal solutions (A.6) and (A.7) obtained in this Appendix with Eqs. (3.68) and (3.69) obtained in Chapter 3, the hyperbolic trigonometric functions arising from the complimentary solutions do not vanish in the present case. Therefore, in order to recover the flow variables by inverting the Fourier transform, two possible approximations for the hyperbolic trigonometric functions are introduced and compared in the following subsection.

[1] Stemming from the Dirichlet boundary conditions (3.13) at the walls, we have $\cos(\xi_1) = 0$, resulting in a simplification.

A.1.2 Continued fraction expansion

After obtaining the modal solutions, one still face the task of inverting the Fourier transform. By contrast to the previous case in Chapter 3, the non-vanishing $q_{\tilde{\phi}}$ at the walls leads to integrands involving hyperbolic functions, which is not elementary. Remembering that the wavenumbers $K \sim O(\eta)$ is a small parameter as ensured by the Fourier basis (3.62), one may expand $\tanh(Ky)$ about $K = 0$ in terms of the Taylor series, yielding

$$\tanh(K) = K - \frac{1}{3}K^3 + \frac{2}{15}K^5 + O(K^7). \tag{A.8}$$

However, a finite truncation of the Taylor series diverges as $K \to \infty$, while $\tanh(K)$ admits a well-defined asymptotic limit

$$\tanh(K) \to 1, \quad \text{as} \quad K \to \infty. \tag{A.9}$$

Alternatively, $\tanh(K)$ can be expanded in a continued fraction [see e.g. 208]

$$\tanh(K) = \cfrac{K}{1 + \cfrac{K^2}{3 + \cfrac{K^2}{5 + \ldots}}}. \tag{A.10}$$

A comparison between $\tanh(K)$ and its leading order approximations using the Taylor series expansion and using the continued fraction expansion are plotted in figure A.2. It is seen that although both the leading order Taylor series expansion and the second order continued fraction expansion diverge as $K \to \infty$, the first order continued fraction expansion

$$\tanh(K) \approx \frac{3K}{K^2 + 3}, \tag{A.11}$$

decays algebraically with K, as in a low-pass filtering.

In order to understand the difference in applying those approximations, a test integral

$$TI = \int_0^\infty \frac{J_1(Kr)}{K^2} \left[1 - K^{-1}\tanh(K)\right] \mathrm{d}K, \tag{A.12}$$

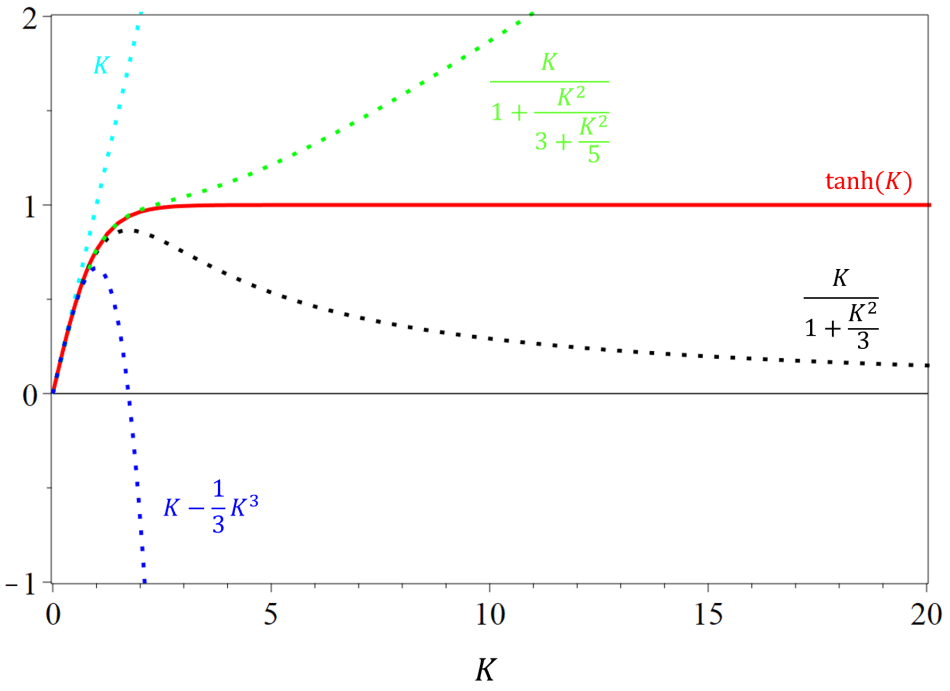

FIGURE A.2: Leading order approximations for the hyperbolic tangent (red line) as (i) the first order Taylor series expansion (cyan dots); (ii) the second order Taylor series expansion (blue dots); (iii) first order continued fraction expansion (black dots); and (iv) second order continued fraction expansion (green dots).

is considered, where $J_1(Kr)$ is the first order Bessel function of the first kind and the wavenumber dependence mimics those of the modal solutions (3.68) and (3.69), provided that $\xi_n = 0$. With the Taylor series expansion truncated up to the second order, the test integral becomes.

$$TI \approx \frac{1}{3}\int_0^\infty J_1(Kr)\mathrm{d}K = \frac{1}{3}r^{-1}. \tag{A.13}$$

Conversely, with the first order continued fraction expansion, the test integral becomes

$$TI \approx \int_0^\infty \frac{J_1(Kr)}{K^2+3}\mathrm{d}K = \frac{1}{3}\left[r^{-1} - \sqrt{3}K_1(\sqrt{3}r)\right], \tag{A.14}$$

where $K_1(\sqrt{3}r)$ is the first order modified Bessel function of the second kind. It is seen that, although the algebraically decaying components from the preceding two approximations are essentially the same, the continued fraction expansion introduces a truncation of the singularity inscribed in the algebraic $1/r$ decay by the modified Bessel functions as $r \to 0$. Figure A.3 displays a direct numerical evaluation of the test integral (A.12) and its approximations by the Taylor series expansion (A.13) and by the continued fraction

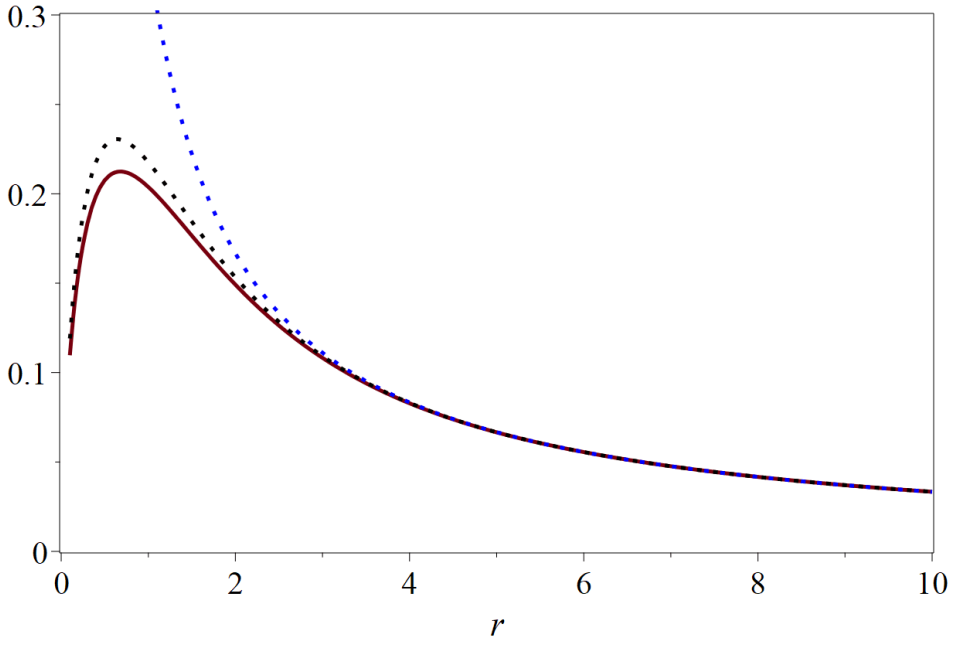

FIGURE A.3: A comparison between the direct numerical evaluation of the test integral (red line) and its leading order approximations by the Taylor series expansion (black dots) and by the continued fraction expansion (blue dots).

expansion (A.14). Although both approximations (A.13) and (A.14) capture the falling off of the tail at the large distances $r \to \infty$, the Taylor series expansion introduces an artificial singularity at the origin. Therefore, it is concluded that the continued fraction expansion constitutes a better approximation for $\tanh(K)$.

Since we are interested in the spatial evolution of large-scale flows, thereby substituting the leading order approximation (A.11) into modal solutions (A.6) and (A.7), and expanding the solutions in partial fractional series of K gives

$$\langle\hat{\phi}\rangle \approx -\mathrm{i}\frac{A\,K_x}{2\pi}\sum_{n=0}^{1}\frac{a_n}{K^2+\xi_n^2}, \tag{A.15}$$

$$\langle\hat{\psi}\rangle \approx -\frac{\alpha A\,K_x K_z}{2\pi\eta K^2}\sum_{n=0}^{1}\frac{a_n}{K^2+\xi_n^2}. \tag{A.16}$$

Here, the fundamental wavenumber $\xi_0 = \sqrt{3}$ stems from the continued fraction approximation (A.11) and the wavenumber dependencies are lumped into the coefficients

$$a_0 = \frac{\xi_0^2\cos(\xi_1)}{\xi_0^2-\xi_1^2}, \quad a_1 = \frac{\xi_0^2\xi_1^{-1}\sin(\xi_1)-\xi_1\sin(\xi_1)-\xi_0^2\cos(\xi_1)}{\xi_0^2-\xi_1^2}, \tag{A.17}$$

for $\xi_1 \neq \xi_0$. In the limit $\xi_1 \to 0$, these coefficients reduce to $a_0 = 1$ and $a_1 = 0$.

A.2 Large-scale flows

In polar coordinates introduced in Eqs. (3.71) and (3.73), the inverse Fourier transforms are evaluated by resorting to the Hankel transforms, yielding

$$\langle\tilde{\phi}\rangle = \frac{A}{2\pi}\cos(\theta)\sum_{n=0}^{1} a_n\xi_n K_1(\xi_n r), \tag{A.18}$$

$$\langle\tilde{\psi}\rangle = \frac{\alpha A}{4\pi\eta}\sin(2\theta)\sum_{n=0}^{1} a_n\left[2(\xi_n r)^2 - \xi_n^2 K_2(\xi_n r)\right]. \tag{A.19}$$

Note that, despite the appearance of the hyperbolic functions in the present case, the solutions to the y-averaged poloidal and toroidal functions are identical to those obtained in Chapter 3, cf. Eqs. (3.80) and (3.81).

Note that, the quantities α, A and η only appear in Eq. (A.18) and (A.19) as amplitudes, not as arguments, they do not affect the topology and the scaling characteristics of the large-scale flow, only its strength. In order to reduce the number of parameters in the display, we choose without loss of generality

$$A = \alpha = \eta = 1. \tag{A.20}$$

Consequently, the qualitative features of the large-scale flow depend only on a single free parameter, here the wavenumber of the forcing ξ_1. Since contributions from forcing with large values of ξ_1 are screened by those with small values, it is reasonable to focus on $\xi_1 \in [0, 2\pi]$.

With poloidal (A.18) and toroidal (A.19) functions, the flow characteristics are given by

$$\begin{aligned}\langle\tilde{u}_x\rangle = &-\frac{\cos(3\theta)}{\pi}\sum_{n=0}^{1} a_n\xi_n\left[(\xi_n r)^{-3} - \frac{1}{8}K_1(\xi_n r) - \frac{1}{2}(\xi_n r)^{-1}K_2(\xi_n r)\right]\\ &-\frac{\cos(\theta)}{8\pi}\sum_{n=0}^{1} a_n\xi_n K_1(\xi_n r),\end{aligned} \tag{A.21}$$

$$\begin{aligned}\langle\tilde{u}_z\rangle = &-\frac{\sin(3\theta)}{\pi}\sum_{n=0}^{1} a_n\xi_n\left[(\xi_n r)^{-3} - \frac{1}{8}K_1(\xi_n r) - \frac{1}{2}(\xi_n r)^{-1}K_2(\xi_n r)\right]\\ &+\frac{\sin(\theta)}{8\pi}\sum_{n=0}^{1} a_n\xi_n K_1(\xi_n r),\end{aligned} \tag{A.22}$$

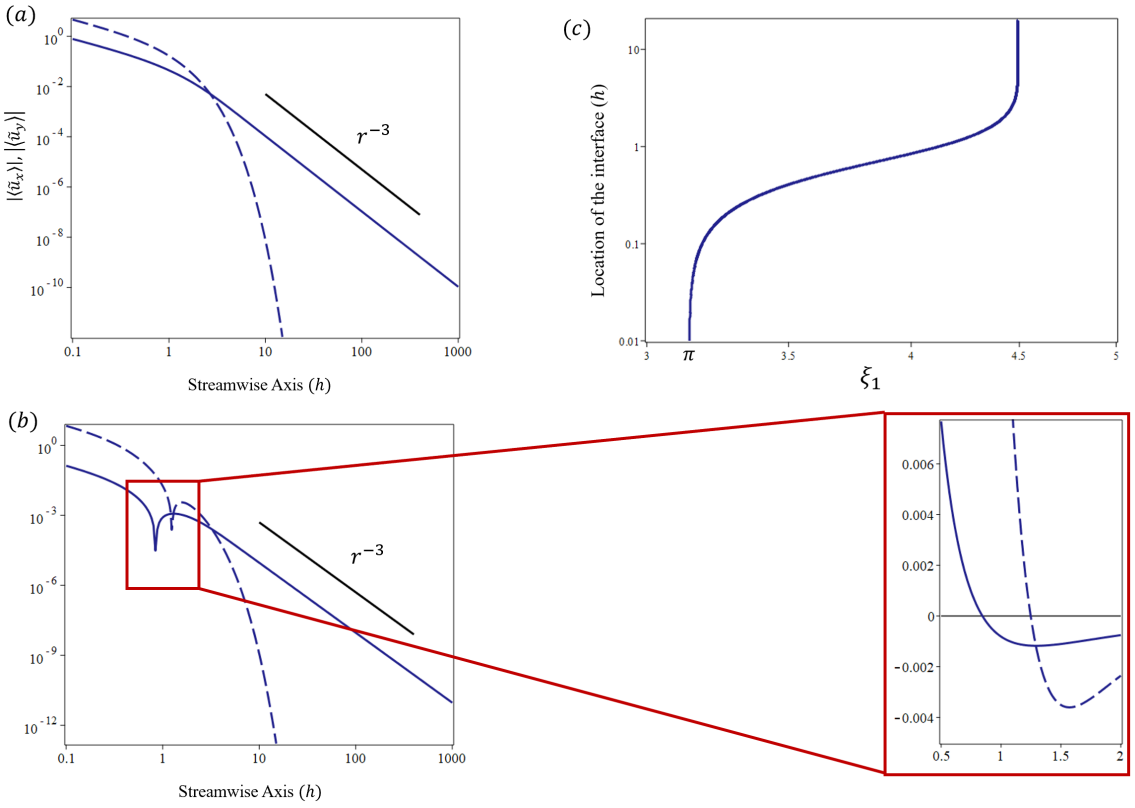

FIGURE A.4: The decay of the intensity of streamwise velocity $|\langle\tilde{u}_x\rangle|$ (sold line) and wall-normal velocity $|\langle\tilde{u}_y\rangle|$ (dashed line) along the normalised streamwise x-axis for (a) $\xi_1 = 0$, and (b) $\xi_1 = 4$, cf. Eqs (A.21) and (A.23). (c) Location of the interface along the streamwise x-axis, where $\langle\tilde{u}_x\rangle = 0$, implicitly plotted as a function of the spatial variable x and the wavenumber of the forcing ξ_1, where only $\xi_1 \in [3, 5]$ is shown, cf. Eq. (A.21).

for the in-plane velocities,

$$\langle\tilde{u}_y\rangle = -\frac{\cos(\theta)}{2\pi}\sum_{n=0}^{1} a_n \sum_{i=0}^{1} b_n^i {\xi_n^i}^3 K_1(\xi_n^i r), \tag{A.23}$$

$$\langle\tilde{\omega}_y\rangle = +\frac{\sin(2\theta)}{4\pi}\sum_{n=0}^{1} a_n \xi_n^2 \left[K_0(\xi_n r) + 2(\xi_n r)^{-1} K_1(\xi_n r)\right], \tag{A.24}$$

for the wall-normal velocity and vorticity, and

$$\begin{aligned}\langle\tilde{p}\rangle = &-\frac{\cos(2\theta)}{2\pi}\sum_{n=0}^{1} a_n \xi_n^2 \left[K_0(\xi_n r) + 2(\xi_n r)^{-1} K_1(\xi_n r)\right] \\ &-\frac{1}{2\pi}\sum_{n=0}^{1} a_n \xi_n^2 K_0(\xi_n r),\end{aligned} \tag{A.25}$$

for the pressure component.

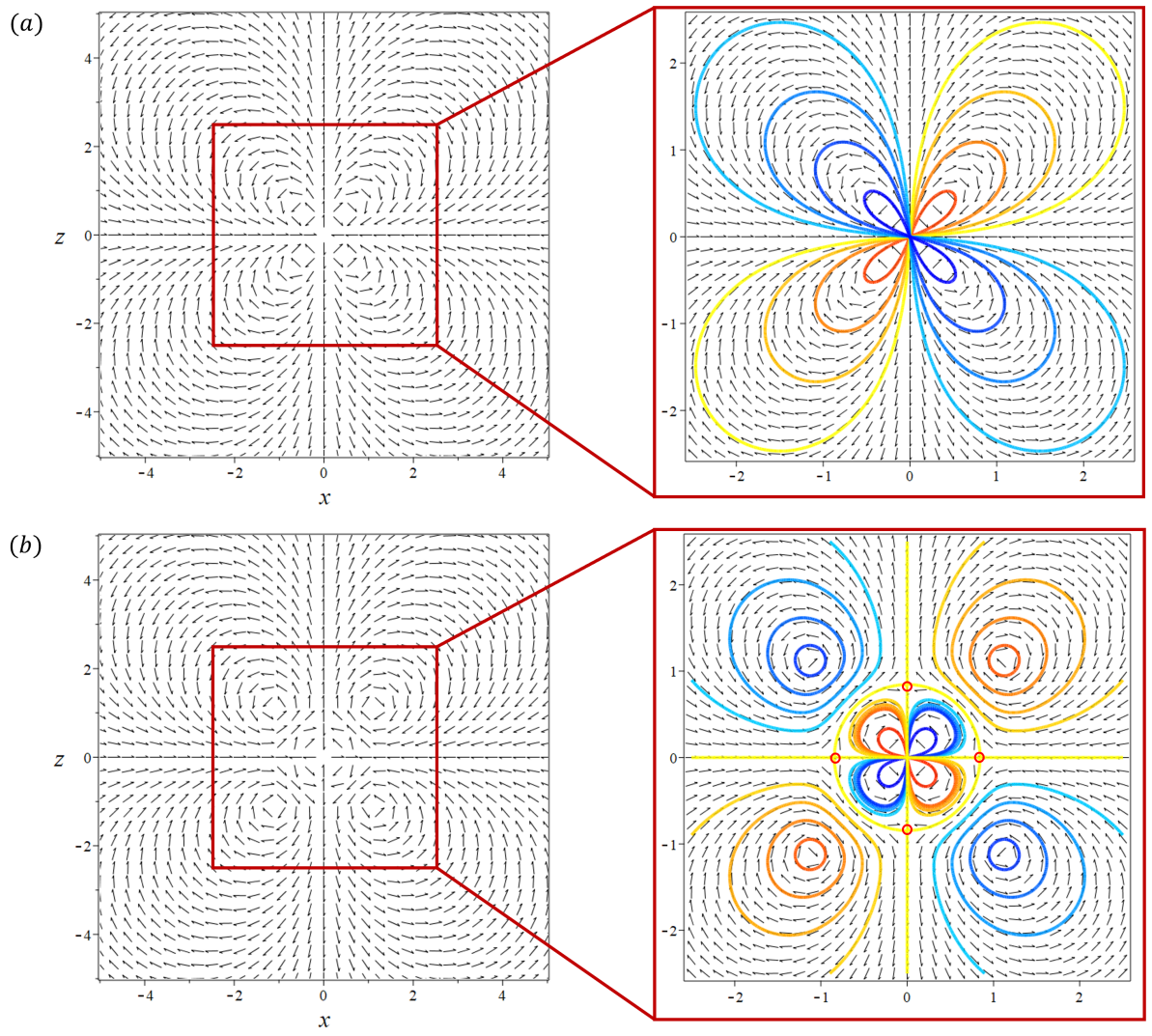

FIGURE A.5: Directional field of the y-averaged in-plane velocities, defined as $\langle\tilde{\boldsymbol{u}}_{2D}\rangle/|\langle\tilde{\boldsymbol{u}}_{2D}\rangle|$, for (a) $\gamma = 0$ and (b) $\gamma = 15$, cf. Eqs (A.21) and (A.22).

In the following, two representative cases $\xi_1 = 0$ and $\xi_1 = 4$ are considered. In parallel to figures 3.2 to 3.3 in Chapter 3, the corresponding figures for the current calculations are presented in the following. Is is seen that, despite the minor deviation in quantities, the results presented here are qualitatively the same as compared with those obtained in Chapter 3. This implies that the topology and the scaling characteristics of the large-scale flow around localised turbulent spots are generic, independent of the details of the forcing nor its boundary conditions at the walls. This observation is compatible with the topological origin of the quadrupolar flows proposed in Chapter 3.

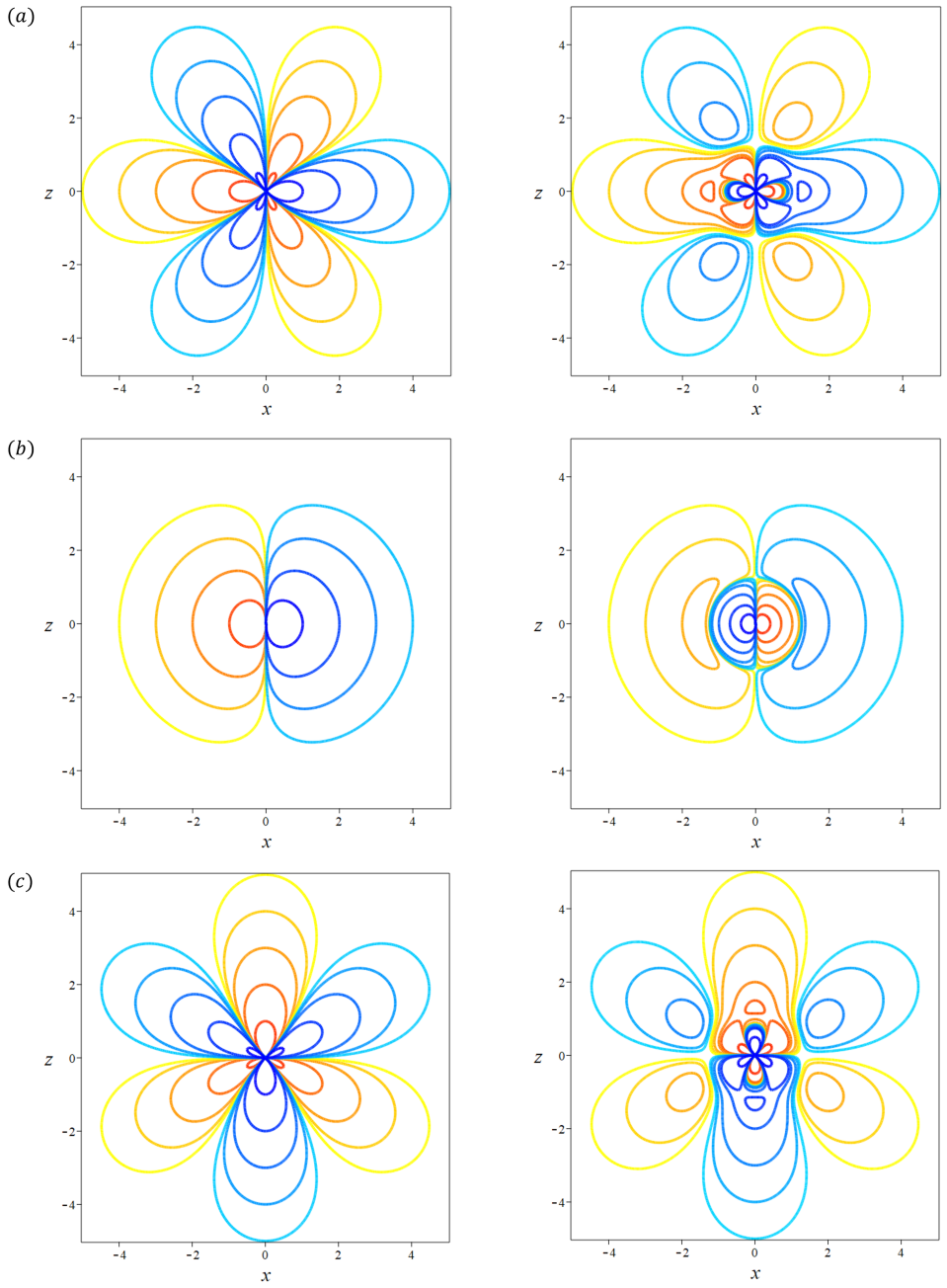

FIGURE A.6: Contour plots for the y-averaged streamwise velocity $\langle \tilde{u}_x \rangle$, where (a) $\xi_1 = 0$ and (b) $\xi_1 = 4$, cf. Eq. (A.21); wall-normal velocity $\langle \tilde{u}_y \rangle$, where (c) $\xi_1 = 0$ and (d) $\xi_1 = 4$, cf. Eq. (A.23) and; spanwise velocity $\langle \tilde{u}_z \rangle$, where (e) $\xi_1 = 0$ and (f) $\xi_1 = 4$, cf. Eq. (A.22).

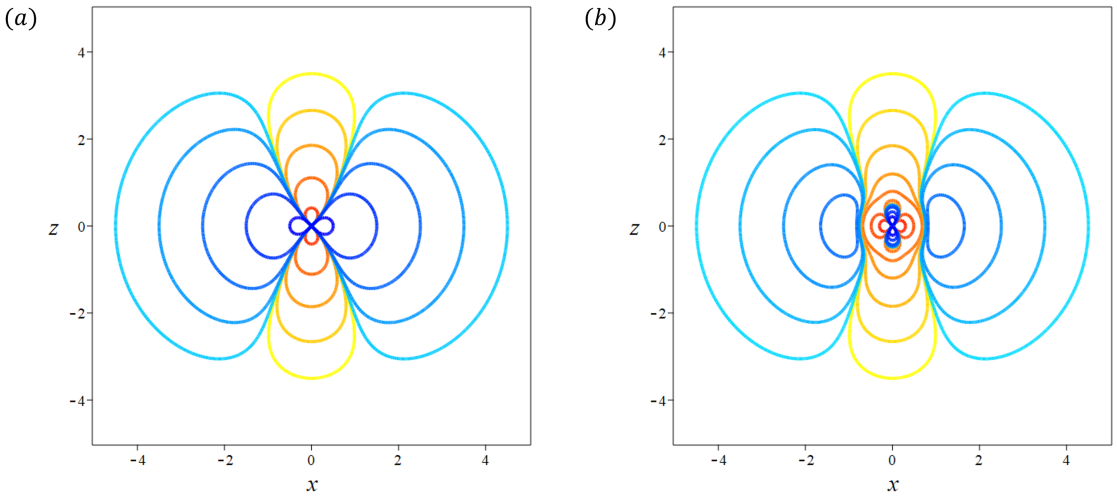

FIGURE A.7: Contours of the y-averaged pressure component $\langle \tilde{p}^{LSF} \rangle$ associated with the large-scale flows : (a) $\xi_1 = 0$ and (b) $\xi_1 = 4$, cf. Eq. (A.25).

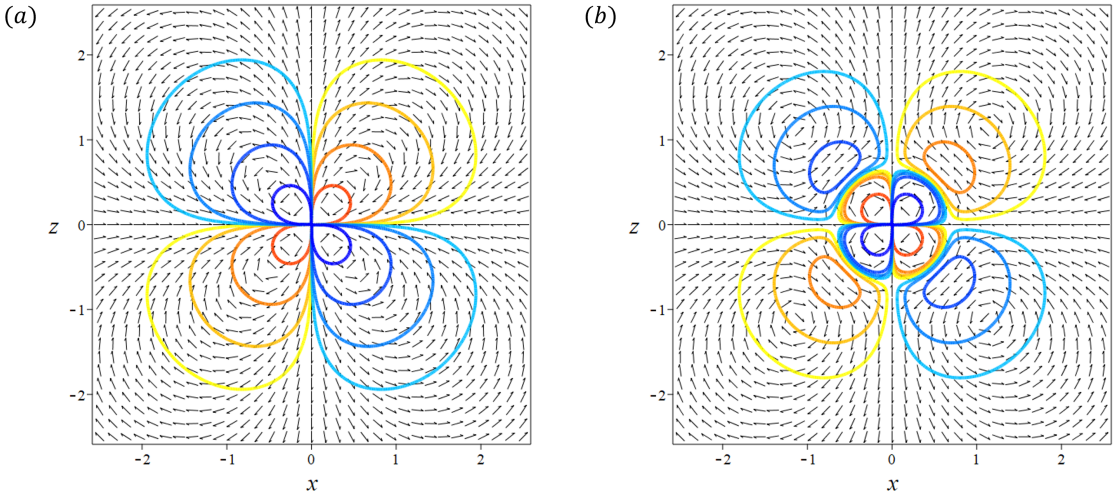

FIGURE A.8: Superposition between the contour plots of the y-averaged wall-normal vorticity $\langle \tilde{\omega}_y \rangle$, where (a) $\xi_1 = 0$ and (b) $\xi_1 = 4$, and the in-plane directional field, cf. Eq. (A.24).

Appendix B

Quadrupolar flows in shear flows between two porous walls

By contrast to the free-slip boundary conditions considered in Chapter 3, in biochemistry applications, it may be interesting to consider a linear shear flow confined between two counter-moving porous walls, e.g. membranes, where the fluid can penetrate through the walls and exchange with the external environment in the wall-normal direction, while the tangential velocities vanish at the walls. Such that, the penetrating no-slip boundary conditions [1] considered in this Chapter reads

$$\tilde{u}_x|_{y=\pm 1} = \tilde{u}_z|_{\pm 1} = 0, \quad \partial_y \tilde{u}_y|_{y\pm 1} = 0. \tag{B.1}$$

As in the previous cases, $\tilde{\cdot}$ denotes the deviation from the laminar base flow, and the walls are at $y = \pm 1$.

Moreover, in order to test the sensitivity of the Kelvin wake formalism, we propose in this appendix a different asymptotic approach.

[1] The penetrating no-slip boundary conditions were suggested to me by Prof. B. Durbrulle during my visit in CEA Saclay, France.

B.1 Governing equations

Since the planar geometry of the flow remains unchanged, as in Chapter 3, the governing equations for the perturbed flow are

$$\left(\eta^2\partial_x^2 + \partial_y^2 + \eta^2\partial_z^2\right)\tilde{\phi} = \alpha y\partial_x\tilde{\phi} - q_{\tilde{\phi}}, \tag{B.2a}$$

$$\left(\eta^2\partial_x^2 + \partial_y^2 + \eta^2\partial_z^2\right)\tilde{\psi} = \alpha y\partial_x\tilde{\psi} + \alpha\partial_z\tilde{\phi} - q_{\tilde{\psi}}, \tag{B.2b}$$

for the poloidal and toroidal functions; and

$$\tilde{p} = 2\eta\alpha\partial_x\tilde{\phi}, \tag{B.3}$$

for the perturbed pressure. Expressed in terms of the poloidal and toroidal functions, the penetrating no-slip boudary conditions (B.1) become

$$\partial\tilde{\phi}|_{y=\pm1} = 0 \quad \text{and} \quad \tilde{\psi}|_{y=\pm1} = 0. \tag{B.4}$$

It is noteworthy that, since the poloidal function no longer vanishes at the walls, the y-averaged in-plane velocity components

$$\langle\tilde{u}_x\rangle = -\eta\partial_z\langle\tilde{\psi}\rangle + \eta\partial_x\langle\partial_y\tilde{\phi}\rangle, \tag{B.5}$$

$$\langle\tilde{u}_z\rangle = +\eta\partial_x\langle\tilde{\psi}\rangle + \eta\partial_z\langle\partial_y\tilde{\phi}\rangle, \tag{B.6}$$

consist of the non-vanishing divergence-free and curl-free components characterised by the stream function $\langle\tilde{\psi}\rangle$ and the velocity potential $\langle\partial_y\tilde{\phi}\rangle$, respectively. Consequently, besides the poloidal and toroidal functions, the first order derivative of the poloidal function $\partial_y\tilde{\phi}$ needs to be calculated simultaneously.

B.1.1 Perturbative expansion

The homogeneity in x and z justifies the use of Fourier transform in the corresponding directions with wavenumbers K_x and K_z. For any function $\tilde{f}$, let $\hat{f}$ be defined as

$$\tilde{f}(x,y,z) = \frac{1}{2\pi}\iint_{-\infty}^{\infty}\hat{f}(y,K_x,K_z)e^{\mathrm{i}(K_xx+K_zz)/\eta}\mathrm{d}K_x\mathrm{d}K_z, \tag{B.7}$$

where the presence of η in the basis function signifies the smallness of wavenumbers $K_x, K_z \sim O(\eta)$ associated with the large-scale motion. Expanding the potential functions $\tilde{\phi}$ and $\tilde{\psi}$, as well as the forcing terms $q_{\tilde{\phi}}$ and $q_{\tilde{\psi}}$, using (B.7) and substituting the expansions into (3.31) gives

$$\left(\partial_y^2 - K^2\right)\hat{\phi} = \alpha y(\mathrm{i}K_x/\eta)\hat{\phi} - q_{\hat{\phi}}, \tag{B.8a}$$

$$\left(\partial_y^2 - K^2\right)\hat{\psi} = \alpha y(\mathrm{i}K_x/\eta)\hat{\psi} + \alpha(\mathrm{i}K_z/\eta)\hat{\phi} - q_{\hat{\psi}}, \tag{B.8b}$$

where $K = \sqrt{K_x^2 + K_z^2}$ is the radial wavenumber. The preceding equations are supplemented with the Fourier-transformed free-slip boundary conditions

$$\hat{\phi}\,|_{y=\pm1} = 0 \quad \text{and} \quad \partial_y\hat{\psi}\,|_{y=\pm1} = 0. \tag{B.9}$$

Analytical solution to Eqs. (B.8) is complicated due to the presence of variable coefficients involving y. More specifically, these equations take the form of the generalised Airy equation (cf. Appendix A in Drazin and Reid [8], see also Brand and Gibson [71], Dubrulle and Zahn [171]). In the absence of the forcing, Eq. (B.8a) is homogeneous, and its solutions are the superposition of Airy functions; while Eq. (B.8b) is inhomogeneous, forced by the inhomogeneity of the solutions for $\hat{\phi}$ in the spanwise direction. In the presence of source terms, both equations (B.8a) and (B.8b) are inhomogeneous, and solutions to these equations involve integrals containing Airy functions, complicating the theoretical treatment.

In his thesis, Lin [136] solved analytically the Orr-Sommerfeld equation with internal singularities by resorting to an asymptotic expansion about $Re \to \infty$. His physical intuition was that the linear instability occurred at Reynolds numbers that are large compared to unity. By contrast to Lin's approach, we focus on the cases where $Re \ll 1$, namely the Stokes regime, such that the reduced Reynolds number α, defined in Eq. (3.20), is small, permitting a perturbative expansion about $\alpha = 0$

$$\hat{\phi} = \hat{\phi}^{(0)} + \alpha\hat{\phi}^{(1)} + O(\alpha^2), \tag{B.10a}$$

$$\hat{\psi} = \hat{\psi}^{(0)} + \alpha\hat{\psi}^{(1)} + O(\alpha^2). \tag{B.10b}$$

Substituting (B.10) into (B.8) and collecting powers of α yields :

$$O(\alpha^0): \quad \left(\partial_y^2 - K^2\right)\hat{\phi}^{(0)} = -q_{\hat{\phi}}, \tag{B.11a}$$

$$O(\alpha^0): \quad \left(\partial_y^2 - K^2\right)\hat{\psi}^{(0)} = -q_{\hat{\psi}}, \tag{B.11b}$$

$$O(\alpha^1): \quad \left(\partial_y^2 - K^2\right)\hat{\phi}^{(1)} = y(\mathrm{i}K_x/\eta)\hat{\phi}^{(0)}, \tag{B.11c}$$

$$O(\alpha^1): \quad \left(\partial_y^2 - K^2\right)\hat{\psi}^{(1)} = y(\mathrm{i}K_x/\eta)\hat{\psi}^{(0)} + (\mathrm{i}K_z/\eta)\hat{\phi}^{(0)}, \tag{B.11d}$$

where the boundary conditions are required to be satisfied at each order in α such that

$$\hat{\phi}^{(0)}\,|_{y=\pm1} = \hat{\phi}^{(1)}\,|_{y=\pm1} = 0 \quad \text{and} \quad \partial_y\hat{\psi}^{(0)}\,|_{y=\pm1} = \partial_y\hat{\psi}^{(1)}\,|_{y=\pm1} = 0. \tag{B.12}$$

This treatment allows one to get around the difficulty arising from the variable coefficients. Here, the advection terms enter as first order corrections, which are, in turn, forced by the solutions of Eqs. (B.11a) and (B.11b) at leading order. Consequently, terms containing the spatial variable y are now part of the forcing, reducing the Airy equations (B.8) to a hierarchy of second-order ordinary differential equations (B.11) with constant coefficients. The latter can be solved classically using the method of undetermined coefficients as soon as the forcing terms $q_{\hat{\phi}}$ and $q_{\hat{\psi}}$ are specified.

B.2 Modal solutions

To minimise the calculation, the forcing is interpreted as arising from an external perturbation with no vertical variation. Following the discussion in Chapter 3, the forcing considered in this Chapter is

$$q_{\tilde{\phi}} = -A\,\delta'(x)\delta(z) \quad \text{and} \quad q_{\tilde{\psi}} = 0. \tag{B.13}$$

Similar to the previous cases, Eqs. (B.2) can be solved by appealing to the series expansion about α and by applying the Fourier transform introduced in Eq. (B.7), one obtains :

$$O(\alpha^0): \quad \left(\partial_y^2 - K^2\right)\hat{\phi}^{(0)} = \mathrm{i}\frac{A\,K_x}{2\pi}, \tag{B.14a}$$

$$O(\alpha^0): \quad \left(\partial_y^2 - K^2\right)\hat{\psi}^{(0)} = 0, \tag{B.14b}$$

$$O(\alpha^1): \quad \left(\partial_y^2 - K^2\right)\hat{\phi}^{(1)} = \mathrm{i}(K_x/\eta)y\hat{\phi}^{(0)}, \tag{B.14c}$$

$$O(\alpha^1): \quad \left(\partial_y^2 - K^2\right)\hat{\psi}^{(1)} = \mathrm{i}(K_x/\eta)y\hat{\psi}^{(0)} + \mathrm{i}(K_z/\eta)\hat{\phi}^{(0)}, \tag{B.14d}$$

where the corresponding Fourier transformed boundary conditions are given by

$$\partial_y \hat{\phi}^{(0)} \,|_{y=\pm 1} = \partial_y \hat{\phi}^{(1)} \,|_{y=\pm 1} = 0 \quad \text{and} \quad \hat{\psi}^{(0)} \,|_{y=\pm 1} = \hat{\psi}^{(1)} \,|_{y=\pm 1} = 0. \tag{B.15}$$

By appealing to the method of undetermined coefficients, Eqs. (B.14) are solved recursively, yielding

$$\hat{\phi}^{(0)} = -\mathrm{i}\frac{A\,K_x}{2\pi K^2}, \tag{B.16}$$

$$\hat{\psi}^{(0)} = 0, \tag{B.17}$$

for the leading order solutions; and

$$\hat{\phi}^{(1)} = -\frac{A\,K_x^2}{2\pi\eta K^4}\left[y - \frac{\sinh(Ky)}{K\cosh(K)}\right], \tag{B.18}$$

$$\hat{\psi}^{(1)} = -\frac{A\,K_x K_z}{2\pi\eta K^4}\left[1 - \frac{\cosh(Ky)}{\cosh(K)}\right], \tag{B.19}$$

for the first order corrections. Although $\hat{\phi}^{(1)}$ is an odd function of y, thereby vanishing through the y-average, its first order derivative is an even function of y, hence introducing a non-vanishing contribution to the in-plane velocities. More precisely,

$$\partial_y \hat{\phi}^{(0)} = 0, \tag{B.20}$$

$$\partial_y \hat{\phi}^{(1)} = -\frac{\alpha A K_x^2}{2\pi\eta K^4}\left[1 - \frac{\cosh(Ky)}{\cosh(K)}\right]. \tag{B.21}$$

B.3 Analytical solutions

Substituting the modal solutions into the decomposition (B.10), and subsequent to an average between the two porous walls gives

$$\langle\hat{\phi}\rangle = -\mathrm{i}\frac{A\,K_x}{2\pi K^2}, \tag{B.22}$$

$$\langle\hat{\psi}\rangle = -\frac{\alpha A K_x K_z}{2\pi\eta K^4}\left[1 - K^{-1}\tanh(K)\right], \tag{B.23}$$

$$\langle\partial_y\hat{\phi}\rangle = -\frac{\alpha A K_x^2}{2\pi\eta K^4}\left[1 - K^{-1}\tanh(K)\right]. \tag{B.24}$$

Using the first order approximation for $\tanh(K)$, cf. Eq. (A.11), and inverting the Fourier transforms, one obtains

$$\begin{aligned}\langle\tilde{\phi}\rangle &= -\frac{A}{4\pi^2}\int_0^\infty \frac{1}{K}K\mathrm{d}K\int_0^{2\pi}\mathrm{i}\cos(\varphi)e^{\mathrm{i}Kr\cos(\varphi-\theta)}\mathrm{d}\varphi\\ &= +\frac{A}{2\pi}\cos(\theta)\int_0^\infty J_1(Kr)\mathrm{d}K\\ &= +\frac{A\cos(\theta)}{2\pi r},\end{aligned} \tag{B.25}$$

for the y-averaged poloidal function,

$$\begin{aligned}\langle\tilde{\psi}\rangle &= -\frac{\alpha A}{8\pi^2\eta}\int_0^\infty \frac{1}{K^2+3}K\mathrm{d}K\int_0^{2\pi}\sin(2\varphi)e^{\mathrm{i}Kr\cos(\varphi-\theta)}\mathrm{d}\varphi\\ &= +\frac{\alpha A}{4\pi\eta}\sin(2\theta)\int_0^\infty \frac{J_2(Kr)}{K^2+3}K\mathrm{d}K\\ &= +\frac{\alpha A}{6\pi\eta}\sin(2\theta)\left[r^{-2}-\frac{3}{2}K_2(\sqrt{3}r)\right],\end{aligned} \tag{B.26}$$

for the y-averaged toroidal function, and

$$\begin{aligned}\left\langle\partial_y\tilde{\phi}\right\rangle &= -\frac{\alpha A}{8\pi^2\eta}\int_0^\infty \frac{1}{K^2+3}K\mathrm{d}K\int_0^{2\pi}\left[1+\cos(2\varphi)\right]e^{\mathrm{i}Kr\cos(\varphi-\theta)}\mathrm{d}\varphi\\ &= -\frac{\alpha A}{4\pi\eta}\left[\int_0^\infty \frac{J_0(Kr)}{K^2+3}K\mathrm{d}K-\cos(2\theta)\int_0^\infty \frac{J_2(Kr)}{K^2+3}K\mathrm{d}K\right]\\ &= +\frac{\alpha A}{6\pi\eta}\cos(2\theta)\left[r^{-2}-\frac{3}{2}K_2(\sqrt{3}r)\right]-\frac{\alpha A}{4\pi\eta}K_0(\sqrt{3}r),\end{aligned} \tag{B.27}$$

for the velocity potential. Compared with the previous cases, the velocity potential arises in responds to the non-vanishing $\tilde{u}_y$ at the porous walls and has impacts on the in-plane velocity components $\langle\tilde{u}_x\rangle$ and $\langle\tilde{u}_z\rangle$. Letting

$$A=\alpha=\eta=1, \tag{B.28}$$

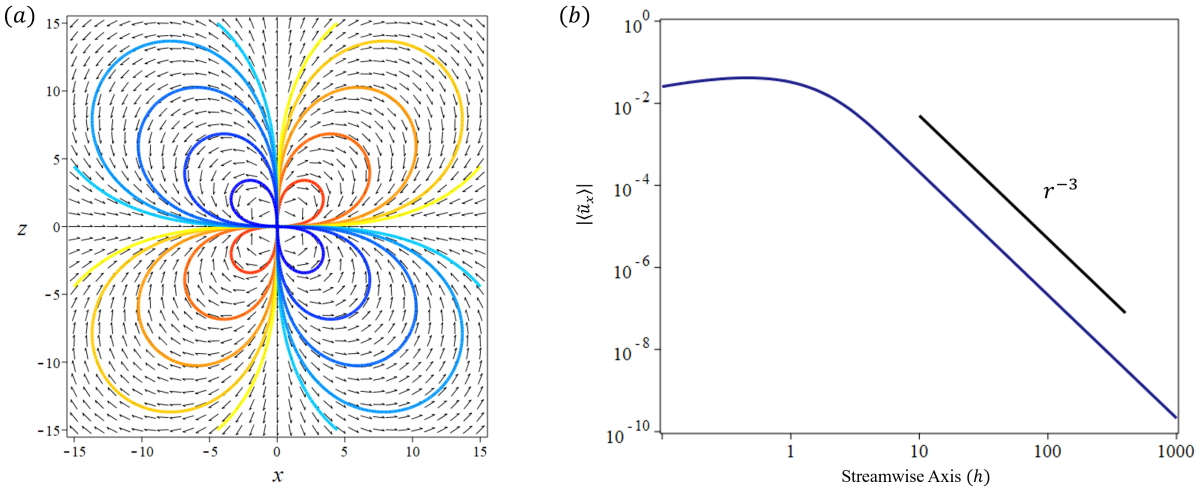

FIGURE B.1: Quadrupolar in-plane flow with penetrating no-slip boundary conditions. (a) in-plane directional field, and (b) the decay of $\langle\tilde{u}_x\rangle$ along the streamwise x-axis, cf. Eq. (B.29).

we obtain

$$\begin{aligned}
\langle\tilde{u}_x\rangle =& -\left[\sin(\theta)\partial_r + \frac{\cos(\theta)}{r}\partial_\theta\right]\langle\tilde{\psi}\rangle + \left[\cos(\theta)\partial_r - \frac{\sin(\theta)}{r}\partial_\theta\right]\langle\partial_y\tilde{\phi}\rangle \\
=& -\frac{2\cos(3\theta)}{3\pi}\left[r^{-3} - \frac{3\sqrt{3}}{8}K_1(\sqrt{3}r) - \frac{3}{2}r^{-1}K_2(\sqrt{3}r)\right] \\
&+ \frac{\sqrt{3}\cos(\theta)}{4\pi}K_1(\sqrt{3}r), \qquad \text{(B.29)} \\
\langle\tilde{u}_z\rangle =& +\left[\cos(\theta)\partial_r - \frac{\sin(\theta)}{r}\partial_\theta\right]\langle\tilde{\psi}\rangle + \left[\sin(\theta)\partial_r + \frac{\cos(\theta)}{r}\partial_\theta\right]\langle\partial_y\tilde{\phi}\rangle \\
=& -\frac{2\sin(3\theta)}{3\pi}\left[r^{-3} - \frac{3\sqrt{3}}{8}K_1(\sqrt{3}r) - \frac{3}{2}r^{-1}K_2(\sqrt{3}r)\right] \\
&+ \frac{\sqrt{3}\sin(\theta)}{4\pi}K_1(\sqrt{3}r). \qquad \text{(B.30)}
\end{aligned}$$

The in-plane directional field as well as the decay of $\langle\tilde{u}_x\rangle$ along the x axis are displayed in figure B.1. It is seen that, despite the use of very different boundary conditions and the approach in solving the governing equations, the quadrupolar angular dependence and scaling behaviours, i.e. the superposition between an algebraic and an exponential decays, of the y-averaged in-plane flow are preserved. The contours for the streamwise $\langle\tilde{u}\rangle$ and the spanwise $\langle\tilde{u}_z\rangle$ components are presented in figure B.2, which resembles those in §3 when $\gamma = 0$.

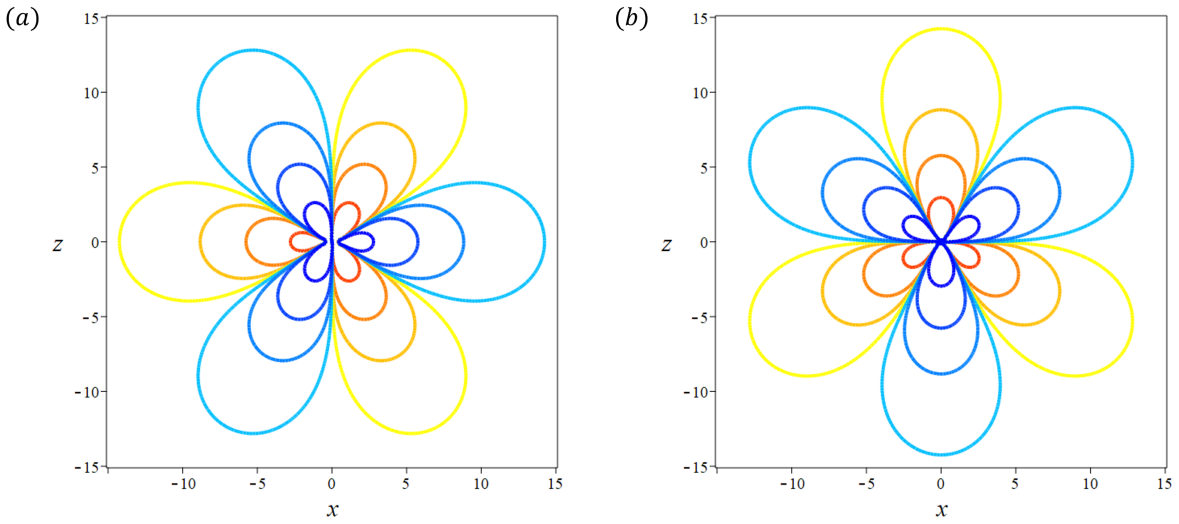

FIGURE B.2: Velocity contours with penetrating no-slip boundary conditions. (a) streamwise velocity $\langle \tilde{u}_x \rangle$, and (b) spanwise velocity $\langle \tilde{u}_z \rangle$ along the streamwise x-axis.

To trace back the origin of this unicity, it is helpful to examine the divergence of the y-averaged in-plane flow $\langle \tilde{\boldsymbol{u}}_{2D} \rangle = (\langle \tilde{u}_x \rangle, \langle \tilde{u}_z \rangle)$, which reads

$$\begin{aligned} \nabla \cdot \langle \tilde{\boldsymbol{u}}_{2D} \rangle &= + \left\{ \partial_r^2 + r^{-1}\partial_r + r^{-2}\partial_\theta^2 \right\} \langle \partial_y \tilde{\phi} \rangle \\ &= -\frac{3\cos(2\theta)}{4\pi} \left[K_0(\sqrt{3}r) + 2(\sqrt{3}r)^{-1} K_1(\sqrt{3}r) \right] - \frac{3}{4\pi} K_0(\sqrt{3}r). \end{aligned} \tag{B.31}$$

It is seen that $\nabla \cdot \langle \tilde{\boldsymbol{u}}_{2D} \rangle$ is exponentially localised, implying that the algebraically decaying component of $\langle \tilde{\boldsymbol{u}}_{2D} \rangle$ is divergence free.

Moreover, both the y-averaged wall-normal velocity

$$\begin{aligned} \langle \tilde{u}_y \rangle &= - \left\{ \partial_r^2 + r^{-1}\partial_r + r^{-2}\partial_\theta^2 \right\} \langle \tilde{\phi} \rangle \\ &= 0, \end{aligned} \tag{B.32}$$

is identically zero, except for the origin where it is undefined; while the y-averaged wall-normal vorticity

$$\begin{aligned} \langle \tilde{\omega}_y \rangle &= - \left\{ \partial_r^2 + r^{-1}\partial_r + r^{-2}\partial_\theta^2 \right\} \langle \tilde{\psi} \rangle \\ &= \frac{3\sin(2\theta)}{4\pi} \left[K_0(\sqrt{3}r) + \frac{2\sqrt{3}}{3} r^{-1} K_1(\sqrt{3}r) \right], \end{aligned} \tag{B.33}$$

is exponentially localised, indicating that the algebraically decaying component of the

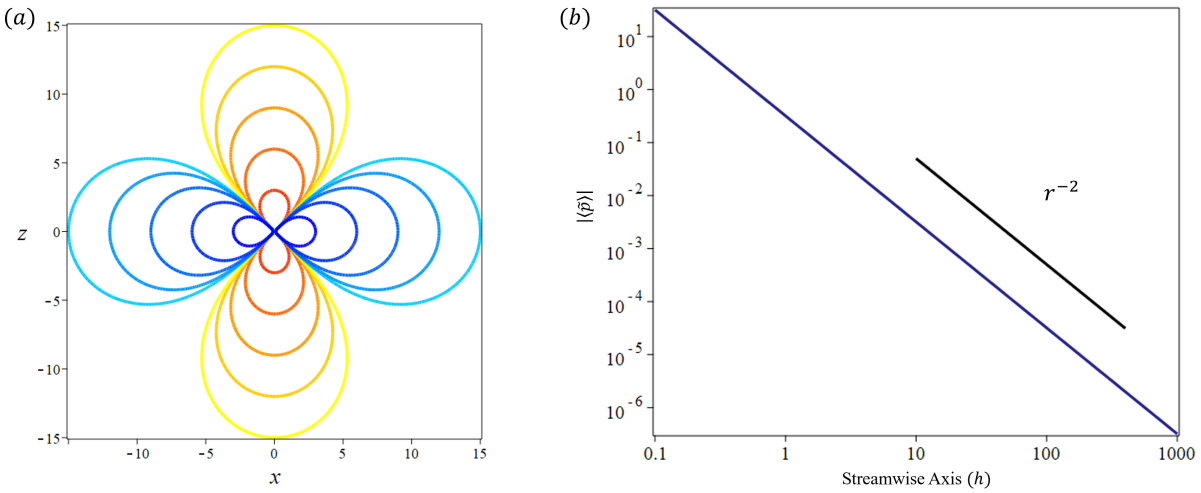

FIGURE B.3: Pressure field with penetrating no-slip boundary conditions. (a) contours, and (b) the decay of $\langle\tilde{p}\rangle$ along the streamwise x-axis, cf. Eq. (B.34).

large-scale flow is curl-free. These, together, suggest that the algebraically decaying component of the three-dimensional perturbed velocity $\tilde{\boldsymbol{u}}$ is (i) two-dimensional, (ii) harmonic. Consequently, the topological argument proposed in Chapter 3 directly applies.

However, as opposite to the previous exponential decay in Chapter 3, here, the perturbed pressure

$$\langle\tilde{p}\rangle = 2\left[\cos(\theta)\partial_r - \sin(\theta)r^{-1}\partial_\theta\right]\langle\tilde{\phi}\rangle = \frac{\cos(2\theta)}{\pi r^2}, \tag{B.34}$$

decays algebraically, despite the unicity of the quadrupolar in-plane flow. The contours of $\langle\tilde{p}\rangle$ as well as its decay along the x-axis are present in figure B.3.

To this end, it is tempting to conclude that the topology and the scaling characteristics of the algebraically decaying component of the perturbed flow around a turbulent spot are generic, independent of the boundary conditions at the walls nor the details of the turbulent spots, except for its index. However, the wall-normal velocity, the wall-normal vorticity, and the pressure depends on the boundary conditions and therefore no unicity can be concluded.

Appendix C

Quadrupolar flows in plane Poiseuille flow

Quadrupolar flows surrounding turbulent spots are robustly observed in all planar shear flows including plane Couette flow, plane Poiseuille flow and Waleffe flow. In this Appendix, we generalise the derivation scheme proposed in §3 to plane Poiseuille flow. Without loss of generality, we shall focus on a plane Poiseuille flow with the following parabola profile:

$$U_x(y) = 1 - y^2, \quad U_y = 0, \quad U_z = 0. \tag{C.1}$$

Note that, the plane Poiseuille flow differs from the previously considered plane Couette flow by the following three aspects:

i Driven mechanisms: plane Couette flow is driven by the relative motion of the plates, while plane Poiseuille flow is driven by pressure gradient in the streamwise direction;

ii Base flow profile: plane Couette flow possesses a linear flow profile, e.g. $U_x^C = y$, hence it is an odd function with respect to the wall-normal spatial variable y and

$$\partial_y U_x^{\mathrm{C}} = 1; \tag{C.2}$$

whereas plane Poiseuille flow takes a parabola shape, hence it is an even function with respect to y and

$$\partial_y U_x^{\mathrm{P}} = -2y, \tag{C.3}$$

iii Spanwise vorticity: plane Couette flow has non-vanishing integrated spanwise vorticity along y

$$\int_{-1}^{1} -\partial_y U_x^{\mathrm{C}} \mathrm{d}y = -2, \tag{C.4}$$

whereas plane Poiseuille flow has vanishing integrated spanwise vorticity along y

$$\int_{-1}^{1} -\partial_y U_x^{\mathrm{P}} \mathrm{d}y = 0, \tag{C.5}$$

where the superscript ^{C} and ^{P} denotes Couette and Poiseuille, respectively. It shall be clear in the following that the difference in (ii) the base flow implies an opposite parity for the effective forcing that leads to the quadrupolar flow.

C.1 Governing equations and forcing selection

By contrast to turbulent spots in plane Couette flow, which are stationary in an Eulerian frame, spots in plane Poiseuille flow are advected downstream. For simplicity, we assume that the plane Poiseuille spot is translated at a constant speed c. Consequently, in a frame of reference (x, y, z) that is attached to a constantly moving spot, the evolution of large-scale flows solves the following linearised Navier-Stokes equations:

$$[\partial_t + (U_x - c)\partial_x]\,\tilde{u}_x = -\partial_x \tilde{p} + \nu\nabla^2 \tilde{u}_x + q_{\tilde{u}_x} - (\partial_y U_x)\,\tilde{u}_y, \tag{C.6a}$$

$$[\partial_t + (U_x - c)\partial_x]\,\tilde{u}_y = -\partial_y \tilde{p} + \nu\nabla^2 \tilde{u}_y + q_{\tilde{u}_y}, \tag{C.6b}$$

$$[\partial_t + (U_x - c)\partial_x]\,\tilde{u}_z = -\partial_z \tilde{p} + \nu\nabla^2 \tilde{u}_z + q_{\tilde{u}_z}, \tag{C.6c}$$

satisfying the incompressibility constraint:

$$\nabla \cdot \tilde{\boldsymbol{u}} = 0. \tag{C.7}$$

Similar to §3, the forcing term $\boldsymbol{q}_{\tilde{\boldsymbol{u}}} = [q_{\tilde{u}_x}; q_{\tilde{u}_y}; q_{\tilde{u}_z}]$ arises mimicking the presence of a sustaining turbulent spot in the laminar background. Consequently, we expect that $\boldsymbol{q}_{\tilde{\boldsymbol{u}}}$

is spatially localised in the homogeneous directions x and z; whereas extended in the wall-normal direction y.

Following the arguments in §3, we drop the vertical pressure gradient and seek for invariant solutions in a co-moving Lagrangian frame

$$x_L = x - (U_x - c)\,t, \quad y_L = y, \quad z_L = z, \tag{C.8}$$

where the constant c is the advection speed of a constantly moving spot, Eqs. (C.6) can be expressed in terms of the poloidal and toroidal functions as:

$$\left(\eta^2\partial_x^2 + \partial_y^2 + \eta^2\partial_z^2\right)\tilde{\phi} = -q_{\tilde{\phi}}, \tag{C.9a}$$
$$\left(\eta^2\partial_x^2 + \partial_y^2 + \eta^2\partial_z^2\right)\tilde{\psi} = -q_{\tilde{\psi}} + \eta\alpha\left(\partial_y U_x\right)\partial_z\tilde{\phi}. \tag{C.9b}$$

Eqs. (C.9) imply that, in an Eulerian frame, we seek for stationary solutions surrounding a constantly moving spot.

At this point, it becomes clear that the governing equations for large-scale flow in planar shear flow is general, whose derivation depends only on (i) the intensity separation, which justifies the linearisation and the use of the Taylor's hypothesis; and (ii) geometric scale separation, which justifies the drop of vertical pressure gradient.

Substituting

$$\partial_y U_x = 1, \tag{C.10}$$

we recover the case of plane Couette flow as in §3; while by substituting Eq. (C.1), the governing equations for large-scale flows surrounding a constantly moving spot in plane Poiseuille flow reads:

$$\left(\eta^2\partial_x^2 + \partial_y^2 + \eta^2\partial_z^2\right)\tilde{\phi} = -q_{\tilde{\phi}}, \tag{C.11a}$$
$$\left(\eta^2\partial_x^2 + \partial_y^2 + \eta^2\partial_z^2\right)\tilde{\psi} = -q_{\tilde{\psi}} - 2\eta\alpha y\partial_z\tilde{\phi}. \tag{C.11b}$$

Comparing with the Eqs. (3.42) for plane Couette flow, the difference in base flow profile contributes to only different coefficients in the second term on the right hand side of Eq. (C.11b). Note that the spatial variable y appeared in Eq. (C.11b) is a part of the forcing not variable coefficient, hence there is no difficulty in solving for modal solutions. However, the presence of y do alter the parity of the solutions in the sense that the odd

component of the poloidal function contributes to the even part of the toroidal function. Since Eq. (C.11a) suggests that the odd component of the poloidal function can only stems from a poloidal forcing of the same parity, we concluded that, by contrast to plane Couette flow, the large-scale flow in plane Poiseuille flow must originate from the odd component of the poloidal forcing.

Given previous parity analysis into account, the minimal forcing for a constantly translating spot in plane Poiseuille flow is:

$$q_{\tilde{\phi}} = Ag(y)\delta'(x)\delta(z), \tag{C.12}$$

$$q_{\tilde{\psi}} = 0, \tag{C.13}$$

where the prime denotes $\eta\partial_x$ and the vertical variation is given by

$$g(y) = \sin(\pi y) - \gamma \sin(3\pi y). \tag{C.14}$$

The modelling for the poloidal forcing $q_{\tilde{\phi}}$ is understood in the following. For $A > 0$ and $\gamma = 0$, Eq. (C.12) models two pinwheels stacked along the y direction, with the upper pinwheel rotating clockwise in $y \in [0, 1]$, while the lower pinwheel rotating counterclockwise in $y \in [-1, 0]$, opposite to the base flow. The vertical dependence $\sin(\pi y)$ ensures that (i) the integrated spanwise vorticity along y is zero; and (ii) the forcing term satisfies the Dirichlet boundary condition at the walls.

The second mode $\sin(2\pi y)$ mimics a correction by turbulent motions inside the spot. More specifically, solving

$$A\int_0^1 g(y)\mathrm{d}y = -A\frac{2(\gamma - 3)}{3\pi} = 0, \tag{C.15}$$

we obtain $\gamma = 3$. For $A > 0$ and $\gamma < 3$, the integrated spanwise vorticity associated with the poloidal forcing is positive, opposite in sign to that of the base flow. For $A > 0$ and $\gamma > 3$, however, the poloidal forcing introduces an overall spanwise vorticity that is aligned with the base flow.

C.2 Solutions for poloidal and toroidal functions

Substituting the forcing terms (C.12) and (C.13) into Eqs. (C.11) gives:

$$\left(\eta^2\partial_x^2 + \partial_y^2 + \eta^2\partial_x^2\right)\tilde{\phi} = -Ag(y)\delta'(x)\delta(z), \tag{C.16a}$$

$$\left(\eta^2\partial_x^2 + \partial_y^2 + \eta^2\partial_x^2\right)\tilde{\psi} = -2\eta\alpha y\partial_z\tilde{\phi}. \tag{C.16b}$$

The preceding equations can be solved by resorting to the Fourier transform:

$$\tilde{f}(x,y,z) = \frac{1}{2\pi\eta}\iint_{-\infty}^{\infty}\hat{f}(y,K_x,K_z)e^{\mathrm{i}(K_x x+K_z z)/\eta}\mathrm{d}K_x\mathrm{d}K_z, \tag{C.17}$$

for an arbitrary function $\tilde{f}$. Expanding the poloidal $\tilde{\phi}$ and the toroidal $\tilde{\psi}$ functions, as well as the forcing terms $q_{\tilde{\phi}}$ and $q_{\tilde{\psi}}$, using (C.17), we obtain

$$\left(\partial_y^2 - K^2\right)\hat{\phi} = -\mathrm{i}\frac{A\,K_x}{2\pi\eta}\sum_{n=1}^{2}a_n\sin(\xi_n y), \tag{C.18a}$$

$$\left(\partial_y^2 - K^2\right)\hat{\psi} = -2\mathrm{i}\alpha K_z y\hat{\phi}, \tag{C.18b}$$

where $K = \sqrt{K_x^2 + K_z^2}$ is the radial wavenumber and

$$a_1 = 1, \quad a_2 = -\gamma, \quad \xi_1 = \pi, \quad \xi_2 = 3\pi. \tag{C.19}$$

The preceding equations are supplemented by the Fourier transformed free-slip boundary conditions

$$\hat{\phi}|_{y=\pm1} = \partial_y\hat{\psi}|_{y=\pm1} = 0. \tag{C.20}$$

Using the method of undetermined coefficients, we obtain

$$\hat{\phi} = +\mathrm{i}\frac{A\,K_x}{2\pi\eta}\sum_{n=1}^{2}a_n\frac{\sin(\xi_n y)}{K^2+\xi_n^2}, \tag{C.21}$$

$$\hat{\psi} = -\frac{\alpha A\,K_x K_z}{\pi\eta}\sum_{n=1}^{2}\frac{a_n}{(K^2+\xi_n^2)^2}\left[y\sin(\xi_n y) + \frac{2\xi_n\cos(\xi_n y)}{K^2+\xi_n^2} - \xi_n\cos(\xi_n)\frac{\cosh(Ky)}{K\sinh(K)}\right]. \tag{C.22}$$

Note that there is no complementary solution arises in $\hat{\phi}$ because the particular solution satisfies the Dirichlet boundary condition.

Applying the wall-normal averaging to the obtained modal solutions

$$\langle\hat{\phi}\rangle = \frac{1}{2}\int_{-1}^{+1} \hat{\phi}\,\mathrm{d}y = 0, \tag{C.23}$$

$$\langle\hat{\psi}\rangle = \frac{1}{2}\int_{-1}^{+1} \hat{\psi}\,\mathrm{d}y = +\frac{\alpha A\,K_x K_z}{\pi\eta\,K^2}\sum_{n=1}^{2}\frac{b_n}{K^2+\xi_n^2} \tag{C.24}$$

where

$$b_n = a_n\cos(\xi_n)/\xi_n \quad \text{such that} \quad b_1 = -\frac{1}{\pi}, \quad b_2 = \frac{\gamma}{3\pi}. \tag{C.25}$$

Note that $\langle\hat{\phi}\rangle = 0$, because it is an odd function of y. In order to understand what is happening on the poloidal field and the related flow variables, e.g. wall-normal velocity and pressure, we consider integrals from the mid-plane $y = 0$ to each walls:

$$\langle\hat{\phi}\rangle_{\text{upper}} = \int_{0}^{+1} \hat{\phi}\mathrm{d}y = +\mathrm{i}\frac{A\,K_x}{2\pi\eta}\sum_{n=1}^{2}\frac{c_n}{K^2+\xi_n^2}, \tag{C.26}$$

$$\langle\hat{\phi}\rangle_{\text{lower}} = \int_{-1}^{0} \hat{\phi}\mathrm{d}y = -\mathrm{i}\frac{A\,K_x}{2\pi\eta}\sum_{n=1}^{2}\frac{c_n}{K^2+\xi_n^2}, \tag{C.27}$$

such that their sum is zero, where

$$c_n = \xi_n^{-1}a_n - b_n \quad \text{hence} \quad c_1 = \frac{2}{\pi}, \quad c_2 = -\frac{2\gamma}{3\pi}. \tag{C.28}$$

Since $\tilde{\psi}$ is an even function of y, we have

$$\langle\hat{\psi}\rangle = \langle\hat{\psi}\rangle_{\text{upper}} = \langle\hat{\psi}\rangle_{\text{lower}}. \tag{C.29}$$

In the following, it would be sufficient to consider the integral (C.26) in the upper half of the flow region $y \in [0, 1]$, and the flow in the lower half can be recovered by:

$$\langle\hat{\phi}\rangle_{\text{lower}} = -\langle\hat{\phi}\rangle_{\text{upper}} \quad \text{and} \quad \langle\hat{\psi}\rangle_{\text{lower}} = \langle\hat{\psi}\rangle_{\text{upper}}. \tag{C.30}$$

Introducing the polar coordinates

$$K_x = K\cos\varphi, \quad K_z = K\sin\varphi, \quad x^\diamond = r^\diamond\cos\theta, \quad z^\diamond = r^\diamond\sin\theta, \tag{C.31}$$

where the spatial coordinates are re-scaled as $x^\diamond = x/\eta$ and $z^\diamond = z/\eta$, so that the spatial coordinates are normalised by the half-gap size h. Dropping the superscript $^\diamond$ and inverting Fourier transform for the y-averaged poloidal and toroidal functions gives

$$\langle\tilde{\phi}\rangle_{\text{upper}} = \frac{1}{2\pi\eta}\int_0^\infty\int_0^{2\pi}\langle\hat{\phi}\rangle_{\text{upper}}e^{\mathrm{i}Kr\cos(\varphi-\theta)}K\mathrm{d}K\mathrm{d}\varphi \tag{C.32}$$

$$= -\frac{A\cos(\theta)}{2\pi\eta^2}\sum_{n=1}^{2}c_n\left[\xi_nK_1(\xi_nr)\right], \tag{C.33}$$

for the poloidal function; and

$$\langle\tilde{\psi}\rangle_{\text{upper}} = \frac{1}{2\pi\eta}\int_0^\infty\int_0^{2\pi}\langle\hat{\psi}\rangle_{\text{upper}}e^{\mathrm{i}Kr\cos(\varphi-\theta)}K\mathrm{d}K\mathrm{d}\varphi \tag{C.34}$$

$$= -\frac{\alpha A\sin(2\theta)}{2\pi\eta^2}\sum_{n=1}^{2}b_n\left[2(\xi_nr)^{-2} - K_2(\xi_nr)\right], \tag{C.35}$$

for the toroidal function, where K_m denotes the m^{th} order modified Bessel function of the second kind as in §3.

C.2.1 Large-scale flows

From the averaged poloidal $\langle\tilde{\phi}\rangle_{\text{upper}}$ and toroidal $\langle\tilde{\psi}\rangle_{\text{upper}}$ functions, the flow variables can be recovered as:

$$\begin{aligned}\langle\tilde{u}_x\rangle_{\text{upper}} &= -\left[\sin(\theta)\partial_r + \cos(\theta)r^{-1}\partial_\theta\right]\langle\tilde{\psi}\rangle \\ &= +\frac{2\alpha A\cos(3\theta)}{\pi\eta^2}\sum_{n=1}^{2}\xi_nb_n\left[(\xi_nr)^{-3} - \frac{1}{8}K_1(\xi_nr) - \frac{1}{2}(\xi_nr)^{-1}K_2(\xi_nr)\right] \\ &\quad + \frac{\alpha A\cos(\theta)}{4\pi\eta^2}\sum_{n=1}^{2}\xi_nb_nK_1(\xi_nr),\end{aligned} \tag{C.36}$$

for the streamwise velocity;

$$\langle\tilde{u}_y\rangle_{\text{upper}} = -\left[\partial_r^2 + r^{-1}\partial_r + r^{-2}\partial_\theta^2\right]\langle\tilde{\phi}\rangle = \frac{A\cos(\theta)}{2\pi\eta^2}\sum_{n=1}^{2}\xi_n^2c_nK_1(\xi_nr), \tag{C.37}$$

for the wall-normal velocity;

$$\langle\tilde{u}_z\rangle_{\text{upper}} = +\frac{2\alpha A\sin(3\theta)}{\pi\eta^2}\sum_{n=1}^{2}\xi_n b_n\left[(\xi_n r)^{-3} - \frac{1}{8}K_1(\xi_n r) - \frac{1}{2}(\xi_n r)^{-1}K_2(\xi_n r)\right] - \frac{\alpha A\sin(\theta)}{4\pi\eta^2}\sum_{n=1}^{2}\xi_n b_n K_1(\xi_n r), \tag{C.38}$$

for the spanwise velocity;

$$\begin{aligned}\langle\tilde{\omega}_y\rangle_{\text{upper}} &= -\left[\partial_r^2 + r^{-1}\partial_r + r^{-2}\partial_\theta^2\right]\langle\tilde{\psi}\rangle \\ &= -\frac{A\alpha\sin(2\theta)}{2\pi\eta^2}\sum_{n=1}^{2}\xi_n^2 b_n\left[K_0(\xi_n r) + 2(\xi_n r)^{-1}K_1(\xi_n)\right],\end{aligned} \tag{C.39}$$

for the wall-normal vorticity; and eventually

$$\begin{aligned}\langle\tilde{p}\rangle_{\text{upper}} &= 2\eta^2\alpha\left[\cos(\theta)\partial_r - \sin(\theta)r^{-1}\partial_\theta\right]\langle\tilde{\phi}\rangle \\ &= \frac{\alpha A\cos(2\theta)}{2\pi}\left[K_0(\xi_n r) + 2(\xi_n r)^{-1}K_1(\xi_n r)\right] + \frac{\alpha A}{2\pi}\sum_{n=1}^{2}\xi_n^2 c_n K_0(\xi_n r),\end{aligned} \tag{C.40}$$

for the pressure. It is observed that, except for minor differences in coefficients, the general structures of the large-scale in-plane flow, i.e. (i) the quadrupolar angular dependence; and (ii) the superposition between an algebraic $1/r^3$ decay and an exponential decay of the opposite sign, remain unchanged.

For illustration, we consider $\gamma = 0$ and $\gamma = 15$ as in §3 and, without loss of generality, we choose $\alpha = A = \eta = 1$. Figure C.1 displays a superposition between the directional field and the y-averaged wall-normal vorticity $\langle\tilde{\omega}_y\rangle_{\text{upper}}$, which is obtained by taking the curl of the in-plane velocity components $\langle\tilde{u}_x\rangle_{\text{upper}}$ and $\langle\tilde{u}_z\rangle_{\text{upper}}$. It is seen that the exponentially localised $\langle\tilde{\omega}_y\rangle$ has opposite sign to direction of circulation of the in-plane circulation, evidencing an reversed quadrupolar flow. The contours for the pressure and velocity components are present in figures C.2 and C.3, respectively. Since plane Poiseuille flow has positive spanwise vorticity in $y \in [0, 1]$ whereas plane Couette has a spanwise vorticity of the opposite sign, the contours of flow variables associated with the poloidal function, namely $\langle\tilde{u}_y\rangle_{\text{upper}}$, $\langle\tilde{p}\rangle_{\text{upper}}$, are opposite in sign to those of plane Couette flow. On the other hand, in the lower half of plane Poiseuille flow, the spanwise vorticity of the base flow is aligned with that of the plane Couette flow, hence we expect contours for $\langle\tilde{u}_y\rangle_{\text{lower}}$, $\langle\tilde{p}\rangle_{\text{lower}}$ are similar to those in plane Couette flow. This relation is also evidenced from Eq. (C.30).

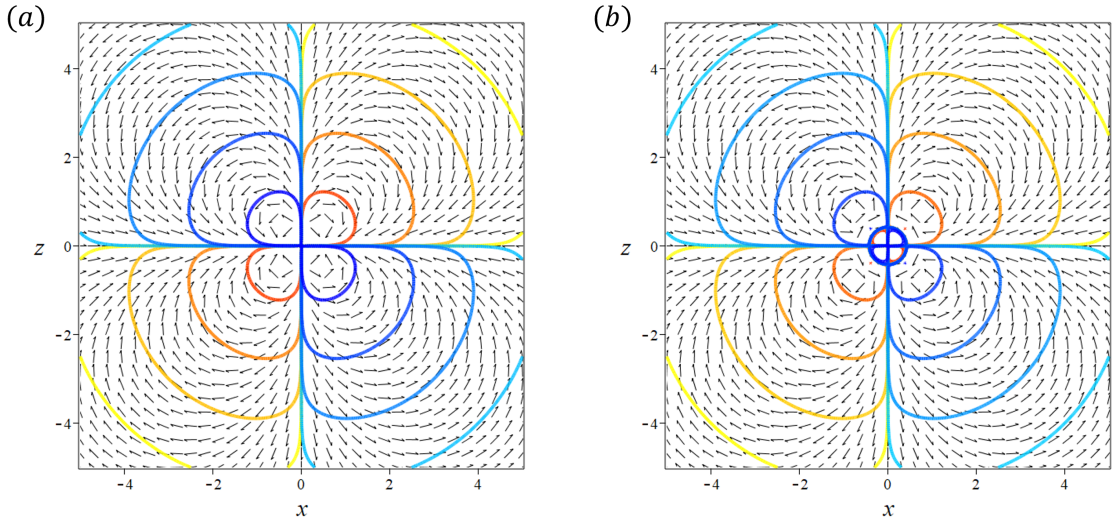

FIGURE C.1: Superposition between the contour plots of the y-averaged wall-normal vorticity $\langle\tilde{\omega}_y\rangle_{\text{upper}}$, where (a) $\gamma = 0$ and (b) $\gamma = 15$, and the in-plane directional field.

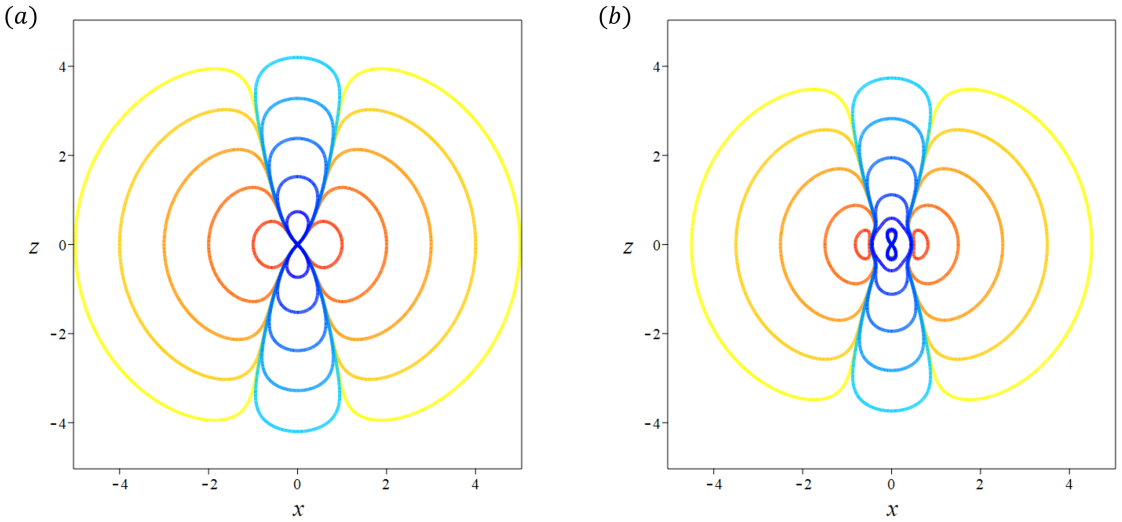

FIGURE C.2: Contours of the y-averaged pressure component $\langle\tilde{p}\rangle_{\text{upper}}$ associated with the large-scale flows: (a) $\gamma = 0$ and (b) $\gamma = 15$.

Note that the change in sign of the y-averaged poloidal function is compensated from the presence of y in term $-2\eta\alpha y\partial_z\tilde{\phi}$. Therefore, the contours of flow variables associated with the toroidal function, namely $\langle\tilde{u}_x\rangle_{\text{upper}}$, $\langle\tilde{u}_z\rangle_{\text{upper}}$, and $\langle\tilde{\omega}_y\rangle_{\text{upper}}$ are qualitatively the same as those in plane Couette flow.

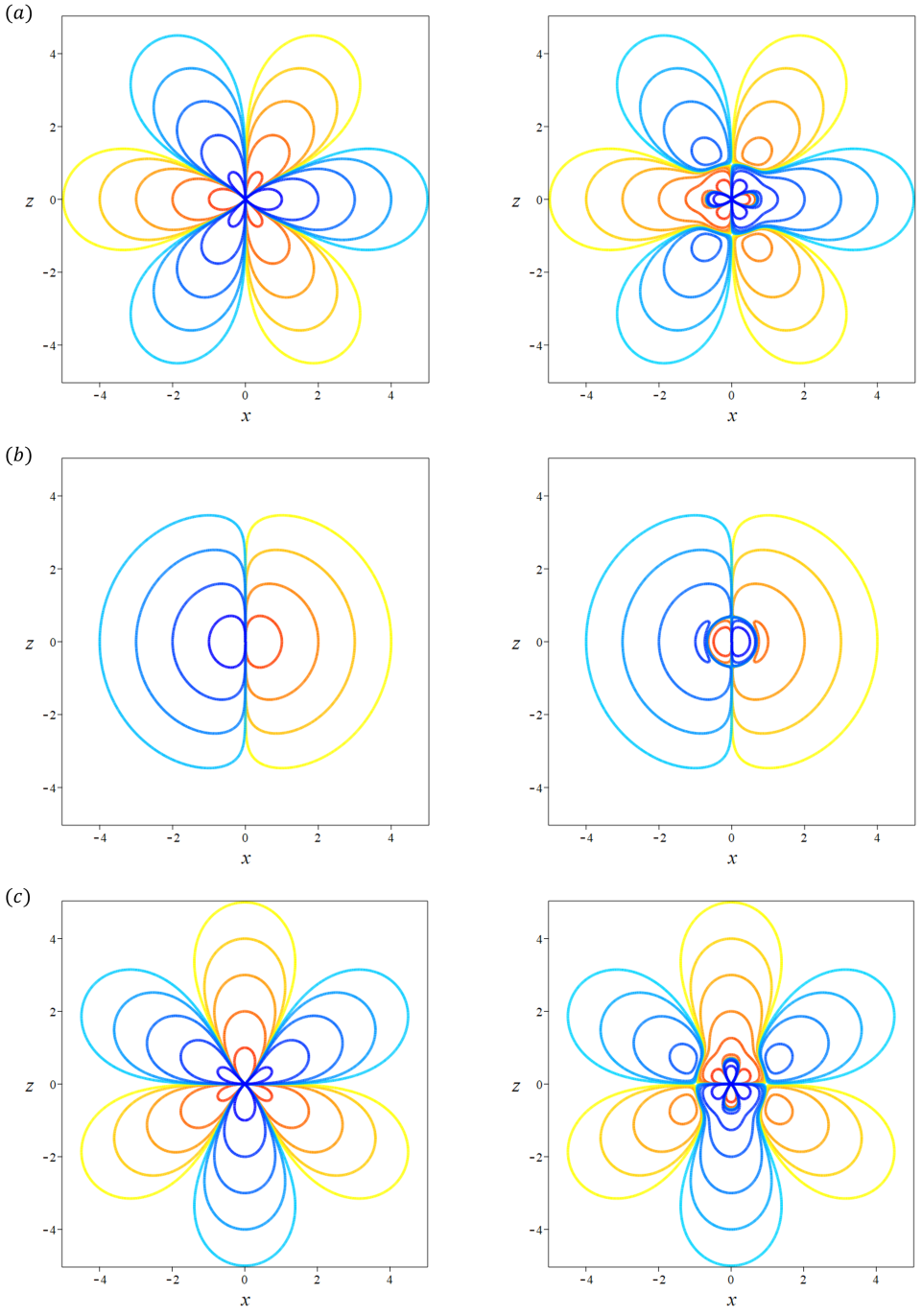

FIGURE C.3: Contour plots for the y-averaged streamwise velocity (a) $\langle\tilde{u}_x\rangle_{\text{upper}}$; (b) wall-normal velocity $\langle\tilde{u}_y\rangle_{\text{upper}}$ and; (c) spanwise velocity $\langle\tilde{u}_z\rangle_{\text{upper}}$, where left: $\gamma = 0$ and right: $\gamma = 15$.

Appendix D

Method of eigenfunction expansion

This appendix compares the method of eigenfunction expansion and the method of undetermined coefficients used in Chapter 3. More specifically, consider the following second order differential equation with Dirichlet boundary conditions

$$y'' - K^2 y = g(x), \quad \text{with} \quad y(-\pi/2) = y(\pi/2) = 0, \tag{D.1}$$

and are supplemented by the following two choices of the forcing $g(x)$:

$$\text{(i)} \quad g(x) = \cos(x), \quad \text{(ii)} \quad g(x) = \sin(x). \tag{D.2}$$

That is, the forcing (i) satisfy the Dirichlet boundary condition; while (ii) does not.

D.1 Solutions obtained from method of undetermined coefficients

In the method of undetermined coefficients, one writes the solution of Eq. (D.1) as a combination of a complementary function $y_c(x)$ (the solution with $g(x) = 0$) and a particular solution $y_p(x)$. Since, for $g(x) = 0$, the complementary solution $y_c(x)$ is given by

$$y_c(x) = A\cosh(Kx) + B\sinh(Kx). \tag{D.3}$$

For the particular solution, one assumes that $y_p(x)$ is of a similar form of $g(x)$, and the task it to determine the coefficients A and B from the Dirichlet boundary condition for the two choices of $g(x)$ in Eq. (D.1).

D.1.1 Solutions forced by an even forcing

For $g(x) = \cos(x)$, the genereal solution takes the form

$$y(x) = y_p(x) + y_c(x) = A\cosh(Kx) + B\sinh(Kx) - \frac{\cos(x)}{K^2+1}. \tag{D.4}$$

The boundary conditions are $y(-\pi/2) = y(\pi/2) = 0$, which gives $A = B = 0$. That is, since the forcing satisfies the Dirichlet boundary condition, there is no complementary solution arises to compensate the mismatch at the boundaries. In this case, the general solution reduces to the particular solution :

$$y(x) = -\frac{\cos(x)}{K^2+1}, \quad \text{for} \quad g(x) = \cos(x). \tag{D.5}$$

D.1.2 Solutions forced by an odd forcing

Similarly, for $g(x) = \sin(x)$, we have

$$y(x) = y_p(x) + y_c(x) = A\cosh(Kx) + B\sinh(Kx) - \frac{\sin(x)}{K^2+1}. \tag{D.6}$$

By contrast to the previous case, the boundary conditions, $y(-\pi/2) = y(\pi/2) = 0$, is not satisfied by the forcing, giving rise to the non-zero complementary solution

$$A = 0 \quad \text{and} \quad B = \frac{1}{K^2+1}\frac{1}{\sinh(\pi K/2)}. \tag{D.7}$$

Substitution gives

$$y(x) = \frac{1}{K^2+1}\frac{\sinh(Kx)}{\sinh(\pi K/2)} - \frac{\sin(x)}{K^2+1}. \tag{D.8}$$

D.2 Eigenfunction expansion

Now we work out the eigenfunction expansion. Denote $\phi_n(x)$ the eigenfunction associated with the eigenvalue λ_n. For operator

$$L = \mathrm{d}_x^2 - K^2, \tag{D.9}$$

then the eigenfunction and the eigenvalue are respectively

$$\phi_n(x) = \cos[(2n+1)x], \quad \lambda_n = -[K^2 + (2n+1)^2], \tag{D.10}$$

for even functions; and

$$\phi_n(x) = \sin(2nx), \quad \lambda_n = -(K^2 + 4n^2), \tag{D.11}$$

for odd functions. A linear combination for Eqs. (D.10) and (D.11) is required for $g(x)$ includes both even and odd components. However, for illustration, we consider in the following only purely even and odd forcing.

D.2.1 Solutions forced by an even forcing

For $g(x) = \cos(x)$, the solution $y(x)$ is given by

$$y(x) = \sum_{n=0}^{\infty} \frac{1}{\lambda_n} \frac{\langle g(x)|\phi_n(x)\rangle}{\langle \phi_n(x)|\phi_n(x)\rangle} \phi_n(x) \tag{D.12}$$

$$= -\sum_{n=0}^{\infty} \frac{\phi_n(x)}{K^2 + (2n+1)^2} \frac{\int_{-\pi/2}^{\pi/2} \cos(x)\cos[(2n+1)x]\mathrm{d}x}{\int_{-\pi/2}^{\pi/2} \cos[(2n+1)x]\cos[(2n+1)x]\mathrm{d}x}. \tag{D.13}$$

Note that, the integral in the denominator reads

$$\int_{-\pi/2}^{\pi/2} \cos[(2n+1)x]\cos[(2n+1)x]\mathrm{d}x = \frac{\pi}{2}, \tag{D.14}$$

while the orthogonality of $\cos[(2n+1)x]$ in the interval $x \in [-\pi/2, \pi]$ suggests only the term satisfying

$$2n+1 = 1, \quad \text{that is} \quad n = 0, \tag{D.15}$$

contributes. Substituting $n = 0$ into Eq. (D.13) gives

$$y(x) = -\frac{\phi_0(x)}{K^2+1}\frac{\pi/2}{\pi/2} = -\frac{\cos(x)}{K^2+1}, \tag{D.16}$$

in agreement with Eq. (D.5).

D.2.2 Solutions forced by an odd forcing

Since

$$\int_{-\pi/2}^{\pi/2} \sin(2nx)\sin(2nx)\mathrm{d}x = \frac{\pi}{2}, \tag{D.17}$$

then with the eigenfunction expansion

$$\begin{aligned} y(x) &= \sum_{n=0}^{\infty} \frac{1}{\lambda_n}\frac{\langle g(x)|\phi_n(x)\rangle}{\langle \phi_n(x)|\phi_n(x)\rangle}\phi_n(x) \\ &= -\sum_{n=0}^{\infty} \frac{\phi_n(x)}{K^2+4n^2}\frac{\int_{-\pi/2}^{\pi/2}\sin(x)\sin(2nx)\mathrm{d}x}{\int_{-\pi/2}^{\pi/2}\sin(2nx)\sin(2nx)\mathrm{d}x} \\ &= -\frac{2}{\pi}\sum_{n=0}^{\infty} \frac{\phi_n(x)}{K^2+4n^2}\int_{-\pi/2}^{\pi/2}\sin(x)\sin(2nx)\mathrm{d}x. \end{aligned} \tag{D.18}$$

Now the difficulty is that, there is no longer any orthogonality to simplify things and one has to evaluate the integral

$$\begin{aligned} \int_{-\pi/2}^{\pi/2}\sin(x)\sin(2nx)\mathrm{d}x &= \left\{\frac{\sin[(2n-1)x]}{2(2n-1)} - \frac{\sin[(2n+1)x]}{2(2n+1)}\right\}\Bigg|_{-\pi/2}^{+\pi/2} \\ &= -\frac{4n\cos(n\pi)}{4n^2-1}, \end{aligned} \tag{D.19}$$

such that

$$\begin{aligned} y(x) &= \frac{2}{\pi}\sum_{n=0}^{\infty}\frac{4n\cos(n\pi)}{(4n^2-1)(K^2+4n^2)}\sin(2nx) \\ &= \frac{2}{\pi}\left\{-\frac{4\sin(2x)}{3(K^2+4)} + \frac{8\sin(4x)}{15(K^2+16)} - \frac{12\sin(6x)}{35(K^2+36)} + \ldots\right\}. \end{aligned} \tag{D.20}$$

Recall the analytic solution obtained from the method of undetermined coefficients, cf. Eq. (D.8), which can be expanded in Fourier series as

$$\frac{1}{K^2+1}\frac{\sinh(Kx)}{\sinh(\pi K/2)} - \frac{\sin(x)}{K^2+1} = \sum_{n=0}^{\infty} c_n \sin(2nx). \tag{D.21}$$

The Fourier coefficients are given by

$$c_n = \frac{2}{\pi}\int_{-\pi/2}^{\pi/2} \left\{ \frac{1}{K^2+1}\frac{\sinh(Kx)}{\sinh(\pi K/2)} - \frac{\sin(x)}{K^2+1} \right\} \sin(2nx)\mathrm{d}x. \tag{D.22}$$

For $n = 0, 1, 2$, one obtains

$$c_0 = 0, \quad c_1 = -\frac{2}{\pi}\frac{4}{3(K^2+4)}, \quad c_2 = \frac{2}{\pi}\frac{8}{15(K^2+16)}, \quad c_3 = -\frac{2}{\pi}\frac{12}{35(K^2+36)}, \tag{D.23}$$

such that

$$y(x) = \frac{2}{\pi}\left\{ -\frac{4\sin(2x)}{3(K^2+4)} + \frac{8\sin(4x)}{15(K^2+16)} - \frac{12\sin(6x)}{35(K^2+36)} + \ldots \right\}, \tag{D.24}$$

in agreement with Eq. (D.20). Due to the presence of complementary solutions, which in turn arise because that the forcing does not satisfy the boundary conditions for the solutions, the orthogonal condition does not apply, and consequently, the method of eigenfunction expansion leads to an infinite sum of terms.

To conclude, for the present application of solving equations of form D.1, the method of undetermined coefficients is superior than the method of eigenfunction expansion. Therefore, the former is used in Chapter 3 and the corresponding Appendices A, B, and C.

Appendix E

Evaluate integrals involving Bessel and rational functions

This appendix contains details for calculating the integral

$$\int_0^\infty \frac{K\, J_2(Kr)}{K^2+\xi^2}\mathrm{d}K. \tag{E.1}$$

Denote $Z_m(x)$ the m^{th} order Bessel functions of the first kind $J_m(x)$, the modified Bessel functions of the second kind $K_m(x)$, and any linear combinations of these functions. The recursion formula reads

$$xZ_{m-1}(x) + xZ_{m+1}(x) = 2mZ_m(x). \tag{E.2}$$

Substituting $m = 1$ and $x = Kr$ into Eq. (E.2), then the Bessel function $J_2(Kr)$ can be expressed as [179]

$$J_2(Kr) = \frac{2}{Kr}J_1(Kr) - J_0(Kr). \tag{E.3}$$

Thus, Eq. (E.1) can be split into two integrals

$$\int_0^\infty \frac{K\, J_2(Kr)}{K^2+\xi^2}\mathrm{d}K = \frac{2}{r}\int_0^\infty \frac{J_1(Kr)}{K^2+\xi^2}\mathrm{d}K - \int_0^\infty \frac{K\, J_0(Kr)}{K^2+\xi^2}\mathrm{d}K. \tag{E.4}$$

Using the identity

$$\frac{1}{K^2+\xi^2} = \frac{1}{\xi^2}\left(1 - \frac{K^2}{K^2+\xi^2}\right), \tag{E.5}$$

the first integral on the right hand side of Eq. (E.4) can be, again, split into two, yielding

$$\int_0^\infty \frac{K\,J_2(Kr)}{K^2+\xi^2}\mathrm{d}K = +\frac{2}{\xi^2 r}\left[\int_0^\infty J_1(Kr)\mathrm{d}K - \int_0^\infty \frac{K^2 J_1(Kr)}{K^2+\xi^2}\mathrm{d}K\right] - \int_0^\infty \frac{K\,J_0(Kr)}{K^2+\xi^2}\mathrm{d}K. \tag{E.6}$$

From the integral table, cf. Gradshteyn and Ryžhik [179], it is found

$$\int_0^\infty \frac{J_m(Kr)}{K}K\mathrm{d}K = \frac{1}{r}, \tag{E.7}$$

and

$$\int_0^\infty \frac{K^m J_m(Kr)}{(K^2+\xi^2)^{\mu+1}}K\mathrm{d}K = \frac{r^\mu \xi^{m-\mu}}{2^\mu \Gamma(\mu+1)}K_{m-\mu}(\xi r), \tag{E.8}$$

for $-1 < m < 2\mu + 3/2$ and $\xi > 0$. Here, $\Gamma(\mu+1)$ is the Gamma function given by :

$$\Gamma(\mu+1) = \mu\,!, \quad \mu \in \mathbb{Z}_+, \tag{E.9}$$

where the symbol ! denotes factorial. Using these formulas, the integral (E.6) becomes

$$\int_0^\infty \frac{K\,J_2(Kr)}{K^2+\xi^2}\mathrm{d}K = \frac{2}{\xi^2 r}\left[\frac{1}{r} - \xi K_1(\xi r)\right] - K_0(\xi r). \tag{E.10}$$

This expression can be further simplified by using the recursion relation (E.2), yielding

$$\int_0^\infty \frac{K\,J_2(Kr)}{K^2+\xi^2}\mathrm{d}K = 2(\xi r)^{-2} - K_2(\xi r). \tag{E.11}$$

Appendix F

Bifurcation analysis for competitively exclusive flows

In the chapter, an example for the competitive exclusion flows is discussed. More specifically, we consider the case where $a = d = -1$ and $b = c = -3$.

Note that, for $(a - c)/(b - d) > 0$, the planar system (4.35) admits an invariant radial line

$$h = \sqrt{\frac{a-c}{b-d}}r, \tag{F.1}$$

on which the kinetic energy of the flow is determined by

$$\mathrm{d}_t|\hat{\boldsymbol{u}}| = k_s|\hat{\boldsymbol{u}}|^3 \quad \text{for} \quad k_s = \frac{ad - bc}{a - b - c + d}. \tag{F.2}$$

Depending of the slop k_s, the kinetic energy of the flow increases algebraically for $k_s > 0$, while it decreases such that the planar flow is everywhere inward on a circle of radius $|\hat{\boldsymbol{u}}|$ centred at the origin. The system is conservative if $k_s = 0$. On the other hand, if $k_s < 0$, the invariant radial line does not exists. The global behaviour of the planar flow is then characterised by the invariant coordinate axes and the fixed points on the plane Σ.

By letting $a = d = -1$ and $b = c = -3$ the planar system (4.35) becomes

$$\mathrm{d}_t r = r(\mu_1 - r^2 - 3h^2), \quad b < -1, \tag{F.3a}$$

$$\mathrm{d}_t z = h(\mu_2 - 3r^2 - h^2), \quad c < -1, \tag{F.3b}$$

and it admits an invariant radial line $h = r$, on which $k_s = -2$.

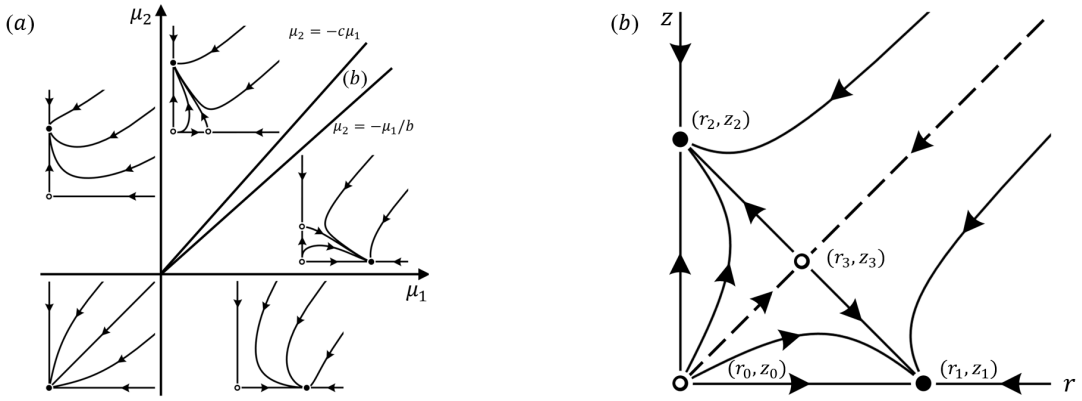

FIGURE F.1: The unfolding of the planar system (F.3): (a) regime diagram in the parameter space, where the solid circles indicate stable fixed points and the hollow ones indicate instability; and (b) the inset containing the phase portrait of the parameter wedge $\mu_2 \in (-\mu_1/b, -c\mu_1)$, where the stable manifold (with dashed line) of the saddle point (r_3, z_3) is the basin boundary separating the coherent helical and the incoherent complex-lamellar modes.

The bifurcation set as μ_1 and μ_2 are varied and the corresponding phase portraits are summarised in figure F.1.

For the planar system, the existence of the trivial fixed point (r_0, z_0) is enforced by the full group symmetry of the system (F.3). This symmetry is broken at the pitchfork bifurcations creating asymmetric fixed points (r_1, z_1) and (r_2, z_2). Before the fixed point (r_3, p_3) is created via the secondary pitchfork bifurcation from (r_1, z_1) or from (r_2, z_2), the dynamics of the flow are dominated by a single mode as all trajectories converge asymptotically to one of the three fixed points on the coordinate axes. In a wedge-shaped region $\mu_2 \in (-\mu_1/b, -c\mu_1)$ in the parameter space, where the fixed point (r_3, z_3) comes into existence, the system exhibits multistability. The stable manifold of (r_3, z_3) separates the phase plane into two regions corresponding to the basins of attraction of stable fixed points (r_1, z_1) and (r_2, z_2) : trajectories initiated below the stable manifold are attracted to (r_1, z_1), indicative of the incoherent complex-lamellar flows; whereas for those started above, the flow is helical, thereby coherent. That is, the qualitative behaviour of the system (F.3) depends on the initial conditions.

It is noteworthy that the stable manifold itself is invariant wherein the coherent and incoherent modes coexist. However, such a coexistence requires very special initial conditions that trajectories start exactly on the manifold and is unstable in the sense that minimal disturbance can kick the trajectory off the manifold, terminating the coexistence. Briefly,

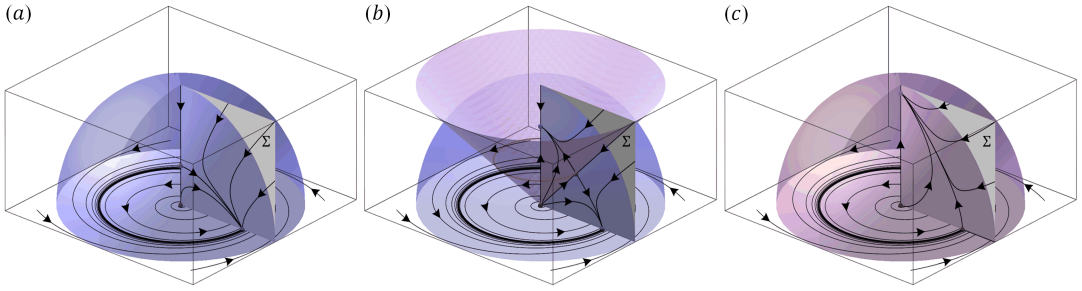

FIGURE F.2: Qualitative bifurcations of the three-dimensional flow (F.4), with a negative half of the phase space mirroring the positive half shown. Keep $b < -1$, $c < -1$, and $\mu_1 > 0$ fixed through out and let μ_2 increase from zero: (a) for $\mu_2 \in (0, -\mu_1/b)$, the flow is incoherent indicated by the blue shaded hemisphere; (b) for $\mu_2 \in (-\mu_1/b, -c\mu_1)$, the flow exhibits multistability indicated by the coexistence of the violet shaded and blue shaded regions; and (c) for $\mu_2 \in (-c\mu_1, \infty)$, the flow is coherent indicated by the violet shaded hemisphere. In three dimensions, the fixed point (r_1, z_1) corresponds to the symmetric periodic orbit indicated by the dense black circles, whereas the saddle point (r_3, z_3) corresponds to the asymmetric periodic orbit.

except for some extremely rare events, the flow exhibits a single mode dominance, reminiscent of the competitive exclusion principle in ecology: "complete competitors cannot coexist" [194]. As the flow evolves asymptotically towards a coherent or an incoherent mode resembling respectively the Beltrami and the complex-lamellar vector fields, it cannot be turbulent. In fact, such single mode dominance can be evidently indicated by peaks at $\cos\theta = 0$ or at $\cos\theta = 1$ of the probability density function of the relative helicity density $\cos\theta$ [118, 122].

Let us now consider the physical implication of the competitive exclusion in three dimensions by restoring the azimuth component φ, yielding

$$\mathrm{d}_t r = r(\mu_1 - r^2 + bh^2), \tag{F.4a}$$

$$\mathrm{d}_t h = h(\mu_2 + cr^2 - h^2), \tag{F.4b}$$

$$\mathrm{d}_t \varphi = \Omega, \tag{F.4c}$$

where, while fixed points on the z-axis remain fixed points, fixed points off the z-axis correspond to periodic orbits, and consequently the pitchfork bifurcations creating (r_1, z_1) and (r_3, z_3) correspond to Hopf bifurcations in three dimensions, see figure F.2. Let us keep $b < -1$, $c < -1$, and $\mu_1 > 0$ fixed throughout and let μ_2 increase from zero. Crossing the line $\mu_2 = 0$, a pitchfork bifurcation occurs, leaving the origin (r_0, z_0) with one positive eigenvalue and creating a stable fixed point (r_2, z_2) and its symmetric conjugate $(r_2, -z_2)$. As μ_2 increases past $\mu_2 = -\mu_1/b$, a pair of unstable periodic orbits emerge simultaneously

from (r_2, z_2) and $(r_2, -z_2)$ via subcritical Hopf bifurcations. Notice that the appearance of those two periodic orbits is enforced by the reflectional symmetry of the system (F.4), while neither of the periodic orbits has the full symmetry. Periodic orbits of this type are referred to as the asymmetric periodic orbits and refer to the orbit in the (r, φ) plane as the symmetric periodic orbit, resembling the symmetric and asymmetric branches of the pitchfork bifurcation. Due to the reflectional symmetry, asymmetric periodic orbits simultaneously collide with the symmetric periodic orbit on the line $\mu_2 = -c\mu_1$ and are annihilated in pairs, leaving the symmetric periodic orbit with one positive eigenvalue. That is, within the wedge-shaped region $\mu_2 \in (-\mu_1/b, -c\mu_1)$ in the parameter space, the system (F.4) admits up to three periodic orbits, with all periodic orbits having frequencies asymptotically approaching ω_0, and no second natural frequency exists. Observing from figure F.2(b) that the stable manifold of the asymmetric orbit spans a pseudo conical surface in three dimensions, dividing the hemispherical phase space into two regimes: the coherent region governed by the fixed point (r_2, z_2) and the incoherent region governed by the symmetric periodic orbit. As μ_2 moves around the origin in the parameter space, the flow undergoes a "regime change". Note that, the parameter space (μ_1, μ_2) represents the details, e.g. shape and amplitude, of the deviation from the exact cyclostrophic balance, the mode dominance of the competitively exclusive flows may be controlled by imposing an external pressure field.

Appendix G

List of Author's Publications

Journal Articles

- Zhe Wang, Claude Guet, Romain Monchaux, Yohann Duguet, and Bruno Eckhardt, "Quadrupolar flows around spots in internal shear flows," submitted to *J. Fluid Mech.*, June 2019.

Conference Proceedings

- Zhe Wang and P. L. So, "On Vorticity Dynamics in the Logarithmic Layer of Wall Turbulence", in *Proc. of the IMA Conf. on Turbulence, Waves and Mixing*, Cambridge, UK, pp. 106-111, July 2016.

Bibliography

[1] Lord Kelvin. On the propagation of laminar motion through a turbulently moving inviscid liquid. *Phil. Mag.*, 24(149):342–353, 1887. 1, 43, 60, 129

[2] G. I. Taylor. Phenomena connected with turbulence in the lower atmosphere. *Proc. R. Soc. Lond. A*, 94(658):137–155, 1918. 1

[3] L. Prandtl. Bemerkungen über die entstehung der turbulenz. *J. Appl. Math. Mech.*, 1(6):431–436, 1921. 1

[4] H. Tennekes and J. L. Lumley. *A First Course in Turbulence*. The MIT Press, 1972. 1, 49

[5] S. B. Pope. *Turbulent Flows*. Cambridge University Press, 2000. 1, 29, 47

[6] P. Holmes, J. L. Lumly, and G. Berkooz. *Turbulence, Coherent Structures, Dynamical Systems and Symmetry*. Cambridge University Press, 1996. 2, 9, 21, 133

[7] O. Reynolds. An experimental investigation of the circumstances which determine whether the motion of water shall be direct or sinuous, and of the law of resistance in parallel channels. *Phil. Trans. R. Soc. Lond. A*, 174:935–982, 1883. 3, 4, 10, 18, 129

[8] P. Drazin and W. Reid. *Hydrodynamic Stability*. Cambridge university press, 1981. 3, 36, 149

[9] Á. Meseguer and L. N. Trefethen. Linearized pipe flow to *r*eynolds number 10^7. *J. Comput. Phys.*, 186:178–197, 2003. 3

[10] K. Avila, D. Moxey, A. de Lozar, M. Avila, D. Barkley, and B. Hof. The onset of turbulence in pipe flow. *Science*, 333(6039):192–196, 2011. 4, 5, 6, 10

[11] B. Dubrulle and E. Knobloch. On the local stability of accretion disks. *Astron. Astrophys.*, 256(2):673–678, 1992. 4, 43, 60

[12] T. Kawata and P. H. Alfredsson. Experiments in rotating plane Couette flow – momentum transport by coherent roll-cell structure and zero-absolute-vorticity state. *J. Fluid Mech.*, 791:191–213, 2016. 4

[13] G. Stokes. On the effect of the internal friction of fluids on the motion of pendulums. *Trans. Cambridge Philos. Soc.*, 9:8–106, 1851. 4

[14] A. Sommerfeld. Ein beitrag zur hydrodynamische erklärung der turbulenten flüssigkeitsbewegungen. In *Proceedings of the 4th International Congress of Mathematicians. III.*, page 116–124, Rome, 1908. 4, 40, 41

[15] K. Avila. *Shear flow experiments: Characterizing the onset of turbulence as a phase transition.* PhD thesis, Georg-August-Universität Göttingen, 2013. 5, 6

[16] U. Brosa. Turbulence without strange attractor. *J. Stat. Phys.*, 55(5-6):1303–1312, 1989. 5

[17] M. Nishi, B. Ünsal, F. Durst, and G. Biswas. Laminar-to-turbulent transition of pipe flows through puffs and slugs. *J. Fluid Mech.*, 614:425–446, 2008. 5, 10

[18] D. Barkley, B Song, V. Mukund, G. Lemoult, M Avila, and B. Hof. The rise of fully turbulent flow. *Nature*, 526:550–553, 2015. 5, 10

[19] H. Faisst and B. Eckhardt. Sensitive dependence on initial conditions in transition to turbulence in pipe flow. *J. Fluid Mech.*, 504:343–352, 2004. 5

[20] B. Eckhardt, T. M. Schneider, B. Hof, and J. Westerweel. Turbulence transition in pipe flow. *Annu. Rev. Fluid Mech.*, 39:447–468, 2007. 5

[21] J. Peixinho and T. Mullin. Decay of turbulence in pipe flow. *Phys. Rev. Lett.*, 96: 094501, 2006. 5

[22] A. P. Willis and R. R. Kerswell. Critical behavior in the relaminarization of localized turbulence in pipe flow. *Phys. Rev. Lett.*, 98:014501, 2007. 5

[23] B. Hof, A. de Lozar, D. J. Kuik, and J. Westerweel. Repeller or attractor? selecting the dynamical model for the onset of turbulence in pipe flow. *Phys. Rev. Lett.*, 101 (21):214501, November 2008. 5, 6, 10

[24] D. Barkley. Theoretical perspective on the route to turbulence in a pipe. *J. Fluid Mech.*, 803:P1, 2016. 6

[25] Y. Pomeau. The long and winding road. *Nat. Phys.*, 12:198–199, 2016. 7

[26] L. D. Landau. On the problem of turbulence. *Dokl. Akad. Nauk SSSR*, 44(8): 339–349, 1944. 7, 129, 133

[27] E. Hopf. A mathematical example displaying features of turbulence. *Commun. Pure Appl. Math.*, 1(4):303–322, 1948. 7, 35, 133

[28] E. N. Lorenz. Deterministic nonperiodic flow. *J. Atmos. Sci.*, 20(2):130–141, 1963. 7

[29] D. Ruelle and F. Takens. On the nature of turbulence. *Commun. Math. Phys.*, 20 (3):167–192, 1971. 7, 9, 133

[30] S. Newhouse, D. Ruelle, and F. Takens. Occurrence of strange axiom a attractors near quasi periodic flows on t^m, $m \geq 3$. *Commun. Math. Phys.*, 64(1):35–40, 1978. 7

[31] J. P. Gollub and H. L. Swinney. Onset of turbulence in a rotating fluid. *Phys. Rev. Lett.*, 35(14):927–930, 1975. 8

[32] H. L. Swinney and J. P. Gollub. The transition to turbulence. *Phys. Today*, 31(8): 41–49, 1978. 8, 9, 130

[33] E. Ott. *Chaos in Dynamical Systems*. Cambridge University Press, 2002. 8

[34] P. Bergé, M. Dubois, P. Mannevillel, and Y. Pomeau. Intermittency in rayleigh-bénard convection. *J. Physics Lett.*, 41(15):341–345, 1980. 8

[35] Y. Pomeau and P. Manneville. Intermittent transition to turbulence in dissipative dynamical systems. *Commun. Math. Phys.*, 74(2):189–197, 1980. 8

[36] Y. Pomeau. Intermittency: A simple mechanism of continuous transition from order to chaos. In *Bifurcation Phenomena in Mathematical Physics and Related Topics.*, pages 155–162. Springer, Dordrecht, 1980. 8

[37] L. D. Landau and E. M. Lifshitz. *Fluid Mechanics*. Pergamon, 1987. 10, 29, 30, 87, 88

[38] P. Manneville. Transition to turbulence in wall-bounded flows: Where do we stand? *Mech. Eng. Rev.*, 3:15–00684, 2016. 10, 11, 13, 21, 26, 133

[39] Y. Pomeau. Front motion, metastability and subcritical bifurcations in hydrodynamics. *Physica D*, 23(1-3):3–11, 1986. 10, 11, 17, 129

[40] B. Song, D. Barkley, B. Hof, and M. Avila. Speed and structure of turbulent fronts in pipe flow. *J. Fluid Mech.*, 813:1045–1059, 2017. 10

[41] D. Samanta, A. De Lozar, and Bjoern Hof. Experimental investigation of laminar turbulent intermittency in pipe flow. *J. Fluid Mech.*, 681:193–204, 2011. 11, 18

[42] Javier Jiménez and Parviz Moin. The minimal flow unit in near-wall turbulence. *J. Fluid Mech.*, 225:213–240, 1991. 11

[43] Y. Pomeau. The transition to turbulence in parallel flows: A personal view. *C. R. Mécanique*, 343(3):210–218, 2015. 11

[44] M. Henkel, H. Hinrichsen, and S. Lübeck. *Non-Equilibrium Phase Transitions Volume I: Absorbing Phase Transitions*. Springer, 2008. 12

[45] G. Lemoult, L. Shi, K. Avila, S. V. Jalikop, M. Avila, and B. Hof. Directed percolation phase transition to sustained turbulence in Couette flow. *Nat. Phys.*, 12:254–258, 2016. 12, 13

[46] M. Sano and K. Tamai. A universal transition to turbulence in channel flow. *Nat. Phys.*, 12:249–253, 2016. 12

[47] X. Xiong, J. Tao, S. Chen, and L. Brandt. Turbulent bands in plane-Poiseuille flow at moderate *r*eynolds numbers. *Phys. Fluids*, 27:041702, 2015. 12

[48] M. Chantry, L. S. Tuckerman, and D. Barkley. Universal continuous transition to turbulence in a planar shear flow. *J. Fluid Mech.*, 824:R1, 2017. 12, 62

[49] H. K. Janssen. On the nonequilibrium phase transition in reaction-diffusion systems with an absorbing stationary state. *Z. Phys. B*, 42(2):151–154, 1981. 13

[50] P. Grassberger. On phase transitions in *s*chlögl's second model. *Z. Phys. B*, 47: 365–374, 1982.

[51] H. Hinrichsen. Non-equilibrium critical phenomena and phase transitions into absorbing states. *Adv. Phys.*, 49(7):815–958, 2000. 13

[52] H. K. Moffatt. Magnetostatic equilibria and analogous euler flows of arbitrarily complex topology. part 1. fundamentals. *J. Fluid Mech.*, 159:359–378, 1985. 14, 30

[53] A. Tsinober. *Turbulence Structure and Vortex Dynamics*, chapter Vortex stretching versus production of strain/dissipation, page 164–191. Cambridge University Press, 2000. 14

[54] J. C. R. Hunt, A. A. Wray, and P. Moin. Eddies, streams, and convergence zones in turbulent flows. *Center for Turbulence Research Report CTR-S88*, page 193, 1988. 14, 89

[55] J. Jeong and F. Hussain. On the identification of a vortex. *J. Fluid Mech.*, 285: 69–94, February 1995. 14, 89

[56] O. Dauchot and F. Daviaud. Streamwise vortices in plane Couette flow. *Phys. Fluids*, 7:901–903, 1995. 14, 20, 26

[57] S. Bottin, O. Dauchot, and F. Daviaud. Experimental evidence of streamwise vortices as finite amplitude solutions in transitional plane Couette flow. *Phys. Fluids*, 10(10):2597–2607, 1998. 20, 130, 135

[58] M. Couliou and R. Monchaux. Growth dynamics of turbulent spots in plane Couette flow. *J. Fluid Mech.*, 819:1–20, 2017. 14, 19, 20, 26, 27

[59] C. van Doorne and J. Westerweel. The flow structure of a puff. *Phil. Trans. R. Soc. A*, 367(1888):489–507, 2009. 14

[60] M. Shimizu and S. Kida. A driving mechanism of a turbulent puff in pipe flow. *Fluid Dyn. Res.*, 41(4):045501, 2009. 14

[61] G. Lemoult, J. L. Aider, and J. E. Wesfreid. Turbulent spots in a channel: large-scale flow and self-sustainability. *J. Fluid Mech.*, 731:R1, 2013. 14, 17, 22, 23

[62] M. Couliou and R. Monchaux. Large-scale flows in transitional plane Couette flow: A key ingredient of the spot growth mechanism. *Phys. Fluids*, 27(3):034101, 2015. 17, 22, 25, 27, 83, 131, 135

[63] M. Couliou and R. Monchaux. Spreading of turbulence in plane Couette flow. *Phys. Rev. E*, 93:013108, 2016. 14, 21, 23, 26, 27, 135

[64] J. Schumacher and B. Eckhardt. Evolution of turbulent spots in a parallel shear flow. *Phys. Rev. E*, 63:046307, 2001. 14, 15, 17, 19, 20, 21, 22, 27, 28, 62, 72, 82, 131

[65] Y. Duguet and P. Schlatter. Oblique laminar-turbulent interfaces in plane shear flows. *Phys. Rev. Lett.*, 110:034502, 2013. 17, 21, 22, 23, 27, 55, 131

[66] M. Chantry, L. S. Tuckerman, and D. Barkley. Turbulent-laminar patterns in shear flows without walls. *J. Fluid Mech.*, 791:R8, 2016. 14, 17, 20, 22, 23, 62

[67] A. Campa, T. Dauxois, D. Fanelli, and S. Ruffo. *Physics of Long-Range Interacting Systems*. Oxford University Press, 2014. 14

[68] P. Bradshaw. *An Introduction to Turbulence and its Measurement*. Pergamon Press, 1971. 14

[69] S. Lundqvist. Award ceremony speech for the 1982 nobel prize in physics. In Gösta Ekspong, editor, *Nobel Lectures, Physics 1981-199*. World Scientific Publishing Co., 1982. 14

[70] M. Lagha and P. Manneville. Modeling of plane Couette flow. i. large scale flow around turbulent spots. *Phys. Fluids*, 19:094105, 2007. 15, 23, 54, 131

[71] E. Brand and J. F. Gibson. A doubly localized equilibrium solution of plane Couette flow. *J. Fluid Mech.*, 750:R3, 2014. 15, 27, 28, 36, 59, 61, 72, 82, 131, 149

[72] O. Dauchot and P. Manneville. Local versus global concepts in hydrodynamic stability theory. *J. Phys. II*, 7(2):371–389, 1997. 17

[73] H. W. Emmons. The laminar-turbulent transition in a boundary layer-part i. *J. Aeronaut. Sci.*, 18(7):490–498, 1951. 17, 18

[74] D. R. Carlson, S. E. Widnall, and M. F. Peeters. A flow-visualization study of transition in plane Poiseuille flow. *J. Fluid Mech.*, 121:487–505, 1982. 20

[75] F. Daviaud, J. Hegseth, and P. Bergé. Subcritical transition to turbulence in plane Couette flow. *Phys. Rev. Lett.*, 69:2511–2514, 1992. 17, 20, 26, 27, 130, 135

[76] D. Coles. Transition in circular Couette flow. *J. Fluid Mech.*, 21:385–425, 1965. 17, 18, 27

[77] A. Prigent, G. Grégoire, H. Chaté, O. Dauchot, and W. van Saarloos. Large-scale finite-wavelength modulation within turbulent shear flows. *Phys. Rev. Lett.*, 89: 014501, 2002. 27

[78] A. Prigent, G. Grégoire, H. Chaté, and O. Dauchot. Long-wavelength modulation of turbulent shear flows. *Physica D*, 174(1-4):100–113, 2003. 19, 27

[79] D. Barkley and L. S. Tuckerman. Mean flow of turbulent-laminar patterns in plane Couette flow. *J. Fluid Mech.*, 576:109–137, 2007. 21, 27

[80] Y. Duguet, P. Schlatter, and D. S. Henningson. Formation of turbulent patterns near the onset of transition in plane Couette flow. *J. Fluid Mech.*, 650:119–129, 2010. 17, 20, 26, 27

[81] J. A. Carlson, A. Jaffee, and A. J. Wiles. *The Millennium prize problems*. American Mathematical Society Bookstore, 2006. 18

[82] P. Ritter, S. Zammert, B. Song, B. Eckhardt, and M. Avila. Analysis and modeling of localized invariant solutions in pipe flow. *Phys. Rev. Fluids*, 3:013901, 2018. 18

[83] M. Gad-El-Hak, R. F. Blackwelderf, and J. J. Riley. On the growth of turbulent regions in laminar boundary layers. *J. Fluid Mech.*, 110:73–95, 1981. 19

[84] F. Alavyoon, D. S. Henningson, and P. H. Alfredsson. Turbulent spots in plane Poiseuille flow-flow visualization. *Phys. Fluids*, 29(4):1328–1331, 1986. 19, 20

[85] L. Klotz, G. Lemoult, I. Frontczak, L. S. Tuckerman, and J. E. Wesfreid. Couette-Poiseuille flow experiment with zero mean advection velocity: Subcritical transition to turbulence. *Phys. Rev. Fluids*, 2:043904, 2017. 19, 20

[86] N. Tillmark and P. H. Alfredsson. Experiments on transition in plane Couette flow. *J. Fluid Mech.*, 235:89–102, 1992. 20, 26, 27, 130, 135

[87] T. Ishida, Y. Duguet, and T. Tsukahara. Transitional structures in annular Poiseuille flow depending on radius ratio. *J. Fluid Mech.*, 794:R2, 2016. 20

[88] Y. Duguet, O. Le Maitre, and P. Schlatter. Stochastic and deterministic motion of a laminar-turbulent front in a spanwisely extended Couette flow. *Phys. Rev. E*, 84 (6):066315, 2011. 20, 26

[89] A. Lundbladh and A. V. Johansson. Direct simulation of turbulent spots in plane Couette flow. *J. Fluid Mech.*, 229:499–516, 1991. 20, 22, 27, 76, 83, 130, 131

[90] O. Dauchot and F. Daviaud. Finite amplitude perturbation and spots growth mechanism in plane Couette flow. *Phys. Fluids*, 7:335–343, 1995. 20, 135

[91] J. Jiménez. Coherent structures in wall-bounded turbulence. *J. Fluid Mech.*, 842: P1, 2018. 20, 21, 45

[92] J. M. Hamilton, J. Kim, and F. Waleffe. Regeneration mechanisms of near-wall turbulence structures. *J. Fluid Mech.*, 287:317–348, 1995. 20, 45

[93] F. Li and M. R. Malik. Fundamental and subharmonic secondary instabilities of görtler vortices. *J. Fluid Mech.*, 297:77–100, 1995. 21

[94] O. J. E. Matsson and P. H. Alfredsson. Curvature- and rotation-induced instabilities in channel flow. *J. Fluid Mech.*, 210:537–563, 1990. 21

[95] P. Andersson, L. Brandt, A. Bottaro, and D. S. Henningson. On the breakdown of boundary layer streaks. *J. Fluid Mech.*, 428:29–60, 2001. 21

[96] P. J. Schmid and D. S. Henningson. *Stability and Transition in Shear Flows*. Springer, 2001. 21, 36, 39, 41, 47

[97] L. S. Tuckerman and D. Barkley. Patterns and dynamics in transitional plane Couette flow. *Phys. Fluids*, 23(4):041301, 2011. 21

[98] L. S. Tuckerman, T. Kreilos, H. Schrobsdorff, T. M. Schneider, and J. F. Gibson. Turbulent-laminar patterns in plane Poiseuille flow. *Phys. Fluids*, 26(11):114103, 2014.

[99] P. Manneville. On the transition to turbulence of wall-bounded flows in general, and plane Couette flow in particular. *Eur. J. Mech. B. Fluids*, 49:345–362, 2015. 21

[100] D. S. Henningson and J. Kim. On turbulent spots in plane Poiseuille flow. *J. Fluid Mech.*, 228:183–205, 1991. 22

[101] B. Eckhardt and R. Pandit. Noise correlations in shear flows. *Eur. Phys. J. B*, 33 (3):373–378, 2003. 22, 63

[102] P. Delplace, J. B. Marston, and A. Venaille. Topological origin of equatorial waves. *Science*, 358(6366):1075–1077, 2017. 22

[103] T. Tsukahara, T. Ishida, and Y. Duguet. Turbulent spot development in constant-mass-flux channel flow. In *14th European Turbulence Conference*, Lyon, France, 2013. 23

[104] P. M. Chaikin and T. C. Lubensky. *Principles of Condensed Matter Physics*. Cambridge University Press, 1995. 22, 24, 80

[105] J. M. Kosterlitz and D. J. Thouless. Ordering, metastability and phase transitions in two-dimensional systems. *J. Phys. C*, 6(7):1181–1203, 1973. 22

[106] T. Khapko, P. Schlatter, Y. Duguet, and D. S. Henningson. Turbulence collapse in a suction boundary layer. *J. Fluid Mech.*, 795:356–379, 2016. 24

[107] V. A. Romanov. Stability of plane-parallel Couette flow. *Funct. Anal. Appl.*, 7: 137–146, 1973. 25, 41

[108] S. Bottin. *Structures cohérentes et transition vers la turbulence par intermittence spatiotemporelle dans l'écoulement de Couette plan*. PhD thesis, Université Paris Sud - Paris XI, 1998. 26

[109] S. Bottin, O. Dauchot, and F. Daviaud. Intermittency in a locally forced plane Couette flow. *Phys. Rev. Lett.*, 79(22):4377–4380, 1997. 27, 135

[110] S. Tardu. Forcing a low Reynolds number channel flow to generate synthetic turbulent-like structures. *Computers & Fluids*, 55:101–108, 2012. 27

[111] P. Schlatter. Tails2010. Private Communication, 2010. 28

[112] C. L. Navier. Mémoire sur les lois du mouvement des fluides. *Mémoires de l'Académie Royale des Sciences de l'Institut de France*, 6:389–440, 1823. 29

[113] G. G. Stokes. On the theories of internal friction of fluid in motion, and of the equilibrium and motion of elastic solids. *Trans. Cambridge Philos. Soc*, 8:287, 1845. 29

[114] A. Tsinober. *An Informal Conceptual Introduction to Turbulence*, volume 483. Springer, 2009. 30, 32, 36

[115] A. J. Majda and A. L. Bertozzi. *Vorticity and Incompressible Flow*. Cambridge University Press, 2002. 30, 32, 33

[116] H. K. Moffatt and A. Tsinober. Helicity in laminar and turbulent flow. *Annu. Rev. Fluid Mech.*, 24:281–312, 1992. 30, 31

[117] H. K. Moffatt. Helicity and singular structures in fluid dynamics. *Proc. Natl. Acad. Sci. U.S.A.*, 111(10):3663–3670, 2014. 30

[118] R. B. Pelz, V. Yakhot, S. A. Orszag, L. Shtilman, and E. Levich. Velocity-vorticity patterns in turbulent flow. *Phys. Rev. Lett.*, 54:2505, 1985. 31, 177

[119] L. Shtilman, E. Levich, S. A. Orszag, R. B. Pelz, and A. Tsinober. On the role of helicity in complex fluid flows. *Phys. Lett. A*, 113(1):32 – 37, 1985.

[120] C. G. Speziale. *Recent advances in engineering science*, chapter On helicity fluctuations and the energy cascade in turbulence, pages 50–57. Springer, 1989.

[121] E. Levich. Coherence in turbulence: new perspective. *Old and New Concepts Phys.*, 6:239–457, 2009. 31

[122] M. M. Rogers and P. Moin. Helicity fluctuations in incompressible turbulent flows. *Phys. Fluids*, 30:2662, 1987. 31, 108, 177

[123] M. Dunajski. *Lecture notes on integrable systems*. Cambridge University, 2012. 32

[124] N. J. Hitchin, G. B. Segal, and R. S. Ward. *Integrable systems: Twistors, loop groups, and Riemann surfaces*. Oxford University Press, 2013. 32

[125] K. R. Sreenivasan. Fractals and multifractals in fluid turbulence. *Annu. Rev. Fluid Mech.*, 23:539–604, 1991. 32

[126] T. Sanada. Helicity production in the transition to chaotic flow simulated by *n*avier-*s*tokes equation. *Phys. Rev. Lett.*, 70:3035 – 3038, May 1993. 32

[127] M. Kholmyansky, M. Shapiro–Orot, and A. Trinober. Experimental observations of spontaneous breaking of reflectional symmetry in turbulent flow. *Proc. R. Soc. A*, 457(2015):2699–2717, 2001.

[128] B. Galanti and A. Tsinober. Physical space properties of helicity in quasi-homogeneous forced turbulence. *Phys. Lett. A*, 352(1–2):141–149, March 2006. 32, 34

[129] R. Hide. Superhelicity, helicity and potential vorticity. *Geophys. Astrophys. Fluid Dyn.*, 48(1-3):69–79, 1989. 34

[130] J. Guckenheimer and P. Holmes. *Nonlinear Oscillations, Dynamical Systems, and Bifurcations of Vector Fields*. Springer, 2013. 34, 80, 90, 99, 101, 106, 113

[131] J. M. Burgers. A mathematical model illustrating the theory of turbulence. *Advances in applied mechanics*, pages 171–199, 1948. 36

[132] W. M. F. Orr. The stability or instability of the steady motions of a perfect liquid and of a viscous liquid. part ii: A viscous liquid. *Proc. R. Irish Acad. A*, 27:69–138, 1907. 40, 41

[133] H. B. Squire. On the stability for three-dimensional disturbances of viscous fluid flow between parallel walls. *Proc. R. Soc. Lond. A*, 142(847):621–628, 1933. 40, 41

[134] L. Rayleigh. On the stability of certain fluid motions. *Proc. Math. Soc. Lond.*, 11: 57–70, 1880. 41

[135] L. Rayleigh. On the stability of certain fluid motions. *Proc. Math. Soc. Lond.*, 19: 67–74, 1887. 41

[136] C. C. Lin. *On the development of turbulence*. PhD thesis, California Institute of Technology, 1944. 41, 129, 149

[137] R. V. Southwell and L. Chitty. On the problem of hydrodynamic stability. i. uniform shearing motion in a viscous fluid. *Phil. Trans. R. Soc. Lond. A*, 229(670-680):205–253, 1930. 41

[138] K. M. Case. Stability of inviscid plane Couette flow. *Phys. Fluids.*, 3:143–148, 1960. 41

[139] L. A. Dikii. On the stability of plane parallel flows of an inhomogeneous fluid. *J. Appl. Math. Mech.*, 24(2):357–369, 1960. 41

[140] L. A. Dikii. On the stability of plane-parallel Couette flow. *J. Appl. Math. Mech.*, 28(2):479–483, 1964. 41

[141] D. D. Joseph. *Stability of fluid motions*, volume 27 of *Tracts in Navtural Philosophy*. Springer, 1976. 41

[142] S. A. Orszag. Numerical simulation of incompressible flows within simple boundaries: accuracy. *J. Fluid Mech.*, 49(1):75–112, 1971. 41

[143] P. S. Marcus and W. H. Press. On Green's functions for small disturbances of plane Couette flow. *J. Fluid Mech.*, 79(3):525–534, 1977. 42, 43, 55, 60

[144] L. Rayleigh. Further remarks on the stability of viscous fluid motion. *Phil. Mag.*, 28(6):609–619, 1914. 43

[145] B. J. Bayly, S. A. Orszag, and T. Herbert. Instability mechanisms in shear-flow transition. *Annu Rev Fluid Mech*, 20(1):359–391, 1988. 43

[146] T. M. Fischer and U. Dallmann. Primary and secondary stability analysis of a three-dimensional boundary-layer flow. *Phys. Fluids A*, 3:2378–2391, 1991.

[147] P. Hall and N. J. Horseman. The linear inviscid secondary instability of longitudinal vortex structures in boundary layers. *J. Fluid Mech.*, 232:357–375, 1991. 43

[148] F. Waleffe. Transition in shear flows: Nonlinear normality versus non-normal linearity. *Phys. Fluids*, 7(12):3060–3066, 1995. 43, 44, 45, 85, 130

[149] W. S. Saric. Görtler vortices. *Annu. Rev. Fluid Mech.*, 26(1):379–409, 1994. 44

[150] L. N. Trefethen, A. E. Trefethen, S. C. Reddy, and T. A. Driscoll. Hydrodynamic stability without eigenvalues. *Science*, 261(5121):578–584, 1993. 44

[151] F. Waleffe. On a self-sustaining process in shear flows. *Phys. Fluids*, 9:883–900, 1997. 44, 45, 85, 86

[152] M. Nagata. Three-dimensional finite-amplitude solutions in plane Couette flow: bifurcation from infinity. *J. Fluid Mech.*, 217:519–527, 1990. 44

[153] F. Waleffe. Three-dimensional coherent states in plane shear flows. *Phys. Rev. Lett.*, 81:4140–4143, 1998. 44, 45

[154] F. Waleffe. Exact coherent structures in channel flow. *J. Fluid Mech.*, 435:93–102, 2001. 44, 45

[155] J. S. Baggett and L. N. Trefethen. Low-dimensional models of subcritical transition to turbulence. *Phys. Fluids*, 9(4):1043–1053, 1997. 45

[156] F. Waleffe. Homotopy of exact coherent structures in plane shear flows. *Phys. Fluids*, 15:1517–1534, 2003. 45, 46

[157] H. Faisst and B. Eckhardt. Traveling waves in pipe flow. *Phys. Rev. Lett.*, 91: 224502, 2003. 45

[158] H. Wedin and R. R. Kerswell. Exact coherent states in pipe flow. *J. Fluid Mech.*, 508:333–371, 2004. 45

[159] B. Hof et al. Experimental observation of nonlinear traveling waves in turbulent pipe flow. *Science*, 305(5690):1594–1598, 2004. 45

[160] T. Ishida, Y. Duguet, and T. Tsukahara. Turbulent bifurcations in intermittent shear flows: From puffs to oblique stripes. *Phys. Rev. Fluid*, 2(7):073902, 2017. 45

[161] A. M. Savill. Recent developments in rapid-distortion theory. *Annu. Rev. Fluid Mech.*, 19:531–575, 1987. 45

[162] J. C. R. Hunt and D. J. Carruthers. Rapid distortion theory and the 'problems' of turbulence. *J. Fluid Mech.*, 212:497–532, 1990. 45, 46

[163] P. W. Terry. Suppression of turbulence and transport by sheared flow. *Rev. Mod. Phys.*, 72:109–165, 2000. 45, 46

[164] J. R. Holton. *An Introduction to Dynamic Meteorology*. American Journal of Physics, 1973. 47, 89

[165] D. G. Andrews. *An Introduction to Atmospheric Physics*. Cambridge University Press, 2010. 48

[166] L. N. Hand and J. D. Finch. *Analytical Mechanics*. Cambridge University Press, 1998. 48

[167] J. Pedlosky. *Geophysical Fluid Dynamics*. Springer, 1987. 49, 88

[168] F. Li and S. E. Widnall. Wave patterns in plane Poiseuille flow created by concentrated disturbances. *J. Fluid Mech.*, 208:639–656, 1989. 52, 54, 131

[169] S. Howison. *Practical Applied Mathematics: Modelling, Analysis, Approximation*. Cambridge university press, 2005. 56, 61

[170] F. Marqués. On boundary conditions for velocity potentials in confined flows: Application to Couette flow. *Phys. Fluids*, 2(3):729–737, 1990. 58, 62

[171] B. Dubrulle and J. P. Zahn. Nonlinear instability of viscous plane Couette flow part 1. analytical approach to a necessary condition. *J. Fluid Mech.*, 231:561–573, 1991. 59, 149

[172] S. Zammert and B. Eckhardt. Streamwise decay of localized states in channel flow. *Phys. Rev. E*, 94(4):041101, 2016. 59

[173] Lord Kelvin. On ship waves. *Proc. Inst. Mech. Eng.*, 38:641–649, 1887. 60, 61, 81

[174] W. O. Criminale and J. Q. Cordova. Effects of diffusion in the asymptotics of perturbations in stratified shear flow. *Phys. Fluids*, 29(7):2054–2060, 1986. 60

[175] S. Sridhar and N. K. Singh. The shear dynamo problem for small magnetic Reynolds numbers. *J. Fluid Mech.*, 664:265–285, 2010. 60

[176] A. D. D. Craik and W. O. Criminale. Evolution of wavelike disturbances in shear flows: a class of exact solutions of the Navier-Stokes equations. *Proc. Royal Soc. Lond*, 406(1830):13–26, 1986. 60

[177] G. I. Taylor. The spectrum of turbulence. *Proc. Royal Soc. Lond*, 164(919):476–490, 1938. 60

[178] M. J. Lighthill. *Waves in Fluids*. Cambridge University Press, 2001. 61

[179] I. S. Gradshteyn and I. M. Ryžhik. *Table of Integrals, Series, and Products*. Academic Press, 2014. 69, 173, 174

[180] M. Abramowitz and I. A. Stegun. *Handbook of Mathematical Functions: with Formulas, Graphs, and Mathematical Tables*. Courier Corporation, 1965. 71

[181] J. Jost. *Riemannian Geometry and Geometric Analysis*. Springer, 1995. 80

[182] S. Lefschetz. *Introduction to Topology*. Princeton University Press, 1949. 80

[183] J. R. Blake. A note on the image system for a stokeslet in a no-slip boundary. *Math. Proc. Cambridge Phil. Soc.*, 70(2):303–310, 1971. 84

[184] N. Liron and S. Mochon. Stokes flow for a stokeslet between two parallel flat plates. *J. Eng. Math.*, 10(4):287–303, 1976. 84

[185] E. Grenier and T. T. Nguyen. Green function of Orr-Sommerfeld equations away from critical layers. *SIAM J. Math. Anal.*, 51(2):1279–1296, 2019. 84

[186] J. Moehlis, H. Faisst, and B. Eckhardt. A low-dimensional model for turbulent shear flows. *New J. Phys.*, 6:56, 2004. 85

[187] J. Moehlis, H. Faisst, and B. Eckhardt. Periodic orbits and chaotic sets in a low-dimensional model for shear flows. *SIAM Journal on Applied Dynamical Systems*, 4(2):352–376, 2005. 85, 128

[188] P. Hall and S. Sherwin. Streamwise vortices in shear flows: harbingers of transition and the skeleton of coherent structures. *J. Fluid Mech.*, 661:178–205, 2010. 85

[189] G. Iooss and W. F. Langford. Conjectures on the routes to turbulence via bifurcations. *Ann. N.Y. Acad. Sci.*, 357(1):489–505, 1980. 87, 94, 133

[190] W. P. Winn, S. J. Hunyady, and G. D. Aulich. Pressure at the ground in a large tornado. *J. Geophys. Res.*, 104(D18):22067–22082, 1999. 89

[191] N. O. D. Rennó and H. B. Bluestein. A simple theory for waterspouts. *J. Atmos. Sci.*, 58(8):927–932, 2001. 89

[192] N. O. Rennó, M. L. Burkett, and M. P. Larkin. A simple thermodynamical theory for dust devils. *J. Atmos. Sci.*, 55(21):3244–3252, 1998. 89

[193] P. Gaspard. Broken $\mathbb{Z}_2$ symmetries and fluctuations in statistical mechanics. *Phys. Scr.*, 86(5):058504, 2012. 94

[194] G. Hardin. The competitive exclusion principle. *Science*, 3409:1292–1297, 1960. 97, 177

[195] J. Guckenheimer and P. Holmes. Local codimension two bifurcations of flows. Private communication, 2016. 99

[196] A. A. Berryman. The orgins and evolution of predator-prey theory. *Ecology*, 73(5): 1530–1535, 1992. 105

[197] H. Y. Shih, T. L. Hsieh, and N. Goldenfeld. Ecological collapse and the emergence of travelling waves at the onset of shear turbulence. *Nat. Phys.*, 12:245–248, 2016. 105

[198] P. Holmes. Unfolding a degenerate nonlinear oscillator: a codimension two bifurcation. *Ann. N.Y. Acad. Sci.*, 357(1):473–488, 1980. 107

[199] L. Shtilman, R. B. Pelz, and A. Tsinober. Numerical investigation of helicity in turbulent flow. *Comput. Fluids*, 16(3):341–347, 1988. 109

[200] J. L. Kaplan and J. A. Yorke. Preturbulence: a regime observed in a fluid flow model of *l*orenz. *Commun. Math. Phys.*, 67(2):93–108, 1979. 111

[201] J. A. Yorke and E. D. Yorke. Metastable chaos: The transition to sustained chaotic behavior in the *l*orenz model. *J. Stat. Phys.*, 21(3):263–277, 1979. 111

[202] R. C. Hilborn. *Chaos and nonlinear dynamics: an introduction for scientists and engineers*. Oxford University Press, 2000. 112, 114, 115

[203] Y. A. Kuznetsov. *Elements of Applied Bifurcation Theory*, volume 112. Springer, 2013. 113

[204] M. H. Jensen, P. Bak, and Tomas Bohr. Complete devil's staircase, fractal dimension, and universality of mode-locking structure in the circle map. *Phys. Rev. Lett.*, 50(21):1637, 1983. 115

[205] C. Grebogi, E. Ott, and J. A. Yorke. Chaos, strange attractors, and fractal basin boundaries in nonlinear dynamics. *Science*, 238:632–638, 1987. 122

[206] J. Barnett, D. R. Gurevich, and R. O. Grigoriev. Streamwise localization of traveling wave solutions in channel flow. *Phys. Rev. E*, 95(3):033124, 2015. 131

[207] Z. Wang, C. Guet, R. Monchuax, Y. Duguet, and B. Eckhardt. Quadrupolar flows around spots in internal shear flows. Submitted to J. Fluid Mech., 2019. 132

[208] H. S. Wall. *Analytic theory of continued fractions*. Courier Dover Publications, 2018. 138